Cranfield UNIVERSITY

Gautam Pulugundla

CFD Design Analysis of Ventilated Disc Brakes

School of Engineering

MSc by Research Thesis

Academic Year 2007-2008

School of Engineering

MSc by Research Thesis

Academic Year 2007-2008

Gautam Pulugundla

CFD Design Analysis of Ventilated Disc Brakes

Supervisor: Dr. David MacManus
Academic Year 2007 to 2008

Abstract

This thesis reports the numerical investigation of the automotive ventilated disc brake rotor. Disc brakes operate on the principle of friction by converting kinetic energy into heat energy. The main objective of a disc brake rotor is to store this heat energy and dissipate it as soon as possible. This work is carried out in a area where there is very limited understanding.

Commercial CFD code FLUENT was used for carrying out the simulations with the rotor rotating in still air. Only one passage and blade were simulated as all the rotor passages were identical. Uniform temperatures were used on the rotor to simulate the braking condition.

Sixteen different blade angle sets were simulated and the range of blade angles having the best aero-thermal performance were identified using mass flow rate, rate of heat dissipation and temperature uniformity as performance metrics. The effect of rotational speed and rotor temperature (corresponding to various braking conditions) on the aero-thermal performance was evaluated. The rotor speed and temperature were observed to have significant effect on the rotor performance.

The number of blades in the ventilated disc brake rotor was also varied and was observed to have an impact on the aero-thermal performance of the disc brake rotor. Detailed design changes like inlet chamfer, blade leading edge rounding, and variable thickness blade and passage aspect ratio were incorporated. All these changes did have an effect on the aero-thermal performance of the disc brake rotor. The inlet chamfer and the leading edge rounding improved both the rate of heat transfer and the temperature uniformity. The variable thickness blade and the lower aspect ratio passage improved the temperature uniformity of the rotor.

Acknowledgements

I wish to express my sincere gratitude to my project supervisor Dr D MacManus for his encouragement, guidance and expertise, to all at Alcon Components for their generous support. I also express my gratitude to Dr. Les Oswald at the Cranfield University IT department for his help while using the high performance computing facility. Last but not the least I would also want to thank my parents and my brother for their support without which this would not have been possible.

TABLE OF CONTENTS

LIST OF FIGURES

1. INTRODUCTION

2. LITERATURE REVIEW

3. DESIGN PARAMETERS

4. METHODOLOGY

5. DEVELOPMENT OF A CFD MODEL

6. PARAMETRIC STUDY- RESULTS AND DISCUSSION

7. DETAILED DESIGN CHANGES AND ANALYSIS

APPENDIX A: RESIDUAL CONVERGENCE PLOTS

NOTATION

CFD: Computational Fluid Dynamics.

GCI: Grid Convergence Index.

Q: Heat transfer rate (W).

h: Heat transfer coefficient (W/m^{2}K).

A: Area (m^2).

T: Temperature (K).

σ: Stefan-Boltzmann constant.

ε: Emissivity.

V: Velocity (m/sec).

ξ : Correlation factor.

D: Diameter (m).

Z: Optimum number of blades.

t: Blade thickness (m)

Nu: Nusselt number.

Re: Reynolds number.

l: Length of the passage (m)

HP: Heat power exchanged (W)

TP: Total power exchanged (W)

β_1: Inlet angle (degrees)

β_2: Outlet angle (degrees)

AR: Aspect ratio.

r: Refinement ratio.

p: Order of the discretisation scheme.

E: Estimated fractional error.

F_s: Factor of safety coefficient.

ρ: Density (Kg/m^3)

P: Pressure (Pa)

λ : Thermal conductivity (W/m-K)

T.D.I: Thermal Distortion Index.

$\dot{m}$: Mass flow rate (kg/sec).

u: Blade speed (m/sec).

C: Relative velocity (m/sec).

Sub-scripts

cond: Conduction.

DC: Disc and wheel carrier interface.

D: Disc.

C: Carrier.

amb/∞: Ambient.

o: Outlet.

i: Inlet.

h: Hydraulic.

atm: Atmospheric.

p: Constant pressure.

op: Operating condition.

w: Wall condition.

f: Fluid.

r: Radial.

t: Tangential.

max: Maximum.

min: Minimum.

s: Surface

1

INTRODUCTION

In this chapter a brief history of brakes and the basic functions of a disc brake are discussed. Advantages of disc brakes over drum brakes are reviewed. The various failure modes of disc brakes like warping, cracking and squeal are discussed. The motivation, aims and objectives of the current project are also presented.

1.0. Historical development of brakes

The main purpose of a brake system is to slow the vehicle or to stop it completely within a reasonable amount of time. A brake system must therefore be reliable in order to provide the operator with a better control.

Any moving vehicle contains kinetic energy by virtue of its motion. The faster the vehicle moves the higher is its momentum or kinetic energy. This energy is proportional to the square of the vehicle's speed. Most brakes use the principle of *friction* to convert this kinetic energy into heat energy. The brakes must therefore store and dissipate all this heat into the surroundings before subsequent braking stages to have a good braking efficiency.

Over the past centuries, as the technology of transportation has increased, the brake systems have also started becoming more reliable and at the same time more complex. During the early 19th century when animal carriages were used for transportation, the animal's power was used for both acceleration and deceleration. Slowly, this was replaced by manually applied friction surfaces that were directly applied to the wheel. These friction surfaces were generally made of wood (fig 1.1). But these had lots of drawbacks and one of them was that it was very difficult to operate in wet conditions.

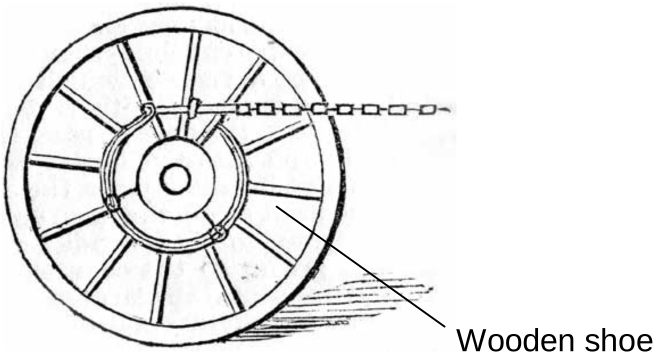

Fig 1.1: Brake system of a horse-carriage (taken from internet source *www.howstuffworks.com*)

Then with the advent of new innovative automotive designs came the invention of *drum brakes* by Louis Renault in 1902. The drum brake system mainly consists of a brake shoe. This brake shoe acts as a friction device and expands internally onto the wheel on the application of force (fig 1.2). In the initial stages, the shoes were operated mechanically by levers and cables. From the 1930s the mechanical system was replaced by a hydraulic system which used cylinders and pistons.

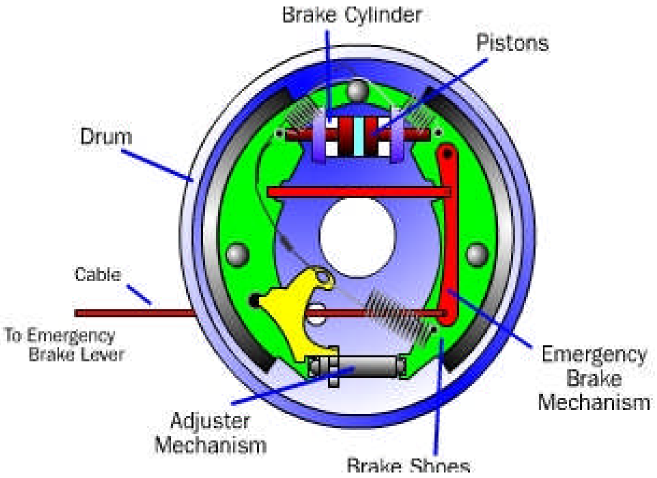

Fig 1.2: A typical drum brake system (taken from internet source *www.howstuffworks.com*)

1.1. Disc brakes

Disc brakes were patented by Frederick William Lanchester in 1902 but the commercial use of these brakes started in the early 1950s. The brake system consists of a rotor made of cast iron or ceramic mounted on to the wheel (fig 1.3). To achieve the braking action, some form of friction material called brake pads is forced onto the disc brake rotor. Piston which moves inside a cylinder pushes the brake pad onto the rotor. This movement of the piston is achieved by the means of a hydraulic fluid. The whole piston-cylinder assembly is machined inside a heavy casting called a calliper. The number of pistons inside the calliper may range from 2 to 4 depending on the requirement.

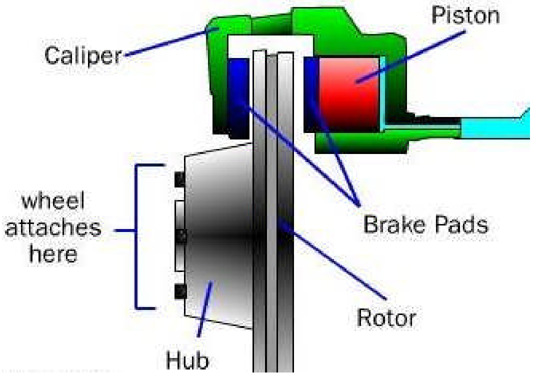

Fig 1.3: Schematic of the hydraulic fluid flow into the rotor of disc brake system (taken from internet source *www.howstuffworks.com*)

One of the important parts of a disc brake system is the rotor. The heat energy produced after the braking action is stored in the brake disc rotor and as mentioned in section 1.1, it is important to dissipate this heat before the subsequent braking action in order to prevent the rotor from thermal distortion. The design of various disc brakes therefore changes. Some disc brakes are manufactured as a solid cast iron cylinder whereas others haves vanes which are joined together by the braking surfaces called the inboard and the outboard surface. These types of disc brakes are called *ventilated* disc brakes (fig 1.4). They help in better heat dissipation from the rotor due to air flow in between the vanes and also due to increase in the area available to heat transfer. Some designs on the other hand have holes drilled through them in the axial direction; this method is called cross-drilling (fig 1.5). Generally when the vehicle passes though water puddles the braking efficiency reduces due to the formation of a water film on the rotor which reduces the friction. Cross-drilling helps in the removal water film thereby increasing the rotor performance. In spite of this advantage it is seldom used as the holes become regions of high stress concentration leading to eventual cracking of the rotor.

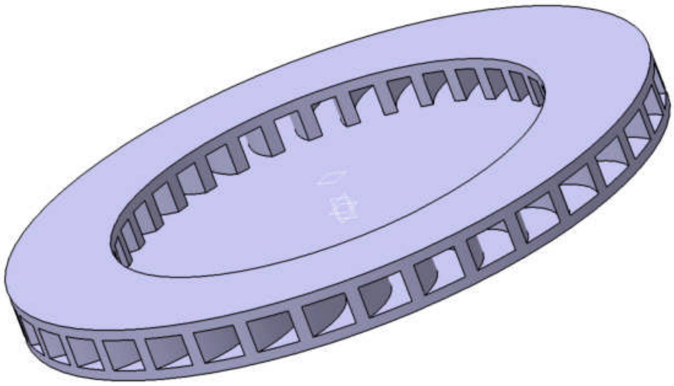

Fig 1.4: Schematic of a ventilated disc brake

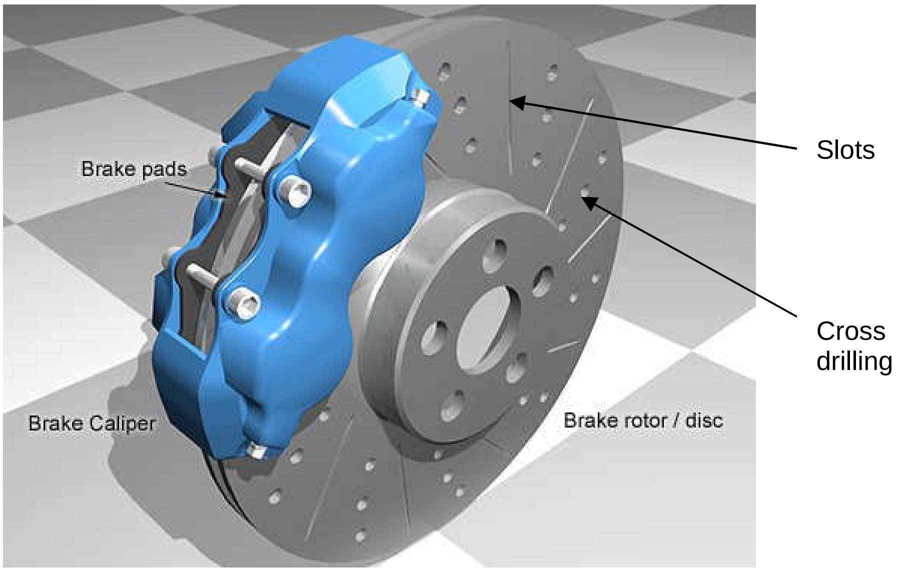

Fig 1.5: Crossed drilled disc brake (taken from internet source *www.howstuffworks.com*)

1.2. Advantages of disc brake system

As with almost any technology, disc brakes have both advantages and disadvantages. The disc brakes dissipate heat directly from its surface to the atmosphere, therefore are better than other types of brake systems in this regard. Brake discs are also lighter compared to other types of braking systems. This reduces the effort when changing the direction while the vehicle is moving. Due to this advantage the disc brake system is used extensively in racing applications. The advent of ceramics has further reduced the weight of a disc brake system.

1.3. Disc brake rotor failure modes

Disc brakes are susceptible to failure as they store all the heat that gets produced during the braking operation before eventually dissipating it to the atmosphere. The various types of disc brake failures are explained in the following sections.

1.3.1. Thermo-mechanical distortion

Thermo-mechanical distortions are caused by overheating of the disc brake rotor. Overheating is often a result of a poor rotor design due to which the efficient and rapid heat dissipation ability of the rotor reduces. As the temperature of the rotor increases the metal becomes softer and gets easily reshaped when the friction pads act on the rotor on the application of brake pedal. Initially, a corrugated or warped longitudinal section (fig 1.6a and1.6b)) is imparted to the friction surface of the rotor leading to a prolonged contact with the friction pads. The corrugation depends on the temperature gradient between the surface and the friction pads. The higher the gradient the more profound is the deformation.

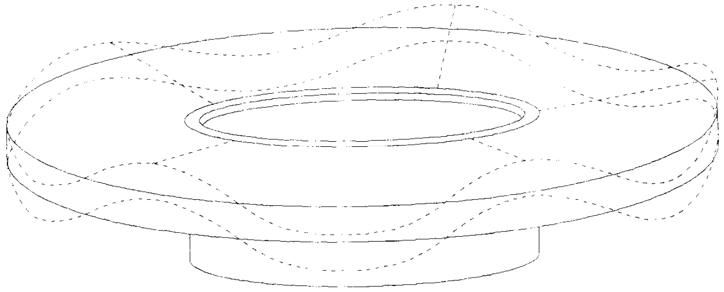

Fig1.6 (a): Corrugated shape imparted to a disc brake rotor (Eggleston [2000])

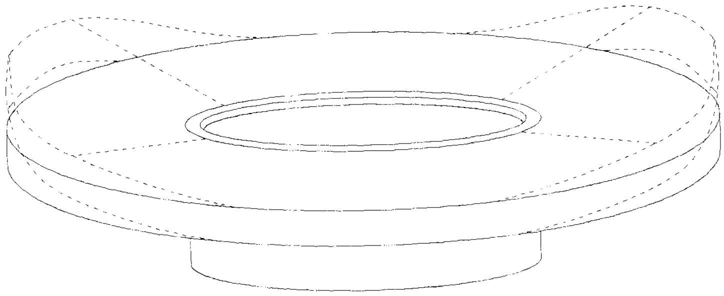

Fig 1.6 (b): Butterfly shape imparted to a disc brake rotor (Eggleston [2000])

In the second instance, the thermal distortion leads to "*disc coning*" (Eggleston [2000]). This is a lateral deformation phenomenon where the rotor is deformed taking the shape of a cone (fig 1.7). This deformation is typically of the order of 200 µm (Sterne [1989])

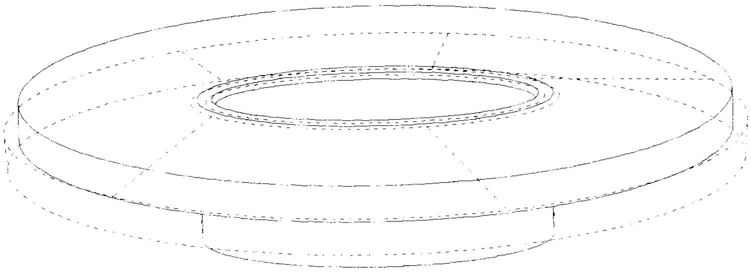

Fig 1.7: Coning of a disc brake rotor (Eggleston [2000])

These failure modes are important for the design of a disc brake rotor as they are a result of improper heat dissipation from the rotor.

1.3.2. Cracking

As mentioned in section 1.2 cross drilled rotors are susceptible to high stress concentration. Cracking is also exemplified due to non-uniform heat generation during braking action. This is leads to formations of regions where the temperature is higher than other regions of the rotor; these regions are called hot spots. This leads to uneven expansion of the rotor leading to the formation of a hairline crack and eventual damage of the whole disc. This can be avoided by designing the rotor to maximise heat dissipation and also temperature uniformity thereby reducing the formation hot spots.

1.4. Project motivation

As explained in section 1.4, most of the disc brake failures concerning the rotor are mainly due to the overheating. Therefore, it is paramount to enhance the heat dissipation of the ventilated disc brake rotor so that it lasts longer and also functions efficiently. Over the past few years many researchers have come up with innovative designs(like backward sweeping of blades, inclusion of turbulence enhancers etc.,) to address this concern by the analysis of both flow and heat transfer characteristics inside a ventilated brake disc rotor.

There are others factors such as weight, thickness of the rotor and sometimes even the number of blades in a rotor that keep changing with the requirement of the car manufacturer. So there is a huge need within the disc brake manufacturing community for sensitivity analysis data so that heat dissipation and temperature uniformity can be maximised in spite of having some parameters fixed.

1.5. Aims and objectives

The main aim of this work is to study and predict the effect of various design parameters (that are presented in section 2) on the aero-thermal performance of a disc brake rotor. The various design parameters include:

- Blade angles.
- Blade speeds.
- Rotor temperature.
- Number of blades in the rotor.
- Passage aspect ratio.
- Blade thickness.
- Blade shape.

These aims are accomplished by performing numerical analysis of the air flow through the rotor passage and by studying the following aspects of the flow which affect the aero-thermal performance of the rotor.

- Rate of heat dissipation for the rotor surfaces.
- Mass flow rate through the rotor passage.
- Temperature uniformity on all the rotor surfaces.
- Detailed aerodynamics of the air flow through the passage.

The commercial CFD package, FLUENT, is used to do the numerical analysis of the disc brake rotor passage flow. The semi-automatic geometric model is created using the package CATIA V5 and the mesh for the model is done using the software GRIDGEN and finally the Post-processing of the results is thoroughly done using FLUENT and is discussed and presented in detail. The analysis is done on a computational domain taken from previous work and the periodic conditions are used to simulate only one blade and a passage. The grid sensitivity analysis is also done to establish grid independent solutions. Grid

Convergence Index (GCI) is used to find out the error in the solution due to the grid.

2

LITERATURE REVIEW

In this chapter all the details of the literature related to previous work performed on disc brakes is presented The whole chapter has been divided based on the aerodynamic and heat transfer results obtained by various authors. Various CFD and experimental predictions of the disc brake system are also been discussed.

2.1. Heat transfer modes

The heat transfer to the ambient air from the disc brake rotor takes place in all the three different modes namely: conduction, convection and radiation. There are previous works on the contribution of each mode being done both experimentally and numerically.

2.1.1. Experimental work

Limpert [1975] has performed experiments and suggested that radiation contributes to less than 5% of the total heat transfer at normal braking conditions. It was shown that at higher temperatures the contribution of radiation is as much as 1/3rd the total heat transfer. The author has represented the variation of radiation heat transfer coefficient with temperature (fig 2.1).

.

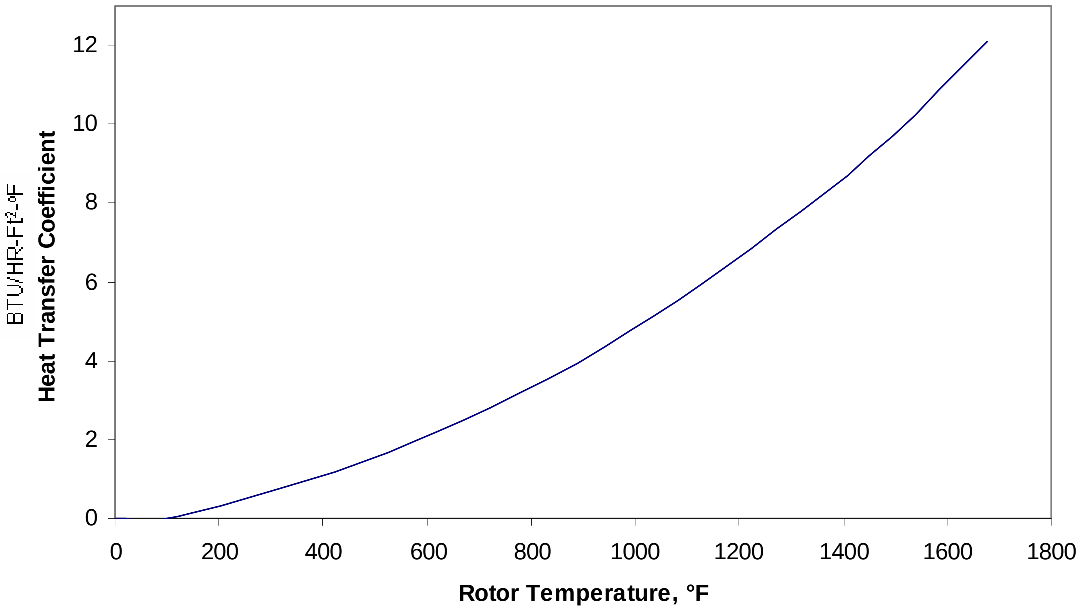

Fig 2.1: Radiation heat transfer coefficient (taken from Limpert [1975])

It was also suggested that the total convective heat transfer coefficient consists of approximately 1/3rd from the blades and 2/3rd from the surfaces, but at higher speeds of around 2000 rpm internal cooling increases to 60%.

Voller [2003] has also done experimental analysis on a ventilated rotor and studied the contribution of each mode of heat transfer (fig 2.2). The author pointed out that conduction was essentially independent of speed and also its significance is higher at lower speeds. The heat dissipated by conduction is given by equation 2.1:

$$Q_{cond} = h_{cond} A_{DC} \left(T_D - T_C \right) \qquad \text{..............} \ (2.1)$$

Where A_{DC} is the area at the disc and wheel carrier interface, T_D, T_C are the temperatures of the disc and wheel carrier respectively and h_{cond} is the conductive heat transfer coefficient.

It was also suggested that radiation is independent of speed whereas convection increases strongly with rotational speed. The heat dissipated by radiation is given by equation 2.2.

$$Q_{rad} = \sigma \varepsilon A_{D,rad} \left(T_D^4 - T_{amb}^4 \right) \qquad \ldots\ldots\ldots\ldots\ldots (2.2)$$

Where σ is the Stefan-Boltzmann constant, ε is the emissivity, $A_{d,rad}$ is the disc area, T_D is the disc temperature and T_{amb} is the ambient temperature.

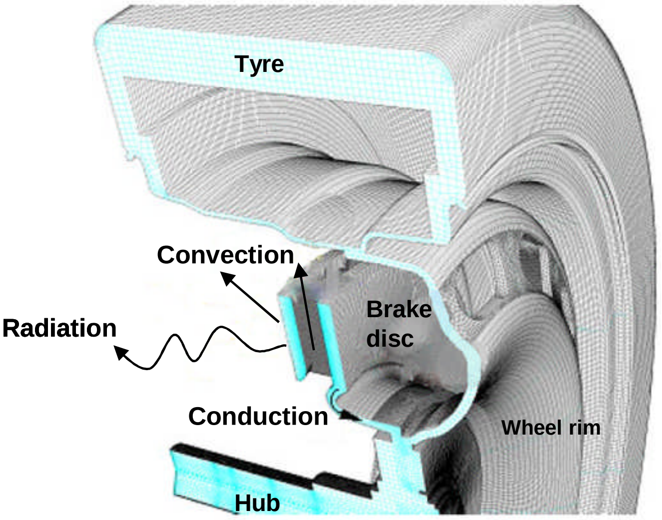

Fig 2.2: Schematic of modes of heat transfer from a brake disc (taken from Polansky [2003])

Initially the experiment was done by Voller [2003] at a temperature of 600^0C and a speed of 150 rpm the contribution of conduction is 18%, convection 39% and radiation 43%. Then at higher speed of 450 rpm, the contribution of convection increased to 57% and the other two modes are essentially independent of speed.

2.1.2. Numerical work

Polansky [2003] has performed CFD studies to evaluate the contribution of different modes of heat transfer. He used commercial CFD code FLUENT to perform the unsteady state simulations. Temperature was taken to be 800K. It was noted that convection was the major contributor with also conduction and radiation have lower contributions. Each was represented as a percentage of total heat transfer. Conduction heat transfer was noted to be at 11%, convection 82% and radiation contribution was 7%. Because of unavailability of any further information regarding Polansky's [2003] work, drawing conclusions is difficult.

2.2. Mass flow rate investigations

One of the important factors affecting the internal cooling of the brake disc rotor is the mass flow rate through the rotor passage. In order to increase the cooling rate, it is important to maximise the mass flow rate. For this reason, the brake disc is often considered as a centrifugal blower with the inner channels shaped like the blades of an impeller. Many researchers have investigated the flow phenomenon through the rotor passage both experimentally and numerically and have suggested some innovative mass flow rate improvement designs.

2.2.1. Experimental work

Johnson [2003] has performed PIV (Particle Image Velocimetry) studies for a flow through the rotor passage. He observed the formation of separation zones at the inlet of the passage where the fluid changes direction from both axial to radial and also tangential to radial. Johnson [2003] also observed that the turbulent kinetic energy was highest at the middle of the passage due to higher gradients between pressure and suction sides of the rotor.

Barigozzi [2002] has investigated the mean and turbulent characteristics of the flow at the exit of the disc brake rotor. Two different geometric configurations were considered, one a blade configuration and the other a multiple pin configuration (fig 2.3(a) and 2.3(b)).

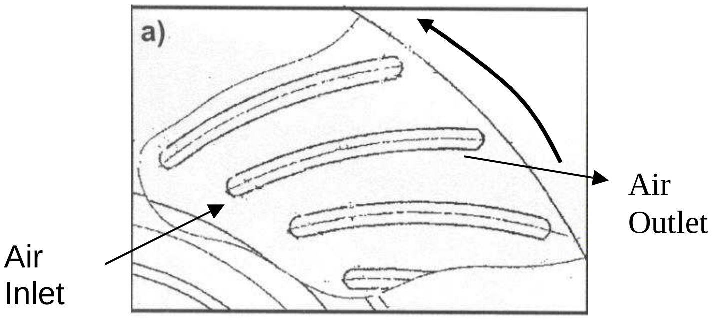

Fig 2.3(a): Blade configuration by Barigozzi [2002]

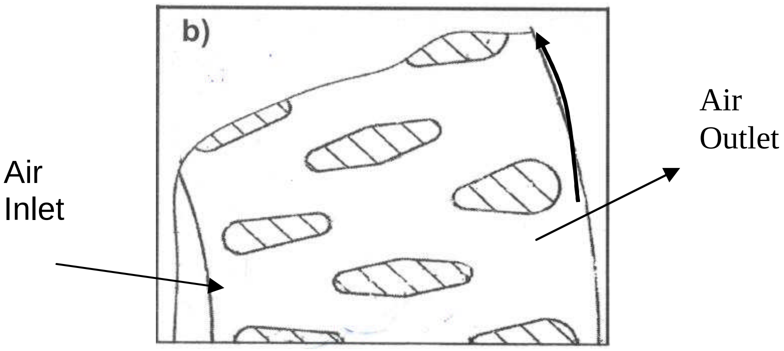

Fig 2.3(b): Pin configuration (taken from Barigozzi [2002])

The experiment was performed for two different speeds, namely 750 rpm and 1500 rpm. The exit values were measured at three different exit positions. Jet and wake patterns were observed in the blade configuration similar to that of a centrifugal blower. The turbulence intensity was observed to be higher in pin configuration due to the complex flow phenomenon in the passages. Bargozzi [2002] also observed that the mass flow rate for both the configurations was linearly proportional to the rotational speed. Finally the effect of calliper was also studied by Barigozzi [2002], it was pointed out that the calliper has a more detrimental effect on the overall mass flow rate through the rotor with the pin configuration than with a blade configuration.

Parish [2003] has performed an experimental investigation using a five-hole pressure probe and a hot wire anemometry system. The effect of disc geometry and rotational speed on mean flow, turbulence intensity and mass flow was studied and it was pointed out that aerodynamic characteristics were reasonably independent of rotational speed but highly dependent on rotor geometry. It was observed that the flow at the exit of the disc brake rotor was characterised by wake and jet patterns and these blockages lead to lower jet strength and higher turbulence intensity.

Sisson [1978] has proposed an expression (2.3) for the average vent speed at the exit of the rotor. He has taken a radial bladded rotor for his experimental analysis.

$$V_{avg} = \xi \omega D_0 / 2 \qquad \text{…………… (2.3)}$$

Where, ξ is the correlation factor given by equation 2.4.

$$\xi = \sqrt{(-0.020 + 0.908 D_i - 0.202 D_i^2)} \qquad \text{…………… (2.4)}$$

Limpert [1975] has also provided an expression (2.5) for the average vent speed at the exit of the rotor, it is given as follows.

$$V_{avg} = V_i / 2\left(1 + A_i / A_0\right)$$

…………… (2.5)

$$V_i = 0.1655 \omega \sqrt{(D_0^2 - D_i^2)}$$

Where, A is the area of inlet or outlet and V_{avg} is the average velocity. Hudson [1997] has pointed out that the value of the average velocity given by Limpert [1975] is one-third lower than that of Sisson [1978].

Hudson [1997] has performed experimental studies on the design modifications for the improvement of mass flow rate through the rotor passage. Radial blades were considered for the analysis and this also reduces the manufacturing cost due to symmetry of the model. He chose to impart pre-rotation to the fluid and direct the flow into the rotor vanes via an inducer (fig 2.4).

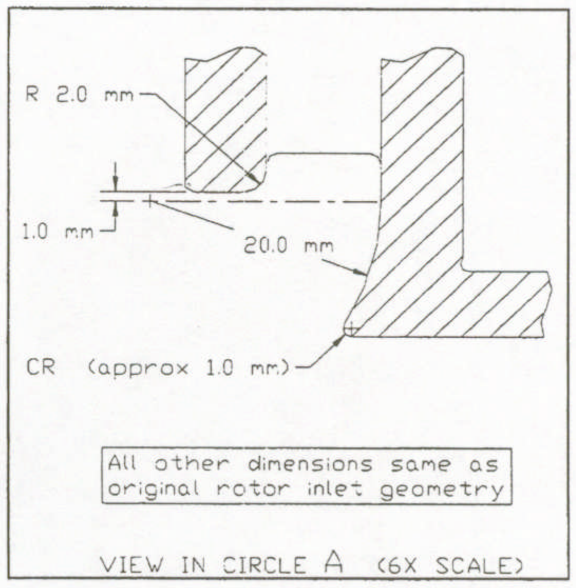

Fig 2.4: Rotor inlet horn (taken from Hudson [1997])

Hudson [1997] compared the exit velocity values for datum rotor, a rotor with inlet horn with the empirical values obtained from Limpert [1975] and Sisson [1978] at two different rotational speeds of 600 and 800 rpm. The increase in the average vent velocity (fig 2.5) due to this inlet horn was observed to be 32%.

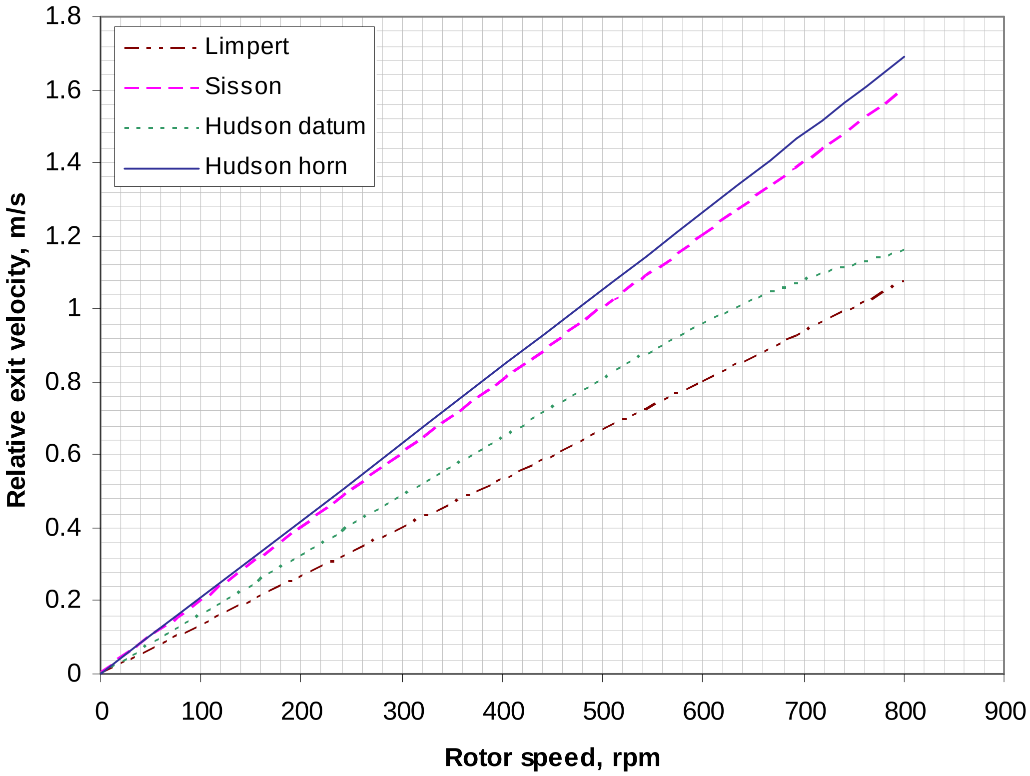

Fig 2.5: Comparison of exit velocities by Limpert [1975], Sisson [1978], Hudson [1997] with a datum and with an inlet horn (data taken from Hudson [1997])

2.2.2. Numerical work

Nestor [2004] has carried on the work of Parish [2003] and has used the same rotor geometries to perform a CFD analysis. He has observed flow inlet separation which greatly affects the mass flow rate through the passage. He also performed a CFD analysis for a pedestal configuration (fig 2.6) and has observed lower mass flow rate than a backward swept blade. This is due to larger inlet blockages and the heat transfer was also observed to be low because of this.

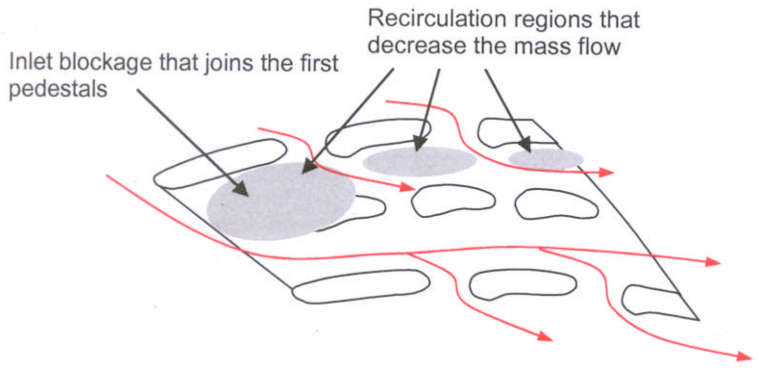

Fig 2.6: Flow pattern in a pedestal configuration (taken from Nestor [2004])

Nestor [2003] proposed a few design modifications (fig 2.7) by removing the first few pedestals so as to reduce the inlet blockage. The schematic representation is as shown below.

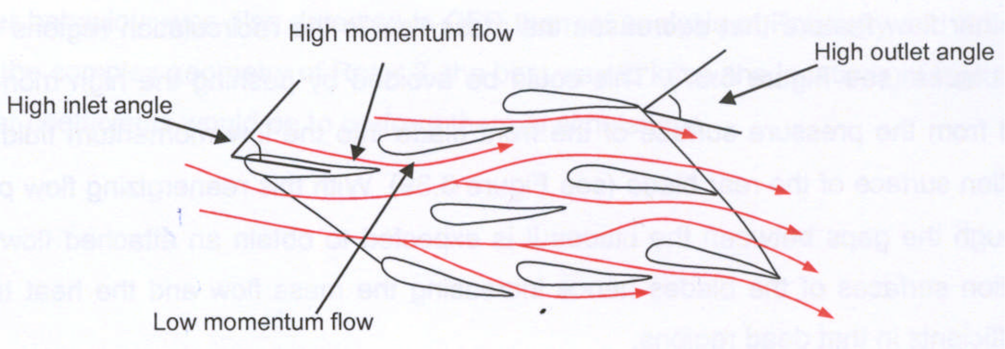

Fig 2.7: Expected Flow pattern in a improved design (taken from Nestor [2004])

Daudi [1999] has performed CFD simulations to compare a 42 radial bladed rotor with a 72 curved fin rotor with an inlet angle of 45^0 and outlet angle of 105^0 and observed an increase in the mass flow rate by 34.8% at 800 rpm. These angles were chosen based on air flow inlet and exit angles obtained from CFD analyses. An addition of an air inducer led to an increase in mass flow rate of

37.2%. Daudi [1999] also gave a 50% inboard and 50% outboard entry and noted an increase of 5% in mass flow rate.

Zhang [1997] performed CFD simulations to study the effect of number of blades on the mass flow rate through the rotor passage. He designed the passage in such a way that the cross-section is square instead of a rectangle. This is because for a given area, a square cross section has the least perimeter and thereby reducing the frictional losses (equation 2.6).

$$Z = \pi D/(w + t) \qquad \text{……………} \; (2.6)$$

Where, Z is the optimum number of vanes, D is the mid-diameter of the rotor, w is the flow passage width and t is the vane thickness. By also including smooth inlet and exit along with the optimum number of vanes Zhang [1997] observed an increase of 42% in the mass flow rate through the passage.

2.3. Heat transfer investigations

2.3.1. Experimental work

Sisson [1978] performed experiments to measure the vent heat transfer coefficient. The measurements were taken by insulating all except the interior passages of the rotor. Expression for non-dimensionalised heat transfer coefficient i.e. Nusselt number (*Nu*) is given in equation 2.7.

$$Nu = 0.045\,\mathrm{Re}^{0.8}(D_0/2)^{0.2}[1 + 6.6(D_0/2)^{0.8}] \text{…………………} \; (2.7)$$

Where, Nusselt number is based on the rotor outer radius (D_0) as the characteristic length.

Limpert [1975] also proposed expressions (2.8 & 2.9) for the Nusselt number (*Nu*). He divided it into two cases based on Reynolds number (*Re*).

For laminar flow (*Re* < 10000)

$$Nu = 1.65\,\mathrm{Re}^{0.33}\left(d_h / l\right)^{0.33} \qquad \ldots\ldots\ldots\ldots\ldots \text{(2.8)}$$

For turbulent flow (*Re* > 10000)

$$Nu = 0.0204[1 + \left(d_h / l\right)^{0.67}]\,\mathrm{Re}^{0.8} \ \ldots\ldots\ldots\ldots\ldots \text{(2.9)}$$

Where, d_h is the hydraulic diameter of a vent passage, l is the length of a passage. Hudson [1997] has pointed out that Sisson's and Limpert's relations for vent heat transfer coefficient agree within 5% at 600 rpm.

Hudson [1997] calculated the heat transfer coefficient values using both Sisson's [1978] and Limpert's [1975] correlations as shown above. The results were obtained on different geometries proposed by Hudson [1997]. The comparison of the values from the two correlations for an inlet with horn geometry is as shown in the figure 2.8.

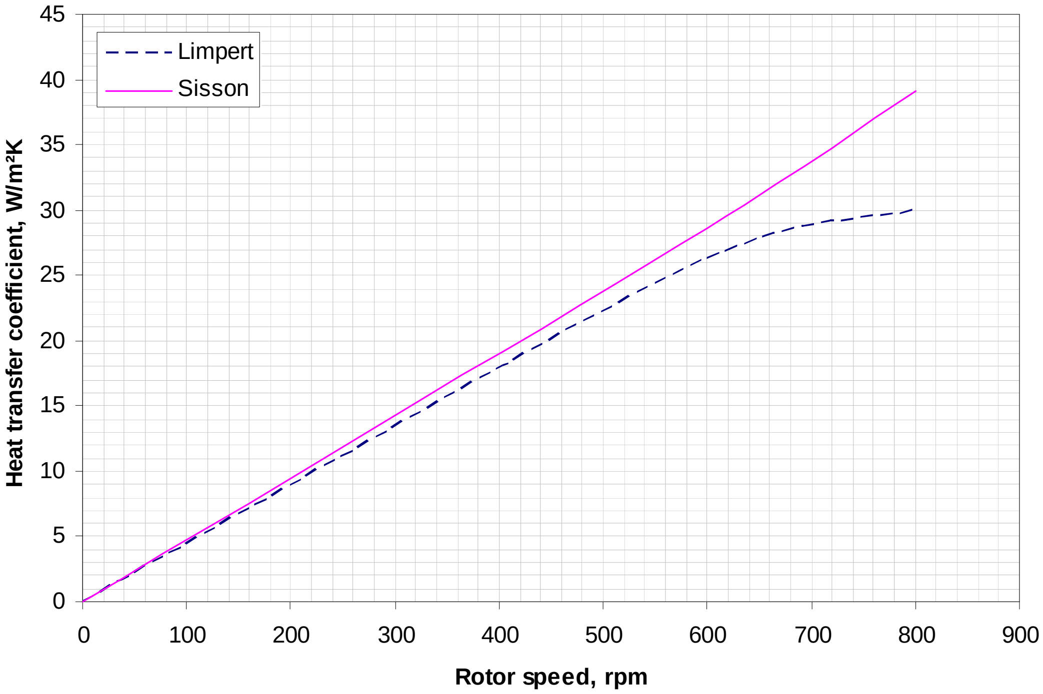

Fig 2.8: Heat transfer coefficient for rotor with inlet horn based on Limpert's [1975] and Sisson's [1978] correlations (data taken from Hudson [1997])

Barigozzi [2003] had carried out experimental analysis on multiple pin geometry disc brakes. The air velocities and temperatures were measured at the exit of the passage at a distance of 3.8 mm and the disc was operated at two different rotational speeds of 750 rpm and 1500rpm. Four different surface temperatures i.e. 101^0C, 191^0C, 256^0C and 320^0C were used to carry out the experiments. It was observed that vented mass flow rate decreases with surface temperature due to decrease in air density. Barigozzi [2003] defines what is known as heat transfer effectiveness (ε) by equation 2.10.

$$\varepsilon = \frac{T - T_{atm}}{T_s - T_{atm}} \qquad \text{…………… (2.10)}$$

Where, T_{atm} is the atmospheric temperature, T_s is the surface temperature and T is the air temperature. The author further points out that heat effectiveness does not change with rotational speed as the transit time of air in the passage decreases with speed. The convective heat transfer coefficients show larger values thus demonstrating a good design of the present geometry. Figure 2.9 provides the non-dimensionalised temperature and velocity plots for different temperatures measured at a distance of 3.8 mm from the exit.

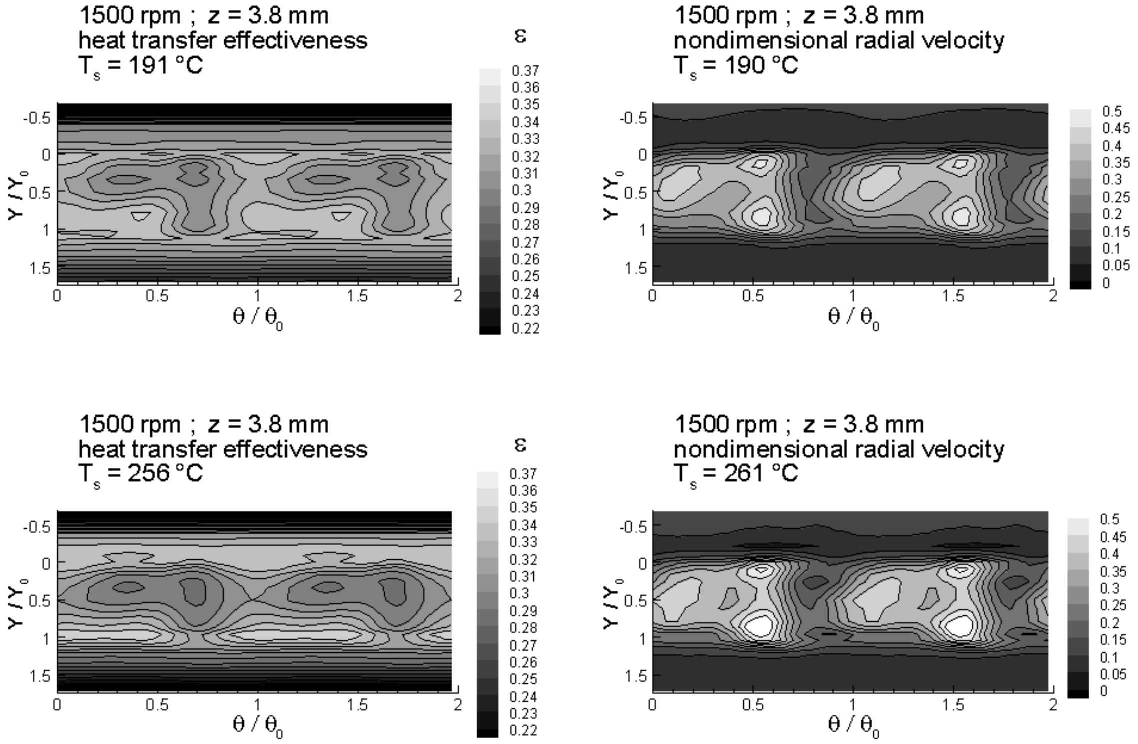
1500 rpm ; z = 3.8 mm
heat transfer effectiveness
T_s = 191 °C

1500 rpm ; z = 3.8 mm
nondimensional radial velocity
T_s = 190 °C

1500 rpm ; z = 3.8 mm
heat transfer effectiveness
T_s = 256 °C

1500 rpm ; z = 3.8 mm
nondimensional radial velocity
T_s = 261 °C

Fig 2.9: Non-dimensional temperature and velocity plots at 1500 rpm (taken from Barigozzi [2003])

2.3.2. Numerical work

Costes [2005] has performed CFD simulations on a disc brake rotor at 1500 rpm at three different temperatures namely, 500K, 800K and 1100K. He defined heat transfer metrics to evaluate the disc brake performance which are as shown in equation 2.11.

$$HP = \iint \rho C_p u_r (T - T_{inlet}) dS \qquad \text{…………………} (2.11)$$

Where, HP is the heat power exchanged whose value is computed at the exit of the rotor passage as a surface integral. Costes [2005] pointed out that the value of heat power exchanged increases with temperature (fig 2.10).

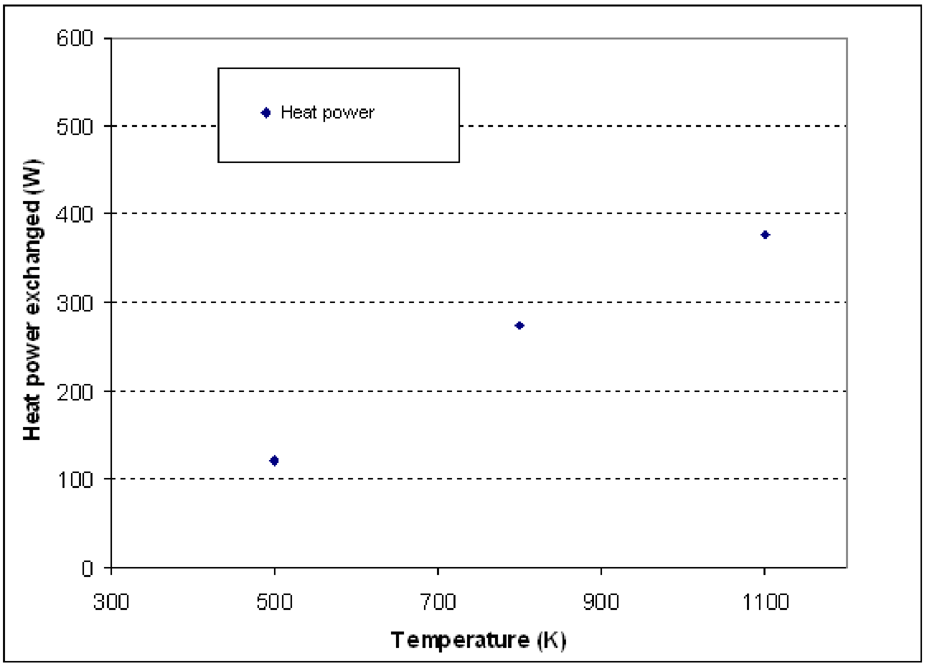

Fig 2.10: Heat power as a function of rotor temperature (taken from Costes [2005])

Another parameter the author used to evaluate the performance of the disc brake rotor was the total power exchanged (TP) as a function global heat flux per Kelvin (hS) (equation 2.12).

$$TP = hS\Delta T \qquad \text{……………} (2.12)$$

The author has observed that the value of this parameter decreases with temperature because the Nusselt number drops with it (table 2.1).

Temperature (K)	500	800	1100
hS (W/K)	38.2	33.7	27.7

Table 2.1: hS variation with temperature (taken from Costes [2005])

Finally the author concludes that the rotor performance decreases with temperature due to the decrease in air density and also due to increase in inlet separation. This phenomenon can be observed in the relative velocity plots through the passage (fig 2.11). There is a constant increase in the inlet separation on the suction side of the blade with temperature due decrease in density and thereby increase in the Reynolds number leading to higher viscous forces.

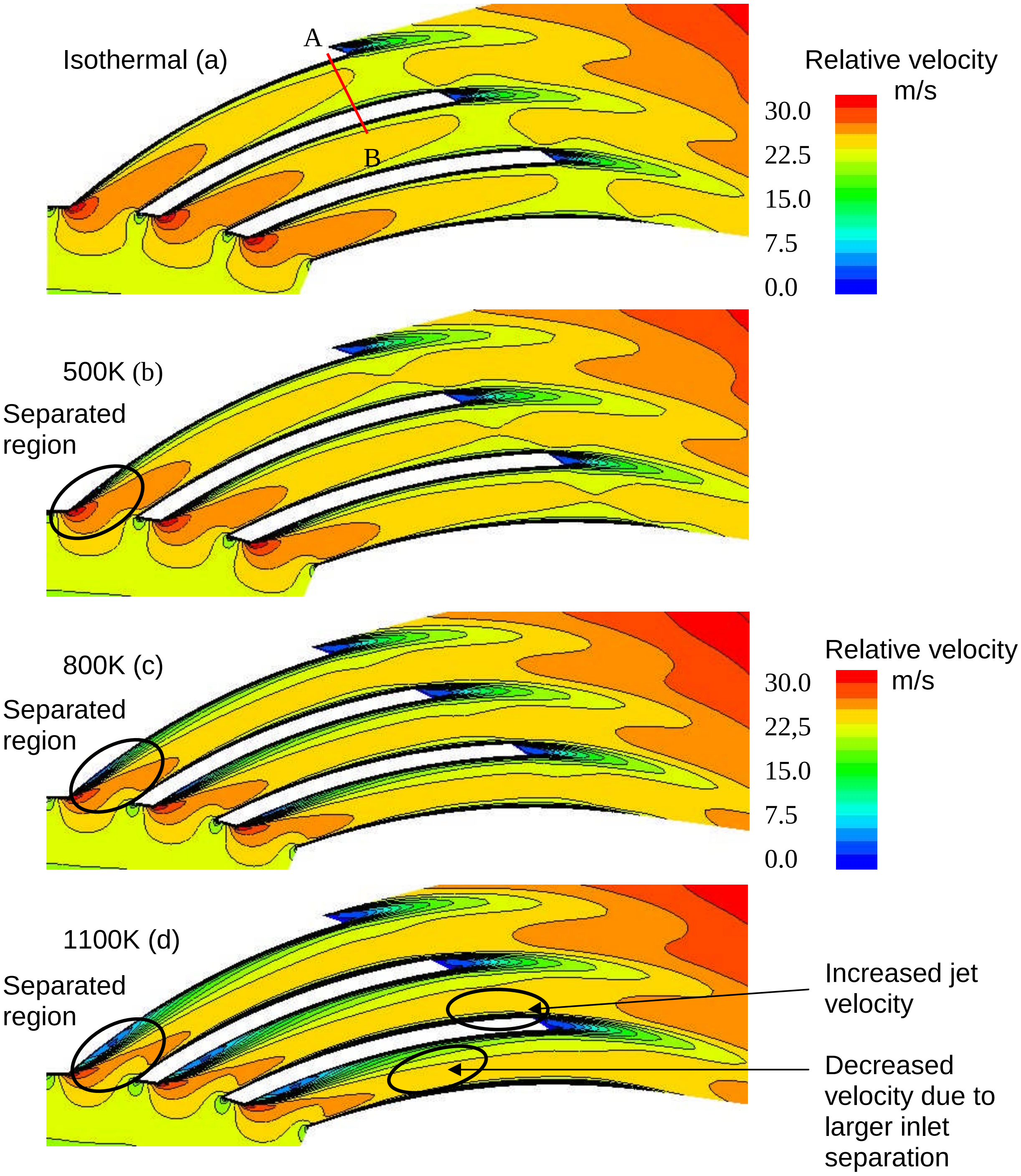

Fig 2.11: Relative velocity at mid-height of the passage (taken from Costes [2005])

Costes [2005] also made a comparison between a datum backward swept rotor and a rotor with ribs. He observed that the capacity of the rotor with ribs to exchange heat was better than the datum rotor for equal mass flow rates. Due to lower mass flow rate through the ribbed rotor, its overall performance is only 10%-15% better than the datum rotor. The graphs shown in figures 2.12 & 2.13 give a clear picture of this variation.

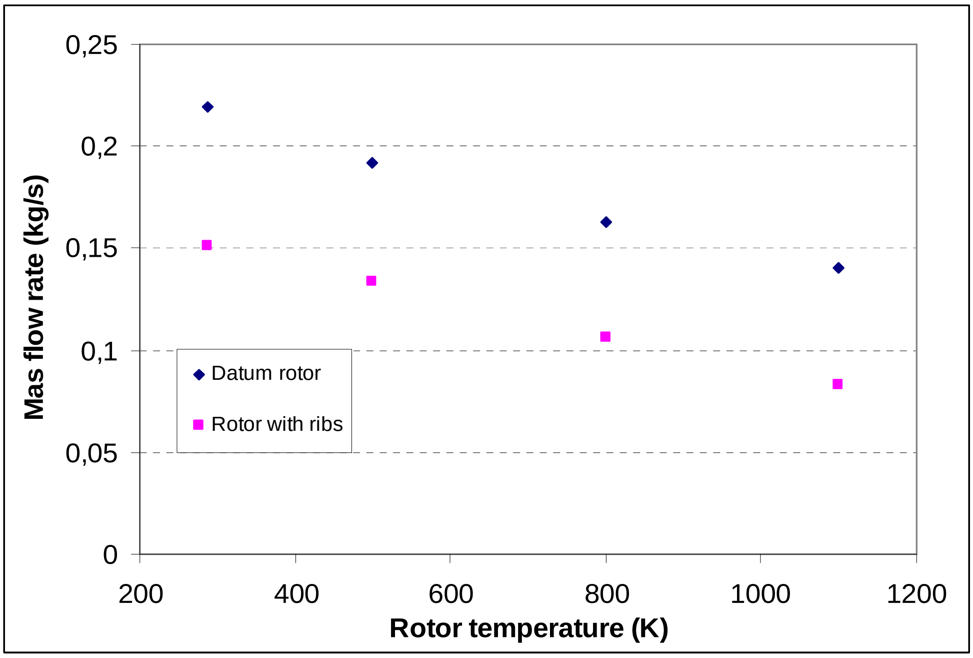

Fig 2.12: Mass flow rate through the passages of ribbed and datum rotor (taken from Costes [2005])

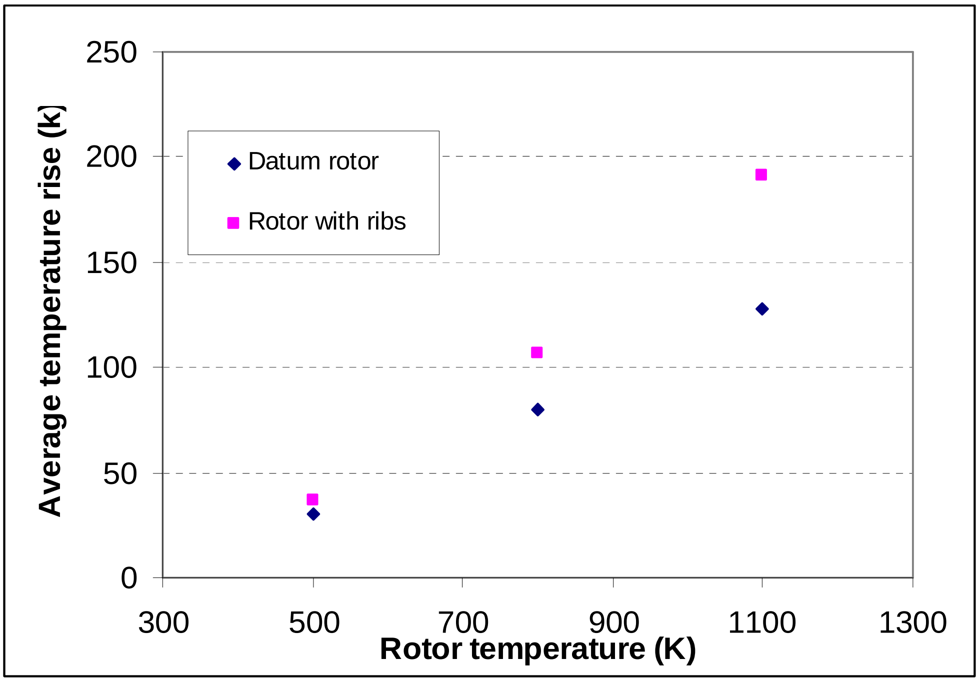

Fig 2.13: Average air temperature rise through the passages of ribbed and datum rotor (taken from Costes [2005])

2.4. Centrifugal impeller work

Centrifugal impeller is a pump that sucks in and pumps out fluid particles. The objective of a centrifugal impeller is to increase the kinetic energy of the fluid particles flowing through the passage which is later on converted into pressure energy with the help of a diffuser. One of the main objectives of a brake disc is to increase the mass flow rate through the passage of the rotor. Thus, the brake disc can be treated as a centrifugal impeller.

Lazarkiewicz [1965] in his impeller work points out that when the blade outlet angle (β_2) is acute ($<90^0$) the flow occurs without any separation whereas with an obtuse outlet angle ($>90^0$) there is a possibility of flow separation. The schematic of the blade angles are as shown in figure 2.14. The author also points out that as β_2 increases, the absolute exit velocity increases thereby increasing the dynamic part of the head rapidly. But forward swept blades are avoided in impellers as higher dynamic head leads to higher losses in the subsequent conversion of kinetic energy to pressure energy in the diffuser. In brake discs, the main objective to get higher mass flow rate through the passage, so it is important to find out the optimum exit angle to avoid flow separation thereby increase the mass flow rate and the performance.

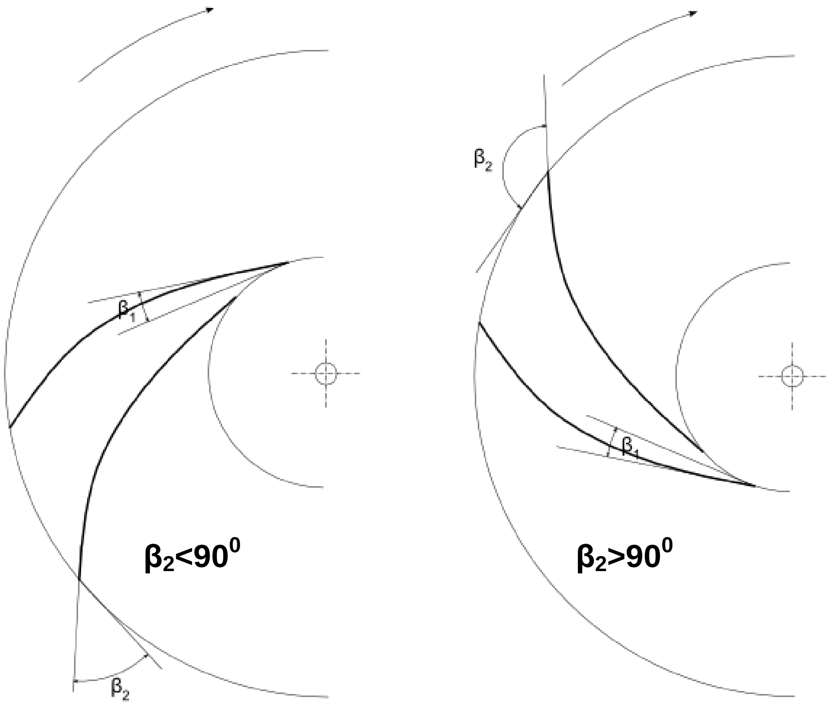

Fig 2.14: Types of rotor blades; (a) blades swept backwards $\beta_2<90^0$, (b) blades swept forwards $\beta_2>90^0$

3

DESIGN PARAMETERS

In this chapter a brief account of all the various disc brake design parameters such as blade angles, blade speeds, number of blades and aspect ratios are presented. The parameters on which the current study is focussed are reviewed. Each of these design parameters is discussed in reasonable detail.

3.1 Introduction

When performing parametric studies on a disc brake rotor it is important to identify the design parameters that have significant effect on the overall performance of a disc brake. The various parameters of a disc brake are shown schematically in the figure 3.1 and each of them is described in the following sections.

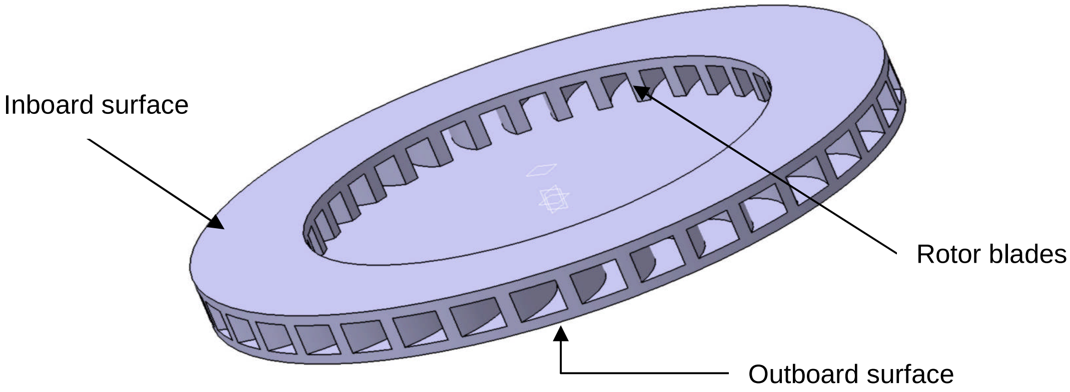

Fig 3.1: Schematic of a disc brake rotor

3.2 Blade angles

The blade angles define the actual shape of the blade of the brake rotor. The blade angles are divided to two sets of inlet and exit angles. The flow of air into the rotor is from axial to radial direction and the inlet angle (β_1) has an impact on the entry of air to the brake disc rotor (Fig 3.2). The outlet angle (β_2) on the other hand affects the total head of the flow through the rotor passage (see section 2.5).

The parametric analysis of the effect of blade angles on the brake disc performance is performed based on the datum rotor that is currently in operation. The inlet and outlet blade angles are gradually varied from the datum configuration. After indentifying the best set of blade angles, the data set are further increased into order to increase of the sensitivity of the study.

The set of blade angles considered initially are as follows:

Datum: Inlet angle (β_1): 43.16^0; Outlet angle (β_2): 35.62^0

Blade inlet angles (β_1): 45^0, 60^0, and 90^0.
Blade outlet angles (β_2): 50^0, 90^0, and 110^0.

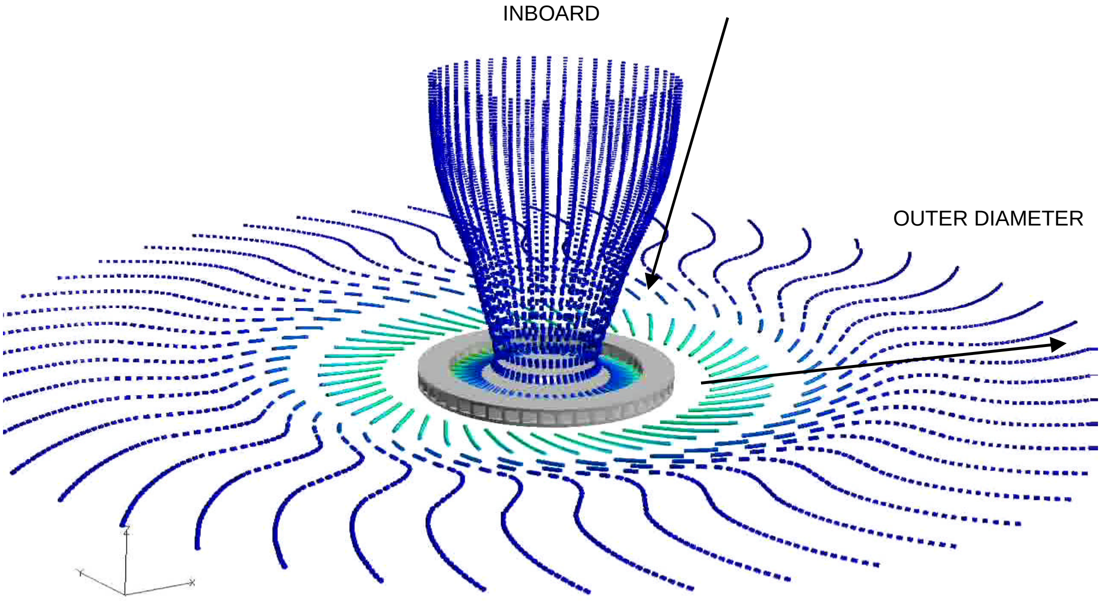

Fig 3.2: Main flow pattern (picture taken from Nestor [2004])

These above mentioned set of blade angles chosen were also based on the centrifugal impeller works by Lazarkiewicz [1965] (see section 2.5). In figure 3.3 the angles are defined schematically.

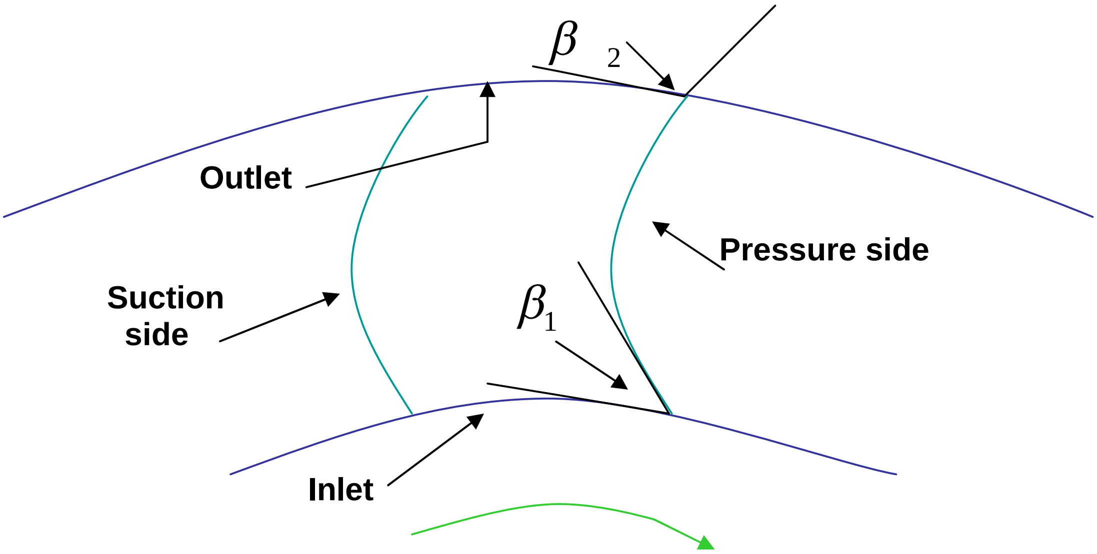

Fig 3.3: Schematic of the blade angles

3.3 Blade speeds

For previous literature it has been observed that the mass flow rate through the passage increases linearly with increase in the blade speed (see section 2.3.1). But the heat transfer on the other hand increases with blade speed only up to 600 rpm and higher speeds the data is insufficient (see section 2.4.1) to understand the effect of blade speed on heat transfer. Also it is important to understand the performance of a best performing set of blade angles at higher speeds as compared to the datum configuration.

Therefore, a set of blade speeds were chosen to perform the CFD analysis of the disc brake rotor. The blade speeds were chosen based on the inputs given by the manufacturers depending on the applications of brake discs. All the values of the speeds lie in the subsonic regime.

Set of blade speeds: 750 rpm, 1500rpm, and 2250 rpm.

3.4 Number of blades

The design parameter that determines the amount of area available for the air to go through the passage of the disc brake rotor is the number of blades. It is very important to optimise the number of blades in order to achieve a balance between the mass flow rate, the amount of losses and the structural strength of the brake disc.

It is important to also optimise the number of blades in order to reduce the inlet blockage (Fig 3.4). Parish [2003] has pointed out in his work that 24 bladed rotors provide the greatest mass flow rate and 48 bladed rotors were over bladed. In order to throw further light on this aspect and also based on the manufacturer's inputs the following numbers of blades were chosen for the parametric study.

Numbers of blades: 36, 48.

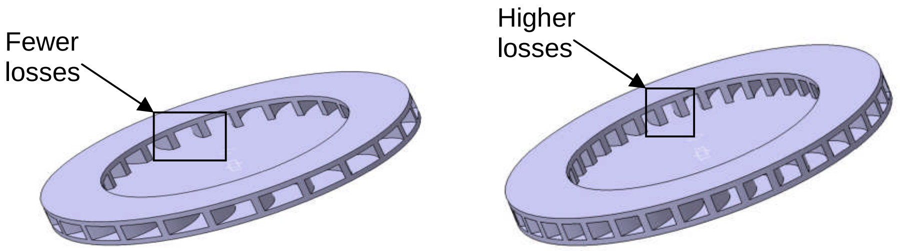

Fig 3.4: Schematic of a 36 and 48 bladed rotor

3.5 Aspect ratio

The aspect ratio (AR) is the length to breath ratio of the area that the entering air sees when it enters the brake rotor passage (Fig 3.5). It is paramount to study the effect of different aspect ratios on the amount of air going through the passage as aspect ratio as plays an important role in the amount of frictional losses that occur.

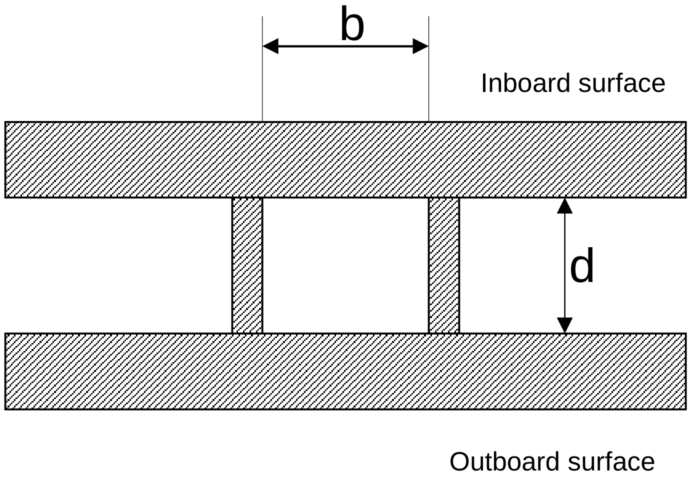

Fig 3.5: Aspect ratio description

$$AR = \frac{b}{d}$$

Where, b is the distance between the blades and d is the distance between rubbing surfaces.

Zhang [1997] has stated that making the aspect ratio 1 (square section vents) reduces the frictional losses as explained in section 3.3.2. Parametric studies were performed by using different sets of aspect ratios to understand in detail the impact of aspect ratio on the mass flow rate through the rotor passage and on the overall heat transfer. This change is achieved partly as the number of blades vary and also by changing the thickness of the inboard and outboard surfaces.

4

Methodology

In this chapter the methodology of the project with explained in detail. The aspects of model creation and its export into grid generation software will be discussed. The details of the mesh used for CFD simulations will also be presented. The CFD simulation details and the post-processing metrics will also be discussed.

4.1. Introduction

Based on the project objectives listed in section 1.6, the project is divided into four parts; the effect of blade angles, the effect of blade speed and temperature, the effect of number of blades and aspect ratio and finally the effect of finer design changes like airfoil shapes and inlet chamfering on the aero-thermal performance of a ventilated brake disc.

Each part of the project is further divided into three steps; the model creation, mesh generation and CFD simulation. Post processing is performed after the simulations reach a specified error residual value. These are explained in the following sections in detail.

4.2. Model creation

The disc brake rotor is rotationally periodic with blades and passages at equal angular spacing. This reduces the computational cost significantly as the analysis can be done only for a single blade and a passage. The model was created in CATIA V5. The actual brake disc consists of two rubbing surfaces separated by the blades. One of the rubbing surfaces (outboard surface) is mounted onto the wheel with the help of 12 mounting bolts. The rubbing surfaces also have grooves on the outside to enhance heat transfer from the outer surface.

Simulating the full geometry is not justified as it is requires a lot of computational effort. As the project deals mainly with the study of blades angles, numbers of blades etc., on the overall performance of a brake disc, the following simplifications are made to the original model (see fig 4.1):

- The outboard side of the brake rotor is simulated as a flat plate because the wheel is mounted on outboard surface and the entry of air can be neglected.

- The bolts and the balancing clips are neglected.

- The grooves on the rubbing surfaces are also neglected.

- The leading and trailing edges match the outer and inner radii of the brake disc rubbing surfaces for the most part of the project although the lips are included later on to get a better analysis.

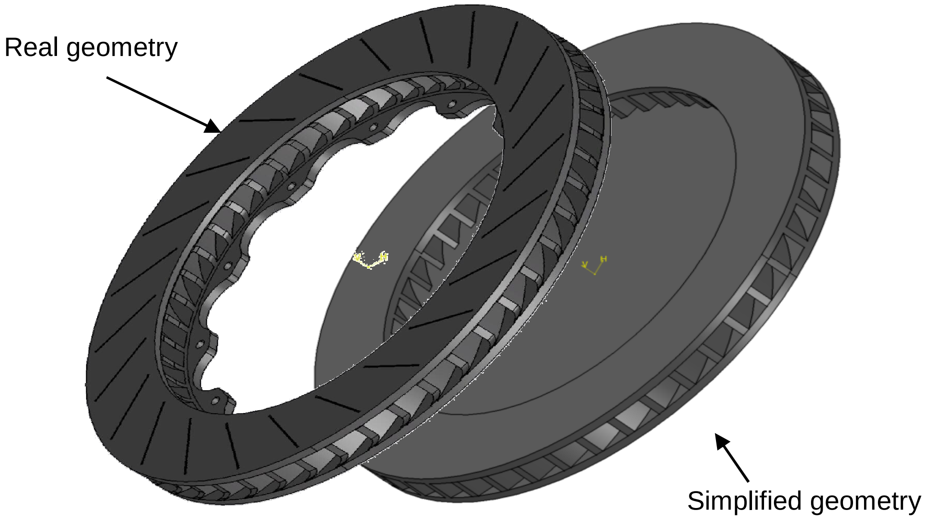

Fig 4.1: Simplification of the original geometry (taken from Nestor [2004])

The model, as mentioned earlier, is created in CATIA V5 as a periodic repeat. The periodic rotational angle is calculated based on the number of blades (see fig 4.2). CATIA V5 works in a tree format offering better control on the parameterisation on the model. For the first part of the project for which the effect of various blade angles is analysed, the model is created in 3 parts; first part is the inboard side with a specified thickness of 7 mm; the second part is the blade with a specified set of inlet and outlet angles and third part was the outboard side, created as a circular plate with a thickness of 7mm. This method enables the parameterisation of the blade angles and any change in the blade angles can be incorporated easily without having to remodel the whole disc brake.

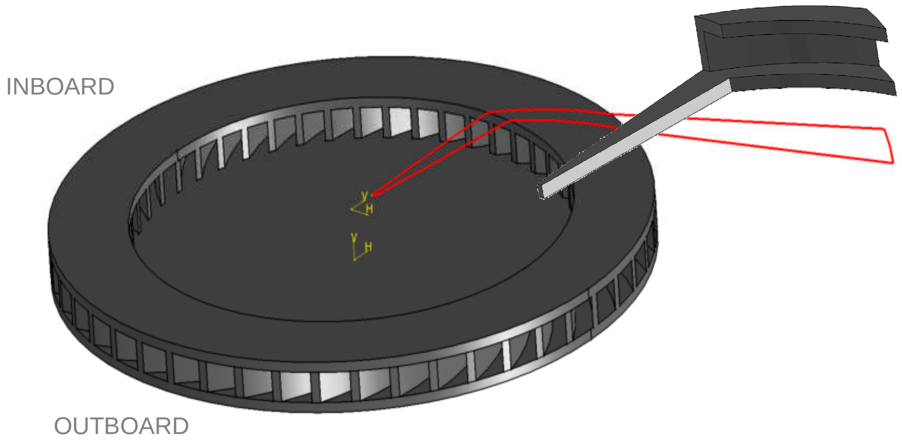

Fig 4.2: Rotational periodic model

The model created is then exported to the grid generating software in an *Initial Graphics Exchange Specification* (IGS/IGES) file format. This format exports the geometry as just curves giving better control while creating the structured mesh with required mesh distribution.

4.3. Mesh generation

For creating the mesh for the brake disc CFD analysis, the brake disc is imagined to be inserted in an imaginary cylinder (domain) to simulate the surroundings (fig 4.3). It is very important to have the right domain configuration to avoid any unnecessary computational effort due to a larger domain and also to avoid any interaction between exit jet and the domain boundaries which happens in a smaller domain. Nestor [2004] has performed domain study to evaluate the influence of the domain size on the computed solutions. A wide range of domain configurations were investigated by him. From the results of Nestor [2004], it was suggested that the appropriate domain size is as given below:

Domain diameter = 4.3x (diameter of the brake disc rotor)……….. (4.1)

Domain height = 2.7x (diameter of the brake disc rotor)……………. (4.2)

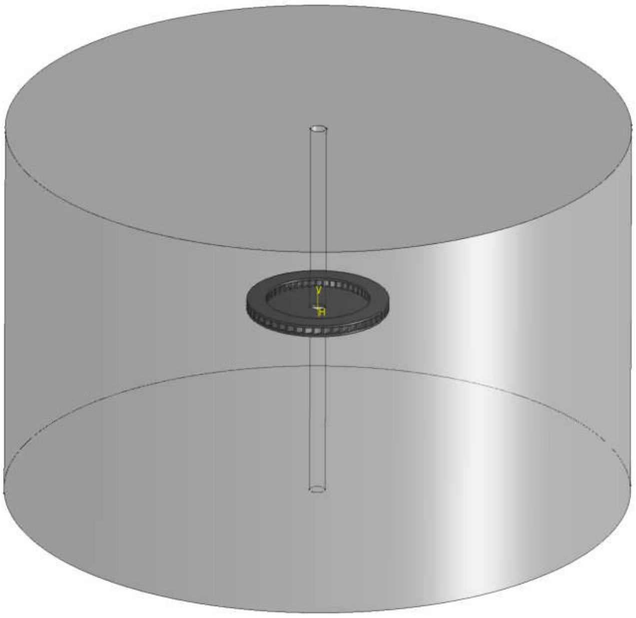

Fig 4.3: Domain representation

Each of the curves representing the CAD model is defined as database entities in the grid generation software GRIDGEN. Connectors are created on the database entities. Connectors are the lines on which grid points can be defined. All the connectors are used to create a mapped structured two dimensional mesh called domains. Domains are then further mapped to form a three dimensional structured block. This method of multi-block gives better control on the grid point distribution by avoiding the formation of highly skewed elements. The passage of the rotor is created as a single three dimensional block. After the initial uniform mesh has been created, a hyperbolic tangent distribution function is used to cluster the grid towards the brake disc inlet and outlet, inboard and outboard surfaces as the gradients in the properties are expected to be sharp in these regions (fig 4.4). This is achieved my modifying the connectors at the exit and entry of the rotor such that the cell size variation is not sharp. The mesh inside the passage though is left uniform but is made sure that the first cell centroid is within the laminar sub-layer ($y^+ \approx 5$).

Once the mesh is generated it is important to perform grid sensitivity analysis to demonstrate the grid independency of the solution. This is done in order to provide credibility to the solution acquired after the CFD simulations have been carried. The exact details of this are explained in the next chapter. In the following section all the theoretical aspects of the grid sensitivity analysis is explained in reasonable detail.

4.3.1. Grid sensitivity analysis

As explained earlier a structured multi-block conformal grid is created for the computational domain using the commercial software GRIDGEN. Hyperbolic tangent distribution function is used to get higher mesh densities near the entry and exit of the brake disc rotor passage where sharp gradients are expected to be present. Grid convergence tests are performed on datum case rotor geometry by using Richardson's extrapolation.

Richardson's extrapolation (Richardson [1910]) links the exact solution of the partial differential equations to the solution due to the presence of a grid using Taylor series of expansions. This process is done first on a fine grid first and then on courser grid by reducing the number of grid points in each direction of a fine grid. The ratio of number of grid points in each direction of a course to the fine grid is called *refinement ratio(r)*. The following equation by Roache [1998] best describes the above relation.

$$f_{exact} \cong f_1 + (f_1 - f_2)/(r^p - 1) \qquad \text{………… (4.3)}$$

Where, f_{exact} is the exact solution of the equation, f_1 is the fine grid solution and f_2 is the coarse grid solution, p is the order of the discretisation method and r is the refinement ratio. Richardson's extrapolation has an accuracy of 4th order if f_1 and f_2 are discretised using 2nd order central differencing schemes or an accuracy of 3rd order if f_1 and f_2 are discretised using 2nd order upwind schemes.

The second term in the right hand side of the equation () is interpreted as the correction to the fine grid solution. Roache [1998] has formulated what is known as an **E**stimated fractional error E_1 for the fine grid solution f_1.

$$E_1[fine] = \varepsilon / \left(r^p - 1\right) \qquad \text{……………. (4.4)}$$

$$\varepsilon = (f_2 - f_1) / f_1 \qquad \text{………….. (4.5)}$$

Roache [1998] further points out that, E_1 is a good approximation when the solution is of reasonable accuracy (E_1<<1) and ε is not a good measure as it does not consider refinement ratio or order of method into consideration. Therefore, he has proposed a parameter called Grid Convergence Index (GCI) for measuring the error band instead of the error bound. The GCI compares the ε obtained by the present method to that of ε obtained from a fine grid solution with r = 2 and p = 2. The expression for GCI is as follows:

$$GCI\left[fine\right] = F_s\left|\varepsilon\right| / \left(r^p - 1\right) \qquad \text{…………. (4.6)}$$

Where, F_s is the coefficient whose value essentially is a factor of safety. Its value is typically 3 and it gives a good comparison with 2nd order methods by grid doubling. The grid is made finer in two stages. First the coarse grid is converted into an intermediate grid and then to a still finer grid. The values are then verified so that they lie in the asymptotic range. Roache [1998] has proposed an expression (equation 4.7) for verification of asymptotic range using the grid convergence index.

$$GCI_{21} = r^p GCI_{32} \qquad \text{………….. (4.7)}$$

Where, GCI_{21} is the fine grid convergence index by coarsening the grid from medium to course grid, GCI_{32} is the grid convergence index by coarsening the grid from fine to medium grid, r is the refinement ration and p is the order of convergence of the discretisation method.

4.4. CFD simulation details

CFD is the method of solving the fundamental non-linear partial differential equations that govern the fluid flow, heat transfer and turbulence of flow. For the present work, CFD simulations are carried using the commercial CFD software package FLUENT.

The governing equations are solved by FLUENT at the cell nodes of the mesh obtained from GRIDGEN using finite volume method and by applying relevant appropriate physics as explained in the following sections. All the aspects of the simulation are presented in detail in the following sections.

4.4.1. Rotating flow

The disc brake being attached to the wheel also rotates at the speed of the wheel of the automobile and the flow inside the rotor is predominantly swirling and rotating. In problems involving rotating motion FLUENT adapts a method called rotating reference frame. The governing equations are solved by considering the walls to be stationary in the relative frame (default) and the fluid to be moving with acceleration of the reference frame. This acceleration of fluid is included as a source in the momentum equation.

4.4.2. Compressibility

The flow in and around the disc brake rotor is incompressible as it is in a very low Mach number regime. But the density varies as a function of temperature because of the heat transfer taking place inside the passage of the rotor. This variation of density with temperature is calculated by FLUENT using the incompressible ideal gas law (equation 4.8).

$$\rho = p_{op} / \left(R / MT \right) \qquad \text{…………. (4.8)}$$

Where, ρ is the density, p_{op} is the operating pressure, R is the universal gas constant, M is the molecular weight of the gas and T is the absolute temperature.

4.4.3. Gas properties

A constant air specific heat capacity of 1006.43 J/Kg.K is used during thermal modelling of disc brakes. Costes [2005] has performed analyses on fluid property variations with temperature and said that the variation of air specific heat capacity in the temperature range of 288K and 1100K is 15.2% and it further comes down to 2.3% when the exit temperature is around 500K. Costes [2005] has pointed out that thermal conductivity (λ) variation with temperature on the range of 288K and 1100K is around 290% and proposed a polynomial expression (equation 4.9) for its change with temperature by comparing it with experimental data by Taine [2004].

$$\lambda = 0.0021 + 9 * 10^{-5} * T - 2 * 10^{-8} * T^{2} \qquad \text{……….. (4.9)}$$

Costes [2005] also pointed out that the variation of viscosity within the particular temperature range is 257% and compared the experimental values given by Taine [2004] with the Sutherland's law of viscosity in FLUENT. Due to this the equation 4.9 was used in the present work to capture the variation of thermal conductivity with temperature and Sutherland's law was used to capture the variation of viscosity with temperature.

4.4.4. Pressure velocity coupling

The boundary conditions at the top and bottom of the domain is given as pressure inlet conditions. The circumferential boundary of the imaginary cylinder is prescribed by a pressure outlet condition (fig 4.4). For an incompressible flow FLUENT uses the Bernoulli's equation to find out the velocity from the pressure and the direction of velocity is as specified at the boundaries. The Navier-Stokes equation is then solved by FLUENT using SIMPLE algorithm for pressure velocity coupling proposed by Patankar [1972]. The non-linear terms are explicitly solved using this algorithm on staggered grids.

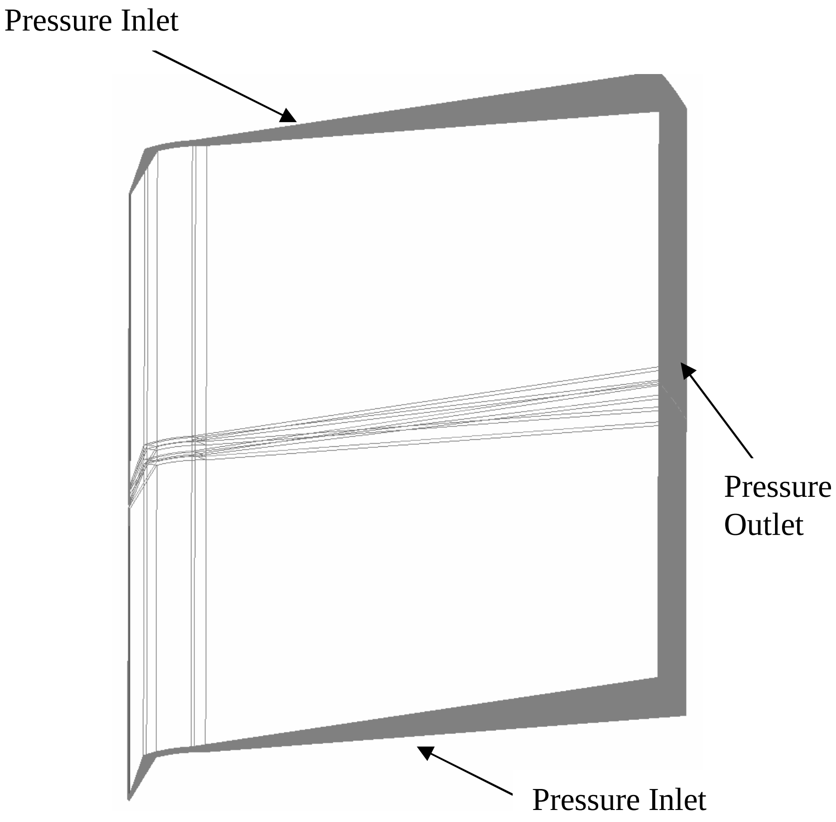

Fig 4.4: Pressure boundaries

4.4.5. Turbulence modelling

RANS eddy-viscosity based two equation K-ω SST model proposed by Menter [1994] is used to simulate the turbulence effects in the flow. The turbulence sensitivity analysis done by Nestor [2004] suggests that K- ω SST model works well for modelling a brake disc rotor turbulence as it resolves the viscous region effects very well compared to other two-equation models. This is because the K-ω SST model uses K-ω in the near wall region and k-ϵ in the free stream region. The mesh details to incorporate this turbulence model are presented in the next chapter.

4.4.6. Thermal modelling

The temperatures that are considered to model the brake disc rotor heat transfer are 500K, 800K, 1100K. These values are specified on the walls of the brake disc (fig 4.5). FLUENT solves the energy equation and calculates the temperature distribution in the domain with rotor wall temperatures as boundary conditions. Only convection from the walls is considered with constant wall temperatures.

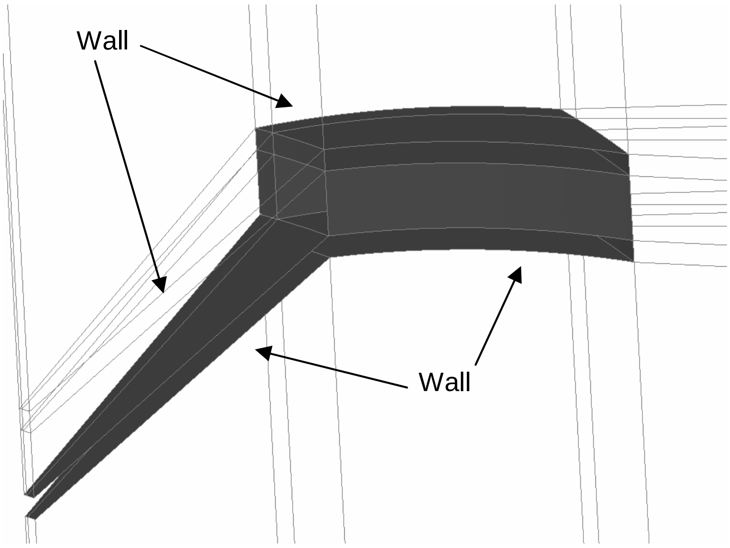

Fig 4.5: Wall boundary conditions

4.4.7. Periodicity

Periodic boundary conditions are used to simulate 1/nth of the rotor, where n is the number of blades. The brake disc rotor is rotationally periodic i.e. the geometry and the flow pattern repeat themselves at a specified angle about the centreline. The flow exiting one periodic plane is same as the flow entering the other periodic plane. Therefore, for simulating flows with periodicity, the number of cells and the face distribution on the periodic boundaries has to match (fig 4.6).

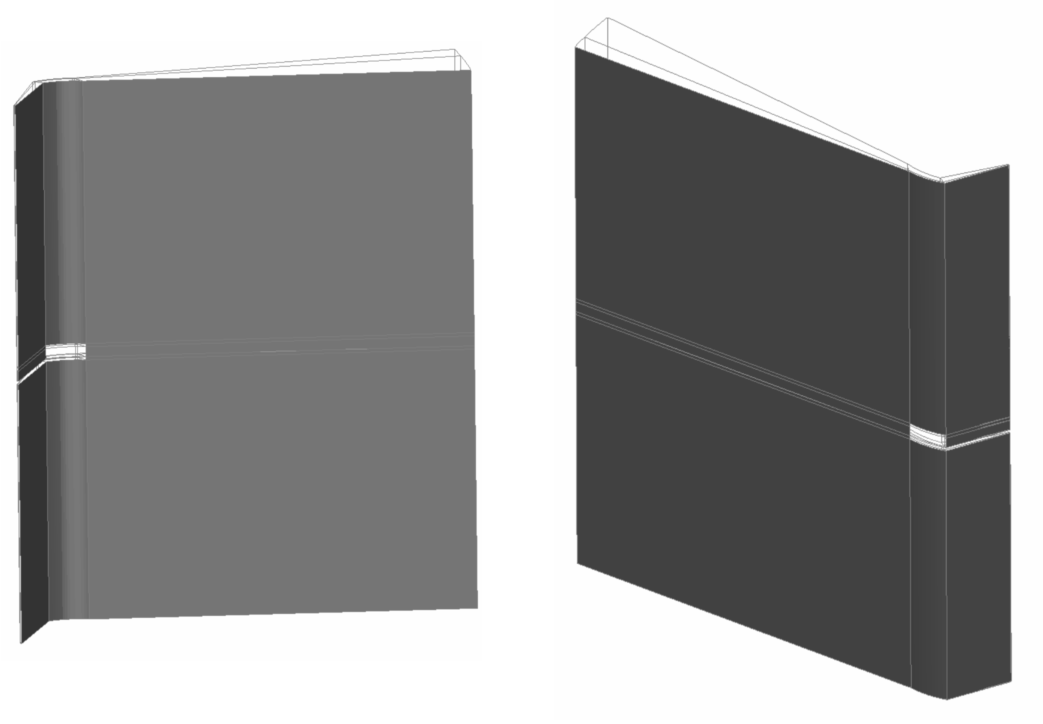

Fig 4.6: Periodic boundaries

4.4.8. Wall roughness

Roughness increases heat transfer at the walls due to higher levels of turbulence. Costes [2005] has performed analysis by inclusion of rough walls. The experimental values obtained from the manufacturers are taken for the analysis. Brake disc has a non-uniform sand grain roughness with a mean of 0.032mm and a peak to valley height of 0.116mm. So, the default value in FLUENT for the roughness height is changed from 0 to 0.032 mm and the roughness factor is made 1 to cater to this non-uniformity.

4.5. Post-processing metrics

The main objective, as mentioned earlier, of the current work is to increase the heat dissipation of the brake disc rotor. Increase in the mass flow rate through the passage decreases the air transit time through the passage there by increasing the rate of heat dissipation. The mass flow decreases with increase in the rotor temperature due to decrease in the air density. Therefore, it is important to optimise the mass flow rate and the amount heat transfer through the passage.

The aerodynamic metrics analysed in this work are the mass flow rate through the passage, flow separations, temperature uniformity, and heat transfer coefficient. Mass flow rate is calculated at the outlet of the passage as a surface integral of the radial velocity of the flow at the exit of the disc brake rotor. Turbulence intensity variation is studied through the passage as turbulence tends to increase heat transfer.

Heat transfer from each of the walls can be calculated as a function of the wall temperature. The rate of heat transfer from the rotor surfaces can be understood by observing the Nusselt number distribution. The heat transfer from the walls tends to increase as the surface temperature increases for the same flow velocity. In order to understand the efficiency of the disc brake rotor design it is important to non-dimensionalise the heat transfer so that it is independent of the rotor temperature. Barigozzi [2003] has defined an expression (see section 2.4.1) for heat transfer effectiveness (equation 4.10). This parameter is a local quantity which varies as the flow progresses through the passage.

$$\varepsilon = \frac{T - T_{atm}}{T_s - T_{atm}} \qquad \text{................ (4.10)}$$

By analysing the heat transfer effectiveness at different sections through the passage from inlet to the outlet, the heat transfer through the passage can be understood. The other non-dimensional parameter used for analysing the global heat transfer through passage of a rotor is the heat power exchanged (see section 2.4.2) proposed by Costes [2005]. This parameter is calculated as a surface integral at the outlet surface of the rotor (equation 4.11).

$$HP = \iint \rho C_p u_r (T - T_{inlet}) dS \qquad \text{.............. (4.11)}$$

The T in the equation 4.11 is the temperature distribution at a specified surface. This parameter is used for comparing different designs of the rotor. The other important aspect is the temperature uniformity on the rotor surfaces. Non-uniform temperature distribution leads to the formation of hot spots. The metric that determines the temperature uniformity is the *thermal distortion index* (T.D.I) (equation 4.12).

$$T.D.I = \frac{T_{\max} - T_{\min}}{T_s - T_\infty} \qquad \text{.............. (4.12)}$$

The lower the value of T.D.I the more the efficient is the disc brake rotor in eliminating the formation of hot spots. T_{max} is the maximum temperature among all the passages surfaces corresponding to the low heat transfer region and T_{low} is the minimum temperature among all the passage surfaces corresponding to the high heat transfer region. T_s is the surface temperature and T_∞ is the ambient temperature.

5

Development of a CFD model

In this chapter the CFD model development details will be presented. A basic turbulent flow over a flat plate analysis is discussed. The boundary layer analysis details are presented. The mesh adapted for the simulation is reviewed in detail. The final section of the chapter deals about the isothermal and heat transfer grid sensitivity analysis.

5.1. Introduction

The mesh defines the accuracy and the stability of the numerical solution computed. The flow governing equations are solved on a meshed domain; therefore the resolution of the entire salient features of the flow depends on the mesh quality and refinement. Boundary layer resolution plays an important role in the computed heat transfer coefficient and the wall shear stress as they depend on the property gradients. Obtaining a proper grid resolution *a priori* is very difficult. Although the higher grid resolution produces more accurate solutions, the computing cost for simulating and post-processing the results increases substantially. In order to analyze the requirements of the mesh for the disc brake geometry, a test case is simulated for turbulent flow over a flat plate with heat transfer and is compared to the analytical solution,

5.2. Turbulent flow heat transfer over a flat plate

It is important to get appropriate near wall mesh distribution when using a turbulence model due to strong interaction between the mean flow and turbulence. This is due to the fact that the *Boussinesq* approximation based models use wall functions for modelling the near wall region. For K-ω SST turbulence model (Mentor [1993]) FLUENT uses wall functions for the buffer layer region where the y+ (= $\rho u_T y/\mu$) value is between 5 and 30. So it is important to ensure that the centroid of the first cell is either fine or course enough to avoid having it in the buffer layer. As y+ is a function of the flow gradients, it is difficult to calculate the required mesh resolution before hand. In order to understand the grid requirement better, this flat plate heat transfer validation case has been performed. A flat plate with the same length as the internal passage of the disc brake is taken and it is simulated for a turbulent flow over it with a specified temperature to the wall. Velocity inlet and pressure outlet boundary conditions (fig 5.1) are used.

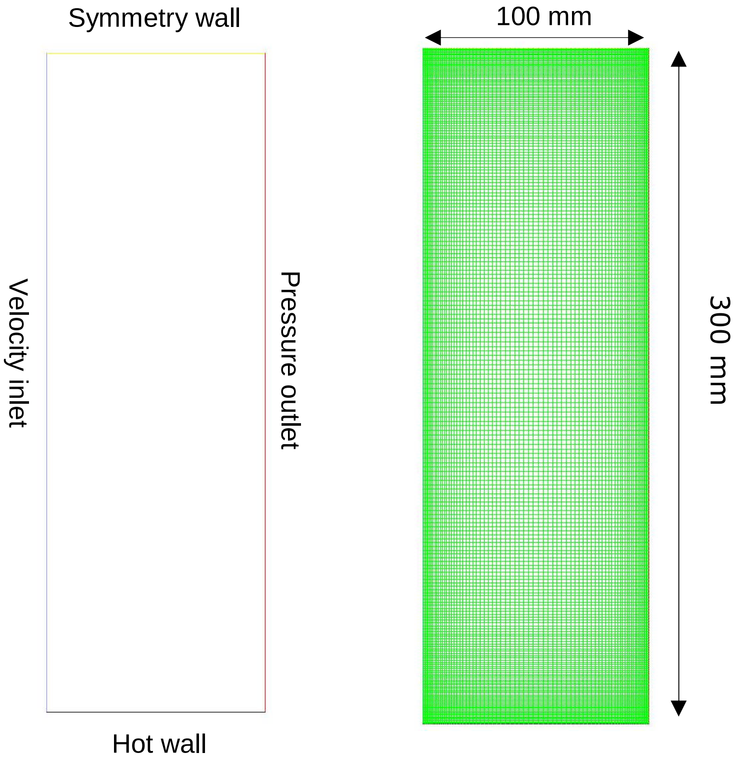

Fig 5.1: Boundary conditions and grid for flow over a flat plate

Various grid sizes (fig 5.2) were considered and the solution was compared with the analytical solution provided by Taine [2004]. Taine proposed an empirical relation for heat transfer due to a turbulent flow over a flat plate based on Reynolds analogy. Because in a turbulent flow the boundary development if affected by fluctuations in the fluid and not by molecular diffusion the boundary growth is independent of Prandtl number. The following equation is valid for Reynolds number less than 10^7.

$$Nu_x = 0.0288\,\mathrm{Re}_x^{\ 0.8}\,\mathrm{Pr}^{(1/3)} \qquad \ldots\ldots\ldots\ldots\ldots\ldots\ (5.1)$$

Initially a 2D coarse grid was chosen with 2581 cells such that the average y+ value at the flat plate was 31 and the agreement with the heat transfer coefficient calculated from the analytical solution was good (fig 5.3) expect in the entry region for the first 10mm. This is because of the fact that the simulation was carried out for an infinitesimally thin plate which is physically unrealistic.

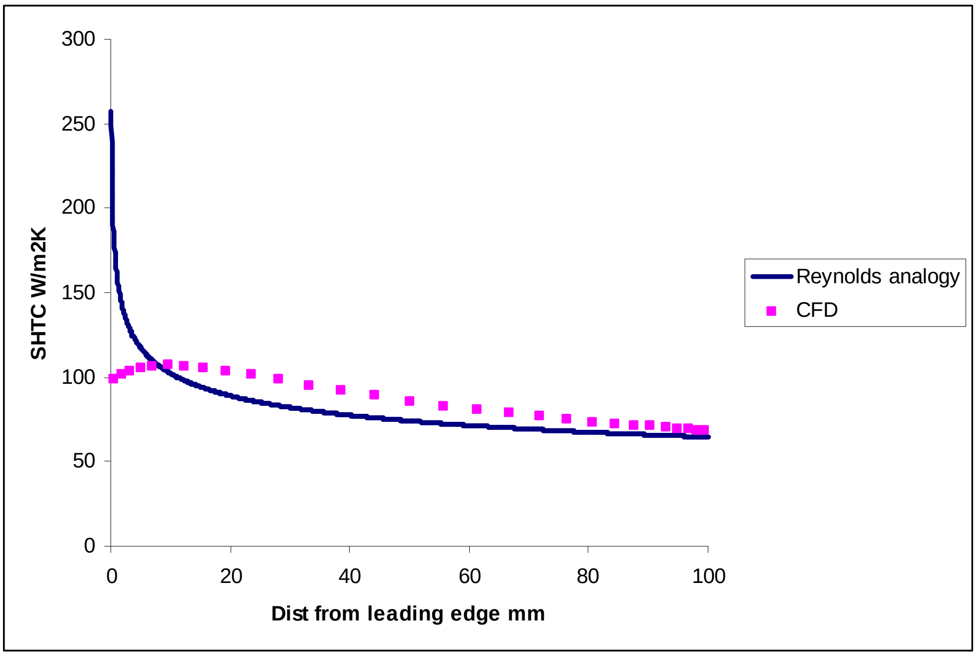

Fig 5.2: A course grid (2500 cells) solution for flow over a flat plate

The grid was made finer to 18841 cells with a y+ value of 13. This, as mentioned above, is the region (buffer region) where the cells should not lie. So, as expected the heat transfer coefficient agreement at the surface of the flat plate with the analytical solution is poor (fig 5.4).

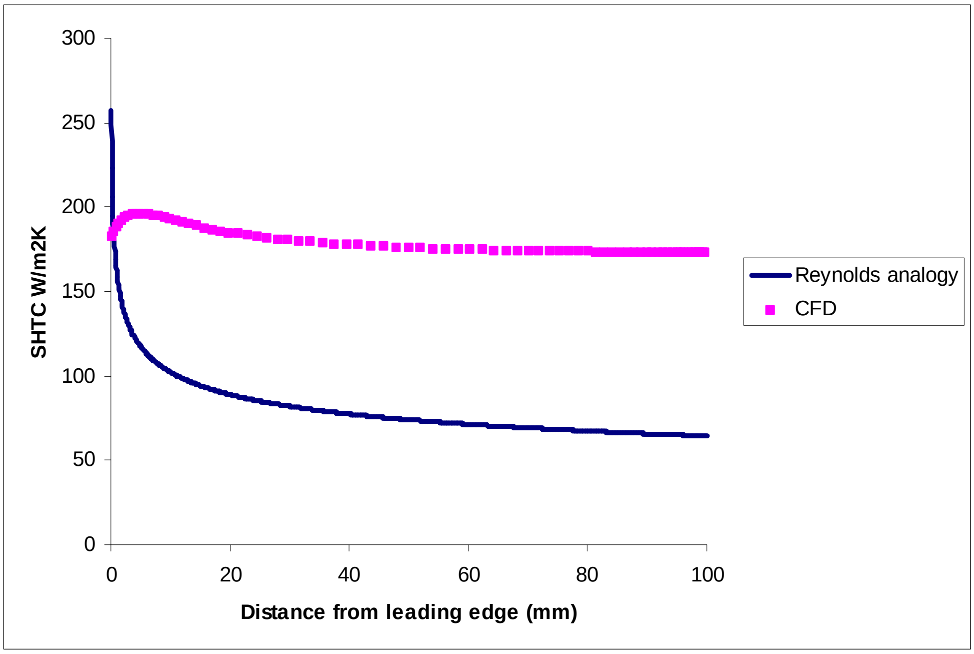

Fig 5.3: A medium grid (18841 cells) solution for flow over a flat plate

The grid was made further fine to 186,501 cells such that the first cell centroid lies in the laminar sub-layer region (y+=3.5). The agreement of the heat transfer coefficient with the analytical solution is within 5.5% (fig 5.5). The entry in the first 10 mm of the plate length shows a variation of 42% from the analytical, this as explained above is due to the infinitesimally thin flat plate assumption made for the simulations.

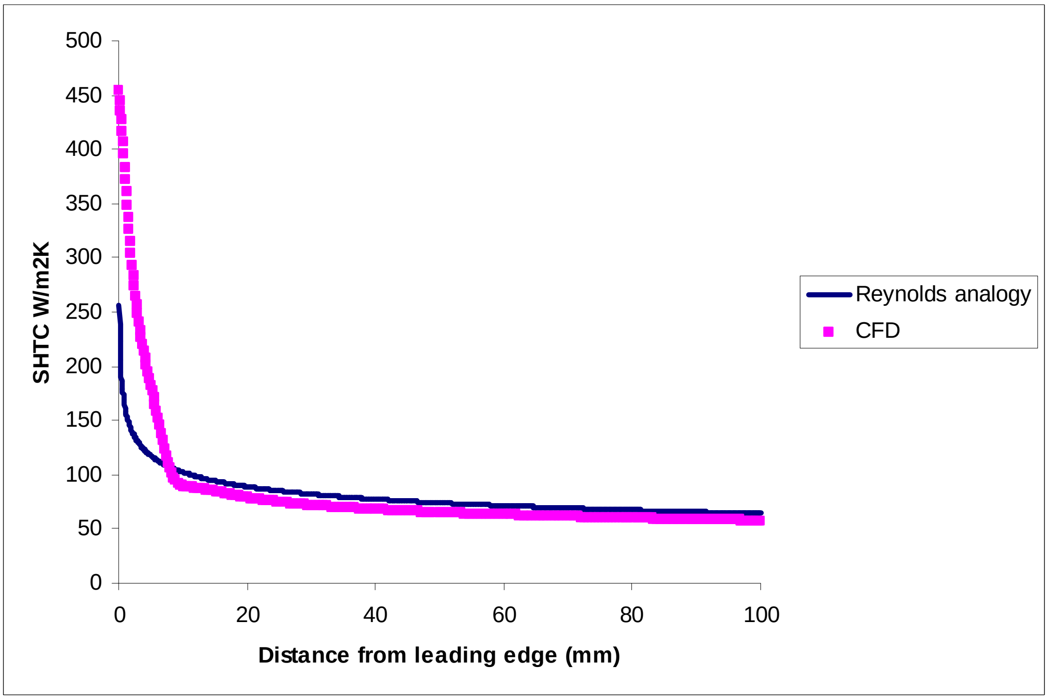

Fig 5.4: A fine grid (186,501 cells) solution for flow over a flat plate

5.3. Boundary layer analysis

As explained in section 5.2, the best agreement with the analytical solution is when the mesh density is such that the first cell centroid lies in the laminar sub-layer. In order to achieve that, boundary layer mesh density inside the rotor passage plays an important role. The boundary mesh can be achieved in two different ways; either by using non-uniform mesh with a spacing ratio small enough such that the first cell lies in the region of interest or by using a uniform but a fine mesh.

Analysis was done initially by using a hyperbolic tangent distribution function with a start value of 0.1 (fig 5.6). This ensures that the cells are clustered near the wall.

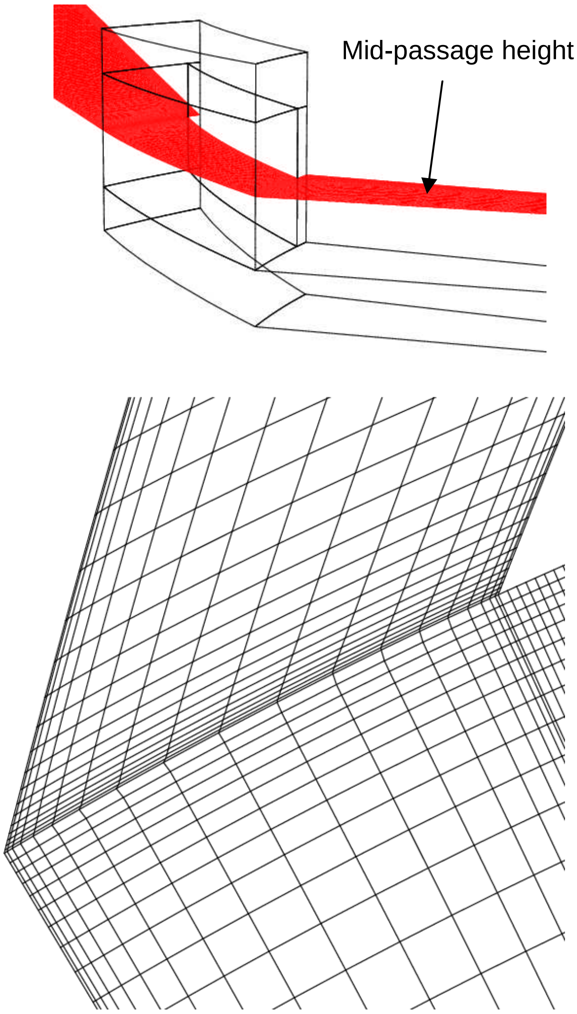

Fig 5.5: Boundary layer meshing inside the passage with spacing ratio 0.1

The simulations performed had difficulties in achieving convergence and the residual error was very high for all the transport equations (fig 5.7). This could be due to sharper changes in the cell sizes from the wall to the core region. In order to avoid this initial value for the hyperbolic tangent was increased from 0.1 to 0.3 but still within the laminar sub-layer region. This gives better control on the grid size variation from the wall to the core region inside the rotor passage (fig 5.8).

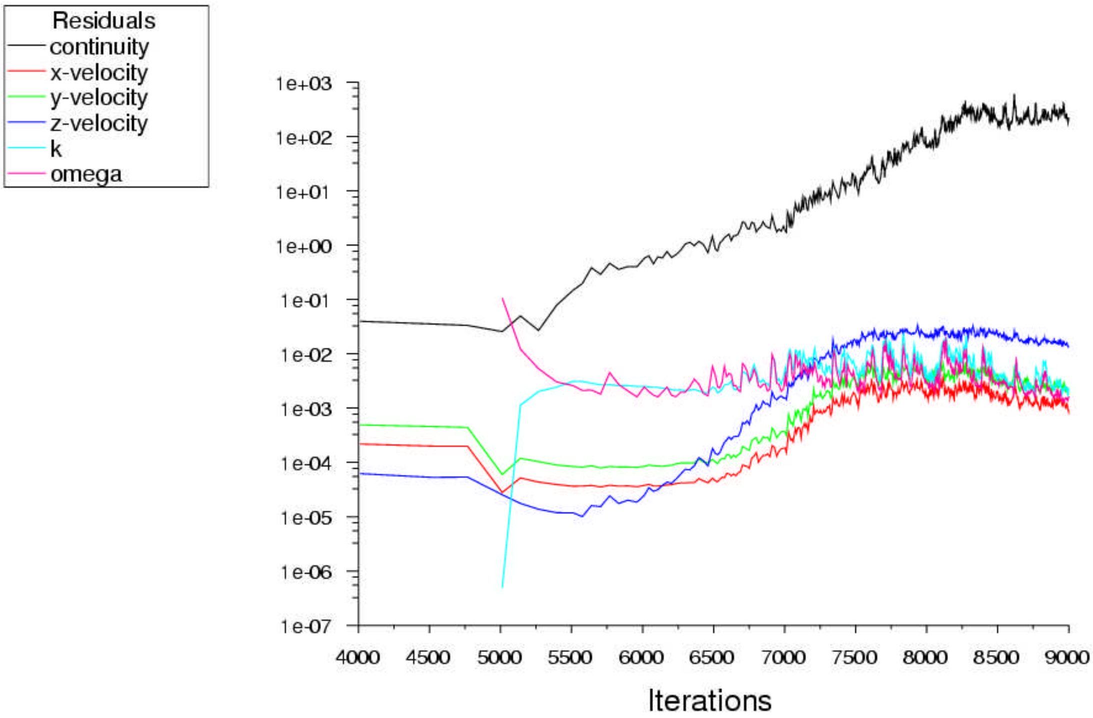

Fig 5.6: Convergence residual plot for a non-uniform grid with an initial cell value of 0.1

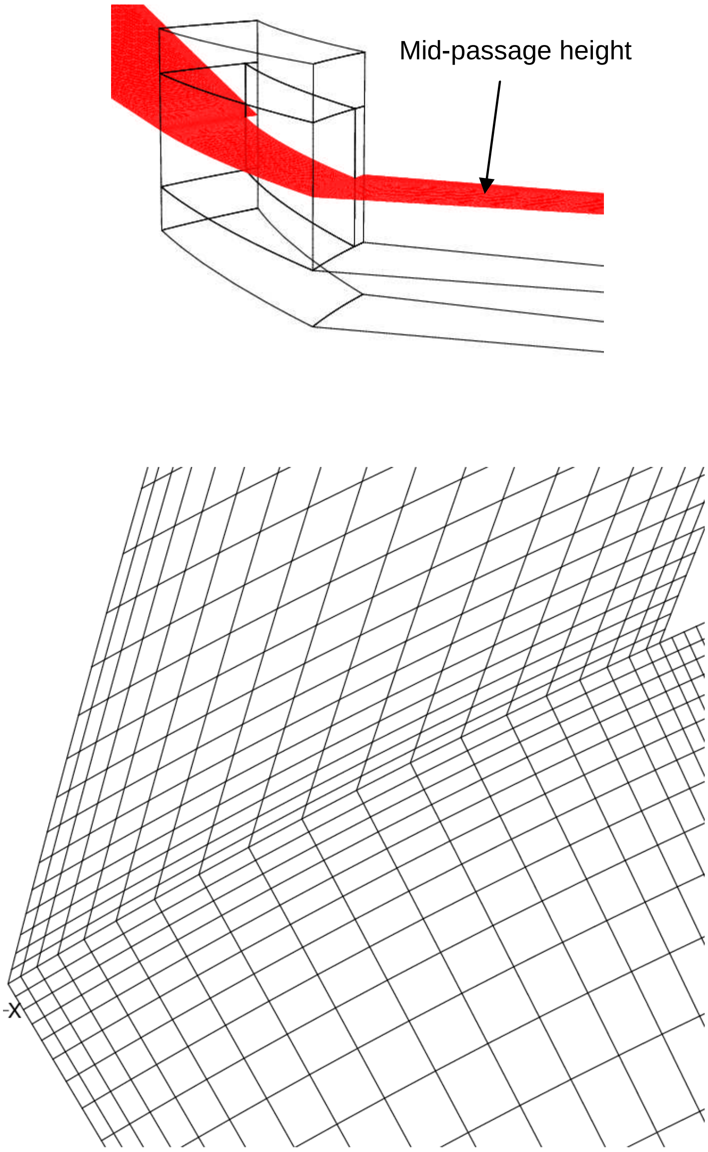

Fig 5.7: Boundary layer meshing inside the passage with spacing ratio 0.3

This change in the initial cell value lent some stability to the numerical computation by reducing the residual error. But the convergence is still not good enough to justify credibility to the numerical computation (fig 5.9).

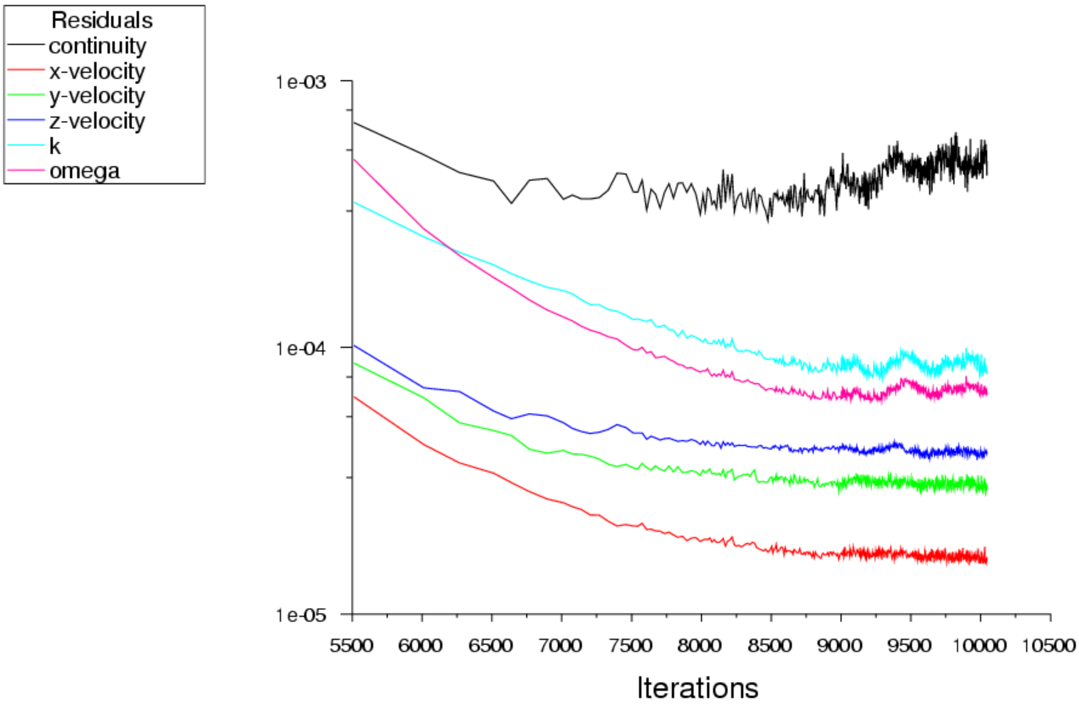

Fig 5.8: Convergence residual plot for a non-uniform grid with an initial cell value of 0.3

In order further enhance the convergence behaviour of the numerical solution, the mesh inside the rotor passage was made uniform but fine enough to incorporate first cell centroid in the laminar sub-layer region (fig 5.10). This change in the mesh distribution dramatically increased the convergence behaviour of the numerical computation (fig 5.11).

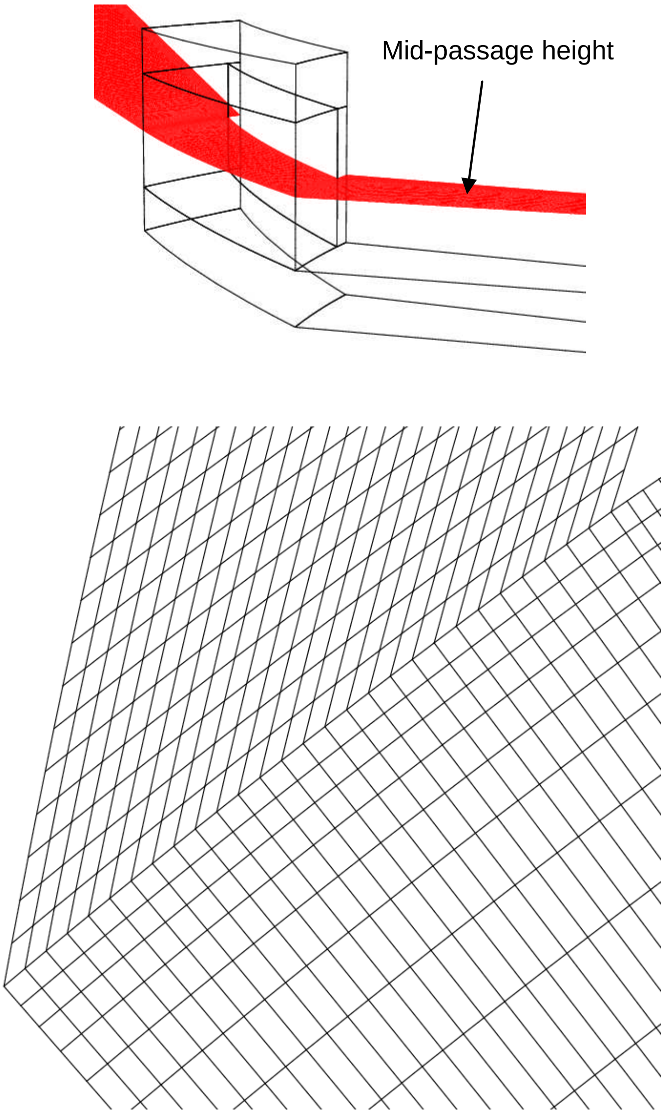

Fig 5.9: Boundary layer meshing inside the passage with uniform mesh

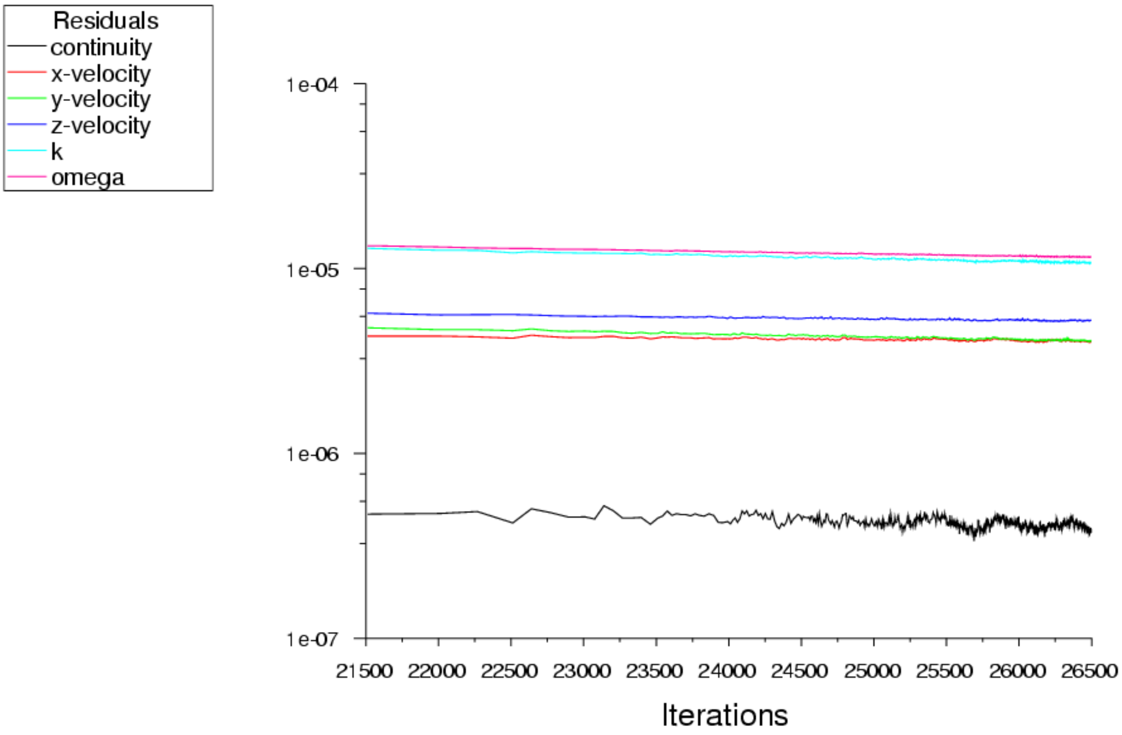

Fig 5.10: Convergence residual plot for a uniform grid

5.4. Multi-block topology and gridding strategy

A uniform mesh is used inside the passage of the rotor geometry (see section 5.3). The complete geometry is divided into 14 blocks for the ease of meshing. Various edges of the brake disc geometry on which the grid points are distributed are shown schematically in figure 5.12. Based on the boundary layer simulations that have been run, the computation time required for various grid sizes has been evaluated and it was decided that the maximum grid resolution for all the jobs is 1.9 million grid points. The details of the grid sensitivity analysis are explained in the following sections.

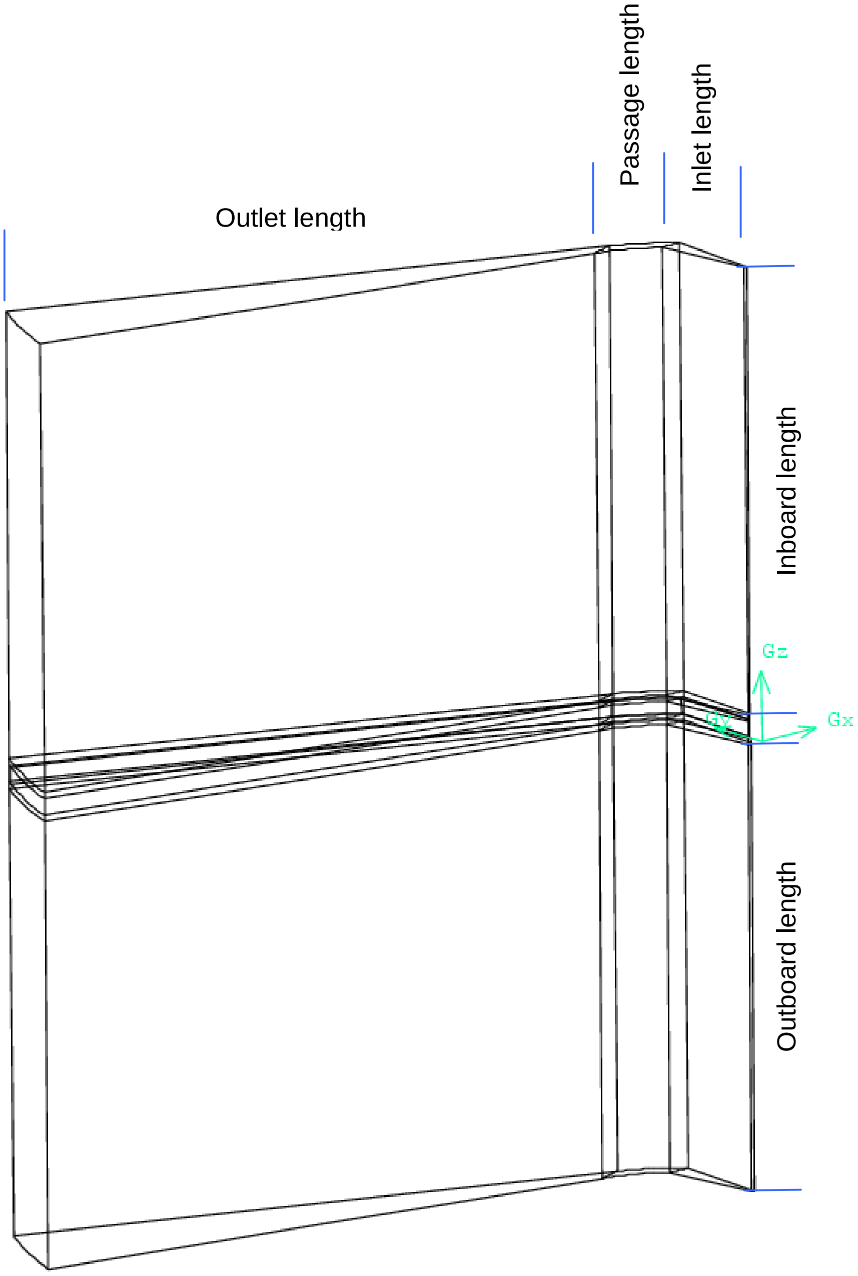

Fig 5.11: Isometric view of the disc brake geometry

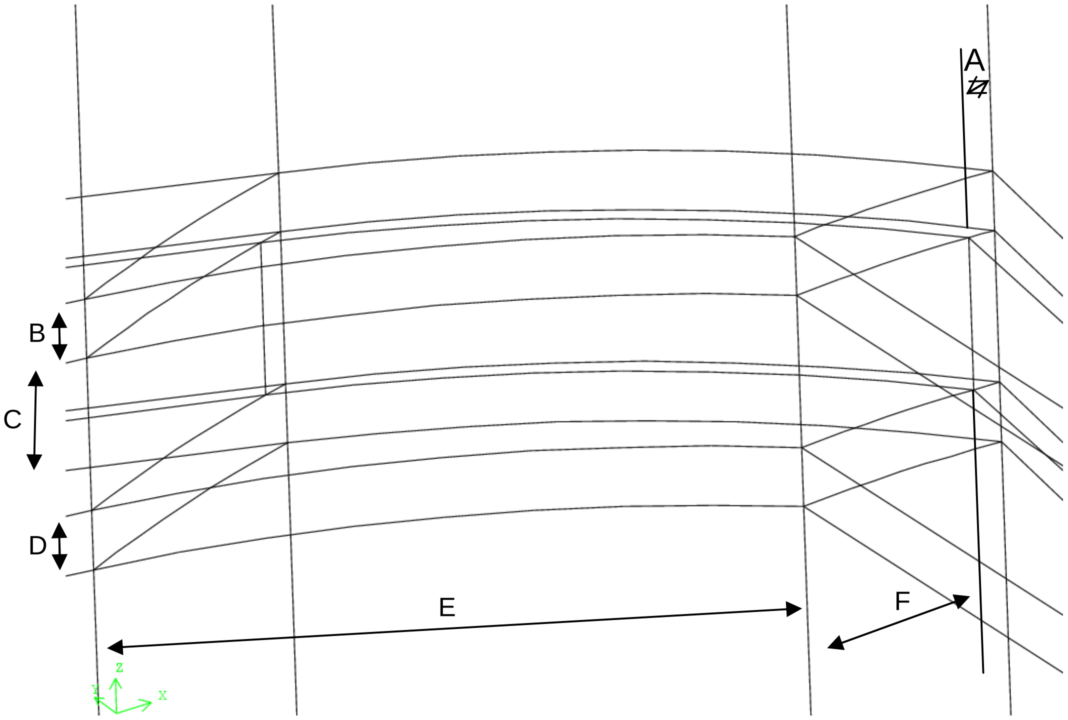

Fig 5.12: Schematic of the disc brake rotor passage

A: Blade thickness

B: Inboard thickness

C: Passage height

D: Outboard thickness

E: Passage length

F: Passage width

Variable	Geometric length (mm)	Number of grid points	GRIDGEN start value and end value for hyperbolic tangent distribution function respectively
Inlet length	117.5	43	-1
Passage length	47.5	300	0
Outlet length	610	60	-1
Blade thickness	3	12	0
Passage circumferential width	24.216	43	0
Inboard length	475	60	-1
Outboard length	475	60	-1
Inboard thickness	7	17	-1
Passage height	18	51	0
Inboard radial length	47.5	43	-1 & -1
Outboard radial length	47.5	43	-1 & -1
Number of cells			1,925,552

Table 5.1: Grid points information for a fine grid rotor geometry

The number of grid points used on each of the connectors and the spacing ratio used for the hyperbolic tangent distribution function is presented in table 5.1. The value of -1 specified in GRIDGEN makes sure that the grid points are aligned with the uniform mesh used inside the passage avoiding the sharp change of grid size in the direction of flow. This also ensures that the grid points are clustered near the inlet and exit of the disc brake rotor where sharp gradients exist (fig 5.13).

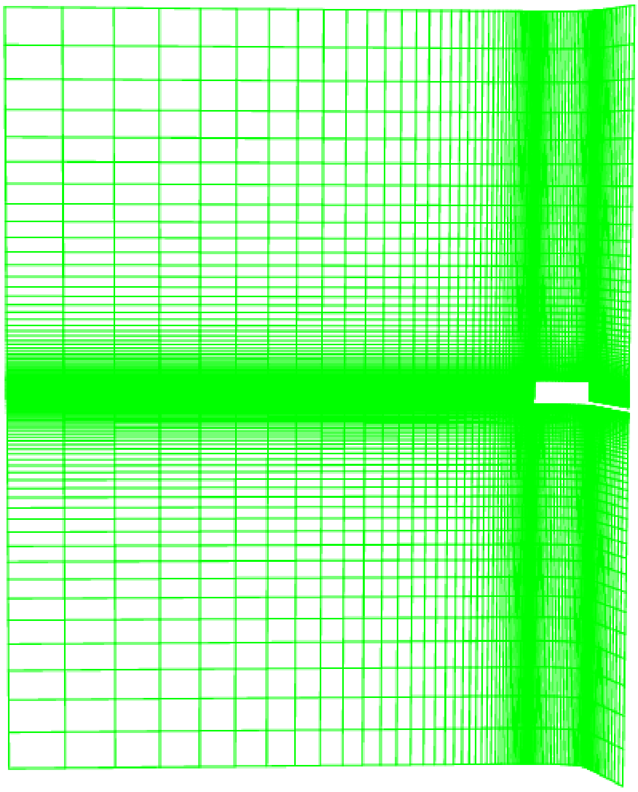

Fig 5.13: Fine grid for the datum rotor

5.5. Grid sensitivity study

The datum rotor was taken as reference to carry out the grid sensitivity analysis. A speed of 1500 rpm was chosen for the simulation. Initially the case was run for an isothermal condition. The mass flow rate is the isothermal parameter whose grid dependency is analysed. Later on the thermal condition was simulated with a uniform surface temperature of 800K for all the internal walls of the rotor passage. The total heat transfer is the thermal parameter whose grid dependency is analysed. The fine grid was coarsened by reducing the number of cells in each direction by a factor of 1.3 so as to reduce the total number of grid points to half. This mesh is referred to as a medium grid (fig 5.14) with 860,664 cells.

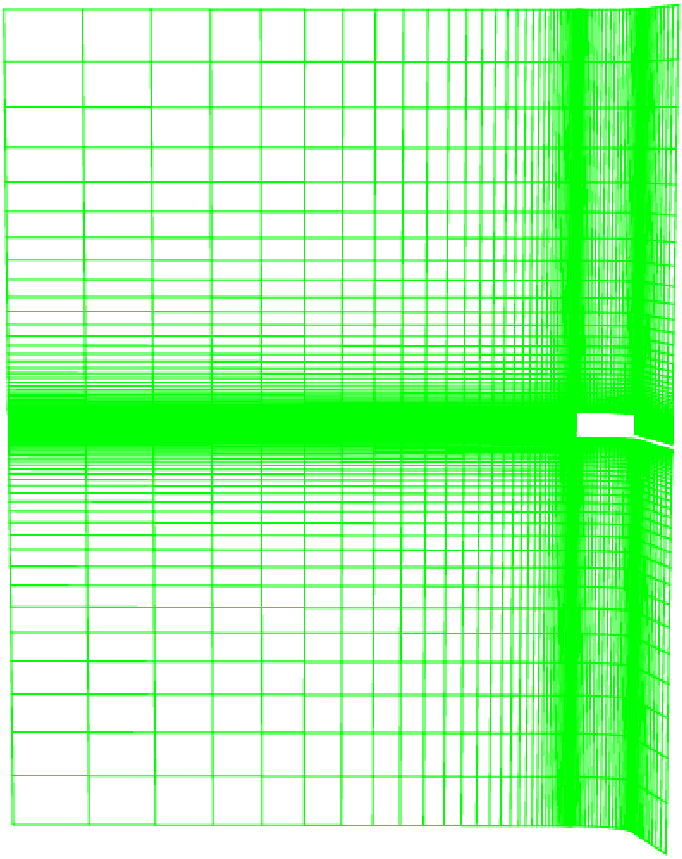

Fig 5.14: Medium grid for the datum rotor

The medium was further coarsened by reducing the grid points in each direction by a factor of 1.3 thus reducing the total number of grid to half. This mesh is referred to as a coarse grid (fig 5.15) with 373,162 cells.

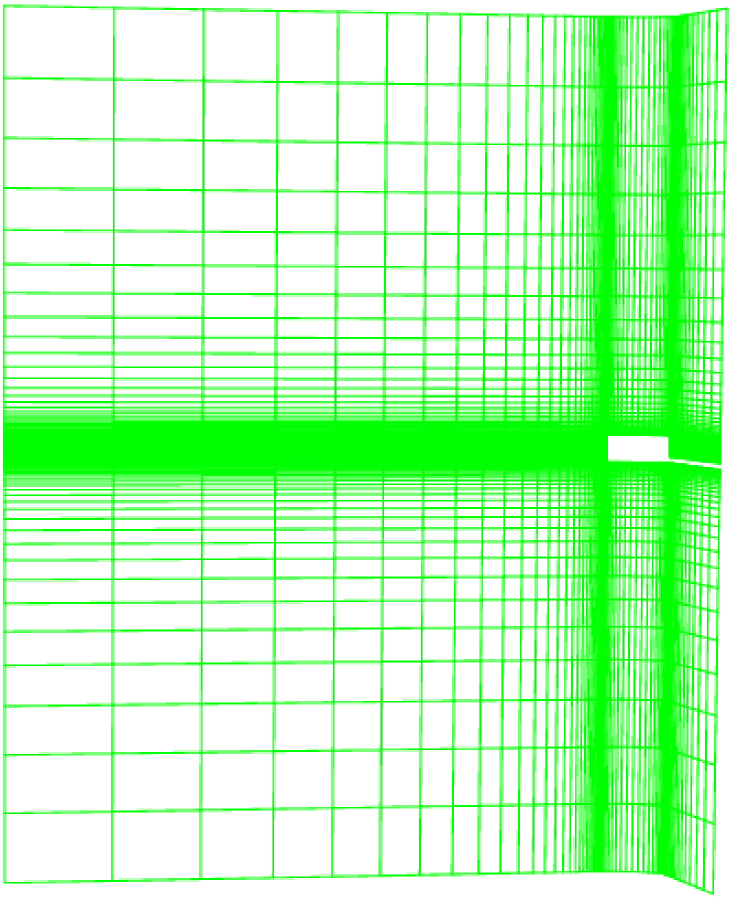

Fig 5.15: Course grid for the datum rotor

5.5.1. Isothermal grid sensitivity

The mass was measured for all the grid sizes by evaluating the surface integral at the exit of the rotor using radial velocity component. The value for different grid sizes is listed in table 5.2.

Grid size	Isothermal mass flow rate kg/sec @1500rpm
Course	0.2690
Medium	0.2554
Fine	0.2479

Table 5.2: Mass flow rates for different grid sizes

The GCI is evaluated for mass flow rate (see section 4.3.1). The GCI for a medium grid by increasing the number of cells from a course grid is calculated as follows.

$$GCI[Medium] = F_s|\varepsilon|/(r^p - 1) \qquad \text{…………..} (5.2)$$

F_s= 3

$$\varepsilon_{2-1} = (f_2 - f_1)/f_1$$

f_1= 0.2690; course grid solution

f_2= 0.2554; medium grid solution

ε_{2-1}= -0.0532

GCI [medium]= 3*(-0.0532)/(1.69-1)

= -0.2313

$$GCI[Fine] = F_s|\varepsilon|/(r^p - 1) \qquad \text{…………..} (5.3)$$

F_s= 3

$$\varepsilon_{3-2} = (f_3 - f_2)/f_2$$

f2= 0.2554; medium grid solution

f3= 0.2479; fine grid solution

ε_{3-2}= -0.0302

GCI [fine]= 3*(-0.1313)/(1.69-1)

= -0.1313

For the solution to lay in the asymptotic range the following condition has to be fulfilled.

$$GCI[Medium] = r^p GCI[Fine] \qquad \text{………… (5.4)}$$

For the grid sensitivity analysis carried out the above condition is not completely satisfied (fig 5.15). The difference in the values of the left hand side and right side of the equation 5.4 presents the deviation in the solution from the asymptotic range. For this analysis the error is within 8%. This error reduces further by increasing the number of grid points.

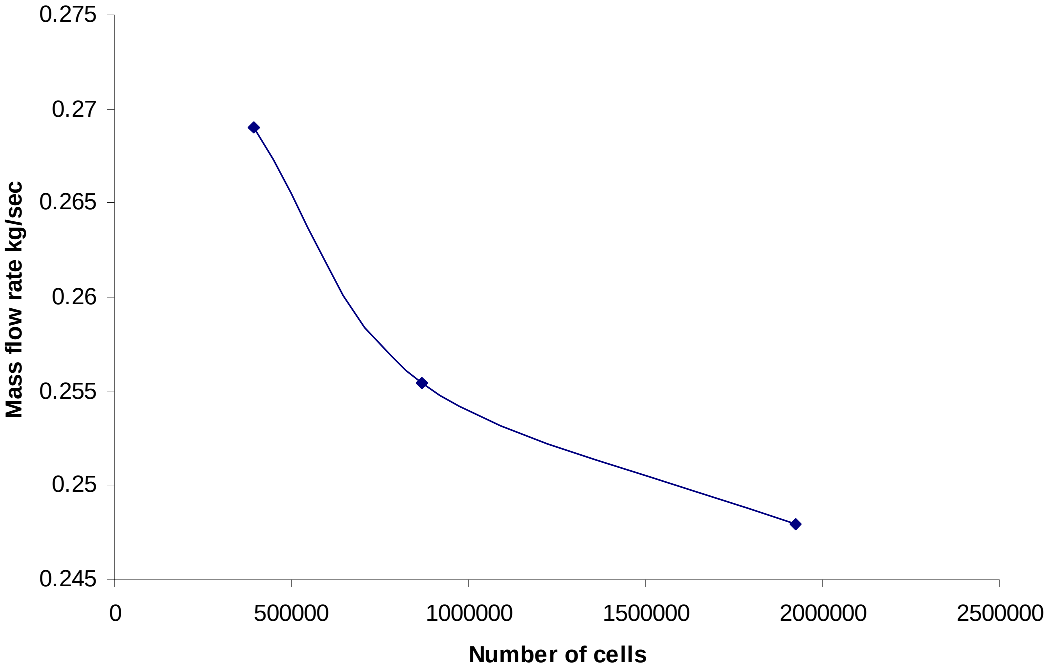

Fig 5.16: Isothermal grid sensitivity analysis

5.5.2. Heat transfer grid sensitivity

The heat transfer from each of the internal surfaces of the rotor passage was measured using the surface heat transfer coefficient. The total heat transfer is the summation of individual heat transfer from each of the passages. This value for different grid sizes is listed in table 5.3.

Grid size	Total heat transfer W @1500rpm and 800 K
Course	262.532
Medium	225.305
Fine	240.709

Table 5.3: Total heat transfer for different grid sizes

The GCI is evaluated for the total heat transfer (see section 4.3.1). The GCI for a medium by increasing the number of cells from a course grid is calculated as follows.

$$GCI\left[Medium\right] = F_s\left|\varepsilon\right| / \left(r^p - 1\right)$$

$F_s = 3$

$$\varepsilon_{2-1} = (f_2 - f_1) / f_1$$

$f_1 = 262.532$; course grid solution

$f_2 = 225.305$; medium grid solution

$\varepsilon_{2-1} = 0.1416$

GCI [medium]= 3*(0.1416)/(1.69-1)

= 0.6156

$$GCI\left[Fine\right]=F_s\left|\varepsilon\right|/\left(r^p-1\right)$$

F_s= 3

$$\varepsilon_{3-2}=(f_3-f_2)/f_2$$

f2= 225.305; medium grid solution

f3= 240.709; fine grid solution

$\varepsilon_{3\text{-}2}$= -0.068

GCI [fine] = 3*(-0.068)/(1.69-1)

= -0.4995

Even though the total heat transfer value does not lie in the asymptotic range (fig 5.16), the absolute error is within 6.8%. The heat transfer grid independency is difficult to accomplish as it strongly depends on the temperature gradients which are directly related to the cell sizes being used. Higher grid sizes lead to better resolution of the near wall temperature gradients leading to a more realistic solution. Since it is computationally very expensive and practically not feasible to run the simulations at higher grid sizes than 1.9 million cells, it was decided to run all the simulations for the current project at 1.9 million cells. This can be justified as the absolute error in the heat transfer is within a reasonable value.

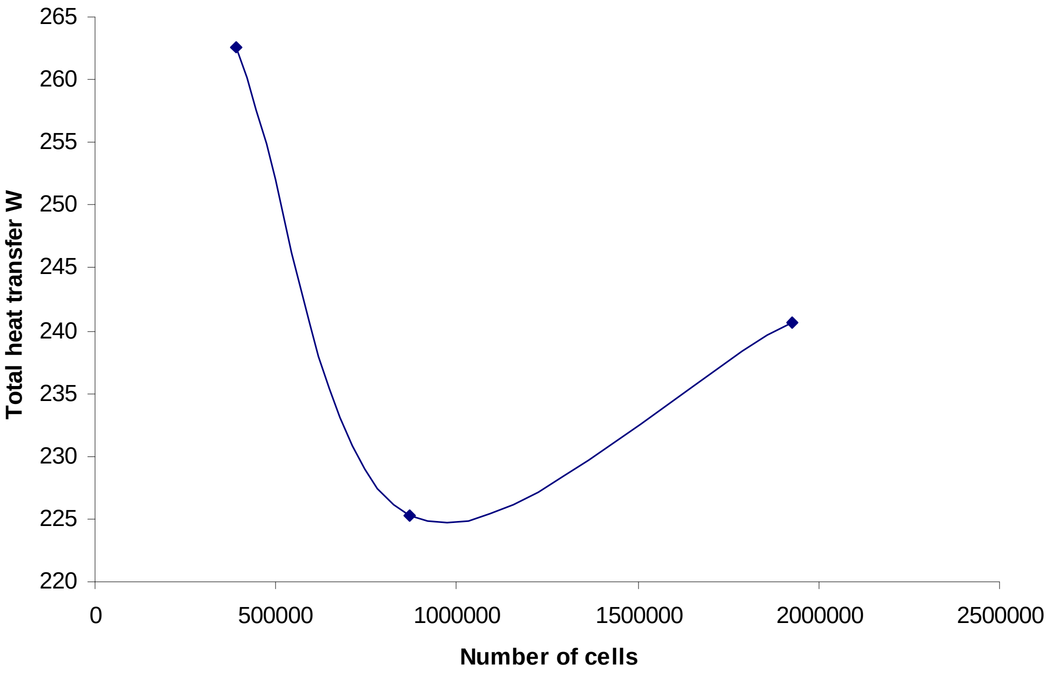

Fig 5.17: Heat transfer grid sensitivity analysis

6

Parametric study- results and discussion

In this chapter the results from the parametric study are presented. The first section deals with the effect of blade angles on the aero-thermal performance of a ventilated disc brake. The section and third sections deal with the effect of blade speeds & temperature, number of blades & aspect ratio respectively on the rotor performance.

6.1. Introduction

The aero-thermal performance of the disc brake rotor is influenced by various parameters like heat transfer rate from the internal surfaces, mass flow rate through the passage, and temperature uniformity on the surfaces. The increase in the mass flow rate through the passage increases the rate of heat dissipation. This is because of higher mass flow rates associated with higher velocities. The other important aspect is the temperature uniformity, the presence of separation zones or flow blockages within the rotor can lead to local low heat transfer regions forming *hot spots* Therefore, it is important for a rotor to not just increase the rate of heat dissipation but also to avoid formation of hot spots. It is also desirable to maximise the efficiency of the cooling air by increasing the work done by it in heat dissipation during its transit through the rotor passage.

6.2. Datum design analysis

The datum rotor is the design that is currently in service. The datum rotor comprises of an inlet angle (β_1) of 43.16^0 and an outlet angle (β_2) of 35.62^0 (fig 6.1). The thickness of the inboard and the outboard surfaces were maintained 7mm (fig 6.2). The model was created by a single curve defining each blade by keeping the blade angles and the number of blades i.e. 48 as constraints. The grid is initially scaled to the appropriate units and the TUI command *grid/modify-zones/make-periodic* in FLUENT is used to make the faces, which are first declared as walls, into periodic faces (fig 4.6).

The simulation was performed at 750 rpm in order to reduce the computational time that would be required for running at higher speeds. Initially an isothermal simulation was performed with a first order upwind scheme and with a convergence criterion of 1e-3. The solution obtained was used as an initial solution and the discretisation scheme was made second order accurate and also the convergence criterion was reduced to 1e-4 in order to reduce the numerical error in the computation (fig 6.3). These isothermal solutions obtained were used as initial solution to simulate the brake disc rotor at a temperature of 800K for the aero-thermal analysis of the rotor.

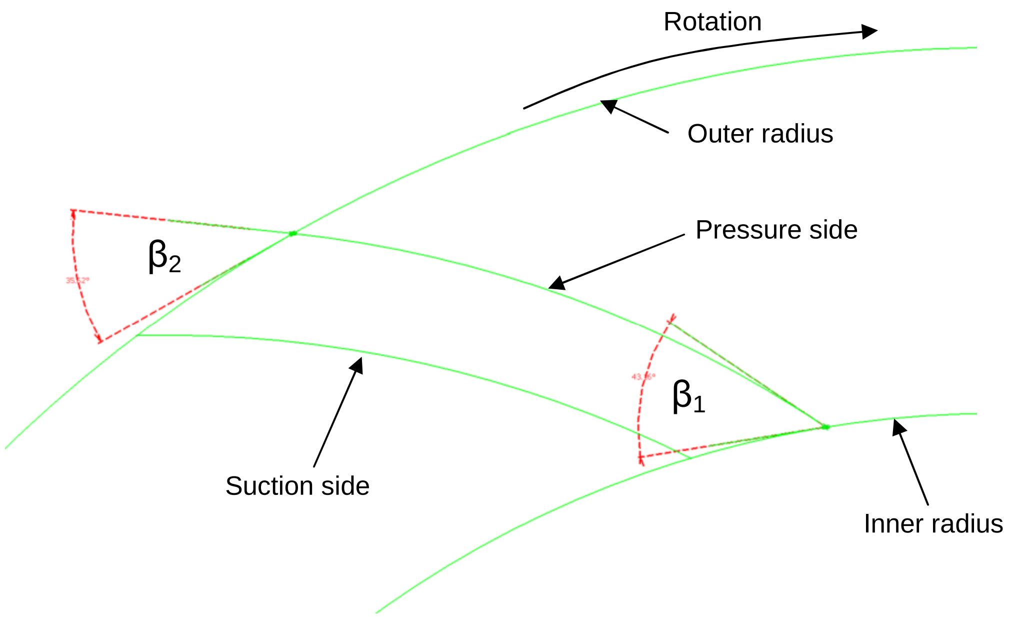

Fig 6.1: Topic view of the datum rotor

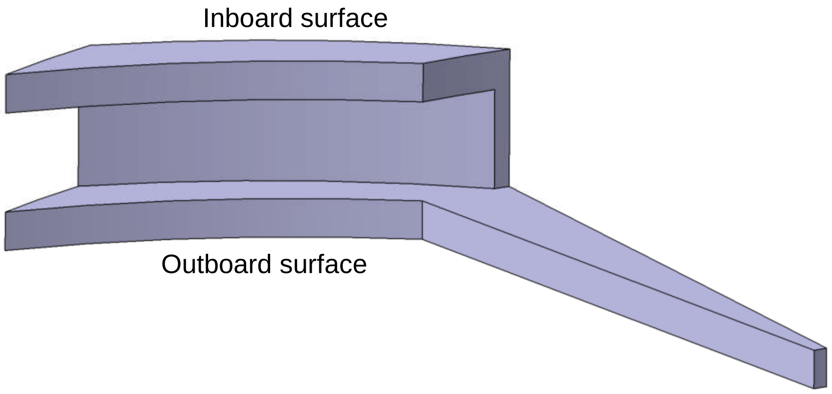

Fig 6.2: Global view of the datum rotor

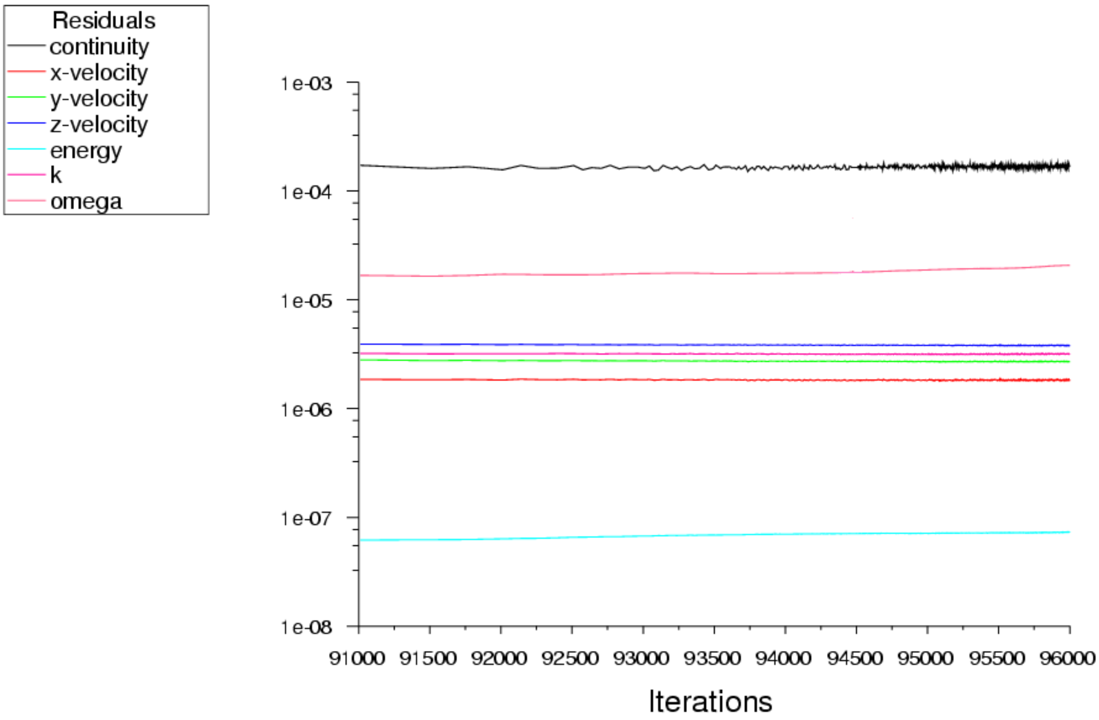

Fig 6.3: Datum convergence residual plot

The mass flow rate through the datum rotor is calculated as function of individual passage mass flow rate ($\dot{m}$). This is evaluated as an area integral at the exit of each passage by using the radial velocity component and the outlet area (A_S) of the passage (fig 6.4).

$$\dot{m} = \iint_{s} \rho u_r A_s ds \qquad \text{………………..} \; 6.1$$

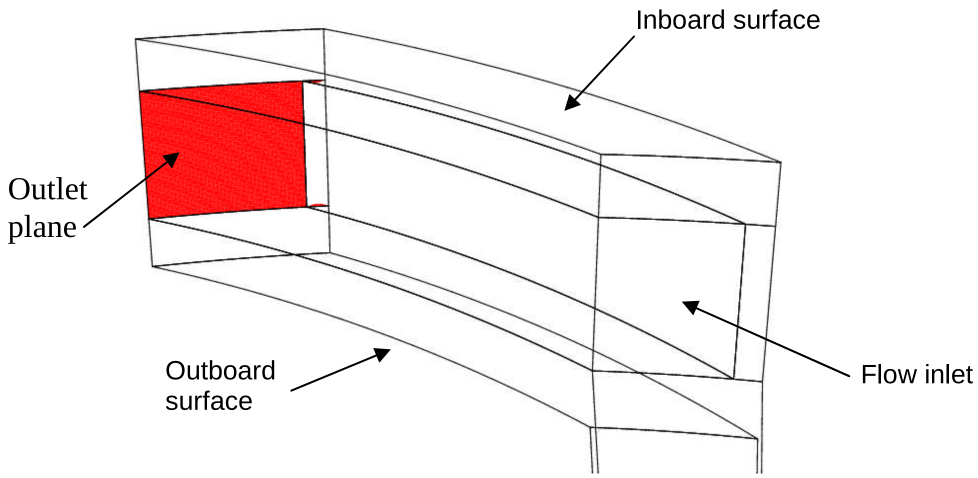

Fig 6.4: Mass flow rate measurement plane

The mass flow rate was observed to be 0.0792 kg/sec from the CFD simulations. From the theory of turbomachinery it is understood that when the air changes direction from axial to radial during its entry into the passage from the inboard side, inlet separation occurs at the inlet of the passage due to deceleration of the flow. This deceleration becomes severe with change in the inlet angle the details of which will be explained in the following sections. This is profound near the inboard of the passage. As the flow approaches the passage outboard surface the inlet separation reduces due to impingement of flow on it (fig 6.5). This phenomenon can be observed from the relative velocity contours close to the passage inboard side (fig 6.6). The region in figure 6.6 indicated by A is the separated region in the flow due to flow direction change from axial to radial and this is at the inlet of the passage inboard side.

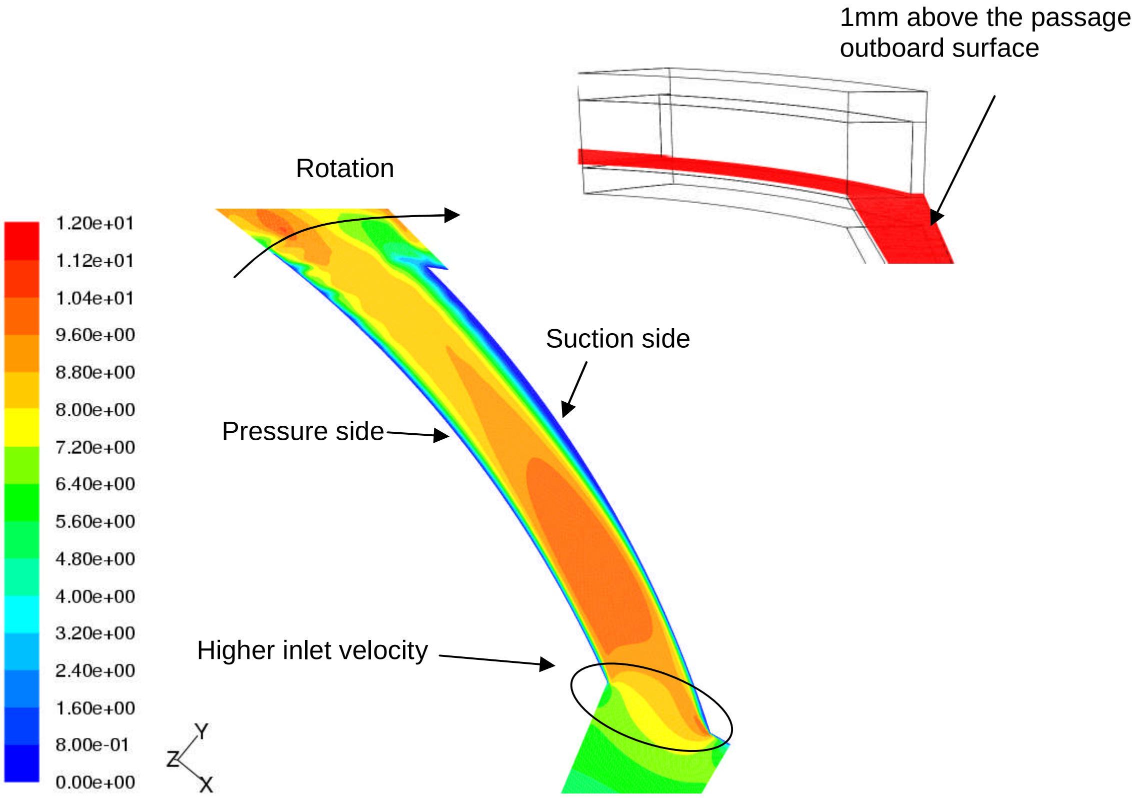

Fig 6.5: Datum relative velocity (m/sec) 1mm above the passage outboard surface at 750 rpm and 800 K

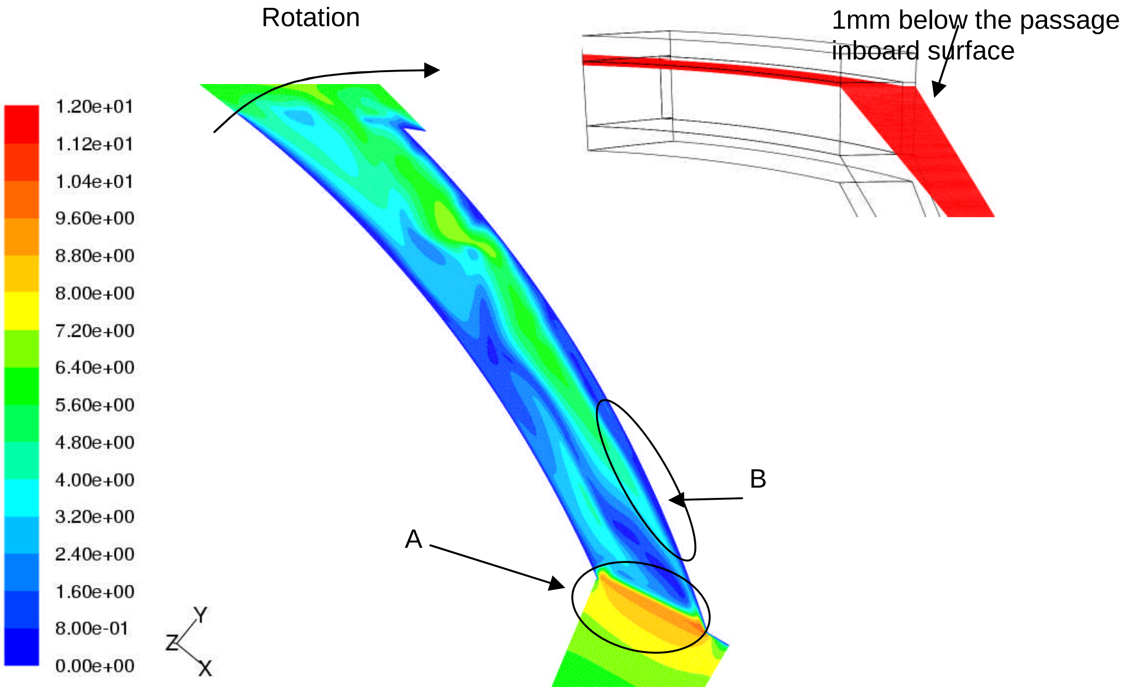

Fig 6.6: Datum relative velocity (m/sec) 1mm below the passage inboard surface at 750 rpm and 800 K

Also, the same feature can be observed due to the change in the air flow direction from tangential to radial. This creates a separation near the suction side of the passage (fig 6.7). These flow separation regions act as blockages thereby reducing the mass flow rate through the passage of the rotor. The region indicated by B in figure 6.6 is the separated region 1mm below the inboard surface due to flow direction change from tangential to radial and this is directed towards the passage suction side.

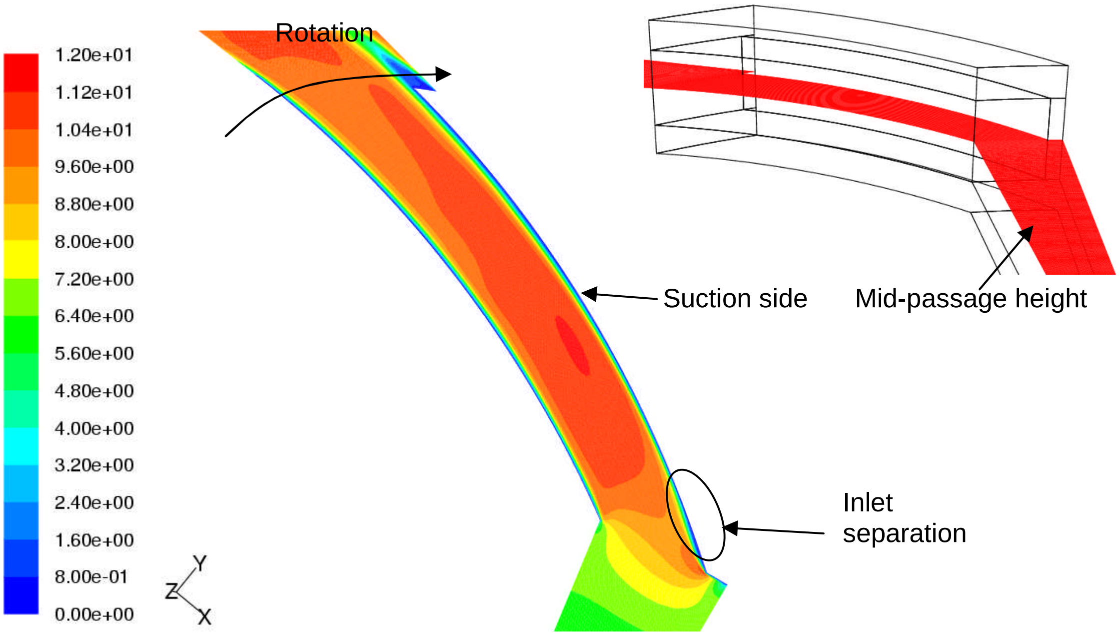

Fig 6.7: Relative velocity (m/sec) at mid-passage height of the rotor

After the energy equation has been solved, FLUENT uses the temperature gradient at the wall to evaluate the heat transfer rate from each of the internal passages of the disc brake rotor. It has been observed that the total heat transfer rate from all the internal surfaces of the passage for a datum rotor is 120.23 W. There is a strong link between the heat transfer from the passage internal surfaces and flow aerodynamics. This can be understood by observing the Nusselt number distribution on each of the internal surfaces along with relative velocity vectors. The flow separation due to change in the air flow direction from axial to radial causes the local Nusselt number to reduce. This reduction in the heat transfer rate is predominant near the inboard side (fig 6.9) and the suction side of the passage (fig 6.10) due to greater influence of the recirculation regions in these regions. The flow impingement on the outboard side from the axial direction increases the Nusselt number. There is also a reduction in the heat transfer rate due to change in the flow direction from tangential to radial. This also reduces the Nusselt number on the suction side and the inboard side. The flow impingement on the pressure side from tangential entry increases the Nusselt number.

From figure 6.11 it can be observed that as the fluid enters through the inboard side of the disc brake rotor as explained above it separates. This is an open separation covering the entire length through the passage near the inboard side. This causes a blockage to the flow there by reducing the heat transfer rate on the inboard surface (fig 6.9) causing hot spots. The fluid flow through at the mid height of the passage is more uniform which does not affect the heat transfer rate. The fluid as it reaches the bottom of passage separates at the inlet; this separated flow becomes a vortex and travels upwards interacting with the separated flow at the inboard surface. The other intriguing aspect of the flow is the deflection of the flow at the exit of the outboard surface at the suction side of the passage. This deflection creates a region a very low velocity at the bottom of the suction side creating a region of very low heat transfer which leads to the formation of hot spots.

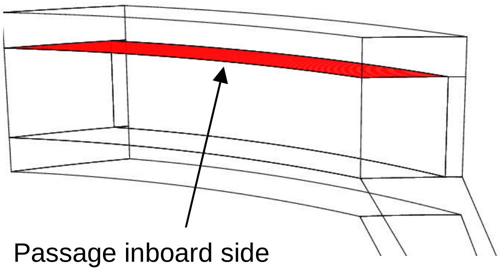

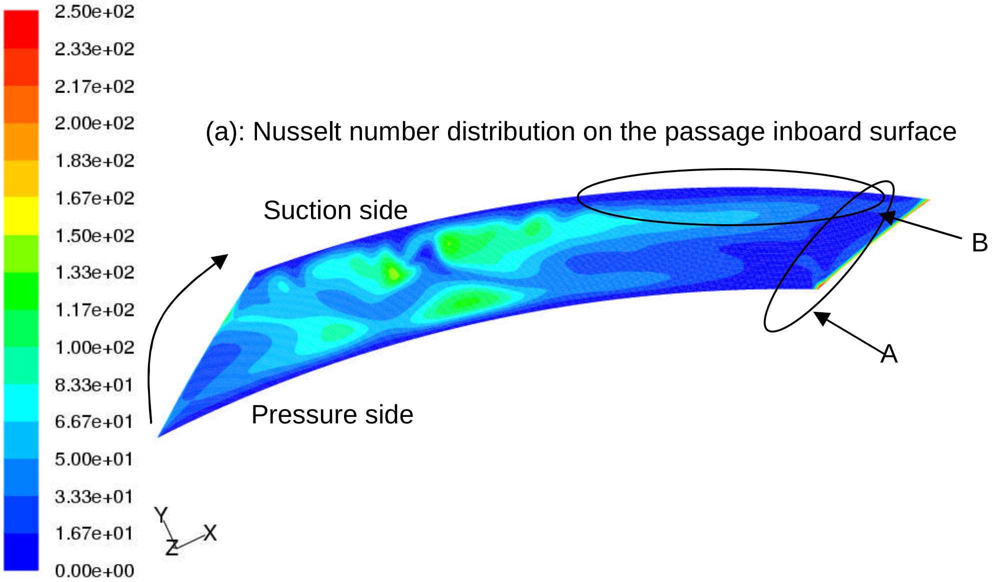

(a): Nusselt number distribution on the passage inboard surface

A: Effect of flow direction change from axial to radial

B: Effect of flow direction change from tangential to radial

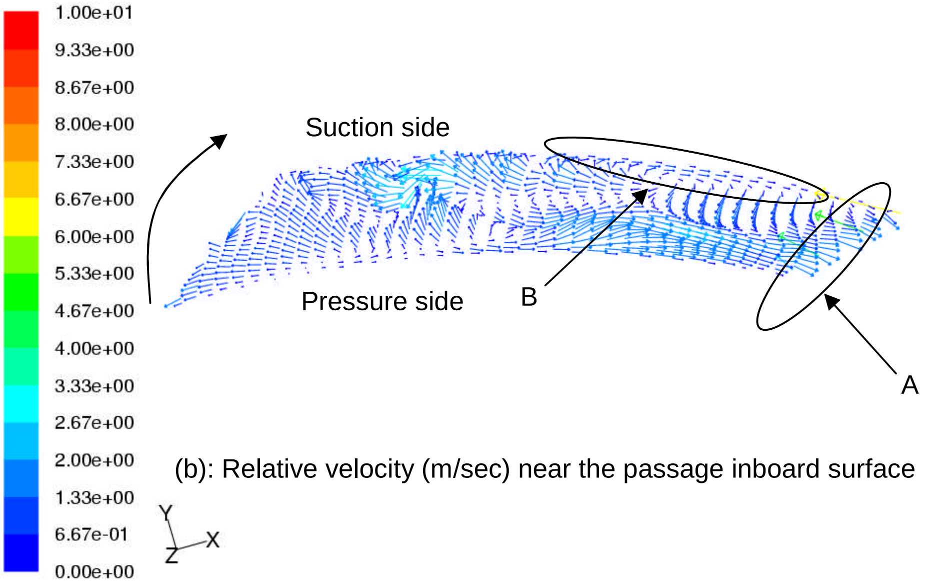

(b): Relative velocity (m/sec) near the passage inboard surface

Fig 6.9: Nusselt number and relative velocity (m/sec) on the passage inboard surface

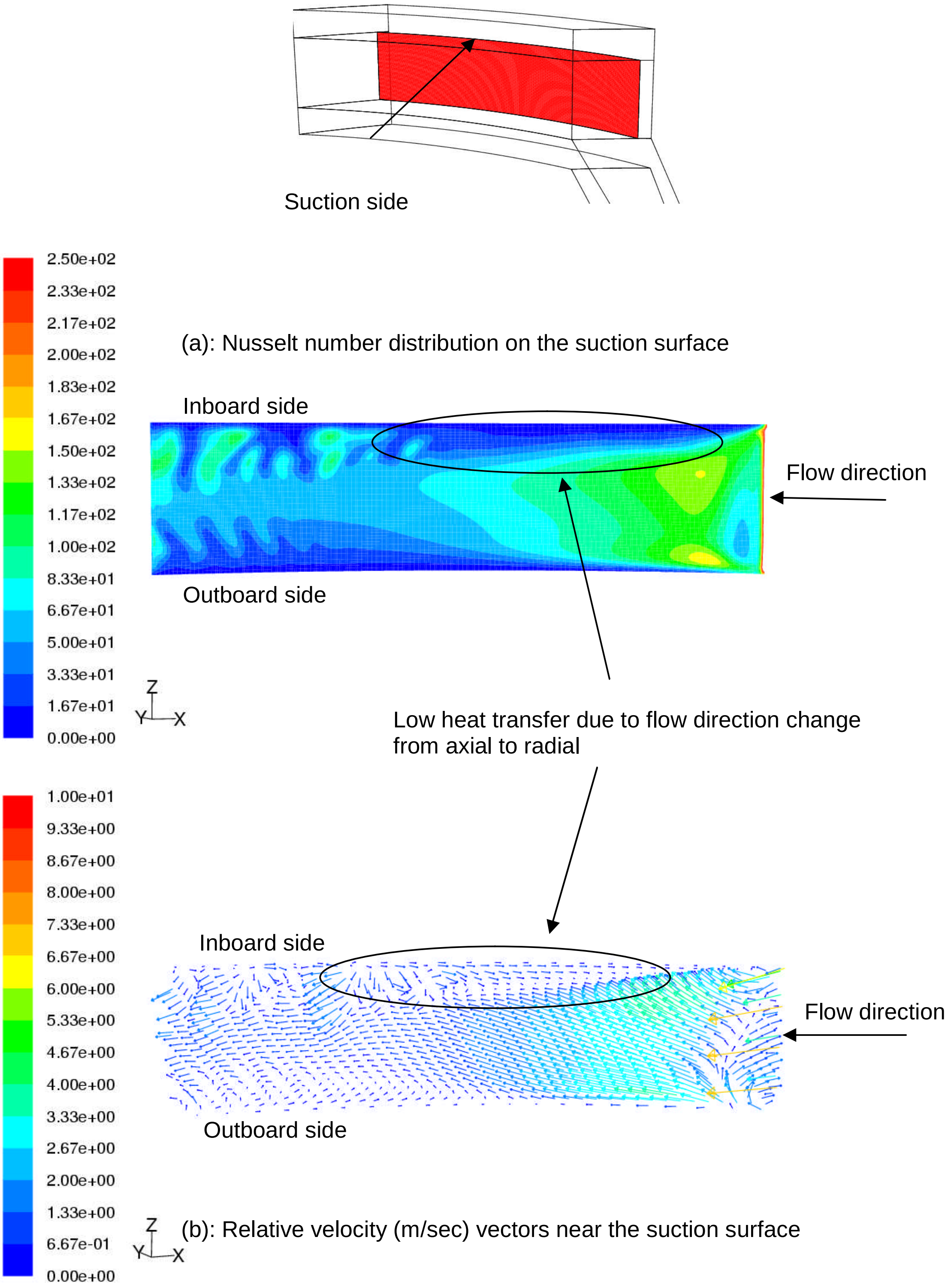

(a): Nusselt number distribution on the suction surface

(b): Relative velocity (m/sec) vectors near the suction surface

Fig 6.10: Nusselt number and relative velocity (m/sec) on the passage suction surface

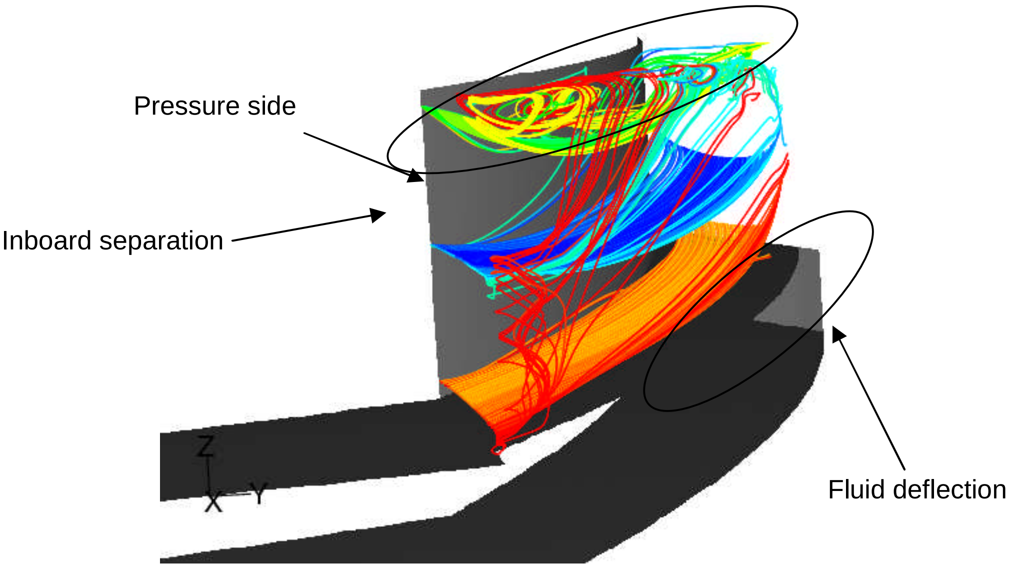

Fig 6.11: Pathlines at different heights through the rotor passage

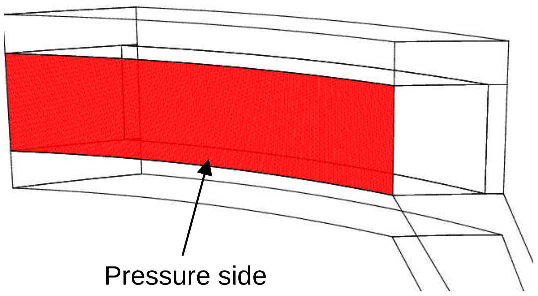

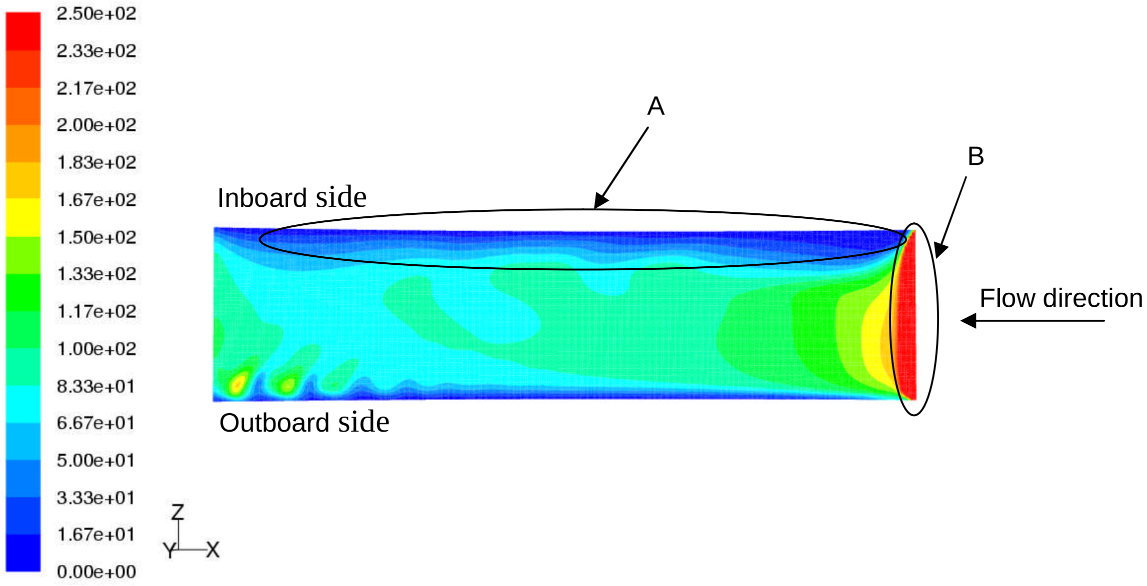

A: Effect of flow direction change from axial to radial

B: Effect of flow impingement on the pressure side inlet

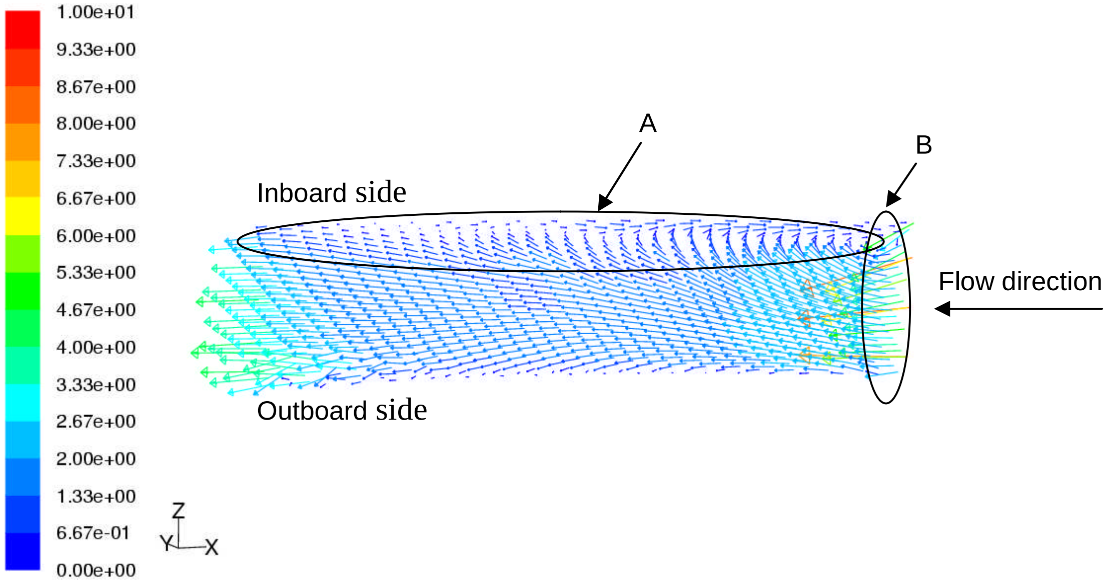

Fig 6.12: Nusselt number and relative velocity (m/sec) on the passage pressure surface

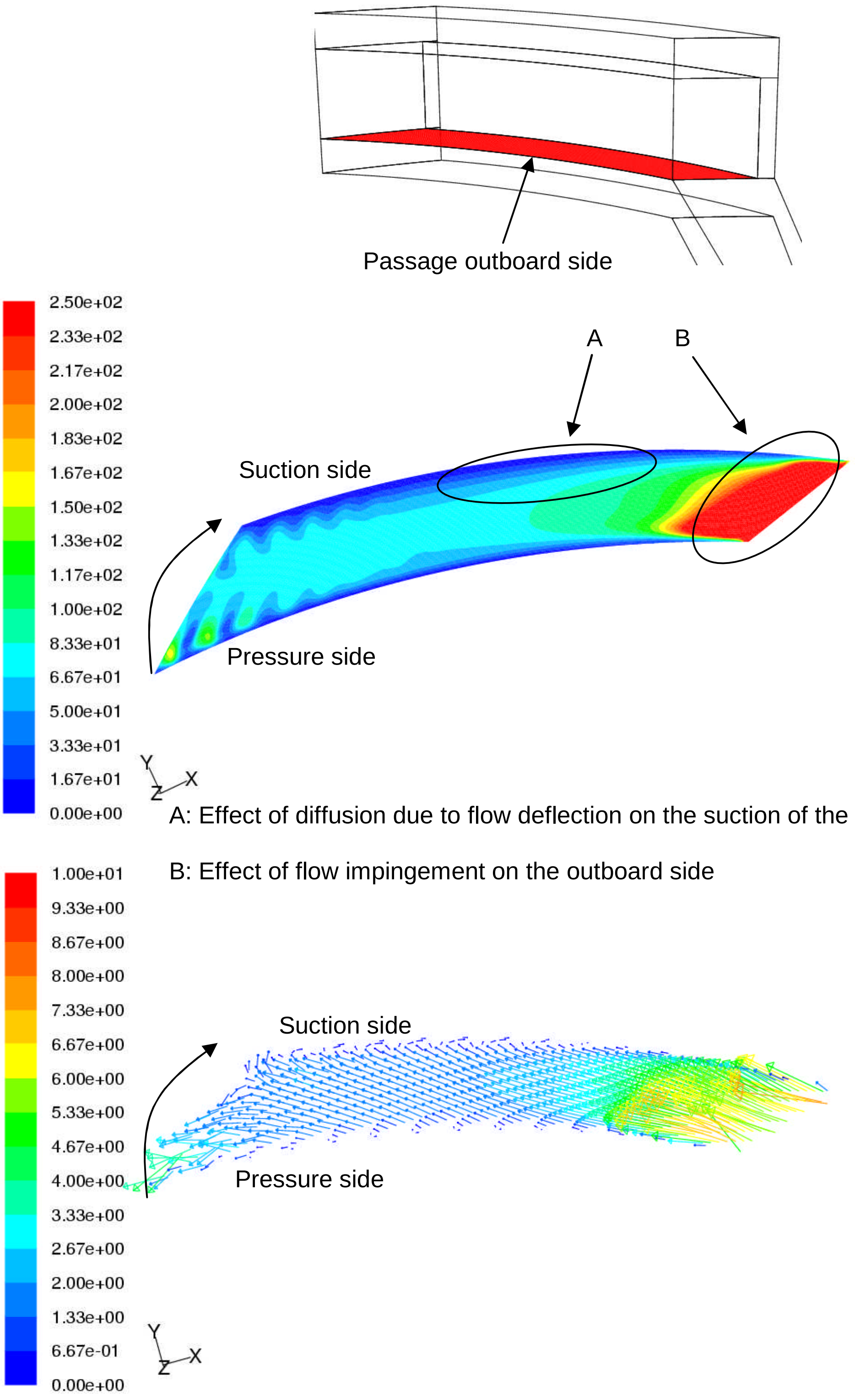

A: Effect of diffusion due to flow deflection on the suction of the outboard surface

B: Effect of flow impingement on the outboard side

Fig 6.13: Nusselt number and relative velocity (m/sec) on the passage outboard surface

6.2.1. Temperature uniformity

Figure 6.14 provides a better understanding of the contribution of each of the internal surfaces of the passage to the total heat transfer rate. The curvature and the orientation are similar for the inboard and the outboard surfaces and also for the suction and the pressure surfaces of the passage. The inboard side of the passage is the worst affected region with regard to the heat transfer rate due to flow separations as explained in the previous sections. The suction surface heat transfer rate is also lower than that of the pressure surface. The heat transfer rate is higher for the pressure and the outboard surface due to the accelerated flow of air. Temperature uniformity is one of the most important aspects of a disc brake performance. Presence of the regions of low and high heat transfer leads to thermal distortion of the disc brake. Heat flux from the surface is directly calculated from the simulations. In order to better understand the temperature uniformity on the surface the heat flux has been used to re-evaluate the wall temperature using the fluid side heat transfer coefficient (equation 6.2).

$$T_w = \frac{\dot{Q}}{h_f} + T_f \qquad \text{……………………… (6.2)}$$

Where T_W is the re-evaluated wall temperature, $\dot{Q}$ is the heat flux obtained from the simulations, h_f is the fluid side heat transfer coefficient and T_f is the first cell fluid temperature. The re-evaluated wall temperature is a direct indication of the temperature uniformity on the surface. There is a large temperature gradient on the pressure and the outboard surface inlets due to flow impingement (fig 6.15). The suction surface and the inboard surface have uniform temperature distribution even the heat transfer rate is lower for these two surfaces. Ideally for a good disc brake rotor should have minimum temperature gradients on each of the surfaces and maximum heat transfer rate from each of the surfaces. Also the thermal distortion index (T.D.I) mentioned in section 4.5 is calculated. It indicates the non-dimensionalised maximum temperature difference. The lower the value of T.D.I the better is the performance of the rotor. The T.D.I for the datum rotor was observed to be 0.2.

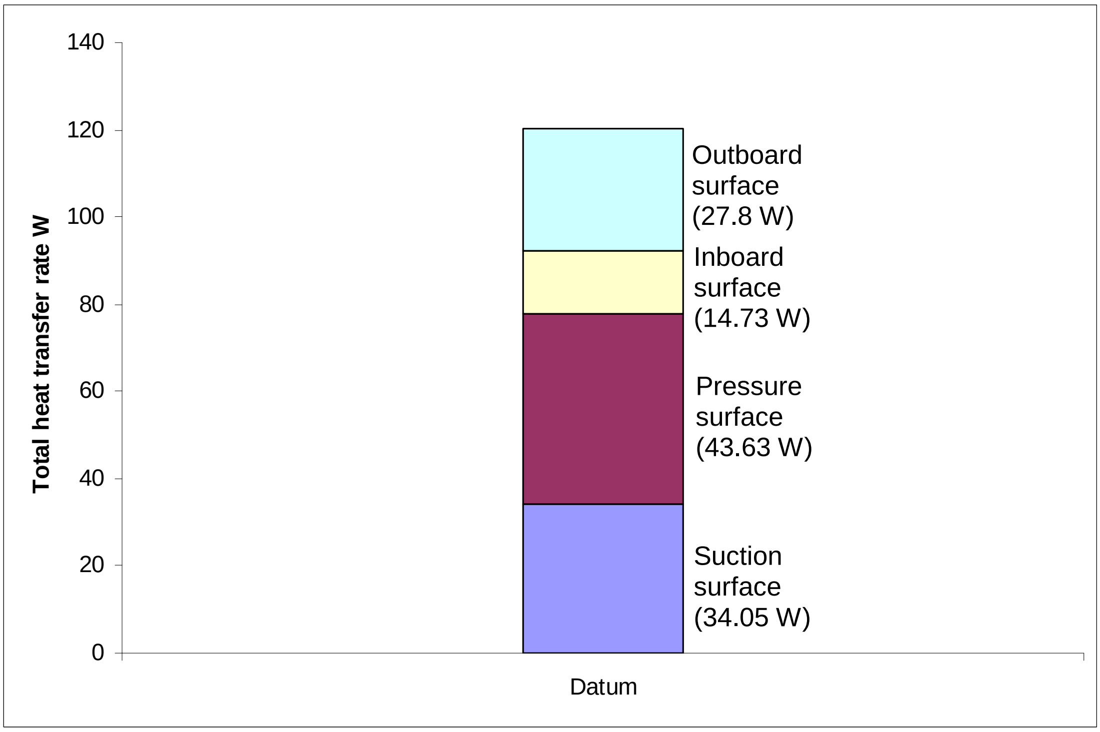

Fig 6.14: Contribution of each of the passage internal surfaces to total heat transfer rate

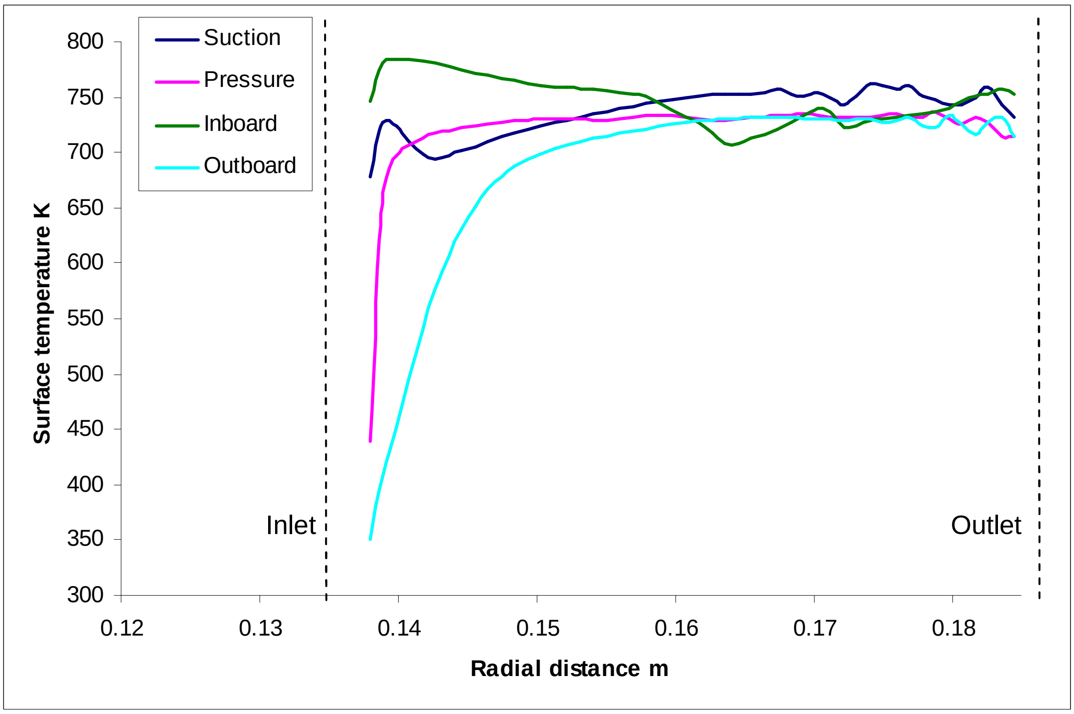

Fig 6.15: Temperature variation with radial distance on all the internal passage surfaces

6.3 Validation of the datum rotor

In order to understand the reliability and to lend some credibility to the CFD process being used, it is important to carry out a validation exercise. Validation studies were performed by comparing the CFD result with an existing experimental solution. Parish [2003] had performed an experimental analysis of the datum at an isothermal condition. His work is used for comparing the CFD results obtained.

6.3.1. Introduction

Contour plots do not offer a comprehensive comparison because of the three-dimensional data that is displayed. In order to offer a comprehensive comparison, the properties are averaged on a particular surface and the obtained results are used to create two dimensional plots. In FLUENT for calculating the circumferential averages, iso-surfaces are drawn at the required surface and then it is divided into required number of bands (equidistant lines) where the properties are averaged. Also the global one-dimensional parameters like mass flow rate were used as comparison metrics.

The experiment was performed by Parish [2003] using pressure probes and hot wire anemometry. The hot-wire measurements are most accurate because the frequency response is high enough to properly identify the wakes. The experimental measurements were carried on the datum rotor with lips (fig 6.16) and the values were measured 2mm from the outlet of the rotor passage.

`

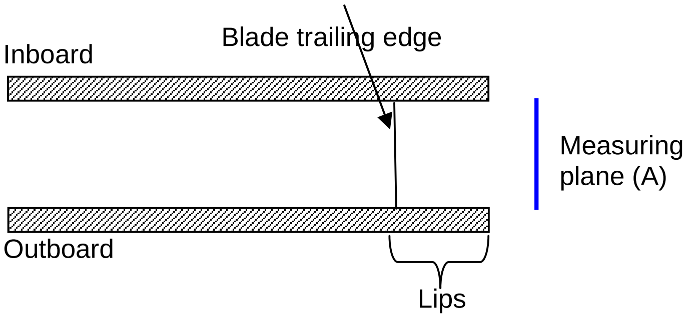

Fig 6.16: Datum rotor with lips and inlet chamfer measurement plane

The datum rotor was also modelled with the same measurements and also with the inclusion of inlet chamfer. The CFD simulation was also run at 1500 rpm isothermally for the validation.

6.2.2. Mass flow rate

The mass flow rate was measured at the plane A for a 48 bladed datum rotor. The mass flow rate from the individual passage was compared (table 6.1). The CFD results are over predicted by 4% when compared to the experimental results. The measurement plane and the outer diameter for both the rotors are same. The rotor with chamfer and lips are taken as reference and consequently the experimental and the computed results are in disagreement.

	Relative exit velocity m/sec	Mass flow rate m/sec
Experimental results (hot wire)	21.45	0.05252
CFD simulation	22.32	0.05468

Table 6.1: Mass flow rate comparison

The reason for the over prediction could be due to the effect of the chamfer which reduces the inlet separation and also due to the accelerated flow on the suction of passage. This reduces the inlet blockage and thereby increases the mass flow rate through the passage. Further details regarding the effect of chamfer on mass flow rate are explained in chapter 7. The over prediction could also be due to the k-ω turbulence model that is being used. This turbulence model is known to under predict the separation regions (Mentor [1991]). The hot wire measurements do not predict the direction of the flow at the exit of the rotor well (fig 6.17).

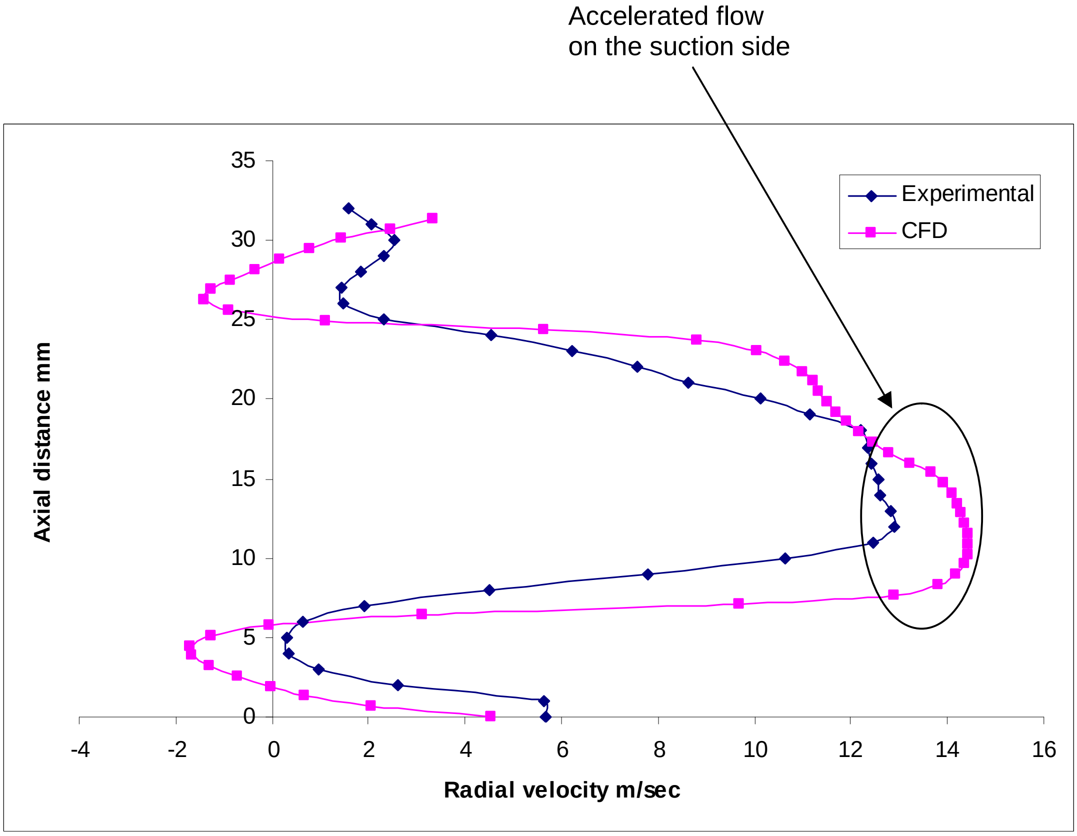

Fig 6.17: Circumferential averaging using experiments and CFD of the radial velocity on plane A

In order to extend the validation process, a detailed analysis of the flow field has to be performed. The contour plots at 2 mm from the exit of the rotor passage are taken from the experiments and are compared with the contour plots obtained from CFD. The experiment analysis took into account the differences between various passages where as for the CFD analysis the brake disc rotor was considered periodic.

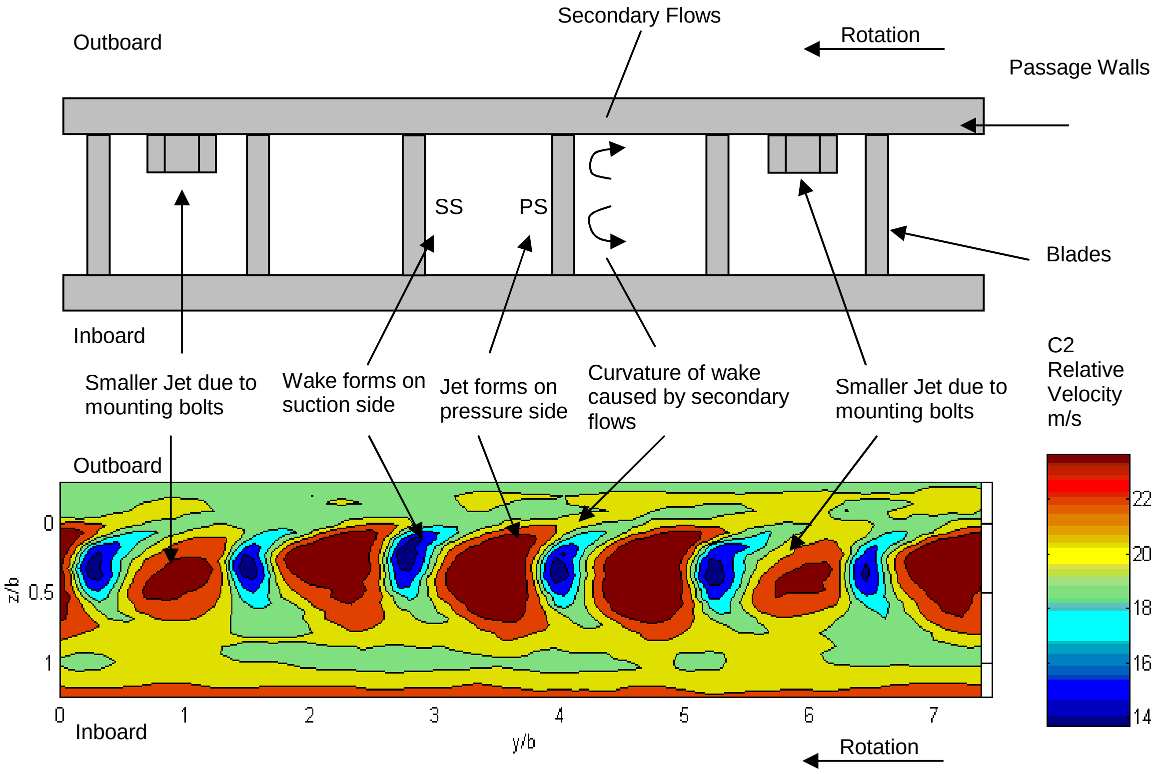

Fig 6.18: Relative velocity contours from experiments (Parish [2003])

Figure 6.18, the jet and the wake pattern can be observed in the relative velocities contours. The wake pattern is towards the suction side of the passage which is affected by flow separations. The flow on the pressure side of the passage is accelerated. The agreement of the CFD results with the experimental value is marginally good (fig 6.19). In the experimental data the jet and wake are displaced towards the inboard and the outboard side of the rotor giving it a curved shape. The computed results on the other hand do not have this profound curved shape. This could be due to higher mass flow rate associated with the CFD results. The wake is displaced towards to the outboard side in the CFD results similar to the trend observed in the experimental results. The displacement in the jet is only towards the inboard side unlike in experimental results where the jet is deflected towards both inboard and the outboard side of the rotor.

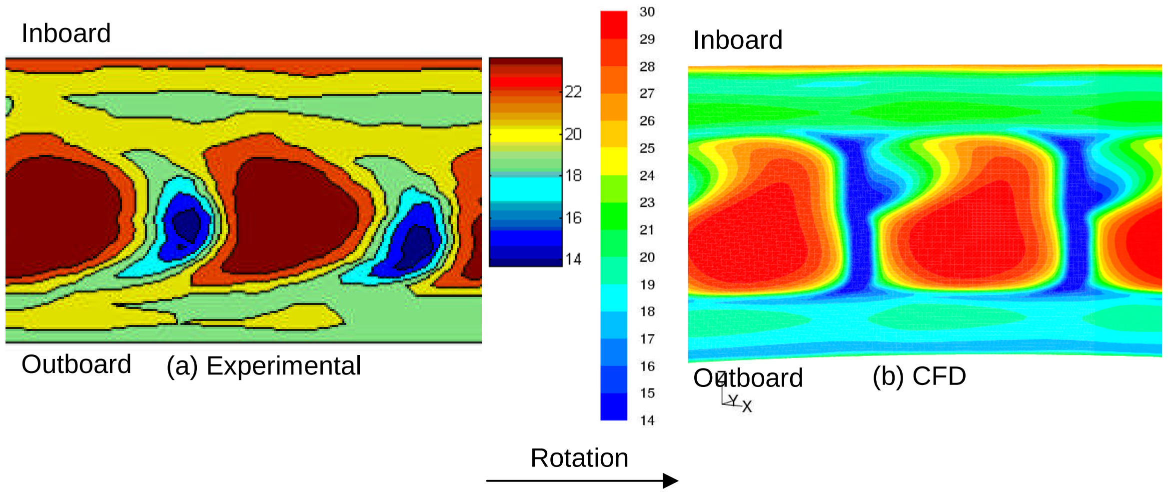

Fig 6.19: Relative velocity contours at 2 mm from the outlet of the rotor

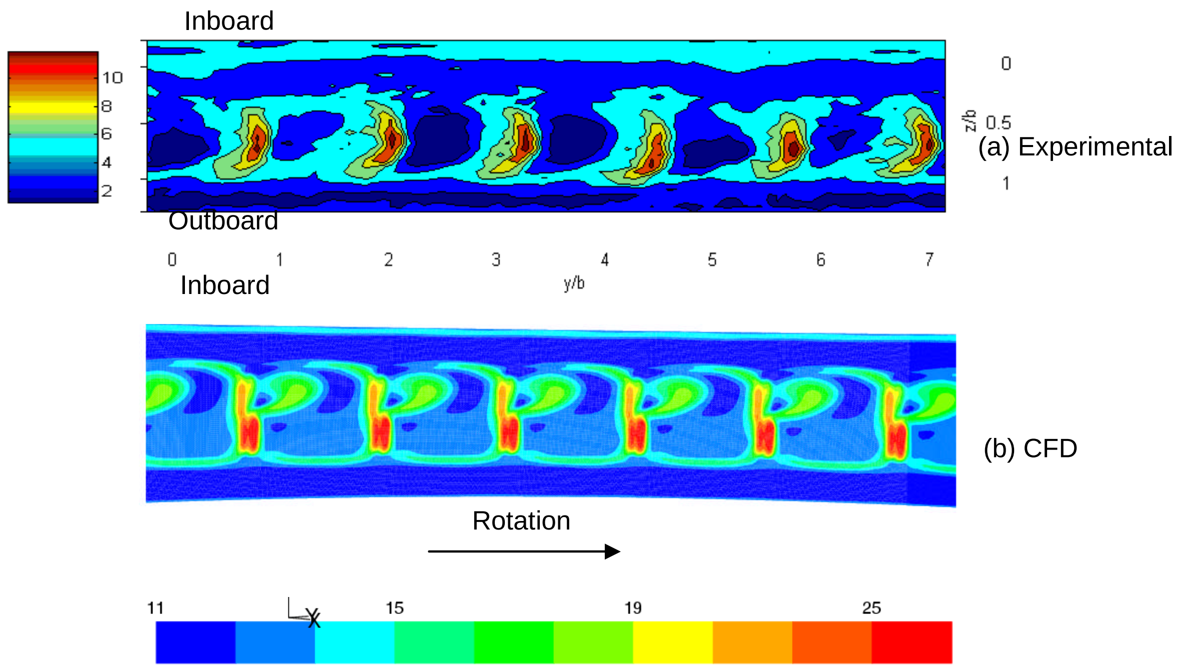

Fig 6.20: Turbulent intensity contours at 2 mm from the outlet of the rotor

Figure 6.20 shows that as expected the wake regions have high turbulence intensity and jets have low intensity. The same trend is again captured by the CFD results. Although the absolute values are over predicted by CFD, this is due to the over prediction of the mass flow rate through the passage.

6.4. Effect of blade angles

The analysis is split into two parts; iteration 1 and iteration 2. Iteration 1 consists of a preliminary set of blade angles (section 3.1). Iteration 2 consists of a secondary set containing finer changes in the blade angles. Before discussing about the results obtained, let us have look at the different frames of reference used while analysing flows over rotating bodies. The method used is velocity triangle formulation. Velocity triangles are used to relate the parameters that define the blade and the flow properties in relative frame with those in the absolute frame of reference. Let us imagine a plan view of the disc brake rotor. The flow comes from axially and changes the direction and enters radially into the rotor passage. Also, there is a change in the flow direction is from tangential to radial (see section 6.2). In drawing the velocity triangle it is important to understand the angle at which the flow enters and leaves the rotor passage in the relative frame of reference (i.e. relative to the rotation of the rotor). Let us assume that the flow enters the rotor passage at approximately at the same angle as that of the blade inlet angle. The inlet velocity triangle (fig 6.21) gives the information about the direction of various velocity components. The absolute velocity (V_1) is the summation of relative velocity (C_1) and speed (U_1) at which the blade is rotating. For the drawing the velocity triangle at the outlet, it is important to note that the flow is assumed to leave the trailing edge approximately at the blade outlet angle in the relative frame of reference. The relative velocity at the outlet can be divided into two components; the tangential component and the radial component. While evaluating the mass flow rate at the outlet of the passage, the component perpendicular to the outlet area is used i.e. the radial component. It can observed from figure 6.22 that higher relative outlet angles (β_2) lead to higher radial velocity for a fixed relative inlet angle (β_1), therefore higher mass flow rates. This idea was also used while selecting the data set for the analysis. This can be seen from figure 6.15 that by increasing the outlet angle say as an example from 35.62^0 to 50^0 the outlet relative velocity component increases. This leads to increase in the radial exit velocity thereby increasing the mass flow rate.

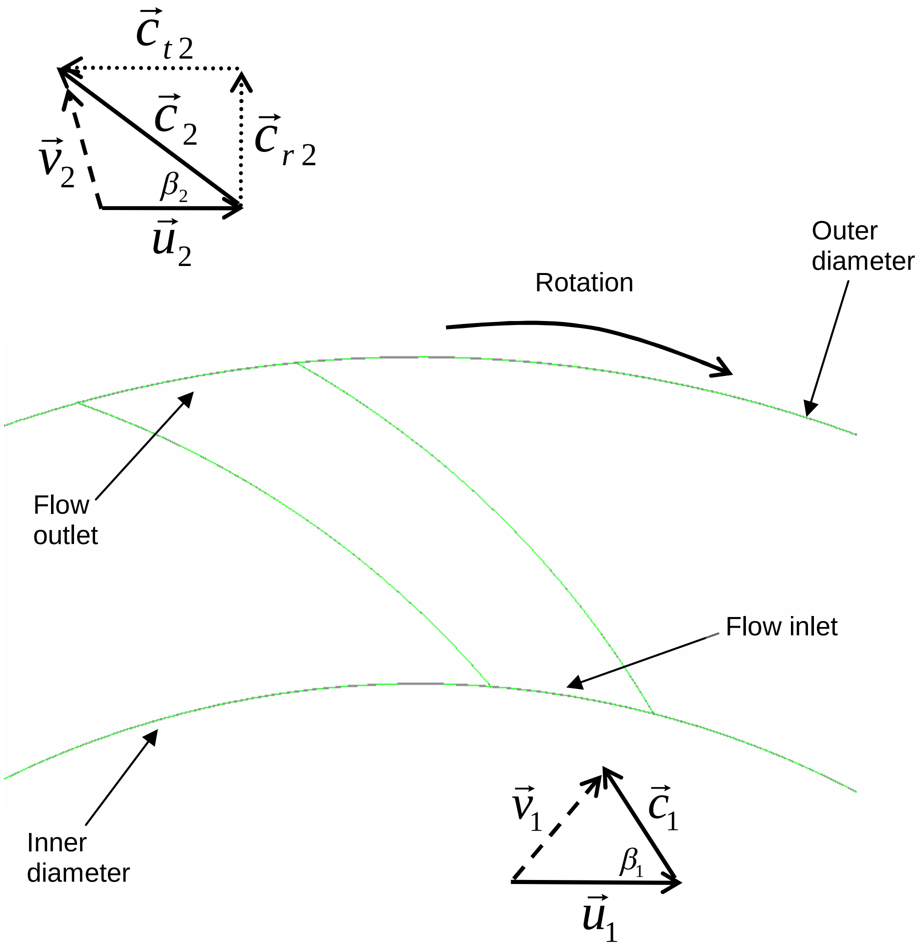

Fig 6.21: Velocity triangles for a disc brake rotor

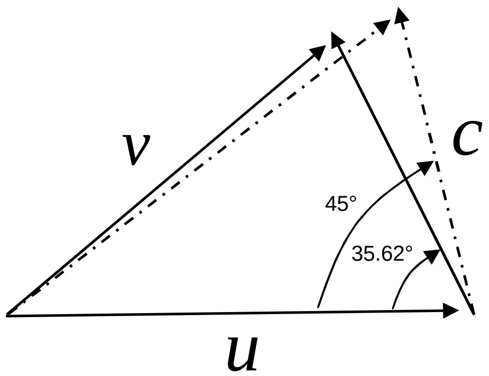

Fig 6.22: Exit Velocity triangles of a disc brake rotor as function of outlet angle

6.4.1. Iteration 1

The blade angles for this initial assessment form a combination of 9 sets (table 6.1). The datum rotor results (section 6.2) are used for comparison. All blade geometries are generated in exactly the same way as was explained in the case of a datum rotor.

Name	Inlet angle (β_1)	Outlet angle (β_2)
Datum	43.16^0	35.62^0
Case 1	45^0	50^0
Case 2	45^0	90^0
Case 3	45^0	110^0
Case 4	60^0	50^0
Case 5	60^0	90^0
Case 6	60^0	110^0
Case 7	90^0	50^0
Case 8	90^0	90^0
Case 9	90^0	110^0

Table 6.2: Preliminary set of blade angles

All the simulations were also performed in exactly the same way as was performed on a datum rotor.

6.4.1.1. Mass flow rate variations

Mass flow rate for the designs were measured using the equation 6.1. This measurement was taken at the very outlet of each of the passages for the entire brake disc. It can be observed from figure 6.23 that the blade angles do have an effect on the mass flow rate through the passage. The effect of outlet angle is more profound in this regard. By changing the outlet angle from 35.62^0 (datum) to 50^0 (case1), the mass flow rate increased by 52.7% (fig 6.23). This is due to the fact that as the outlet angle increases the radial velocity at the outlet also increases thereby increasing the mass flow as explained in section 6.3. This can be better understood by looking at the velocity triangles for each of the case. From figure 6.21 it can be seen that the inlet velocity triangle for both datum and case 1 rotor are similar as the inlet angles are similar. But the outlet angle increases from datum to case 1, therefore for a given blade speed the average velocity induced by the datum rotor is less compared to case 1 rotor design (fig 6.22). Also the separation region near the inboard side of the datum rotor that extends through out the passage acts as a flow blockage thereby reducing the mass flow rate through the datum rotor.

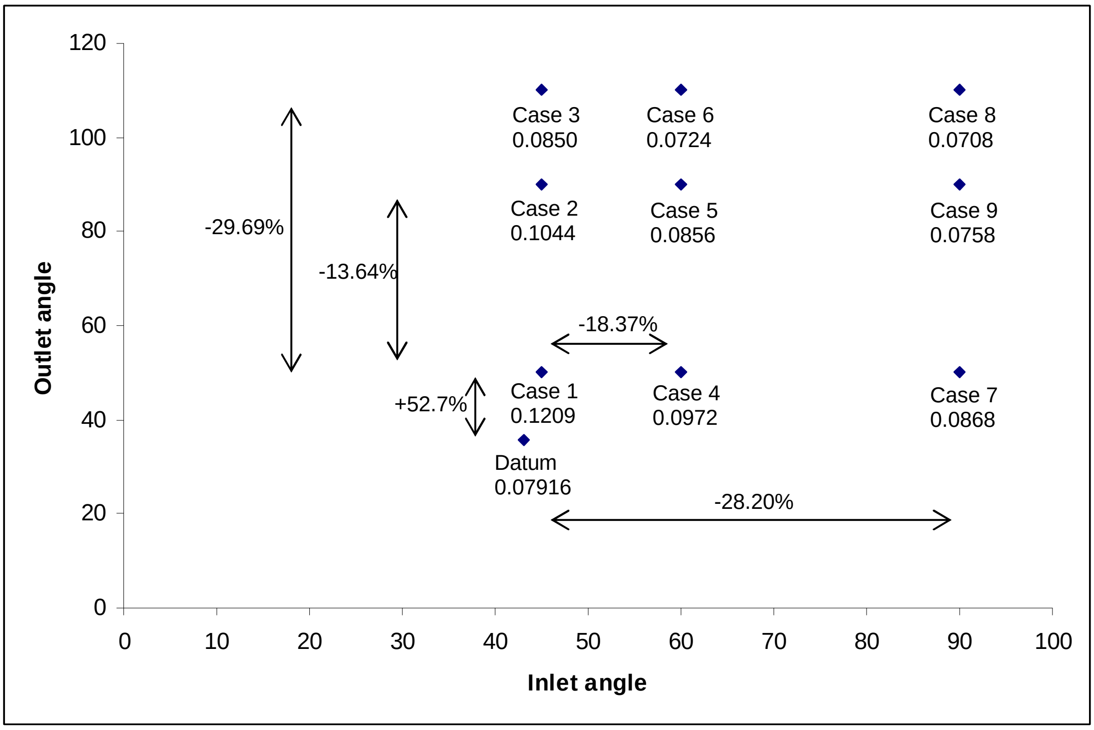

Fig 6.23: Mass flow rate (kg/sec) as a function of inlet and outlet angles

From the incompressible continuity equation for mass conservation it is known that increase in area decreases the velocity. The decrease in the velocity increases the pressure. Due to the geometry of the disc brake rotor there is natural increase in the flow area from inlet to outlet and this geometrical increase depends on the blade angles. The area increase is more for case 1 than for datum rotor creating a higher adverse pressure gradient. This pressure creates higher diffusion for case 1 as compared to the datum rotor (fig 6.23). Diffusion results in lower heat transfer thereby creating hot spots. The heat transfer details will be explained in detail in the following sections.

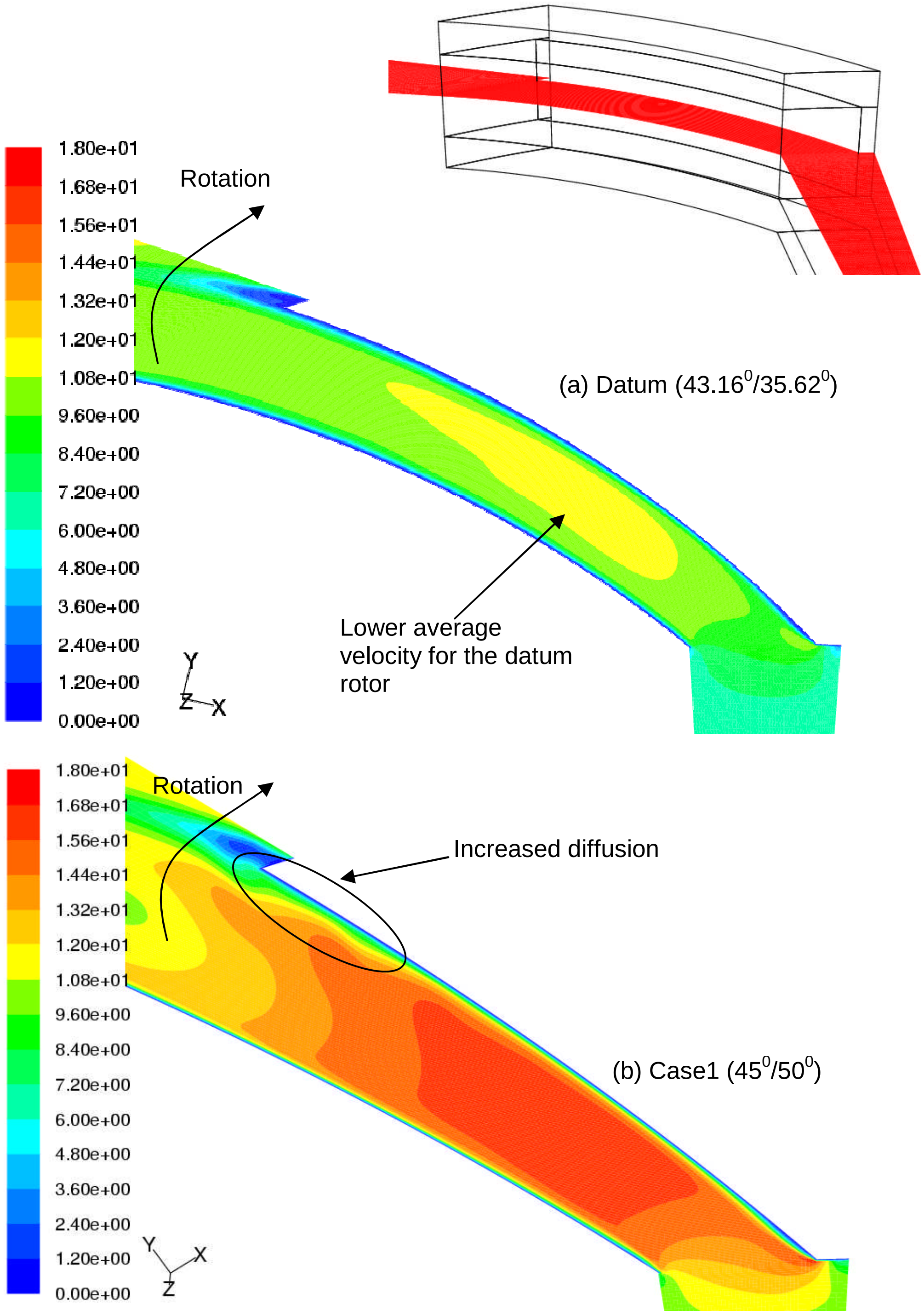

Fig 6.24: Datum and case 1 rotor relative velocity (m/sec) contours at a mid-passage plane at 750rpm and 800 K

By increasing the outlet angle further from 50^0 (case1) to 90^0 (case2) the profile of the blade changes, the suction becomes convex from concave. Due to this is the adverse pressure gradient the flow encounters on the suction side increases and the flow separates (fig 6.25). As can be seen from figure 6.26, after the flow enters the passage it tries to follow the blade but due to the profile of the blade the adverse pressure that is created causes the flow to separate near the suction side of the passage. This separation zone extends till the mid-height of the passage. This reduces the mass flow rate for case 2 by 13.64 % compared to case 1 as the separation acts as a flow blockage.

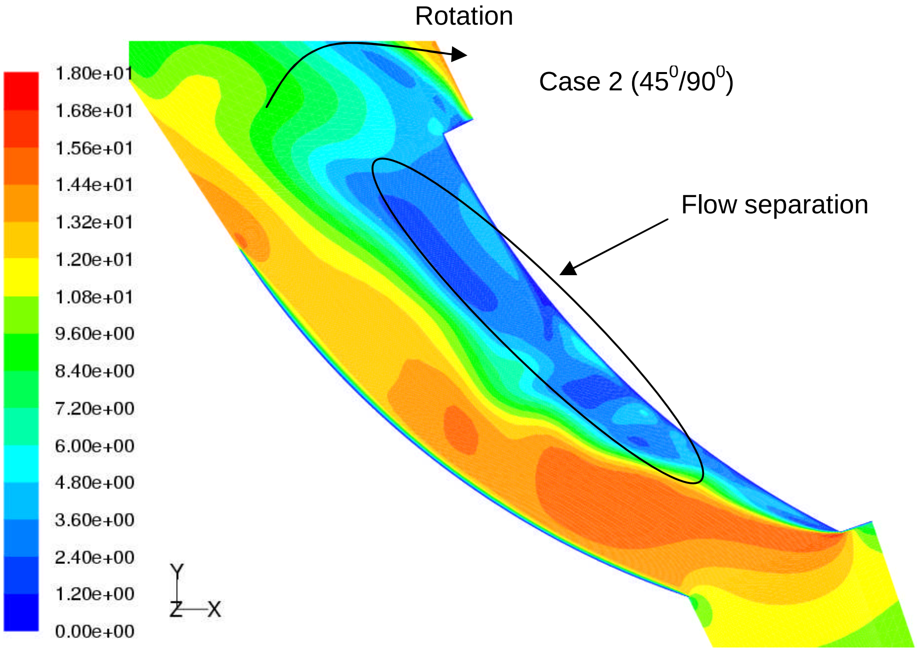

Fig 6.25: Case 2 rotor relative velocity (m/sec) contours at mid-passage plane

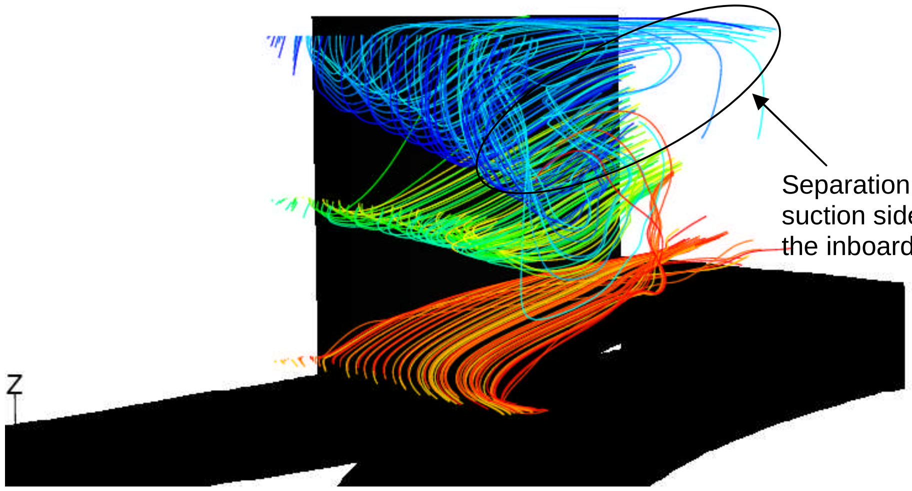

Separation near the suction side close to the inboard surface

Fig 6.26: Case 2 rotor pathlines through the passage

On further increase of the outlet angle to 110^0 (case 3), the radial component of the exit velocity decreases which reduces the mass flow rate through the passage. This is similar to the change in outlet angle from datum to case 1 except that the blades have a different profile. From figure 6.27 it can be seen that due to the profile of the blade after the initial impingement of air on the pressure side it twists and turns as the ait goes through the passage. This finally creates a region of very low velocity at the trailing edge of the suction side (fig 6.28). This region reduces the local heat transfer from the passage on the suction side thereby creating hot spots.

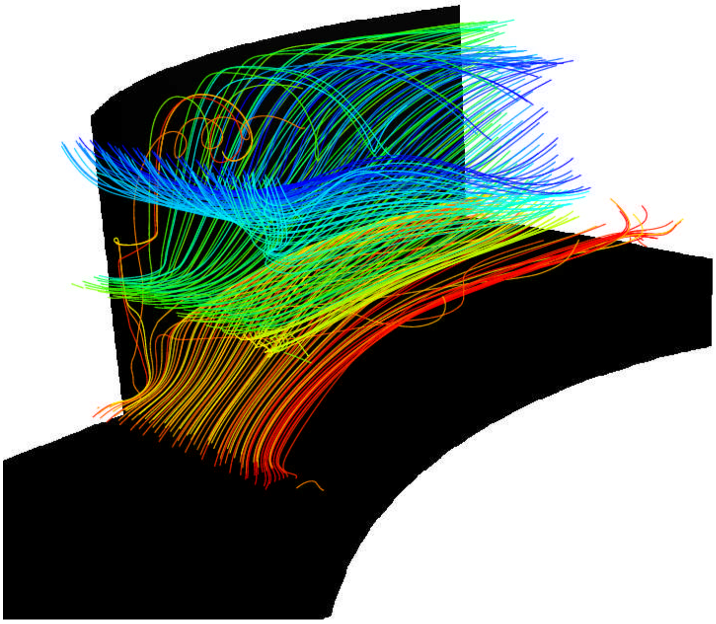

Fig 6.27: Case 3 rotor pathlines through the passage

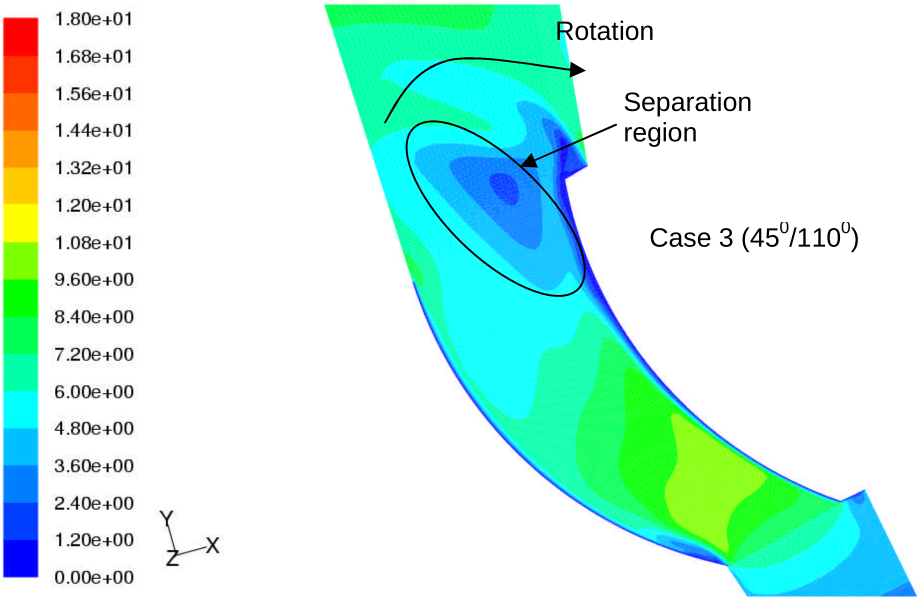

Fig 6.28: Case 3 rotor relative velocity (m/sec) contours at mid-passage plane

From figure 6.29 a trend can be observed in the variation of mass flow rate with outlet angle. At an inlet angle of 45^0 it was observed in the previous section that the mass flow increases initially from datum to case 1 and then decreases with further increase in the outlet angle. The same trend was observed even at higher inlet angles of 60^0 and 90^0. This is due to change in the profile of the blade as explained earlier.

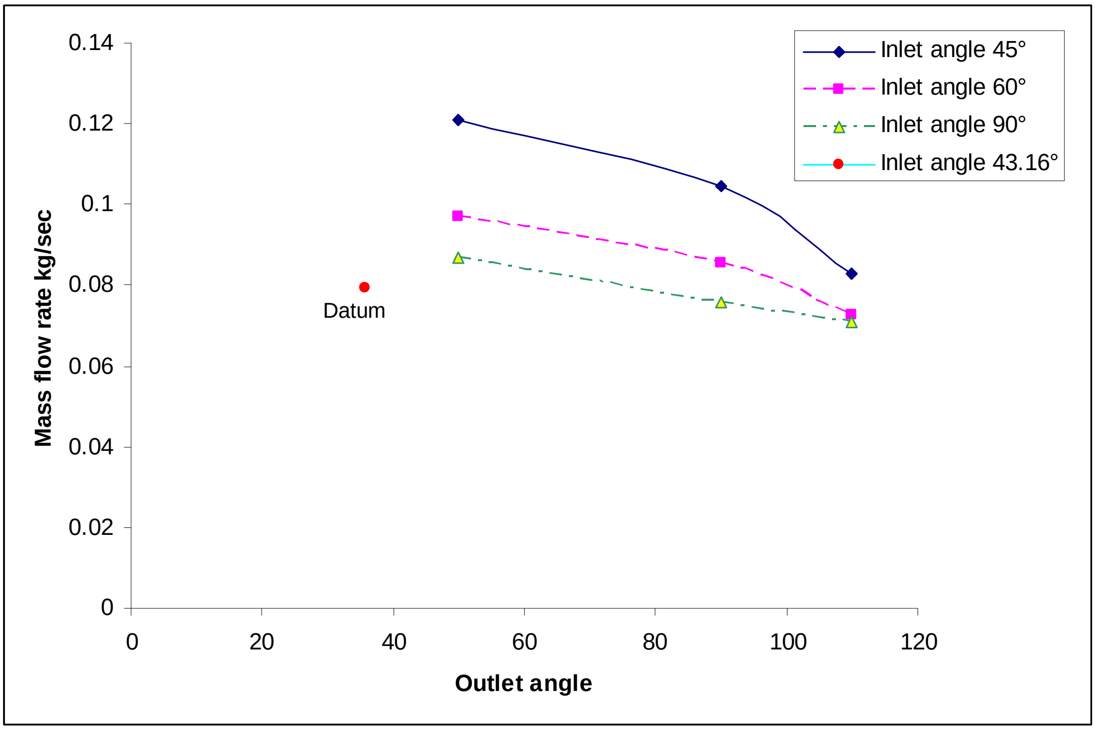

Fig 6.29: Mass flow rate (kg/sec) variation with outlet angle at different inlet angles

Variation in inlet angle was also observed to affect the mass flow rate through the passage. As the inlet angle increases from 45^0 (case 1) to 60^0 (case 4) the curvature of the blade becomes more profound leading to a higher adverse pressure gradient due to which separation at the inlet as the flows changes direction from tangential to radial increases (fig 6.30). The velocity induced by the case 4 rotor is also lower than that of the case 1 rotor. This curvature of the blade also leads to earlier diffusion than for a rotor will lower inlet angle.

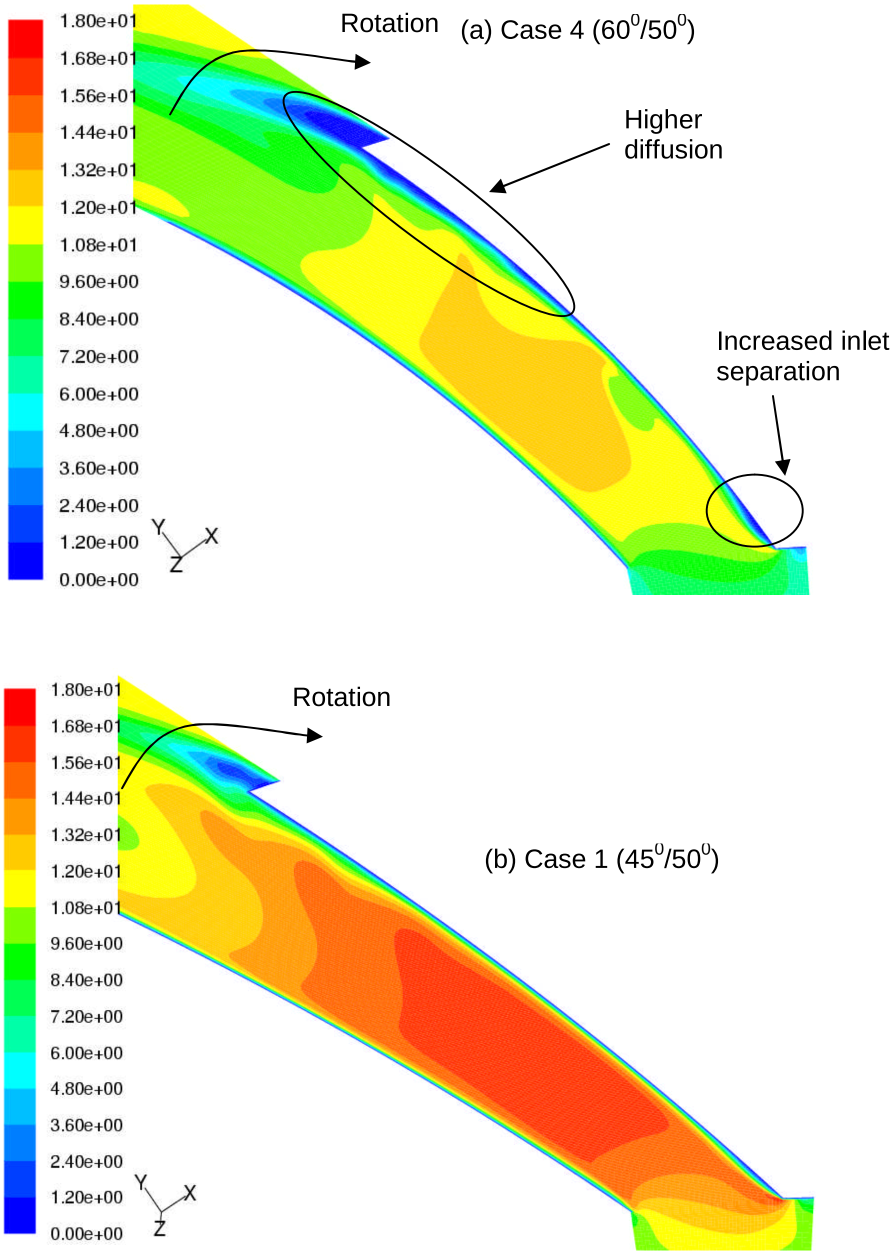

Fig 6.30: Case 4 and case 1 relative velocity (m/sec) contours at mid-passage plane showing increased inlet separation and diffusion.

As the inlet angle is increased further to 90^0, the inlet separation increases rapidly on the suction side due to a further increase in the adverse pressure gradient due to stronger change in the curvature and causes a blockage to flow (fig 6.31). Due to this the mass flow rate through the passage also decreases by almost 28% from case 1.

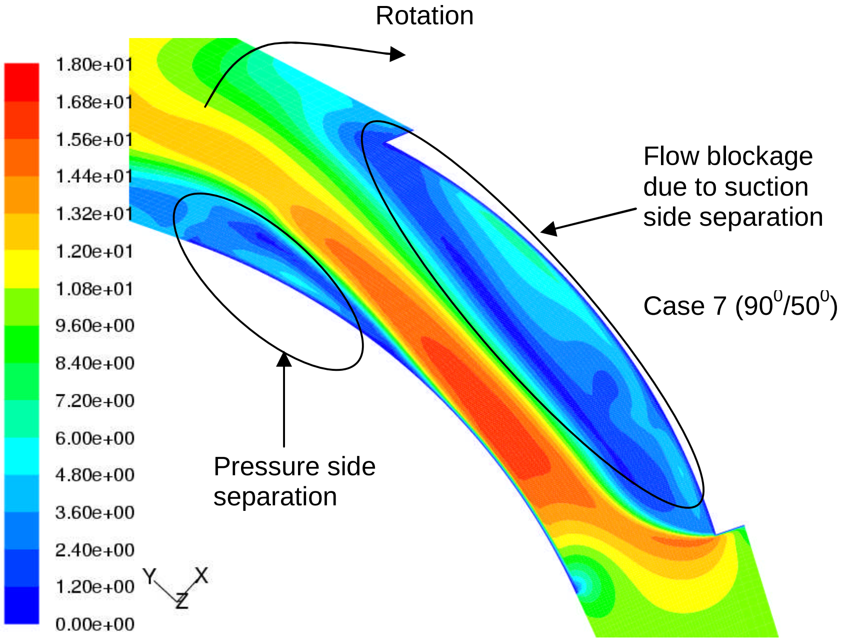

Fig 6.31: Case 7 relative velocity contours at mid-passage plane showing flow blockage on the suction side.

Separation is observed on the pressure side leading to multiple flow blockages affecting the mass flow rate. The pressure side separation is also due to the adverse pressure gradient due to the curvature of the blade the flow encounters.

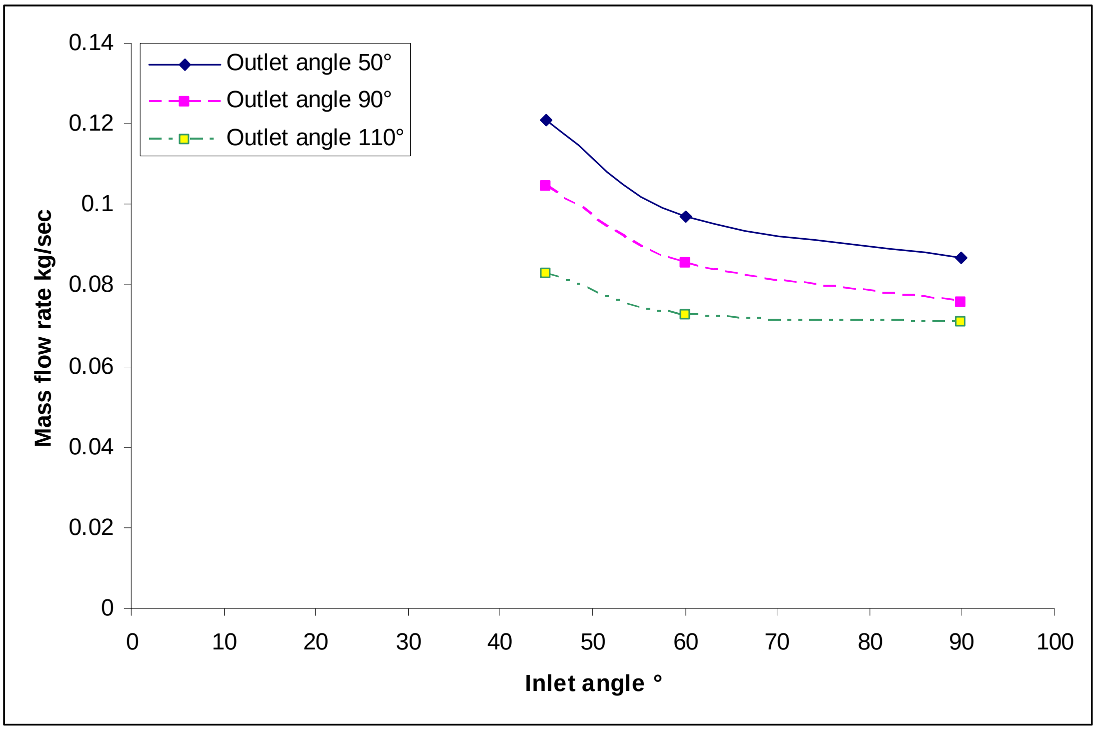

Fig 6.32: Mass flow variation (kg/sec) with inlet angle at various outlet angles

The trend in the variation of mass flow rate is maintained at higher outlet angles as well (fig 6.32). Though the absolute values are higher for rotor with lower inlet and also lower outlet angles.

Mass flow rate measurement is only one of the parameters that determine the performance of a design brake rotor. The other thermal parameters which determine the heat transfer performance of the rotor should also be evaluated. The thermal analysis details are explained in the following sections.

6.4.1.2. Heat transfer variation

Heat transfer from the rotor passage is calculated as a summation of heat transfer from individual passages. It can be observed that total heat transfer rate is also affected by the blade angles variation. Due to the increase in the blade outlet angle from 35.62^0 (datum) to 50^0 (case 1), there is an increase in the total heat transfer rate by 31.15% (fig 6.33). This is due to the higher mass flow rate associated with case 1 (fig 6.34 and 6.35). Also the separation zones near the inboard surface due to the flow direction change from axial to radial and tangential to radial are higher in datum then in case 1 which reduces the heat transfer from the inboard surface (fig 6.36). The diffusion on the suction side of case 1 creates a region of low heat transfer on the suction causing non-uniform heat transfer; this could lead to the formation of hot spots (fig 6.36).

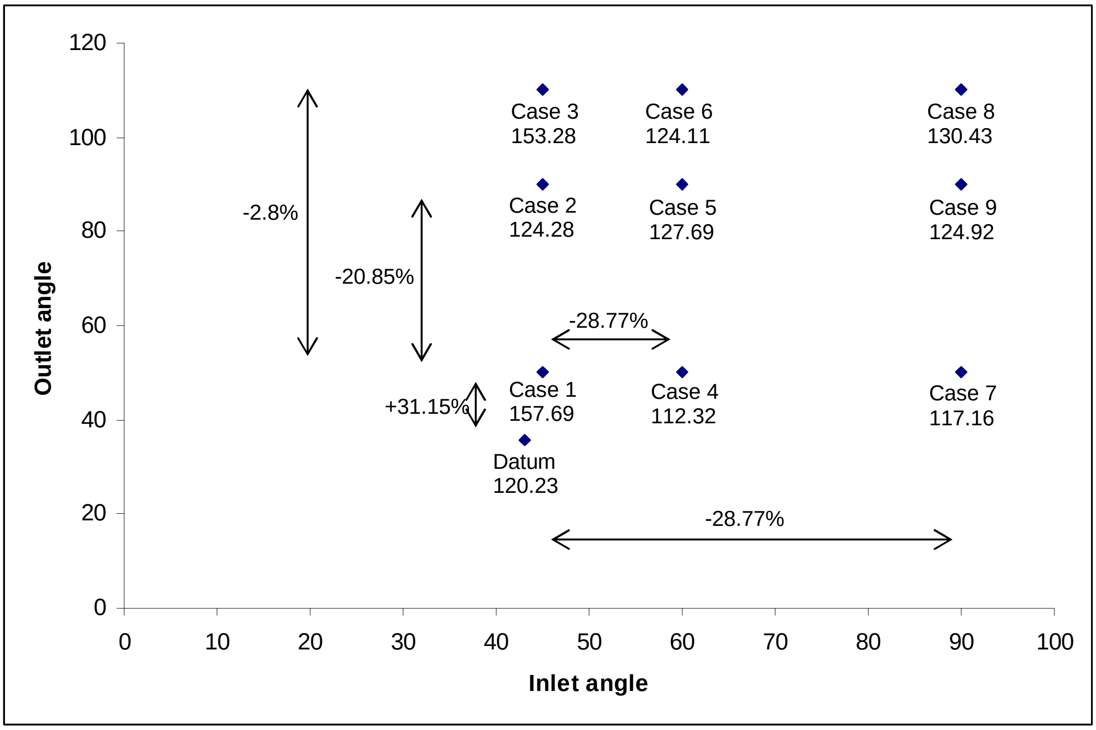

Fig 6.33: Total heat transfer rate (W) as a function of inlet and outlet angles

Also the suction separation on the datum side is larger than in case 1 due to the deflection of flow as explained in section 6.2 this leads to the formation of a region of low heat transfer near the suction surface in the datum rotor thereby compensating for the loss of heat transfer due to diffusion on the suction side of case 1 (fig 6.36). The heat transfer rate from the suction of the datum rotor is 34.05 W as opposed to 40.67 W for case 1. As can be observed from figure 6.33, the separation region on the pressure side near the inboard surface of the datum rotor decreases the heat transfer. Also higher core velocities associated with the flow also increase the heat transfer for case 1 as compared to the datum rotor. The pressure surface heat transfer rate for the datum rotor is 43.63 W as opposed to 48.09 W for case 1. The inboard separation that was explained in section 6.2 for the datum extends through out the surface the rotor on the inboard side. This reduces the heat transfer by a considerable about on the inboard side of the datum rotor. The attached flow on the other hand for case 1 on the inboard surface ensures the heat transfer rate is uniform (fig 6.37). The passage inboard surface heat transfer rate for datum is 14.73 W when compared to case 1 which is 28.44 W. As can be observed from figure 6.33 the higher core velocities associated with case 1 rotor increase the heat transfer rate. Due to strong impingement of flow after its direction change from axial to radial the heat transfer rate is increased at the inlet of the outboard surface for both the cases. The deflection of flow from the corners of the rotor passage (see section 6.2) reduces the heat transfer rate at the outlet of the outboard surface for datum rotor. The heat transfer rate for datum passage outboard surface is 27.8 W as compared to 40.49 W for case 1.

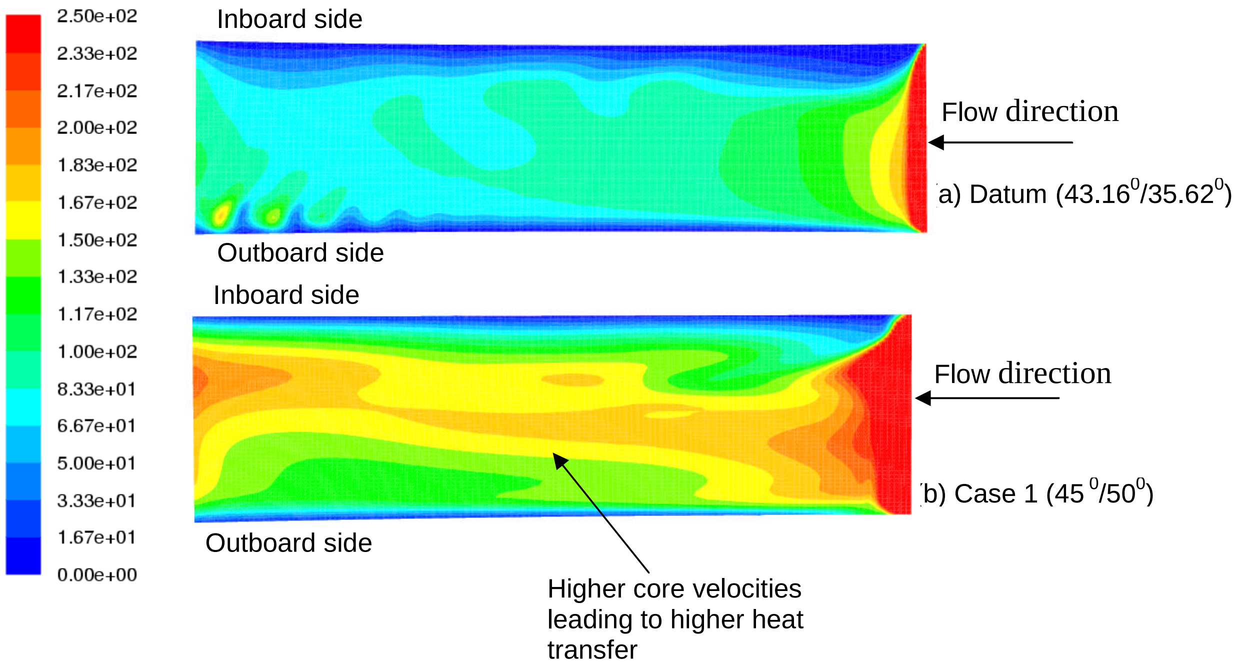

Higher core velocities leading to higher heat transfer

Fig 6.34: Pressure Surface Nusselt number distribution for datum and case 1

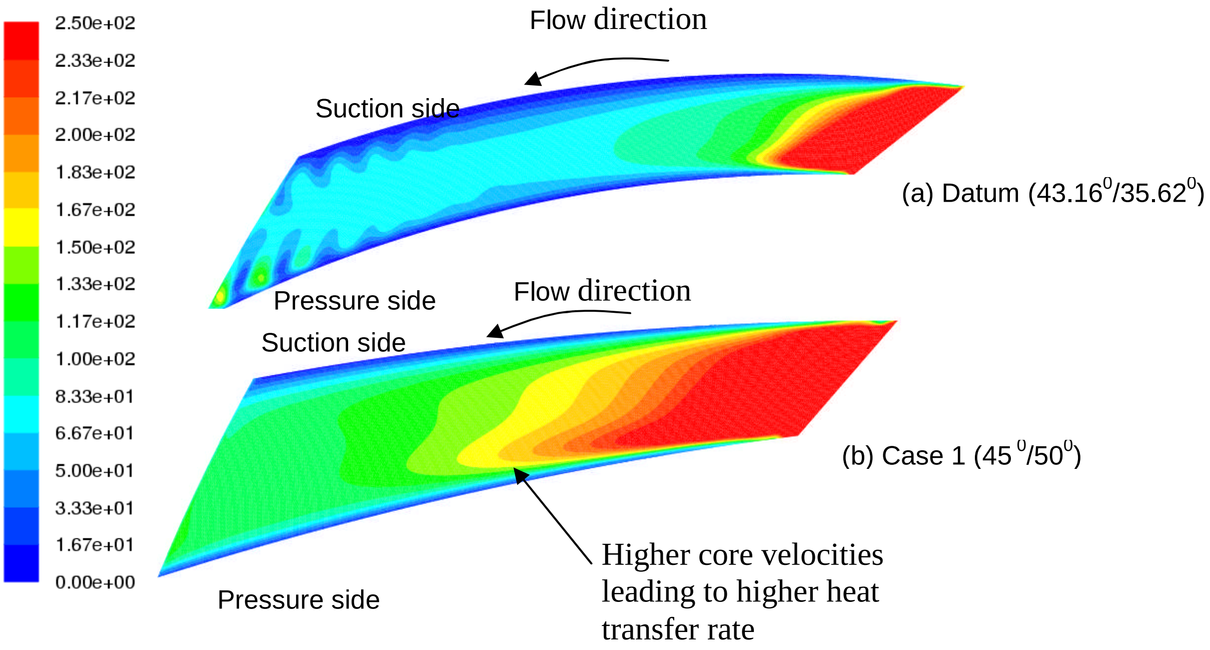

Fig 6.35: Passage outboard Surface Nusselt number distribution for datum and case 1

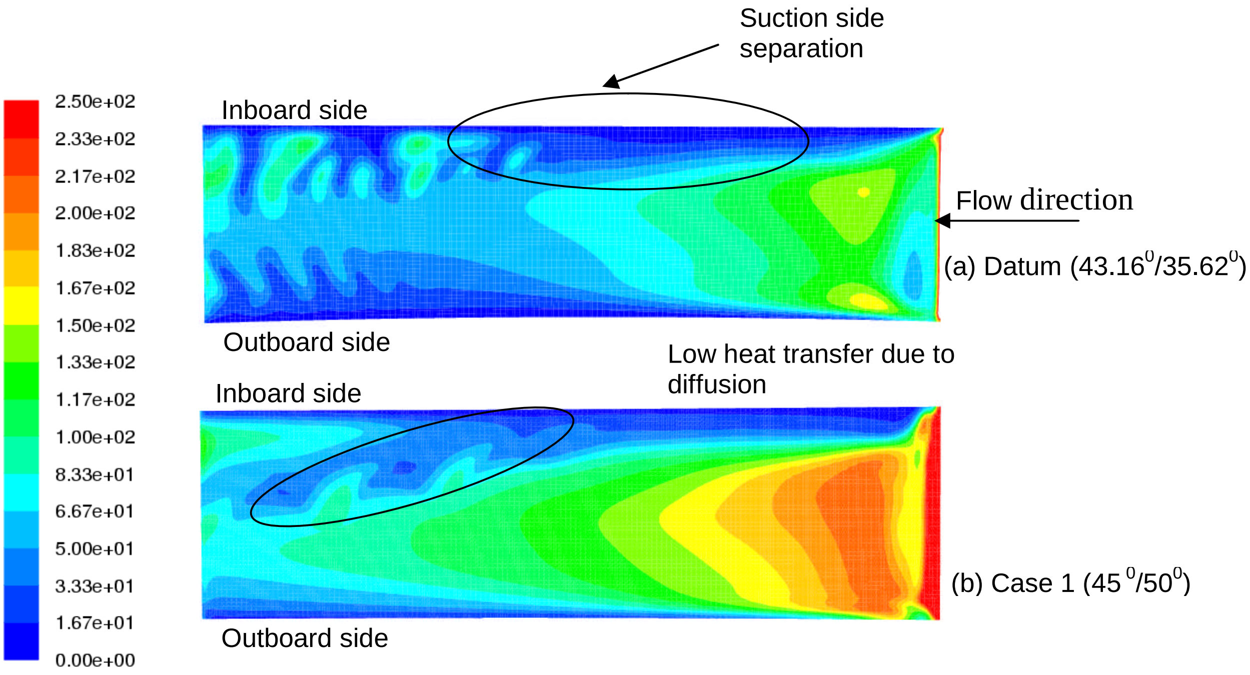

Fig 6.36: Suction Surface Nusselt number distribution for datum and case 1

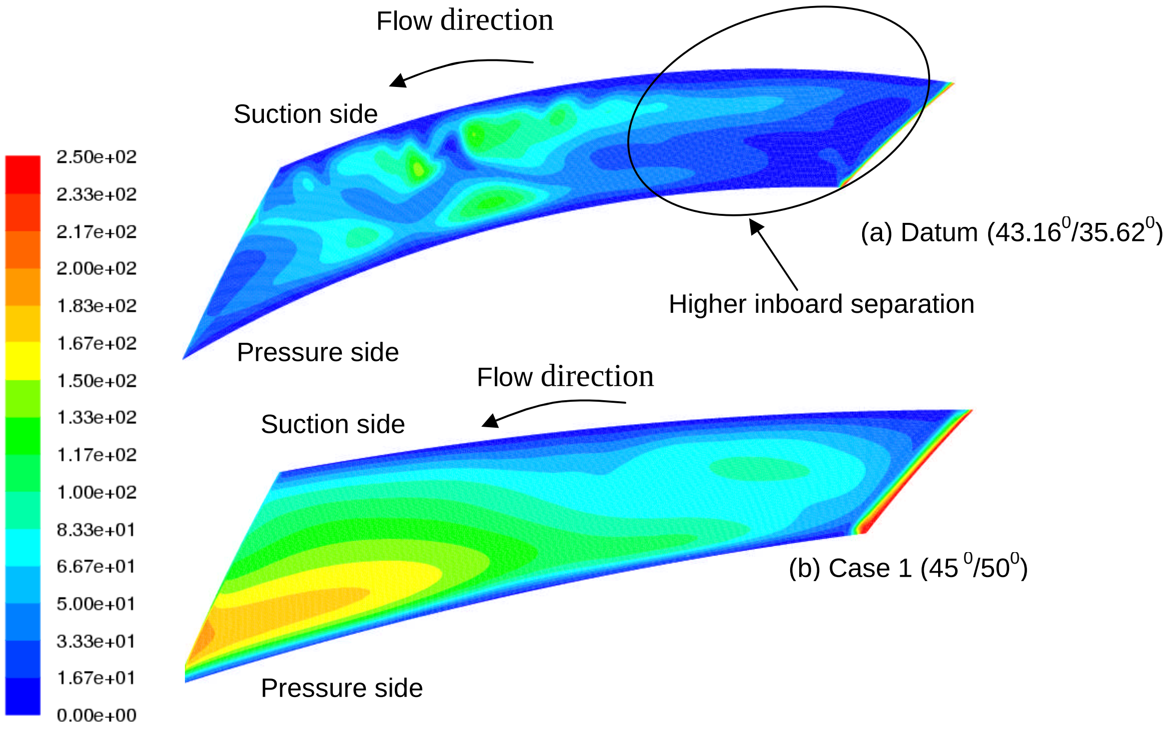

Fig 6.37: Passage inboard Surface Nusselt number distribution for datum and case 1

The other important aspect of the aero-thermal analysis is the amount of work done by the cooling air. As explained in section 6.2, specific enthalpy is used as the metric. The specific enthalpy for datum is 73590.258 J/K and for case 1 it is 81802.04 J/K. The datum inboard surface separation actually helps in reducing the temperature gradients at the inboard side due to the eddying motion of the recirculated flow. This increases the cooling air effectiveness at the inboard surface. For case 1 also the inboard separation at the inlet due to flow direction change from axial to radial helps in reducing the temperature gradients and thereby increasing the cooling air effectiveness (fig 6.38). The diffusion at the trailing edge of the suction also helps in increasing the effectiveness even though the surface heat transfer rate decreases due to it. The reader has to remember that the increase in effectiveness is by no means compensated for the drop in the mass flow rate and the surface heat transfer rate. The surface heat transfer rate is an important parameter as it determines the formation of hot spots on the surface.

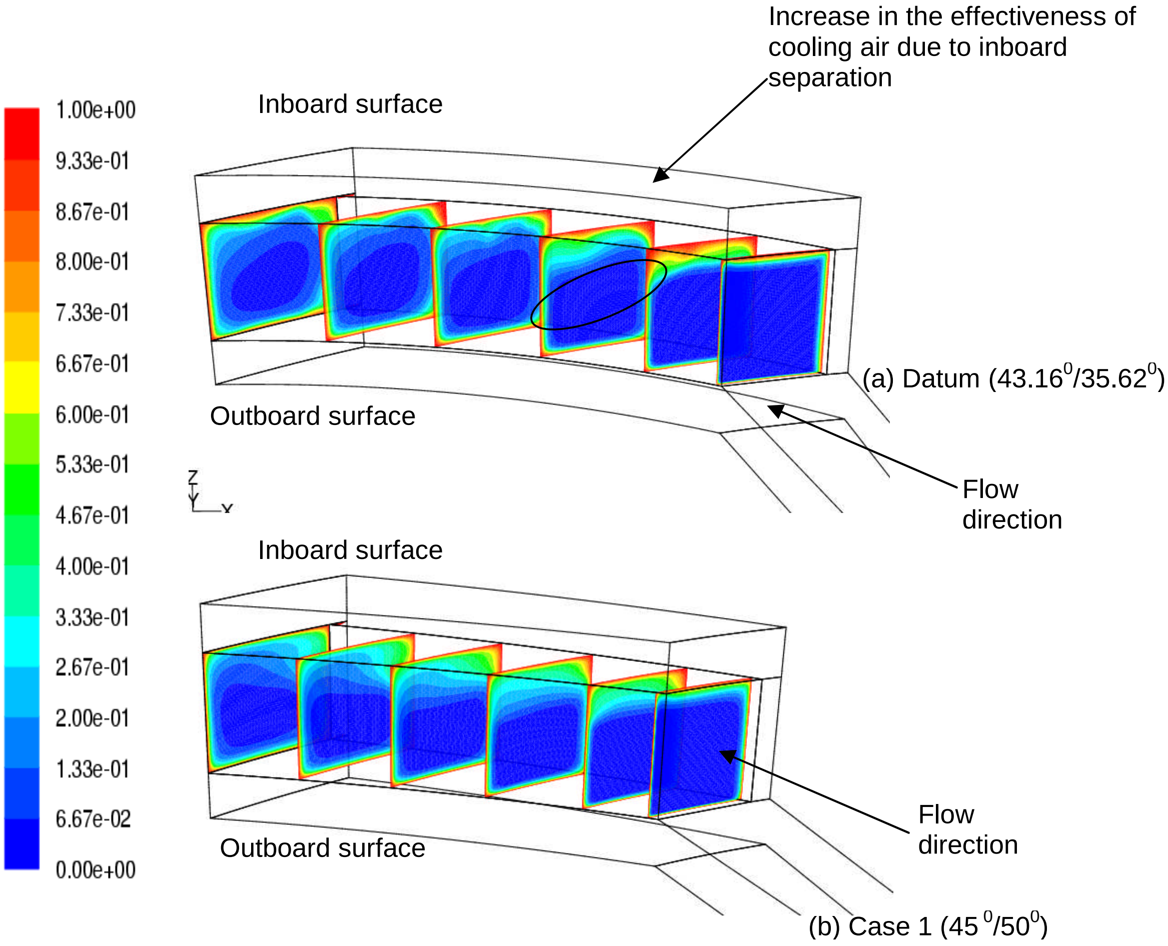

Fig 6.38: Effectiveness at different radial distances through the passage for datum and case 1

It was observed that by increase in the outlet angle from 50^0 to 90^0 the total heat transfer rate decreases by 20.85%. This is due a large suction side separation region created by the curvature of the blade for case 2 as explained in section 6.3.1.1. From figure 6.39 it can be observed that the suction heat transfer rate is poor (20.11 W as opposed to 40.67 for case 1). This is due to the separation in the flow as the flow direction changes from tangential to radial. This separation blocks the flow almost entirely on the suction side and the air is redirected towards the pressure side producing higher velocities. These higher velocities increase the heat transfer rate from the pressure surface (45.26 W as compared to 48.09 W for case 1) (fig 6.40). The inboard side is the most badly affected region due to flow direction change from both axial to radial and tangential to radial thereby increasing the separation region. This is leads to a very low heat transfer rate from the inboard surface (fig 6.41). The outboard surface heat transfer rate is uniform except near the suction surface where there is the separation region that again acts as a barrier for heat transfer (fig 6.42).

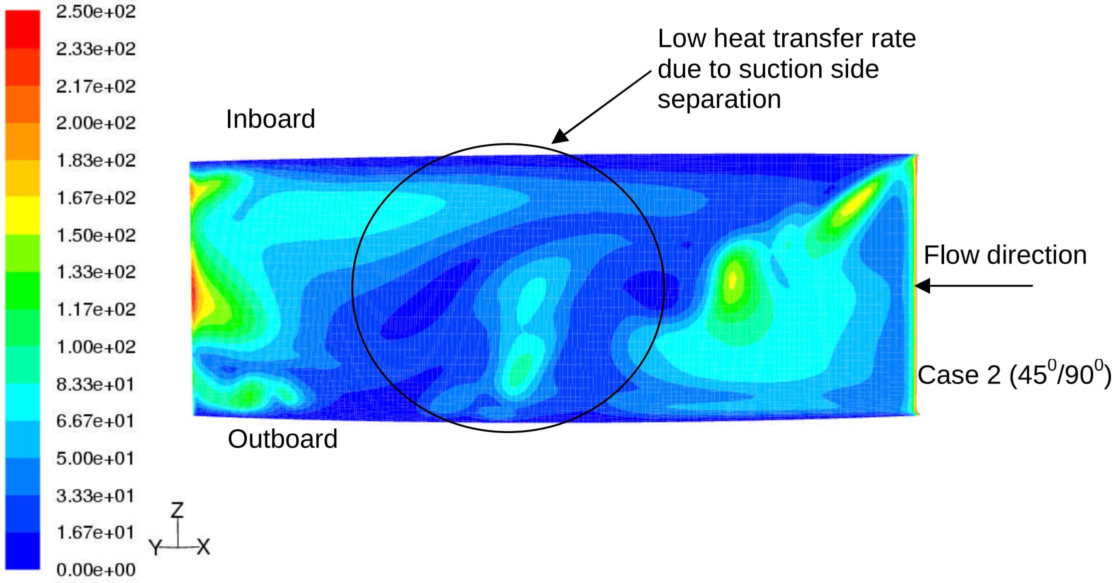

Fig 6.39: Suction surface Nusselt number distribution for case 2

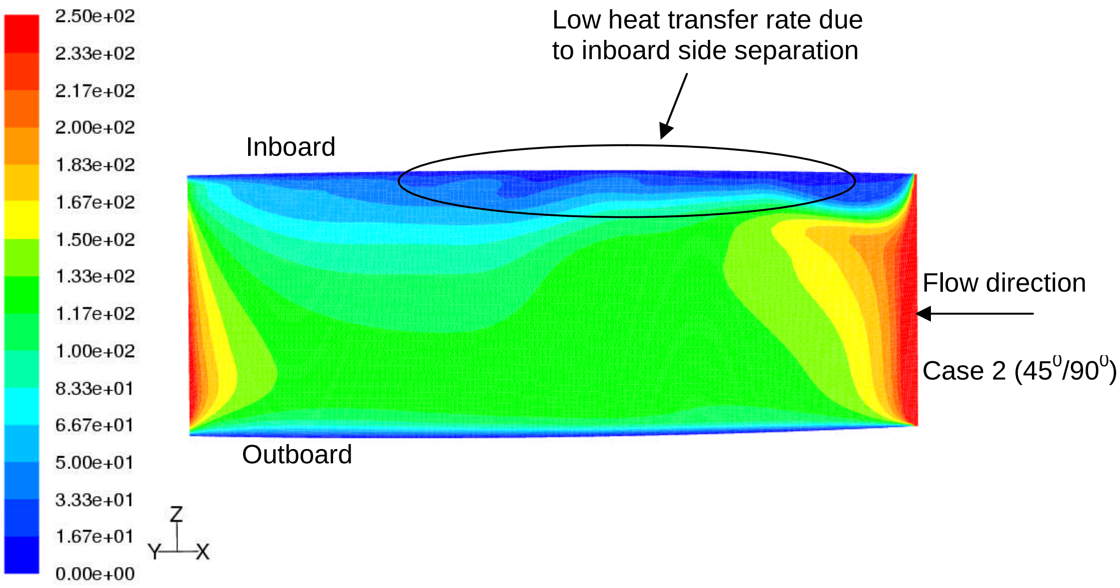
Low heat transfer rate due to inboard side separation

Fig 6.40: Pressure surface Nusselt number distribution for case 2

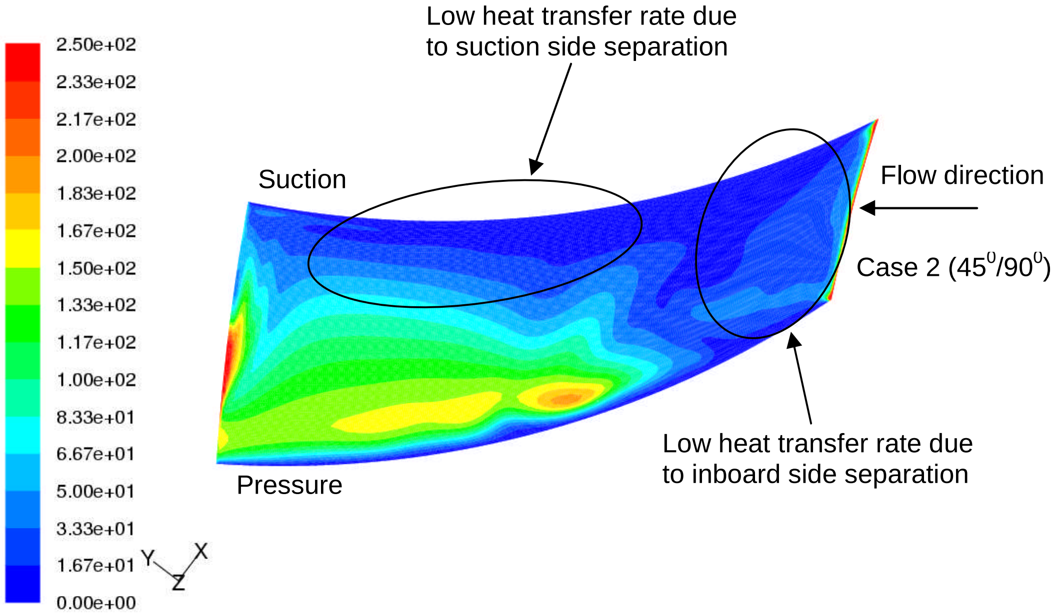
Low heat transfer rate due to suction side separation

Low heat transfer rate due to inboard side separation

Fig 6.41: Passage inboard surface Nusselt number distribution for case 2

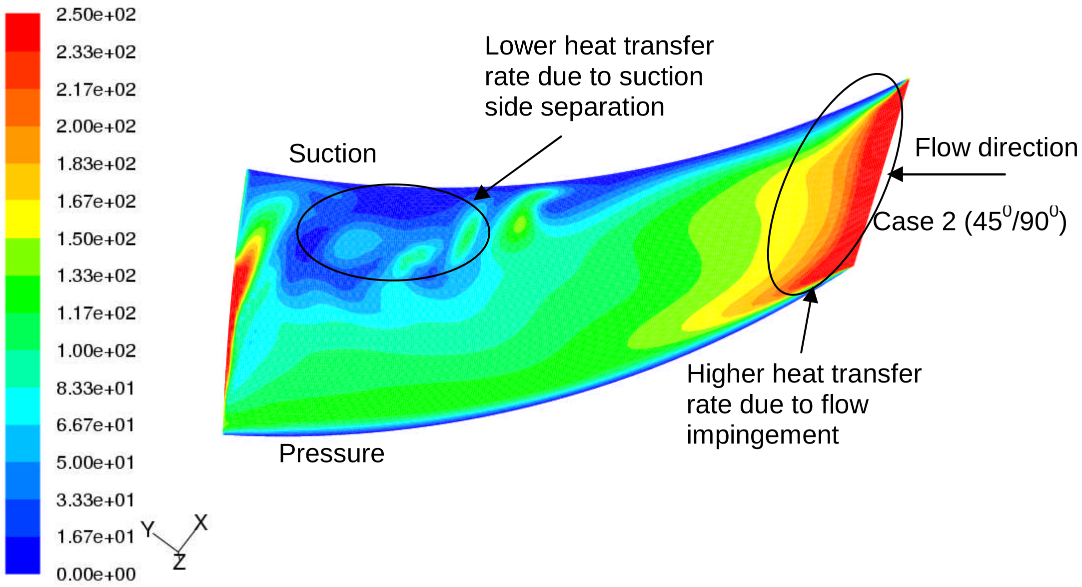

Fig 6.42: Passage outboard surface Nusselt number distribution for case 2

The specific enthalpy for case 2 design rotor is 79254.94 J/K. This can be understood by analysing the effectiveness of the cooling air through the passage of the rotor. From figure 6.43 it can be observed that the effectiveness of air is higher near the suction side of the passage and very low near the pressure side. The recirculation region near the suction side of passage that almost extends through out the passage reduces the temperature gradients due to the eddying motion of the fluid which enhances the momentum and heat exchange between the different fluid layers. The fluid velocity being higher near the pressure reduces the air residence time thereby decreases the effectiveness of the cooling air.

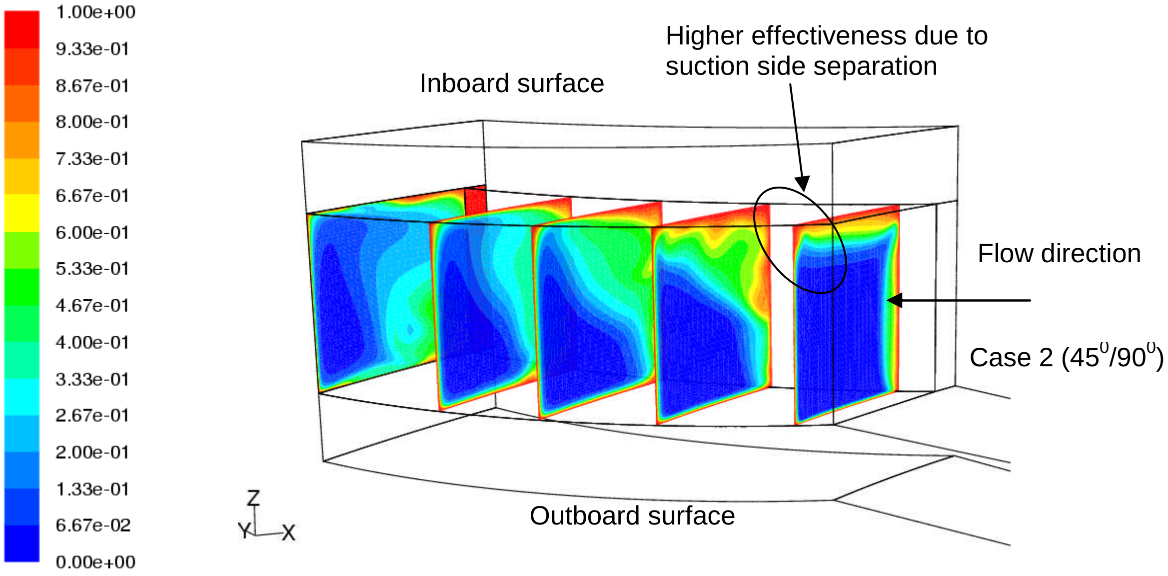

Fig 6.43: Effectiveness of the cooling air through the rotor passage for case 2

The increase in the inlet angle from 45^0 (case 1) to 60^0 (case 4), changes the curvature of the blade marginally but enough to increase the diffusion on the suction side compared to case 1. This diffusion creates regions of low heat transfer on the suction side causing the formation of hot spots (fig 6.44). The heat transfer from the pressure side is more uniform due uniform velocities associated with it (fig 6.45). Also the change in the inlet angle increases the inlet separation thereby reducing the heat transfer at the inlet of the inboard surface (fig 6.46). The behaviour of case 2 rotor is almost similar to that of the case1 but due to lower mass flow rate the heat transfer rate decreases.

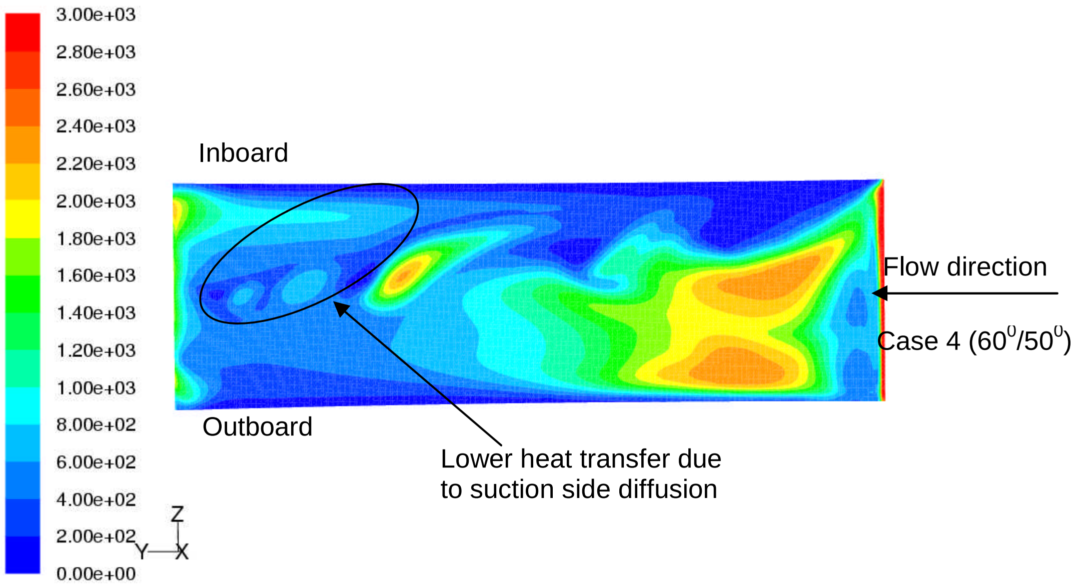

Fig 6.44: Suction surface Nusselt number distribution for case 4

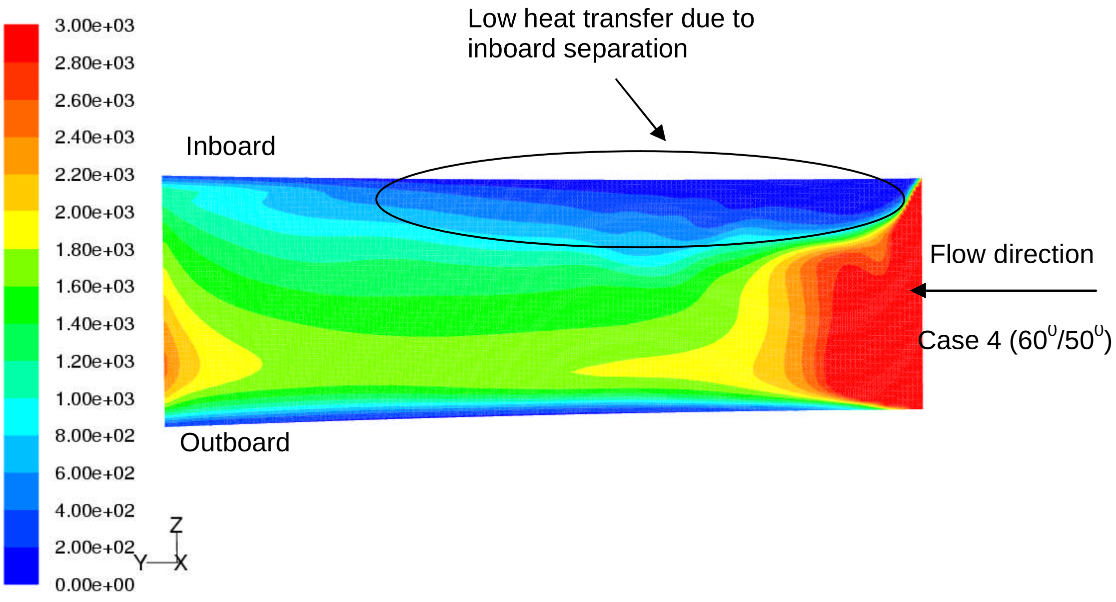

Fig 6.45: Pressure surface Nusselt number distribution for case 4

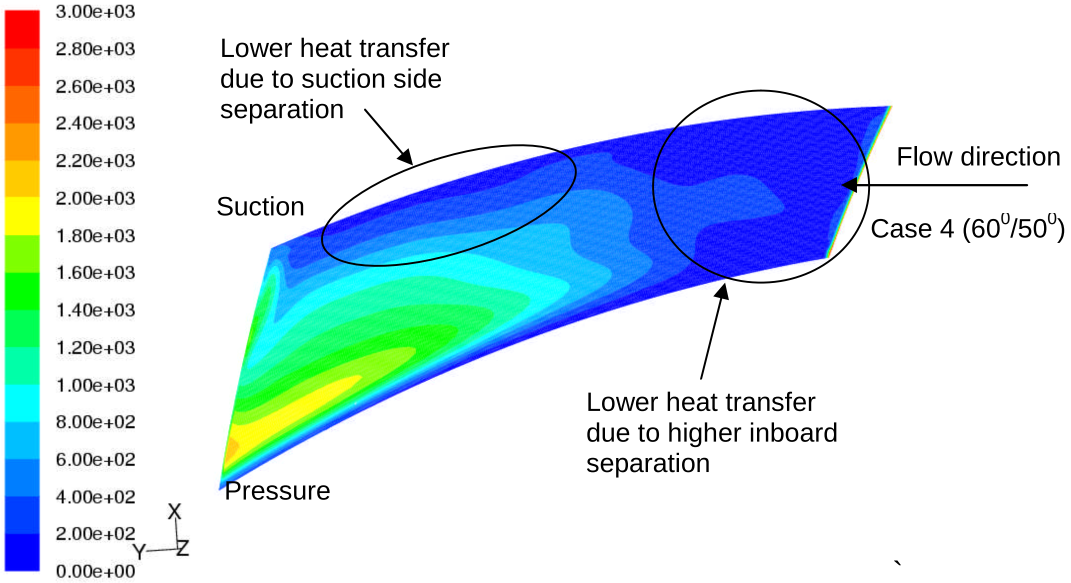

Fig 6.46: Passage inboard side Nusselt number distribution for case 4

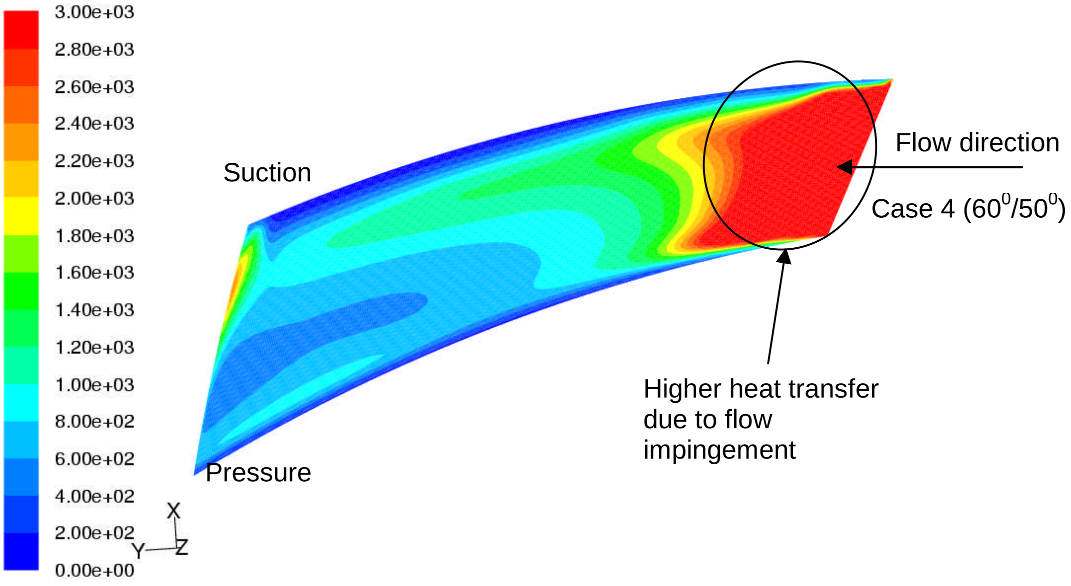

Fig 6.47: Passage outboard side Nusselt number distribution for case 4

The specific enthalpy for the case 4 design rotor is 68508.35 J/K. The lower specific enthalpy for case 4 as compared to case 1 with 81802.04 J/K is due to 18.37% drop in the mass flow rate through the passage. The effectiveness distribution for case 2 is very similar to that of case 1. The diffusion on the suction side trailing reduces the temperature gradients thereby increasing the effectiveness of the cooling air (fig 6.48).

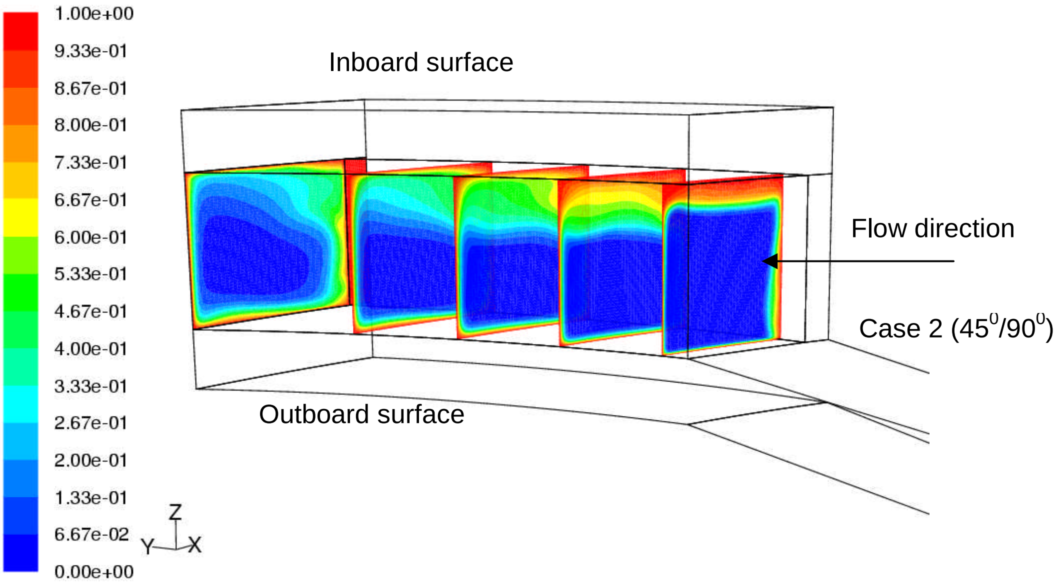

Fig 6.48: Effectiveness of the cooling air through the rotor passage for case 4

There is a strong relation between aerodynamics through the passage and heat transfer rate from the internal surfaces of the passage. So it is difficult establish a trend in the variation of the total heat transfer rate with blade angles (fig 6.49) unlike the mass flow rate. In the previous sections a few cases were discussed to understand the aero-thermal behaviour of various disc brake rotor designs. From figure 6.48 it can be observed that at different outlet angles the total rate of heat transfer decreases with increase in the inlet angle except for the radial bladed rotor. This is because of the higher heat transfer from the pressure side of the radial bladed rotor owing to the huge separation on the suction side. The case 1 design rotor was observed to have the highest the total rate of heat transfer of 157.69 W. Similarly the total rate of heat transfer variation with outlet angle also doesn’t follow a particular trend (fig 6.50). The total heat transfer rate was again observed to be higher for case 1.

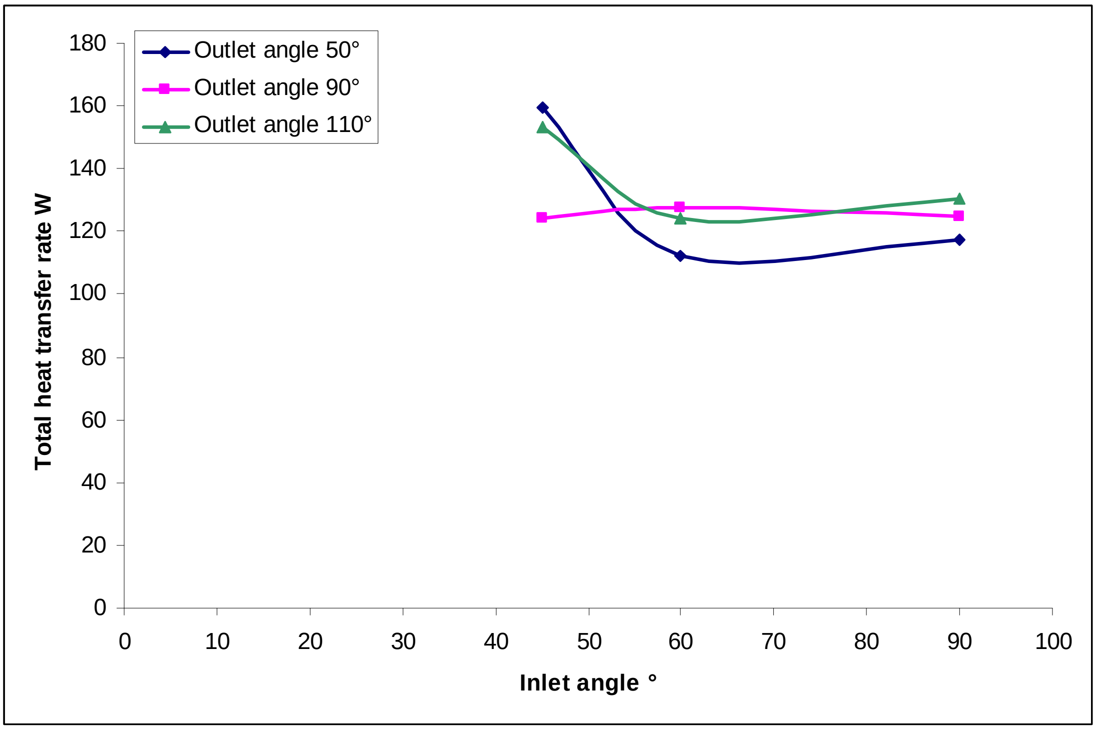

Fig 6.49: Total heat transfer rate W as a function of inlet angle

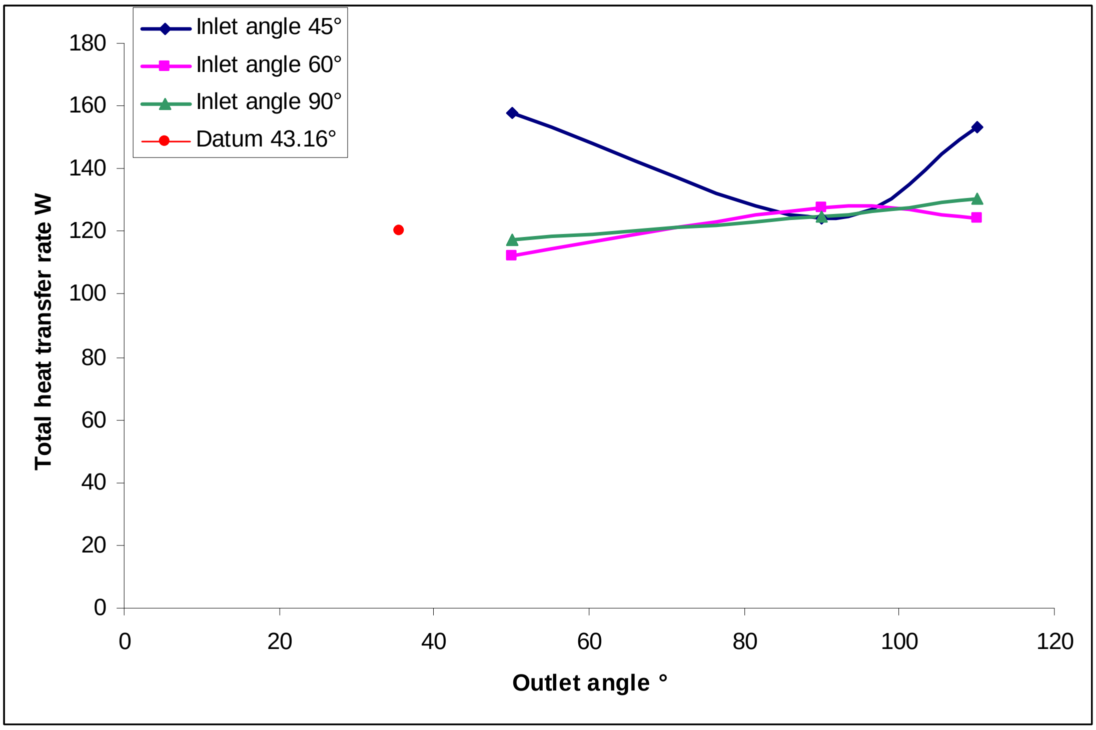

Fig 6.50: Total heat transfer rate W as a function of outlet angle

6.4.1.3. Heat transfer distribution

It is important to understand the heat transfer rate contribution from the individual surfaces to the total heat transfer. This provides the basis for understanding the surfaces of concern in each of the designs. A few aspects that affect the heat transfer from the rotor surfaces are the inlet separation which affects the suction surface and the inboard surface near the inlet of the passage. Also diffusion at the suction side trailing edge affects heat transfer rate from both suction and the outboard surfaces of the passage. In some designs the curvature of the blade also creates separation region at the trailing edge of the pressure surface thus affecting heat transfer rate. In order to provide the reader with a better understanding of this phenomenon in each of the designs, a histogram has been plotted indicating the heat transfer rate from each of the internal passages (fig 6.51).

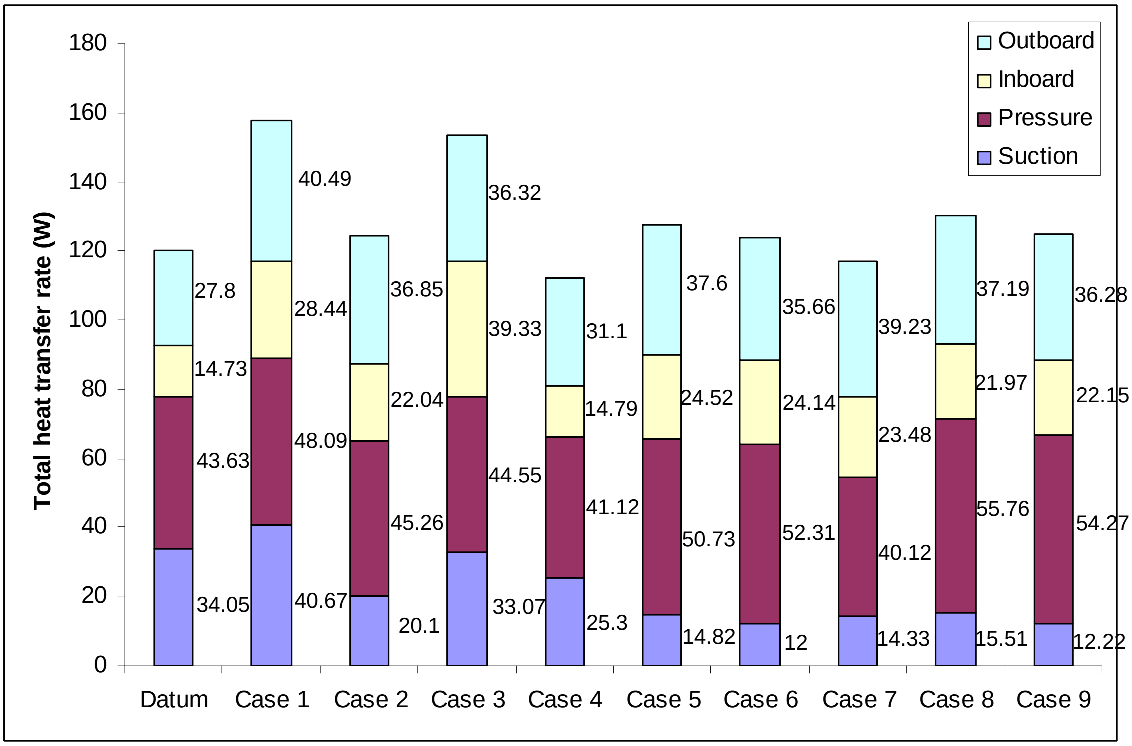

Fig 6.51: Contribution of internal surfaces heat transfer rate to the total heat transfer rate

The maximum non-dimensional temperature difference provides an understanding about the amount of thermal distortion the rotor undergoes. The thermal distortion index (T.D.I) explained in section 4.5 is the metric used. Maximum and minimum temperatures in the rotor are maximum and minimum respectively among the individual rotor surface temperature averages.

$$T.D.I = \frac{T_{\max} - T_{\min}}{T_s - T_\infty} \qquad \text{………………………..} \ (6.3)$$

The lower the value of T.D.I the higher is the uniformity of temperature within the rotor. As was observed in the previous sections, with increase in the outlet angle at lower inlet angles, the blade surface curvature increases thereby increasing the suction side separation. This reduces the heat transfer from the suction side. This can also observed from the variation of T.D.I with outlet angle (6.52). The temperature uniformity is better at lower outlet angles and is 43.5% better for Case 1 as compared to the datum rotor. With increase in inlet angle the T.D.I increases and is lower at lower inlet angles (fig 6.53). This indicates that at lower inlet and outlet angles the temperature uniformity is better thereby decreasing the formation of hot spots. This parameter is important along with rate of heat dissipation and mass flow rate to judge the performance of a disc brake rotor. This is due to the fact that apart from higher heat transfer rate a good disc brake rotor should also avoid the formation of hot spots.

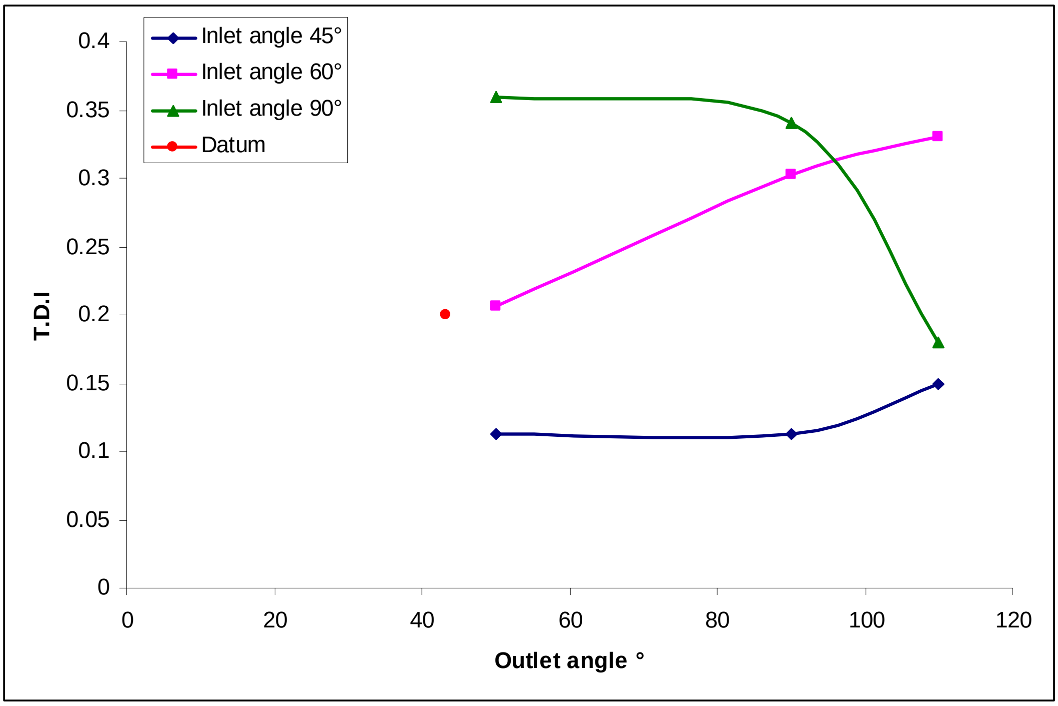

Fig 6.52: Thermal distortion index variation with outlet angle

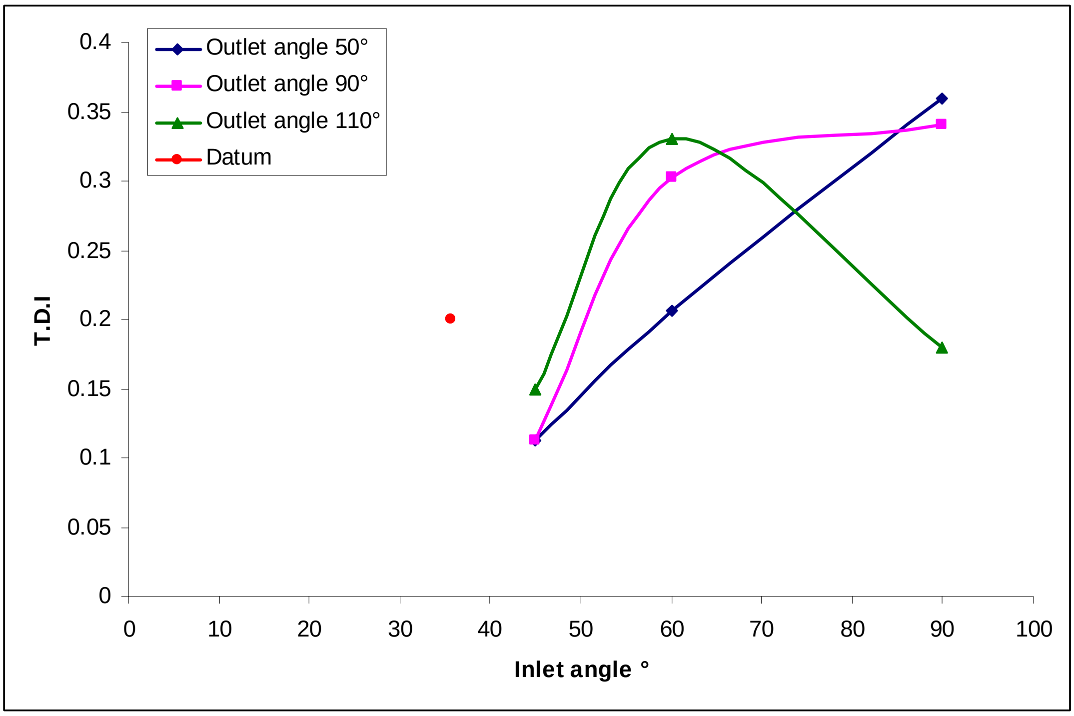

Fig 6.53: Thermal distortion index variation with inlet angle

6.4.1.4. Summary

Based on the analysis performed on the preliminary set of blade angles, it has been observed that the case 1 design rotor has better aero-thermal performance based on the performance metrics like mass flow rate and total heat transfer rate. The mass flow rate was 52.7% more than the datum and the total rate of heat transfer was 31.15% for the case 1 design rotor. It was also observed that the performance metrics decrease with increase in both outlet and inlet angles from case 1. So in order to increase the sensitivity of the parametric analysis and to locate an optimum set of blade angles a second set of blade angles have been selected. The variations in the values of inlet and outlet angles for the second set are closer to the case 1 rotor design. The results and discussion from the second set are presented in the next section.

6.4.2. Iteration 2

New models are created with less variation in the outlet and inlet angles. The case 1 design rotor was taken as reference for the analysis as the performance of case 1 was observed to be better than all other sets of blade angles after iteration 1. Seven new sets of blade angles were chosen for the analysis (table 6.3). The models and the mesh are similar to those used in iteration 1.

Name	Inlet angle (β_1)	Outlet angle (β_2)
Case 10	35^0	50^0
Case 11	45^0	70^0
Case 12	45^0	40^0
Case 13	45^0	60^0
Case 14	40^0	60^0
Case 15	40^0	50^0
Case 16	45^0	55^0

Table 6.3: Secondary set of blade angles

6.4.2.1. Mass flow rate variation

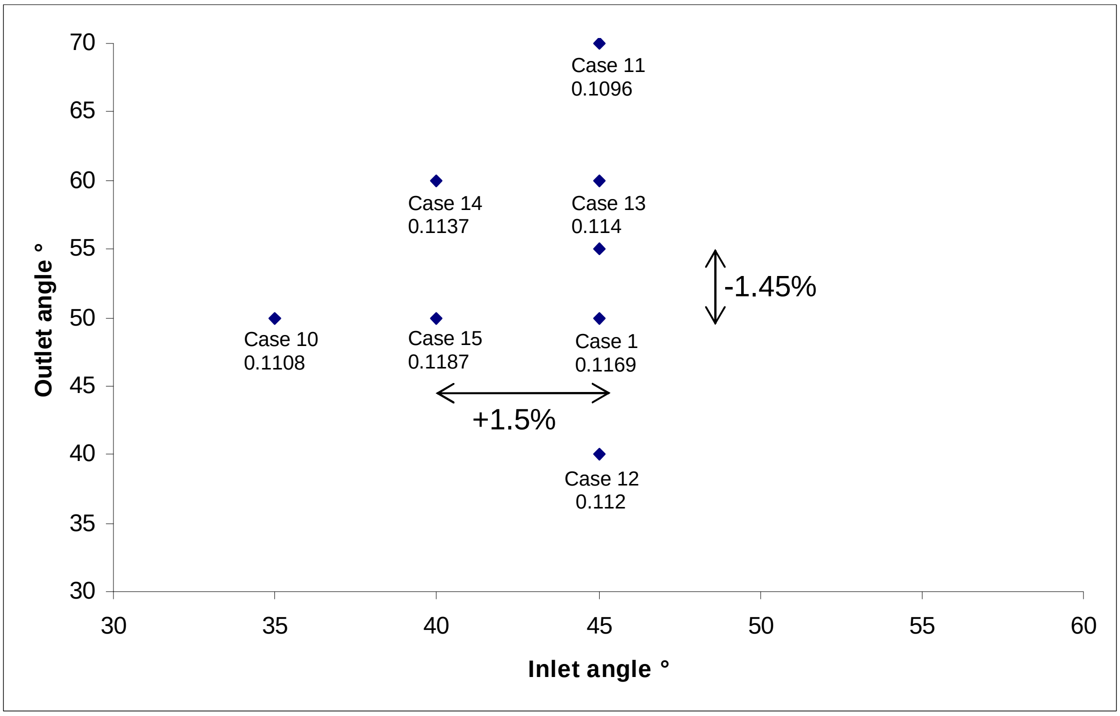

Fig 6.54: Mass flow rate (kg/sec) as a function of inlet and outlet angles

As the outlet angle is increased from 50^0 (case 1) to 55^0 (case 16) the mass flow rate drops by 1.45% (fig 6.54). This is due to increased diffusion on the suction side at the trailing edge of case 16 as compared to case 1 rotor design (fig 6.55). As the blade outlet angle was increased initially from datum to case 1, diffusion started to occur on the trailing edge of the suction side of case 1. On further increase in the outlet angle to 55^0 the diffusion occurs earlier for case 16. The outlet angle was decreased from 50^0 (case 1) to 40^0 (case 12) to bring the design closer to the datum rotor. Due to this decrease in the outlet angle the mass flow rate dropped by 5.8%. The amount of diffusion occurring in case 1 rotor got reduced due lower area change from inlet to the outlet of the passage. There is increased inlet separation due to the curvature of the blade as the flow direction changes from tangential to radial (fig 6.56). As the inlet angle was reduced from 45^0 to 40^0, the mass flow rate was observed to have increased by 1.53%. But the diffusion at the trailing edge of the suction is higher for case 15 than case 1 (fig 6.57). By further decreasing the inlet angle to 35^0, the mass flow rate drops by 5.2%. This drop is due to increased suction side separation and diffusion (fig 6.58).

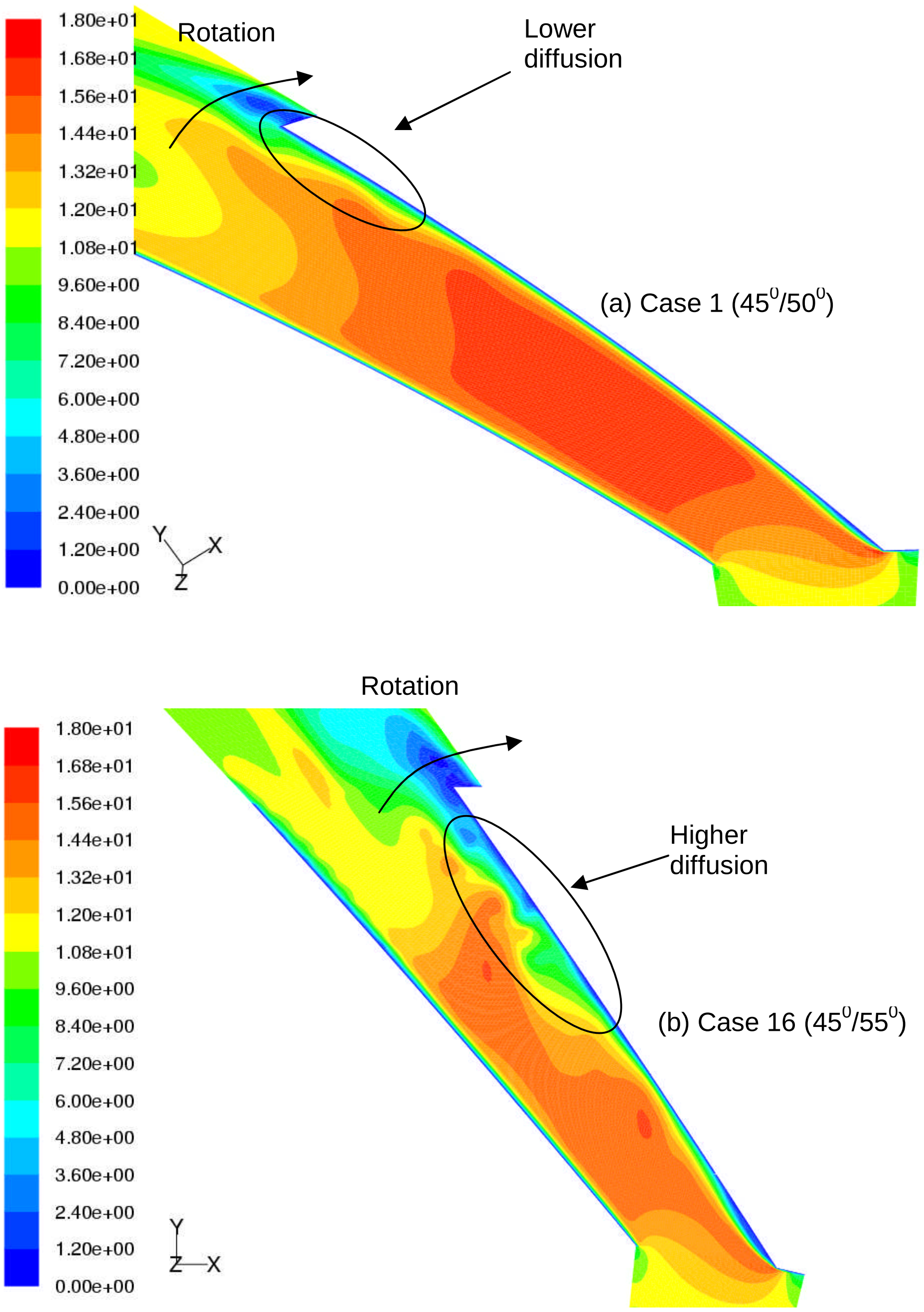

(a) Case 1 ($45^0/50^0$)

(b) Case 16 ($45^0/55^0$)

Fig 6.55: Relative velocity at the mid-passage height for case 1 and case 16

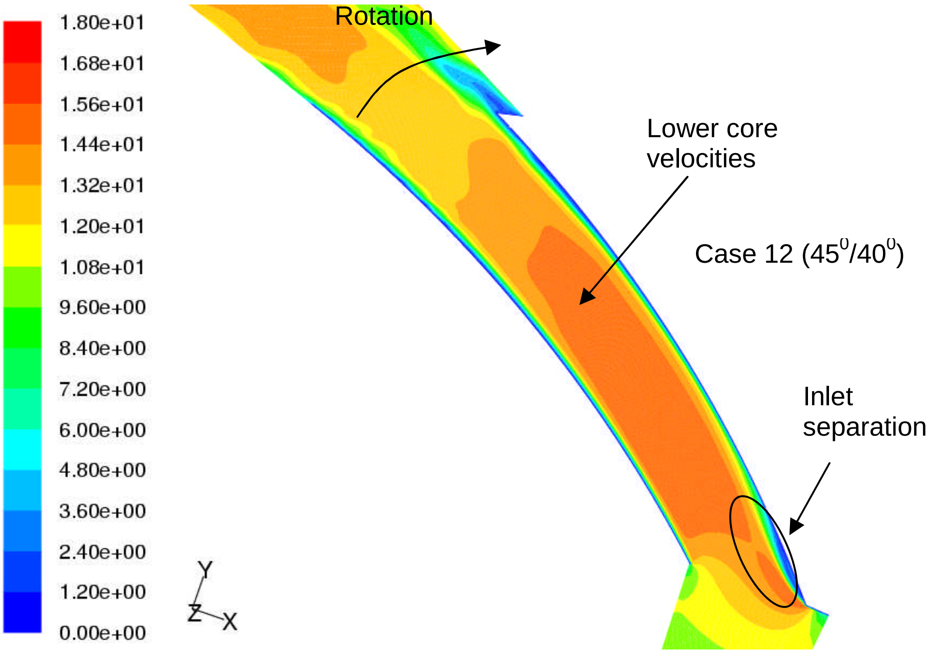

Fig 6.56: Relative velocity at the mid-passage height for case 12

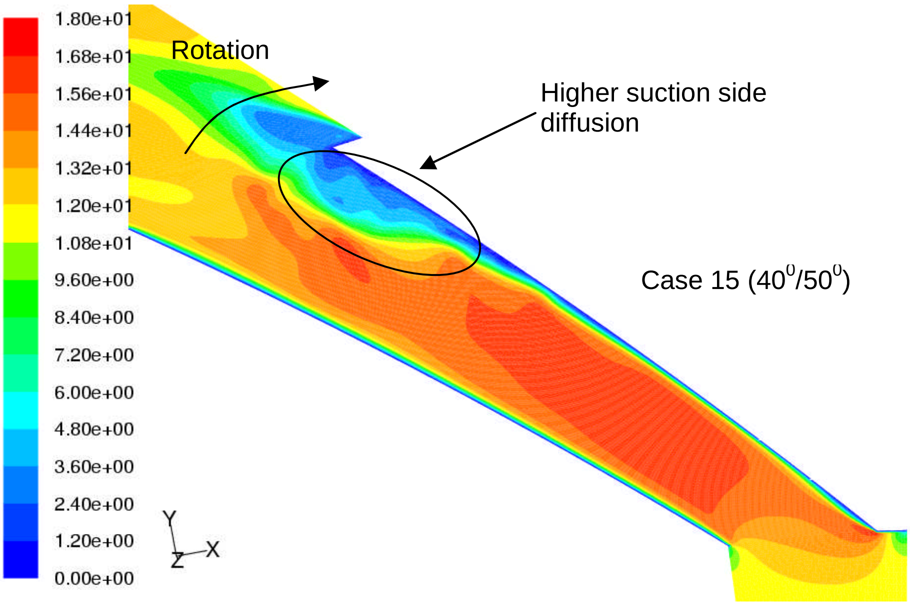

Fig 6.57: Relative velocity at the mid-passage height for case 15

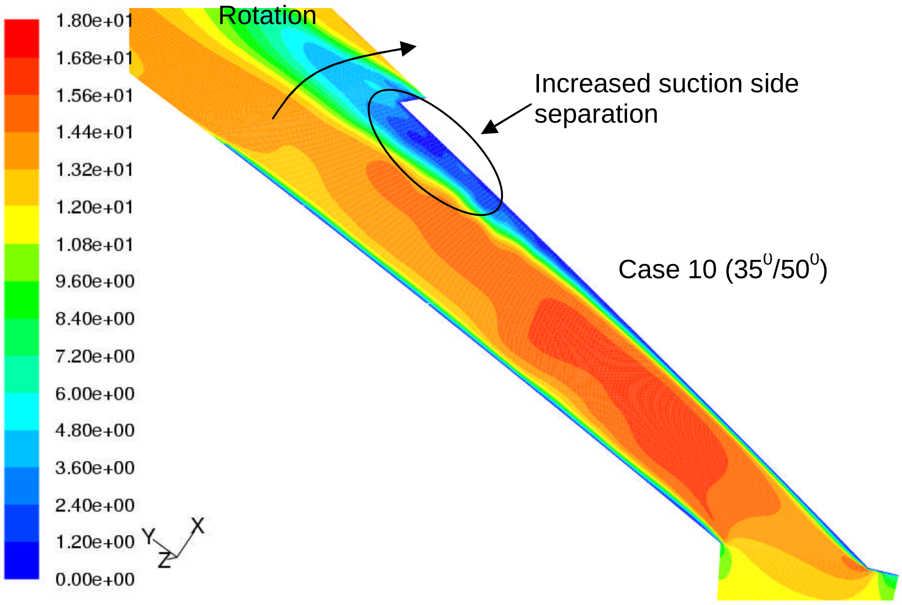

Fig 6.58: Relative velocity at the mid-passage height for case 10

A trend can be captured from the results in the mass flow rate obtained from the iteration 2 (fig 6.59). The mass flow rate increases from case 12 to case 1 with increase in the outlet angle. Further increase in the outlet angle reduces the mass flow rate due to increased diffusion on the suction side of the passage. A similar trend can be observed in the variation of mass flow rate with inlet angle. From case 10 to case 15 the mass flow rate increases as the suction side separation decreases but there is increase in the diffusion due to the increase in the outlet area. With Further increase in the inlet angle from case 15 to case 1 the mass flow rate decreases by 5.2% (fig 6.60).

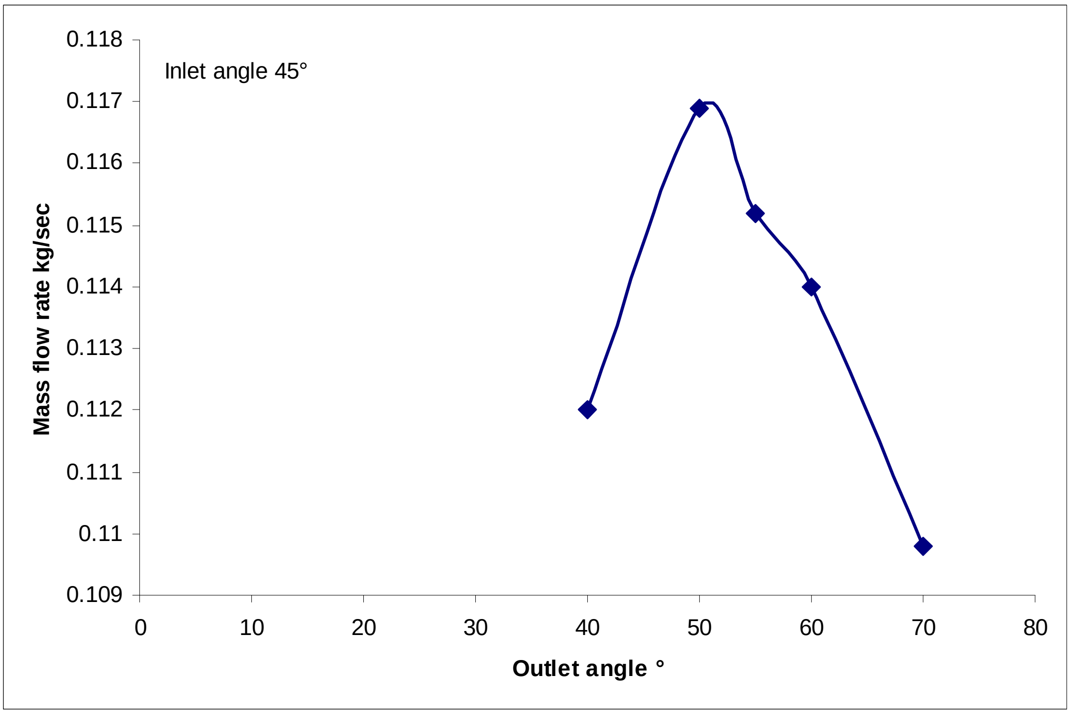

Fig 6.59: Mass flow rate (kg/sec) as a function of outlet angle

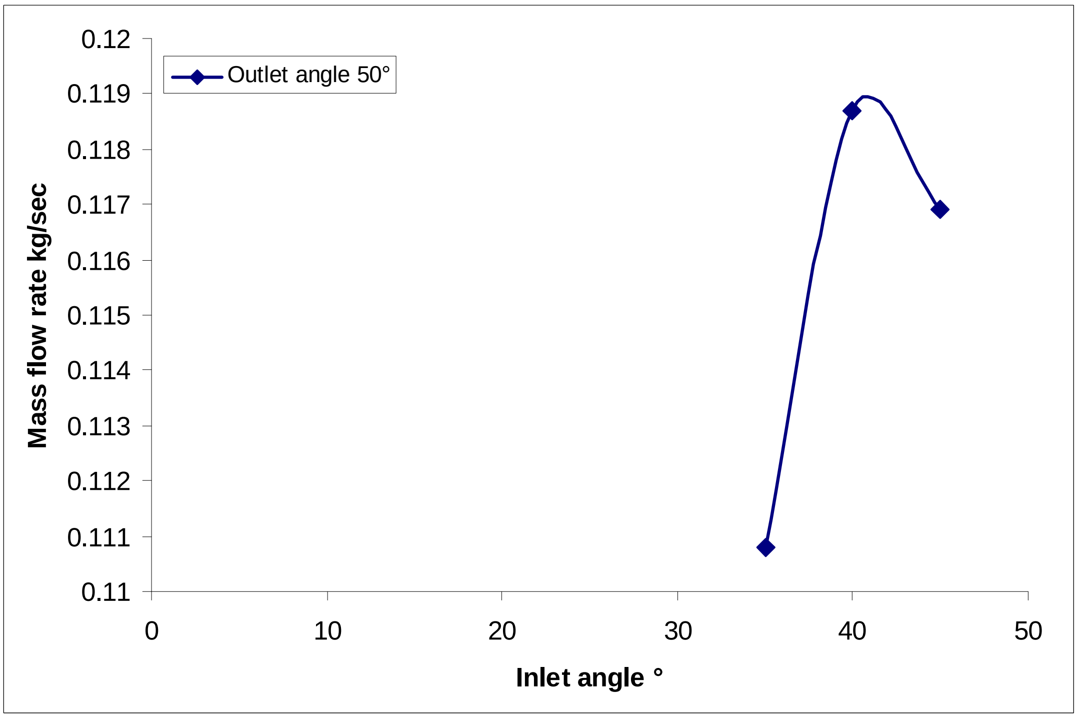

Fig 6.60: Mass flow rate (kg/sec) as a function of inlet angle

6.4.2.2. Heat transfer variation

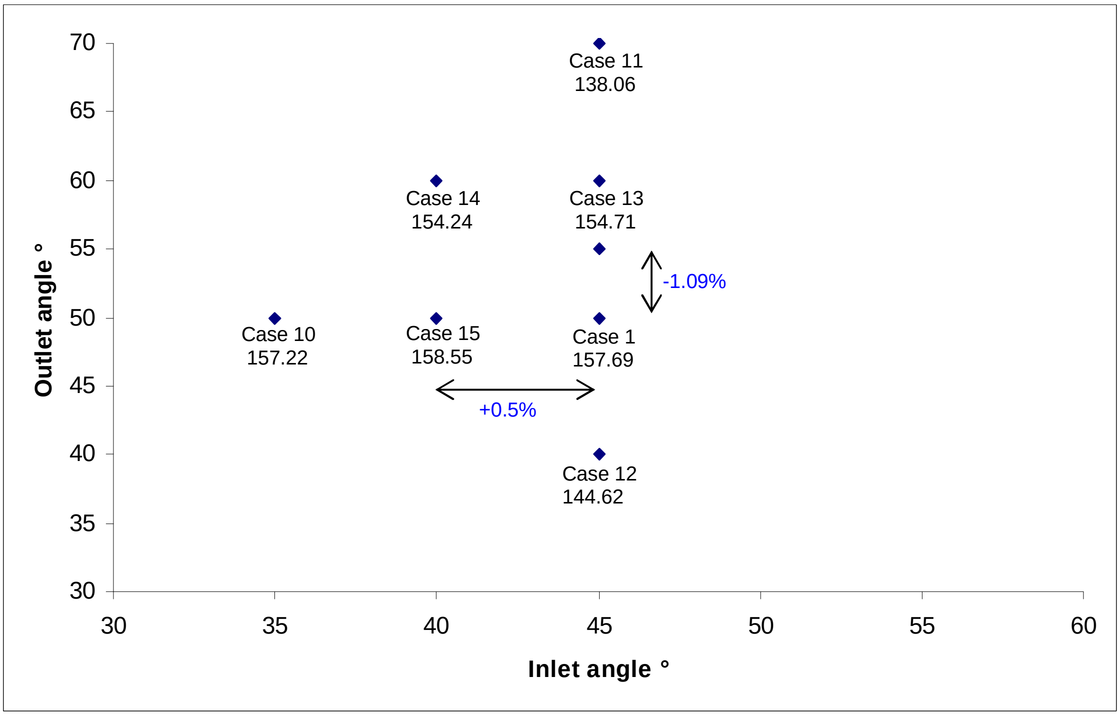

Fig 6.61: Total heat transfer rate (W) as a function of inlet and outlet angles

Due to the increase in the outlet angle from 50^0 (case 1) to 55^0 (case 16), there is a decrease in the total heat transfer rate by 1.91% (fig 6.61). Even though the reduction in the heat transfer rate is only small the heat transfer distribution for case 16 is not uniform as it was for case 1. From figure 6.62 it can seen that as the fluid flows through the case 16 rotor passage there is diffusion occurring on the suction side of the passage almost immediately after entry into the passage. This reduces the heat transfer from the suction surface of the passage (fig 6.63). The interesting aspect though is the strong swirling of fluid particles in the passage near the pressure side. This movement increases the heat transfer locally due enhanced mixing. This leads to the formation of hot spots on the pressure side of the passage at the trailing edge (fig 6.64). The diffusion of the fluid also reduces the rate of heat transfer from the inboard side of the passage. There is a region of high heat transfer rate towards the pressure side of the inboard surface due to the transverse movement of fluid as mentioned above (fig 6.65). The outboard surface heat transfer rate is more uniform but the trailing edge region on both suction and pressure side have very low heat transfer due to the aforementioned reasons (fig 6.66). In spite of the fact that the total heat transfer rate for case 16 is high the presence of low heat transfer regions lead to the formation of hot spots there by affecting the performance of the ventilated disc brake.

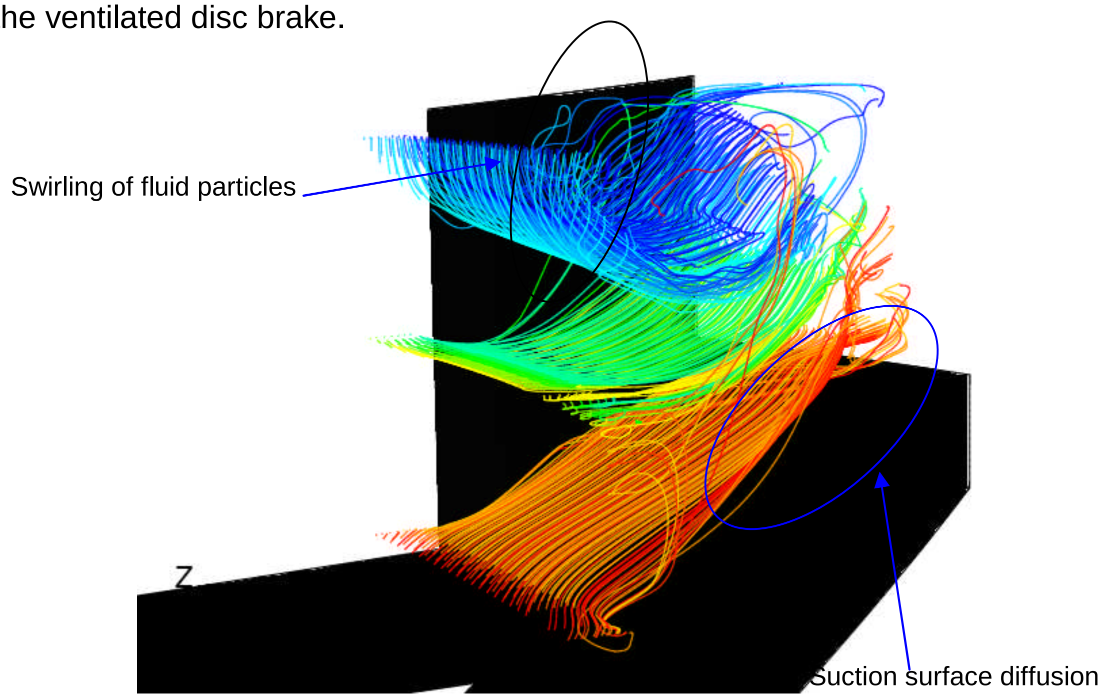

Fig 6.62: Case 16 pathlines through the passage

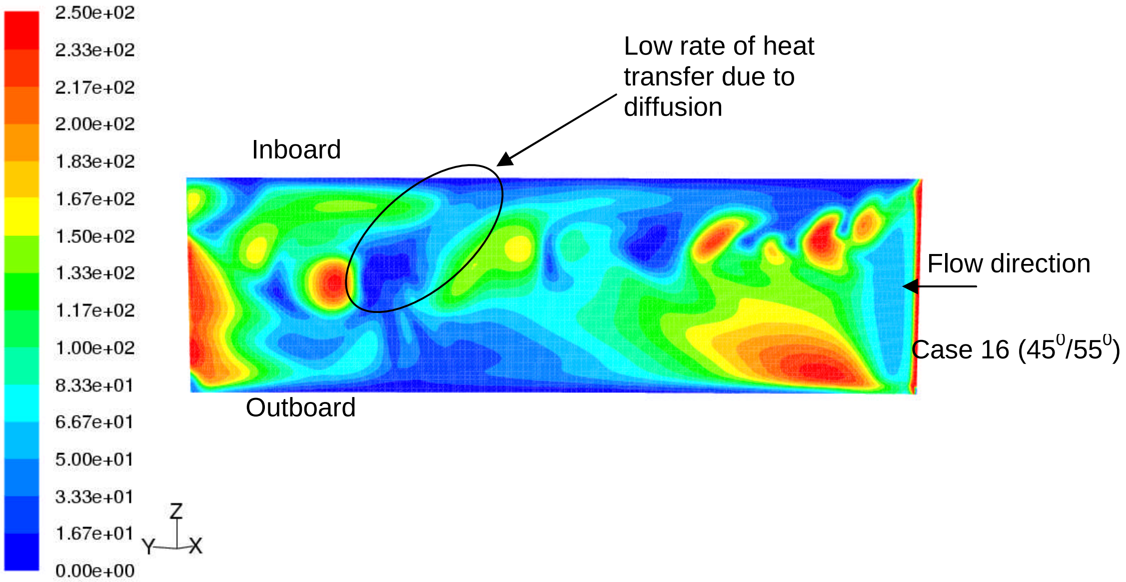

Fig 6.63: Suction surface Nusselt number distribution for case 16

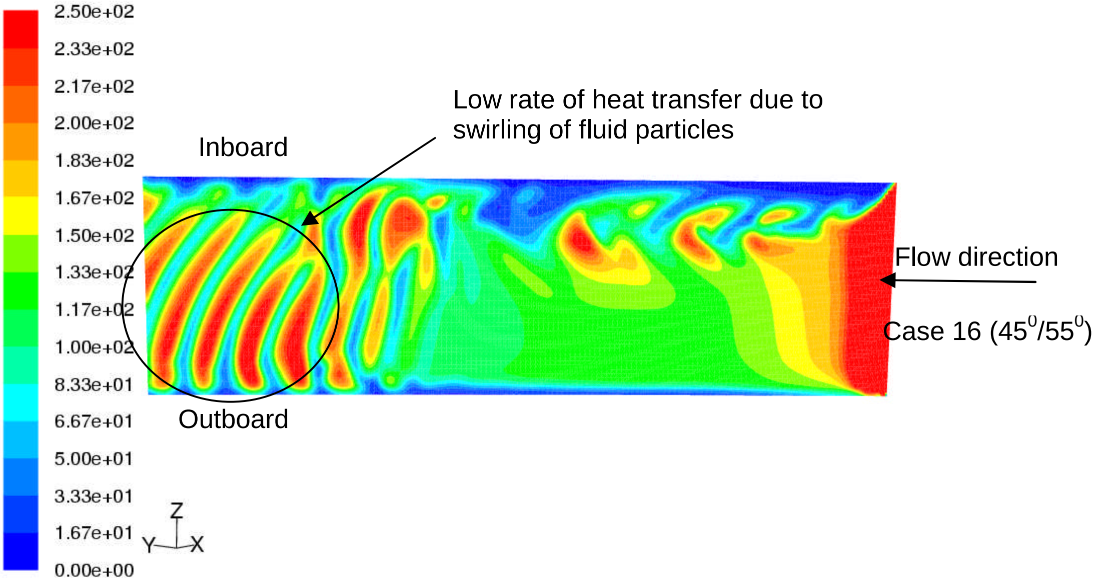

Fig 6.64: Pressure surface Nusselt number distribution for case 16

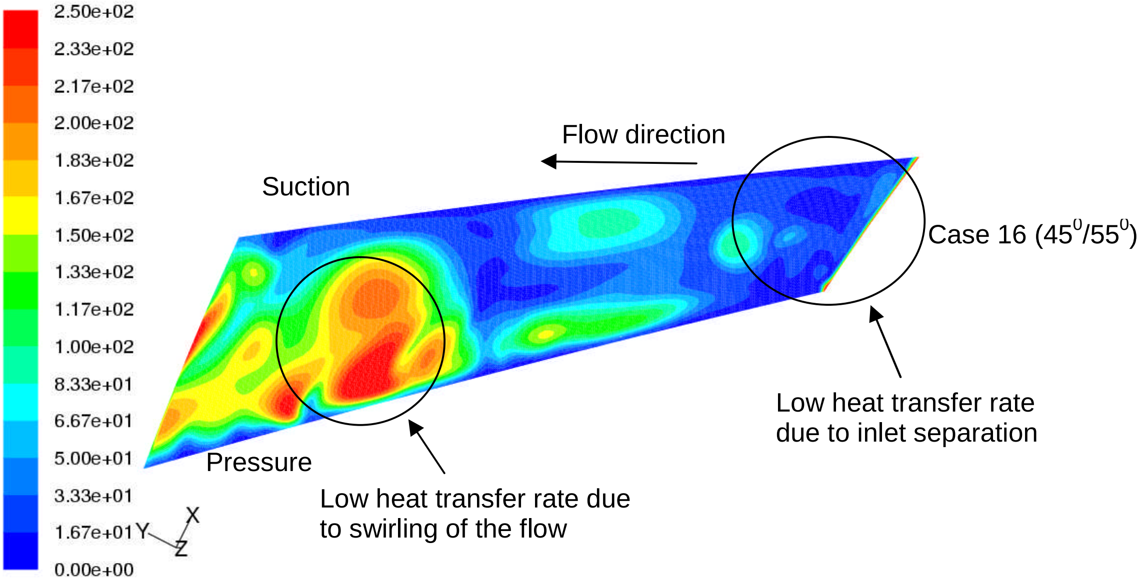

Fig 6.65: Passage inboard surface Nusselt number distribution for case 16

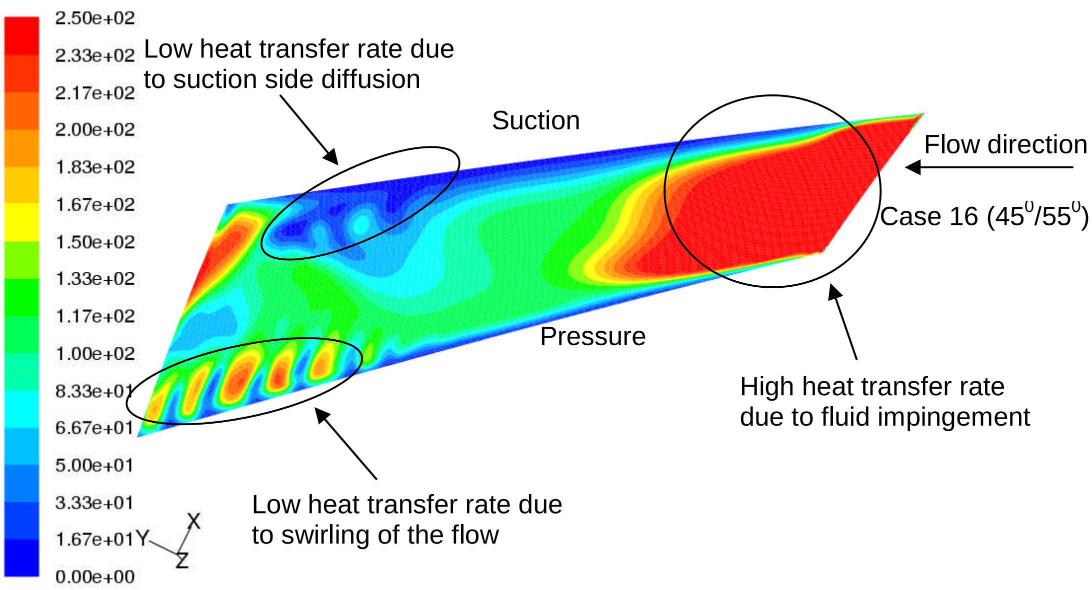

Fig 6.66: Passage outboard surface Nusselt number distribution for case 16

It was observed that by increasing the inlet angle from 45^0 (case 1) to 40^0 (case 15) there is an increase in the total heat transfer rate by 0.54%. This is due to higher mass flow rates associated with case 15. The suction side diffusion due to area change from inlet to outlet is more for case 15 than case 1 leading to the formation of regions of low and high heat transfer. The suction side of the passage has regions of low heat transfer at the trailing edge of the blade to the diffusion of air. The inboard side of the suction surface has low heat transfer rate due to the change in direction of flow from axial to radial (figure 6.67). The pressure surface on the other hand has a more uniform heat transfer rate due to the attached flow associated with it. The inboard side of the pressure surface also has low heat transfer due to the above mentioned direction change (figure 6.68). The inboard surface of the passage has a poor heat transfer rate due to the direction changes from axial to radial and also from tangential to radial. The diffusion also hinders the heat transfer rate at the suction side of the inboard surface (figure 6.69). The outboard side as expected had a uniform heat transfer rate due to impingement of fluid on it. The suction side of the outboard surface though has low heat transfer coefficient due to the diffusion of air at the trailing edge (figure 6.70).

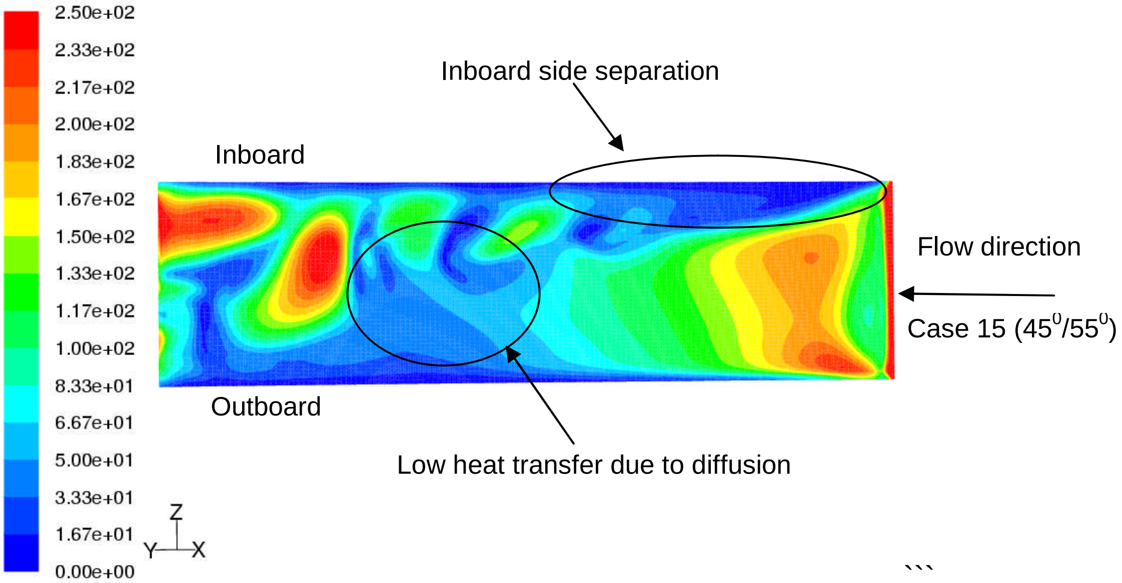

Fig 6.67: Suction surface Nusselt number distribution for case 15

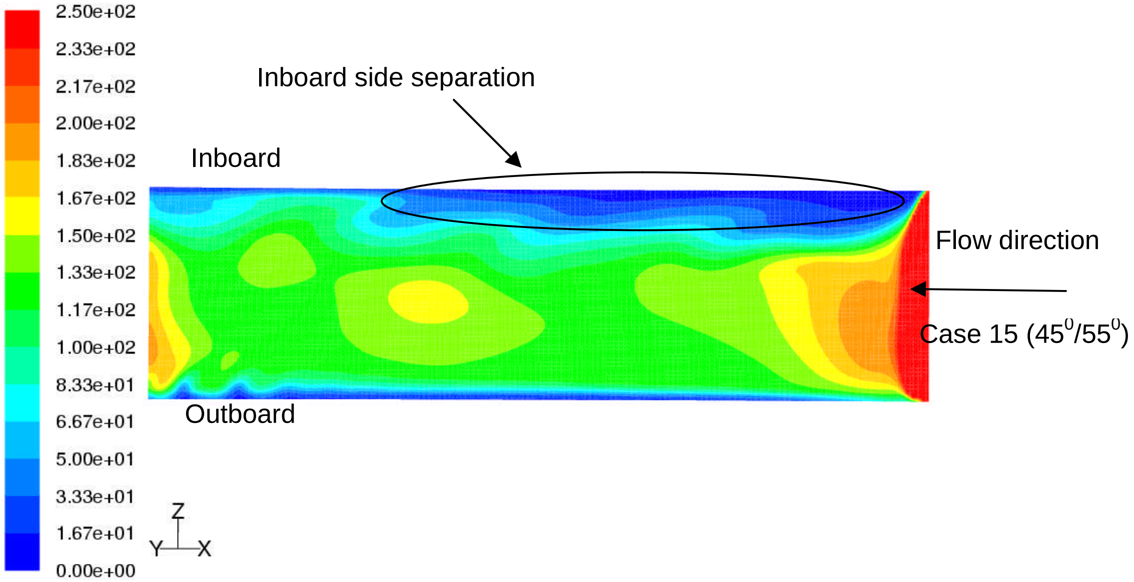

Fig 6.68: Pressure surface Nusselt number distribution for case 15

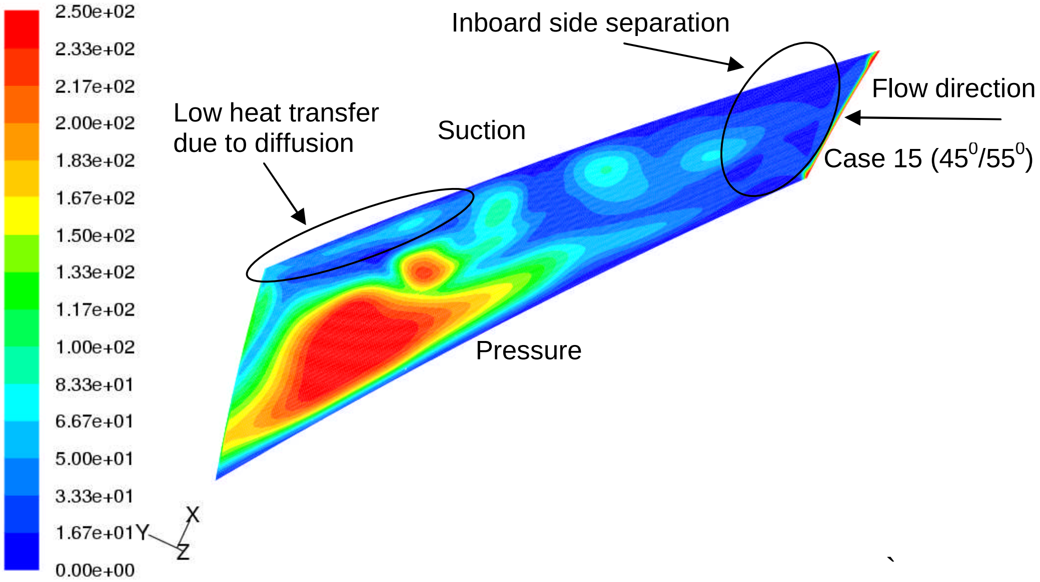

Fig 6.69: Passage inboard surface Nusselt number distribution for case 15

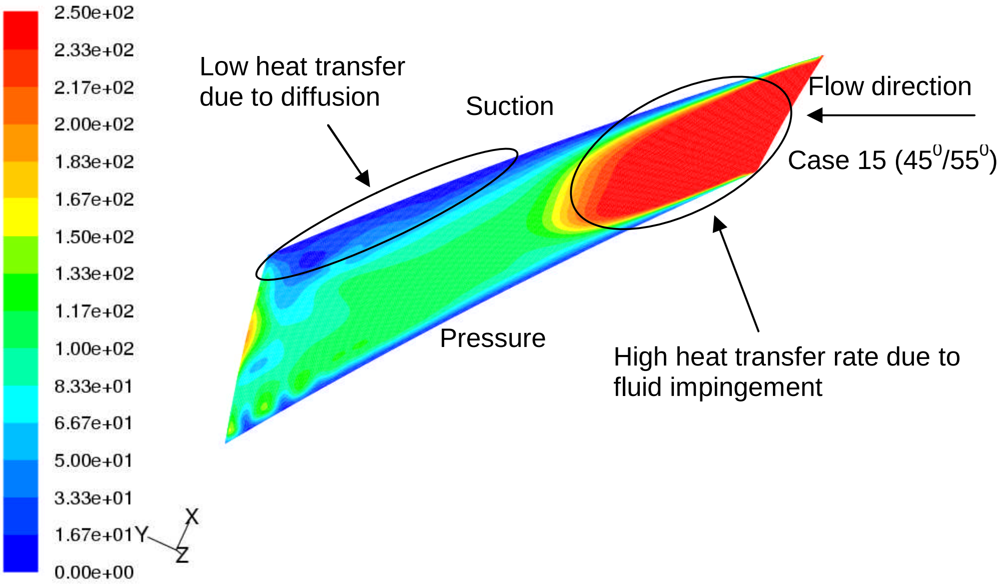

Fig 6.70: Passage outboard surface Nusselt number distribution for case 15

6.4.3.3. Heat transfer distribution

The total heat transfer rate difference between various designs in iteration is very small. But the uniformity of heat transfer on the internal surfaces changes for different designs. The main area of concern for the blade angle sets in iteration 2 is the diffusion that occurs at the trailing edge of the suction side. This affects the heat transfer rate on the suction side considerably. Figure 6.71 indicates this variation clearly.

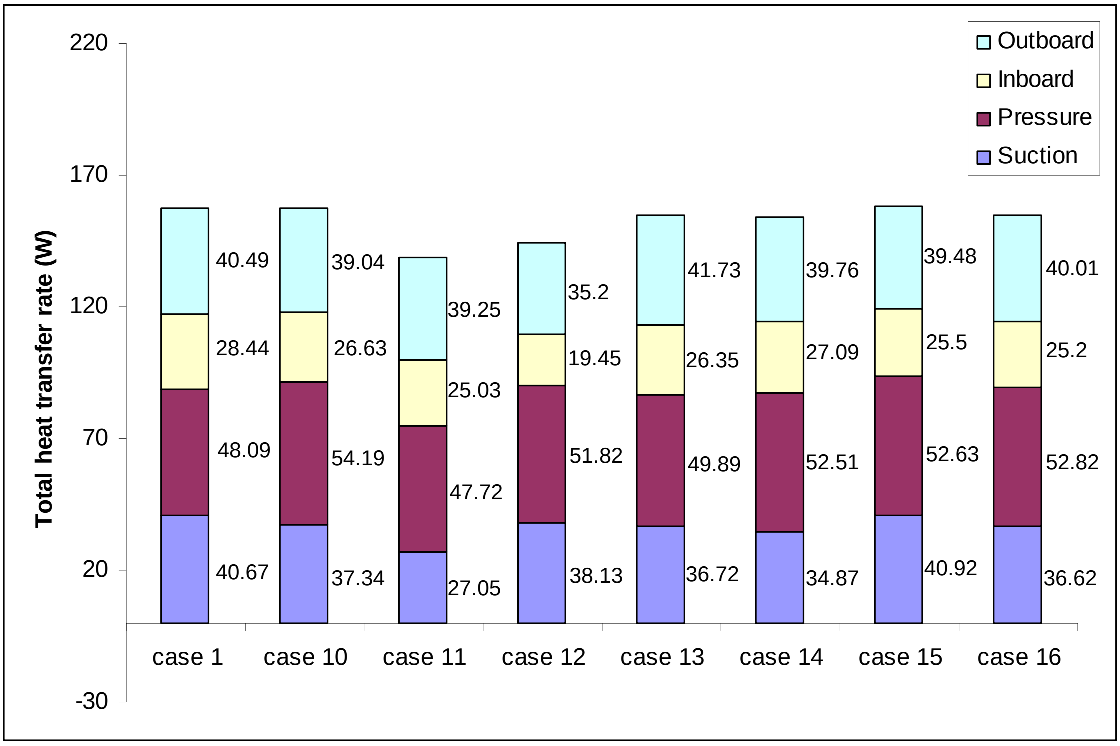

Fig 6.70: Contribution of internal surfaces heat transfer rate to the total heat transfer rate

The temperature uniformity was calculated for the iteration 2 using thermal distortion index (T.D.I). It was observed that due to increase in the outlet angle from 40^0 to 50^0 the T.D.I reduces and then increases for increase in outlet angle further. The increase in inlet angle reduces the T.D.I. So the temperature uniformity is better at lower outlet angles and higher inlet angles for iteration 2 (fig 6.72 and 6.73).

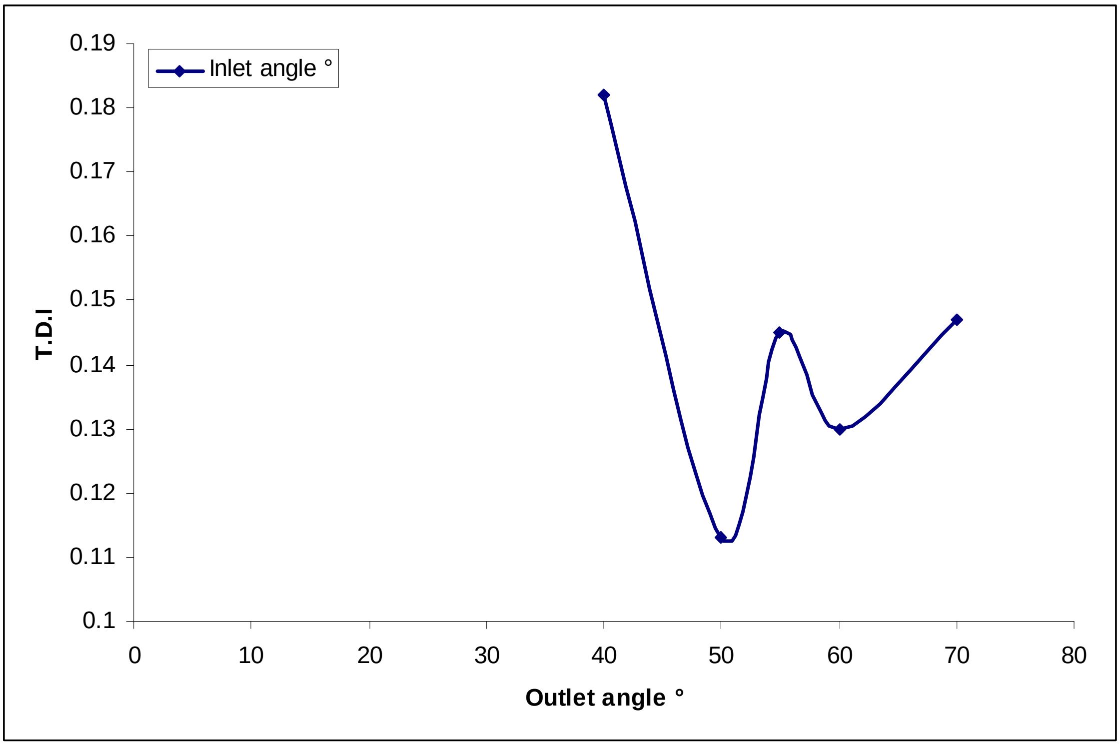

Fig 6.72: Variation of temperature distortion index with outlet angle

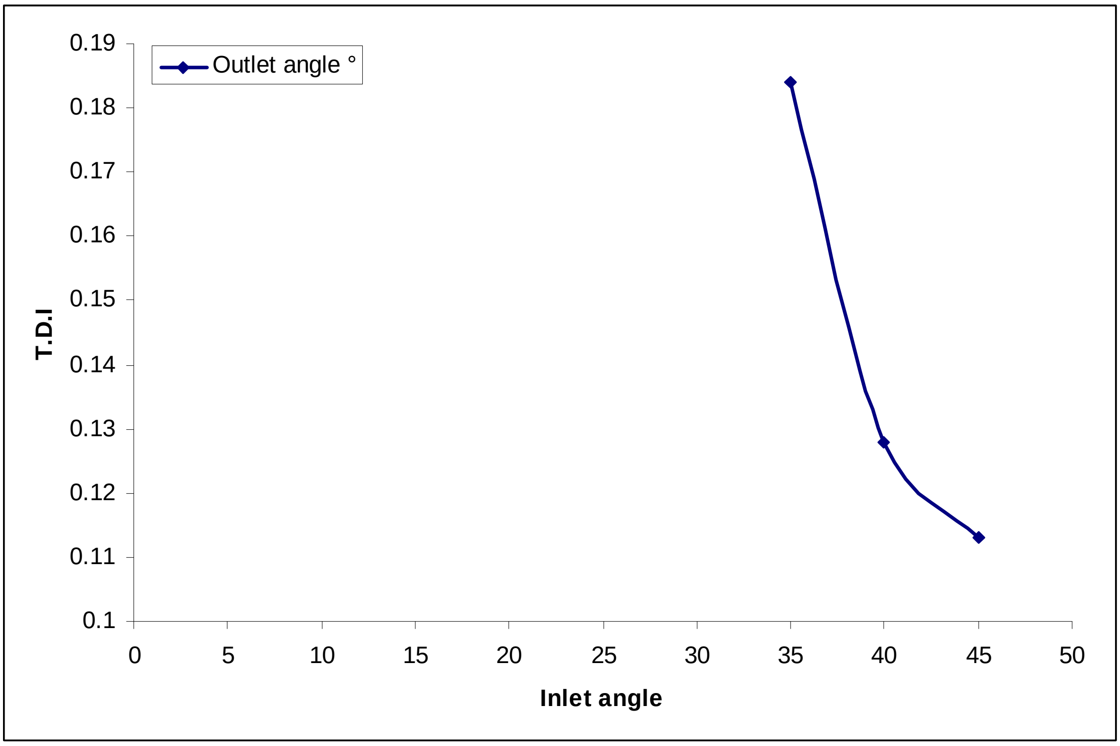

Fig 6.73: Variation of temperature distortion index with inlet angle

6.5. Summary

After the analysis of the blade angles was performed, the following conclusions were drawn.

- The blade angles (inlet and outlet) have an effect of the aero-thermal performance of a ventilated disc brake.

- The effect of outlet angle is more profound in this regard and at outlet angles more than 55^0 the aero-thermal performance of the disc brake decreases.

- At inlet angles higher than 45^0 the aero-thermal performance of a ventilated disc brake decreases.

- Case 15 design rotor was identified to the best performance design with mass flow rate increase of 49.67% and total heat transfer rate increase of 31.87% when compared to the datum rotor.

- The case 15 has to be simulated at different temperatures and speeds to order to understand the complete aero-thermal performance of the disc brake rotor at all braking conditions.

- The case 15 has the problem of diffusion on the suction side of the passage, so by inclusion of variable thickness blade the area change from inlet to outlet reduces thereby controlling the amount of diffusion. The effect of which will be studied in the following chapters.

6.6. Effect of speed of rotation

In order to analyse the aero-thermal performance of the ventilated disc brake at various different driving speeds of the vehicle, the simulations were carried out at 3 different rotational speeds of 750 rpm, 1500 rpm and 2250 rpm. The analysis was performed for the case 15 rotor. This particular rotor was chosen based on the parametric analysis performed on blade angles. All the simulations were carried out at a temperature of 800 K.

6.6.1. Aero-thermal flow analysis

It is known that for different rotational speeds the average velocity at the outlet changes. While performing the simulations the same grid has been used for all the rotational speeds. The near wall grid density must be changed to cater for the change in Reynolds number. This is important so as to meet the requirements of the turbulent model being used. However, the change in Reynolds number is not large and for all the cases is within the same order of magnitude. Because of this the variation in the y+ value at the walls is not large. It has been that with increase in the rotational speed the mass flow rate through the passage increases (table 6.4).

Speed of rotation rpm	Average exit velocity m/sec	Mass flow rate kg/sec
750	8.71	0.1187
1500	16.602	0.2472
2250	24.9	0.3689

Table 6.4: Case 15 rotor as a function rotor speed

It can be seen from figure 6.74 that a linear proportionality is achieved for the variation of mass flow rate with rotor speed. The increase in the mass flow rate is mainly due to the increase in the exit velocity. As the speed of rotation increases the diffusion on the trailing edge of the suction side reduces. This is again due to higher energy in the flow which can overcome the adverse pressure gradient due to change in area from inlet to outlet (fig 6.74). This is very useful as diffusion creates regions of low heat transfer thereby causing hot spot formation.

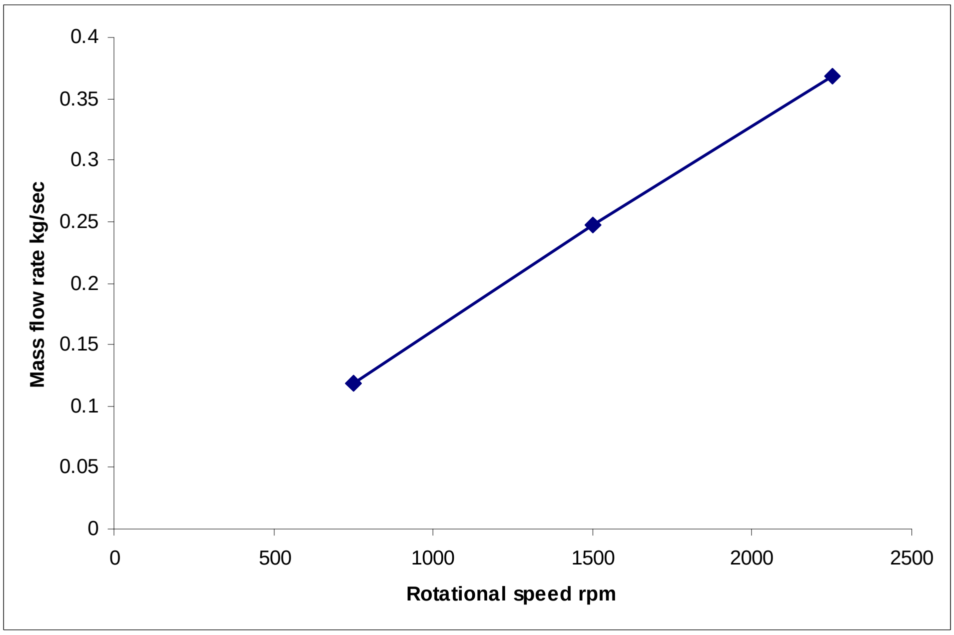

Fig 6.74: Mass flow rate (kg/sec) as a function of rotor speed

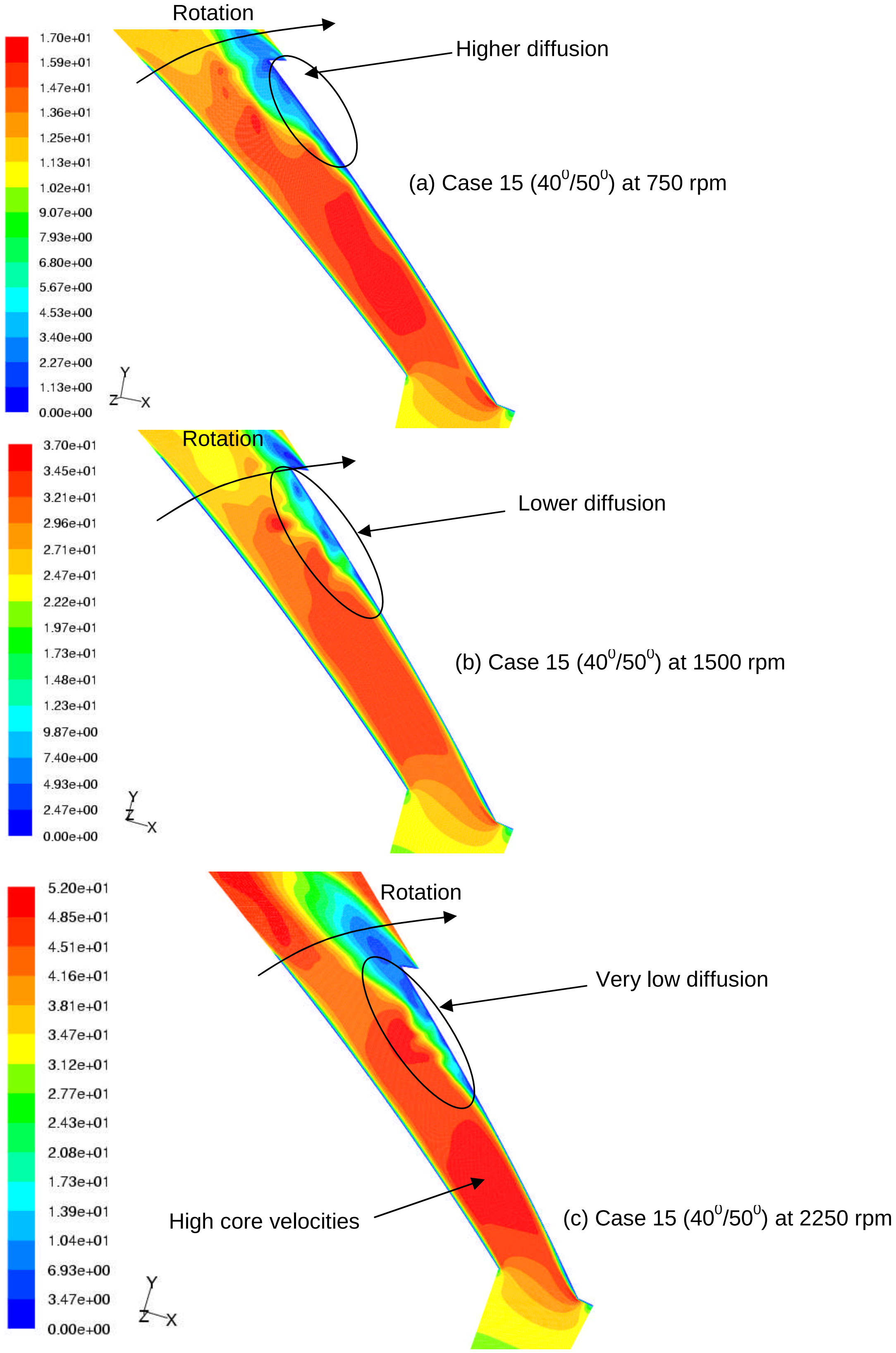

(a) Case 15 ($40^0/50^0$) at 750 rpm

(b) Case 15 ($40^0/50^0$) at 1500 rpm

(c) Case 15 ($40^0/50^0$) at 2250 rpm

Fig 6.75: Relative velocity at the mid-passage height of the passage for case 15 at different rotational speeds

It has also been observed that the total heat transfer rate through the passage also increases with increase in the blade speed. This is mainly due to the increase in the mass flow rate through the passage. But the variation of total heat transfer rate is not linear (fig 6.76). It indicates that the change is not just due to increase in the mass flow rate but also due to change in the flow aerodynamics at higher rotational speeds. This can be better understood by observing the Nusselt number distribution on each of the internal surfaces at various speeds. The suction side heat transfer is affected by inlet separation due to flow direction change from tangential to radial, axial to radial and also due to the diffusion on the trailing edge. From figure 6.77 it can be observed that with increase in speed the diffusion on the trailing edge is reduced thereby improving the heat transfer rate. But the inlet separation increases with increase in the speed thereby affecting the rate of heat transfer from the suction side of the passage. The reader should keep in mind that the scales of measurement are different for different speeds.

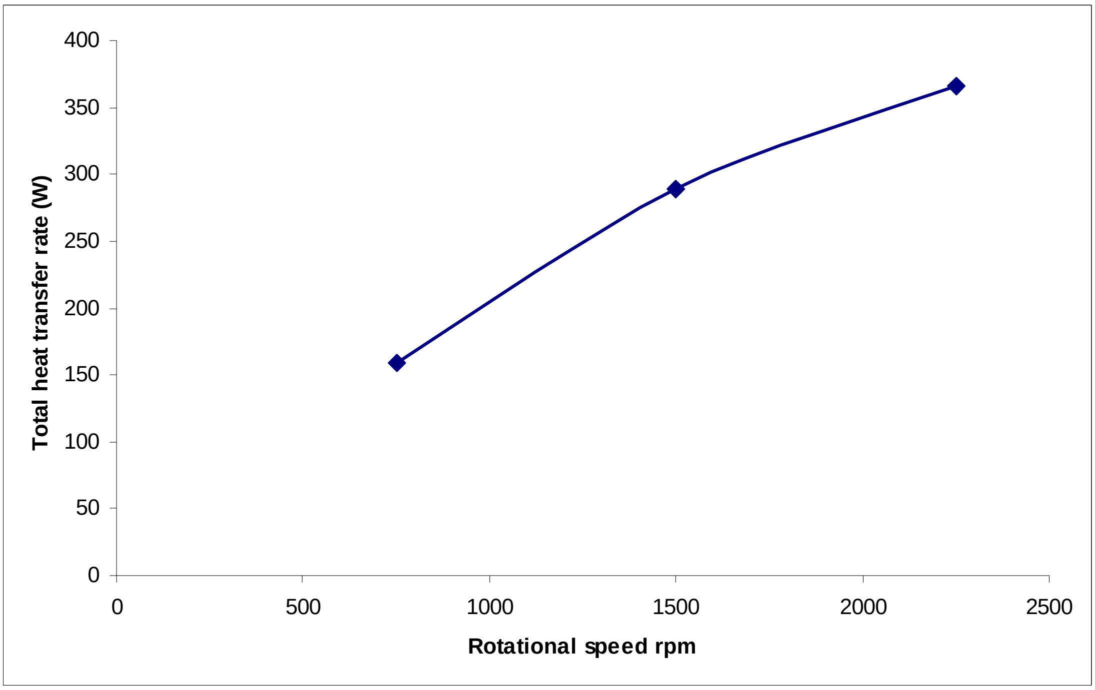

Fig 6.76: Total heat transfer rate (W) as a function of rotor speed

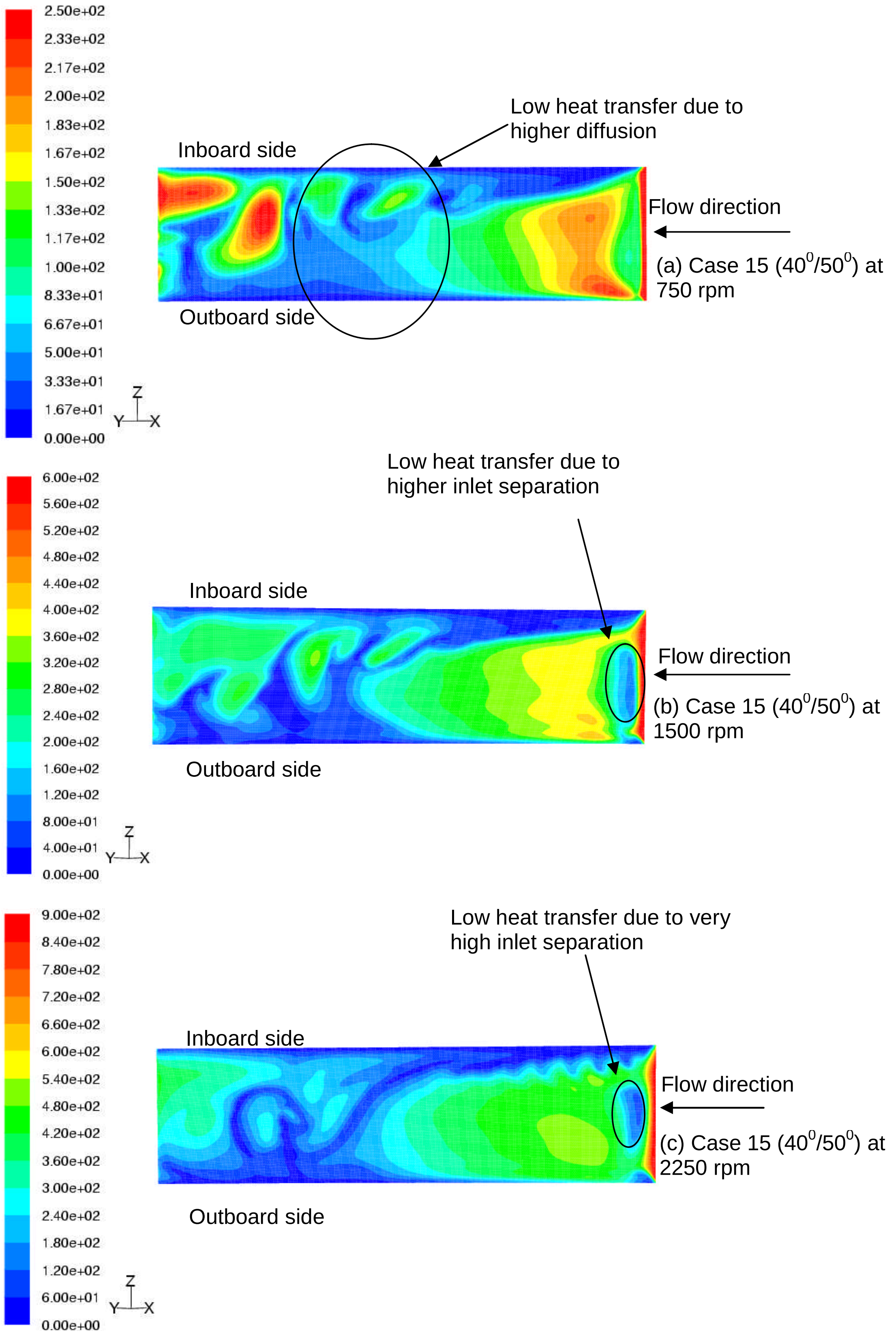

(a) Case 15 ($40^0/50^0$) at 750 rpm

(b) Case 15 ($40^0/50^0$) at 1500 rpm

(c) Case 15 ($40^0/50^0$) at 2250 rpm

Fig 6.77: Suction side Nusselt number distribution at different rotational speeds

The pressure surface heat transfer distribution uniformity improves with the increase in the rotational speed (fig 6.78). This is due to highly accelerated flow towards the pressure side of the passage. Due to the marginal increase in the inlet separation with rotational speed the flow is accelerated more towards the pressure side at higher speeds thereby improving the heat transfer. The inboard side of the passage is affected by the flow separation at the inlet. This reduces the heat transfer at all different speeds. The heat transfer distribution on the outboard is also similar at higher speeds. This is due to high fluid velocities associated on the outboard surface due to flow impingement

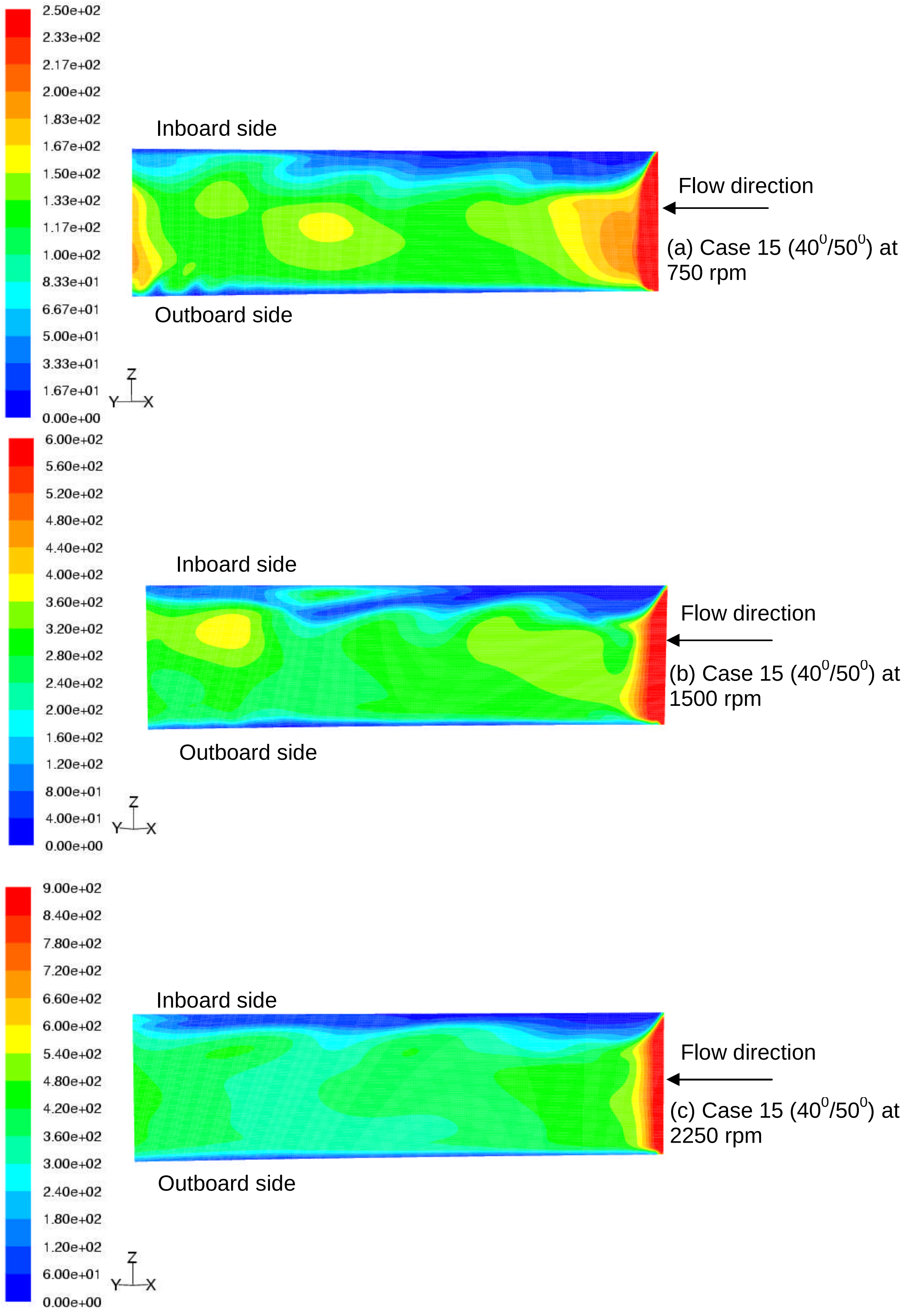

(a) Case 15 ($40^0/50^0$) at 750 rpm

(b) Case 15 ($40^0/50^0$) at 1500 rpm

(c) Case 15 ($40^0/50^0$) at 2250 rpm

Fig 6.78: Pressure side Nusselt number distribution at different rotational speeds

6.6.2. Temperature uniformity

The temperature uniformity improves with increase in the rotor speed. As explained in section 6.6.1 with increase in speed the suction side heat transfer rate improves due to lower diffusion. The temperature uniformity can be better understood from the variation of thermal distortion index with rotor speed. The variation also shows the expected trend. The T.D.I decreases with increase in speed indicating better temperature uniformity (fig 6.79).

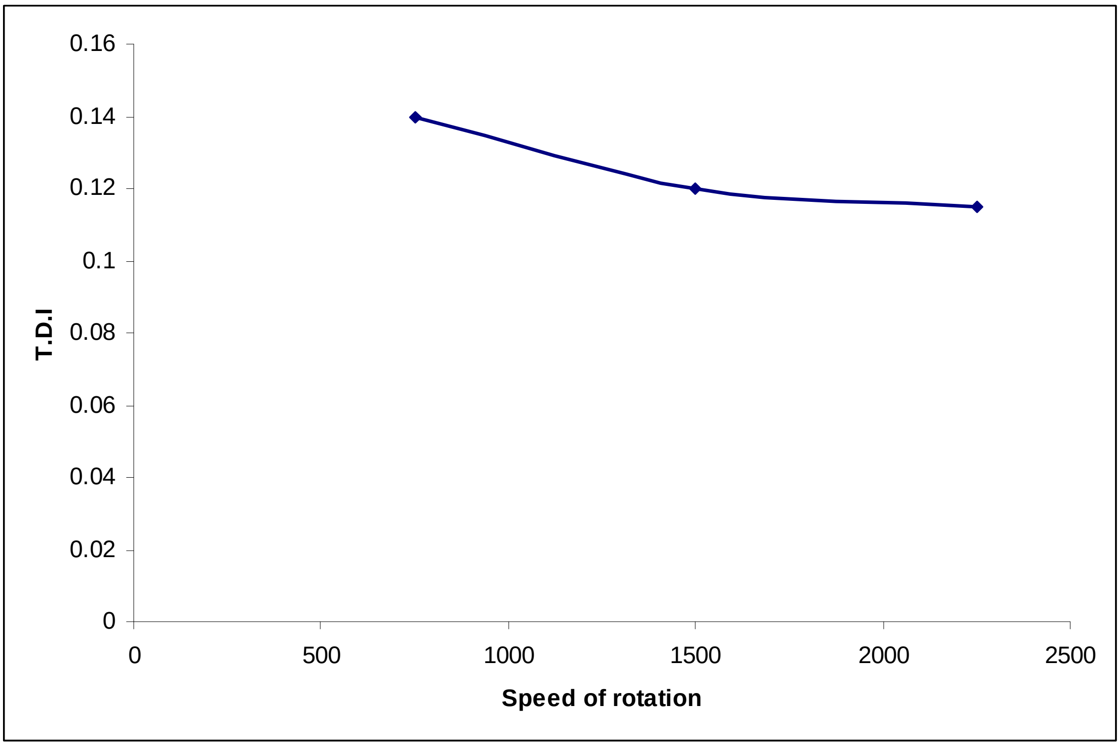

Fig 6.79: Variation of thermal distortion index with rotor speed

6.7. Effect of rotor temperature

In order to analyse the aero-thermal performance of the ventilated disc brake at various braking conditions, the simulations were carried out at 3 different temperatures of the rotor of 500 K, 800 K and 1100 K. The analysis was performed for the case 15 rotor. This particular rotor was chosen based on the parametric analysis performed on blade angles. All the simulations were carried out at a speed of 1500 rpm.

6.7.1. Aero-thermal flow analysis

It has been observed from the simulations that the mass flow rate through the rotor decreases with increase in the temperature. This variation is non-linear (fig 6.80). This drop in the mass flow rate is mainly due to decrease in the air density. But the drop in the mass flow rate is not entirely dependent on the decrease in the density. The decrease in the density decreases the Reynolds number of the flow thus leading to higher viscous forces. This increases the inlet separation that occurs near the inboard and the suction surfaces of the passage (fig 6.81). There is also increased diffusion on the suction side of the passage due to increase in the temperature. This is also due to increased viscous forces that the fluid has to overcome at the suction surface trailing edge.

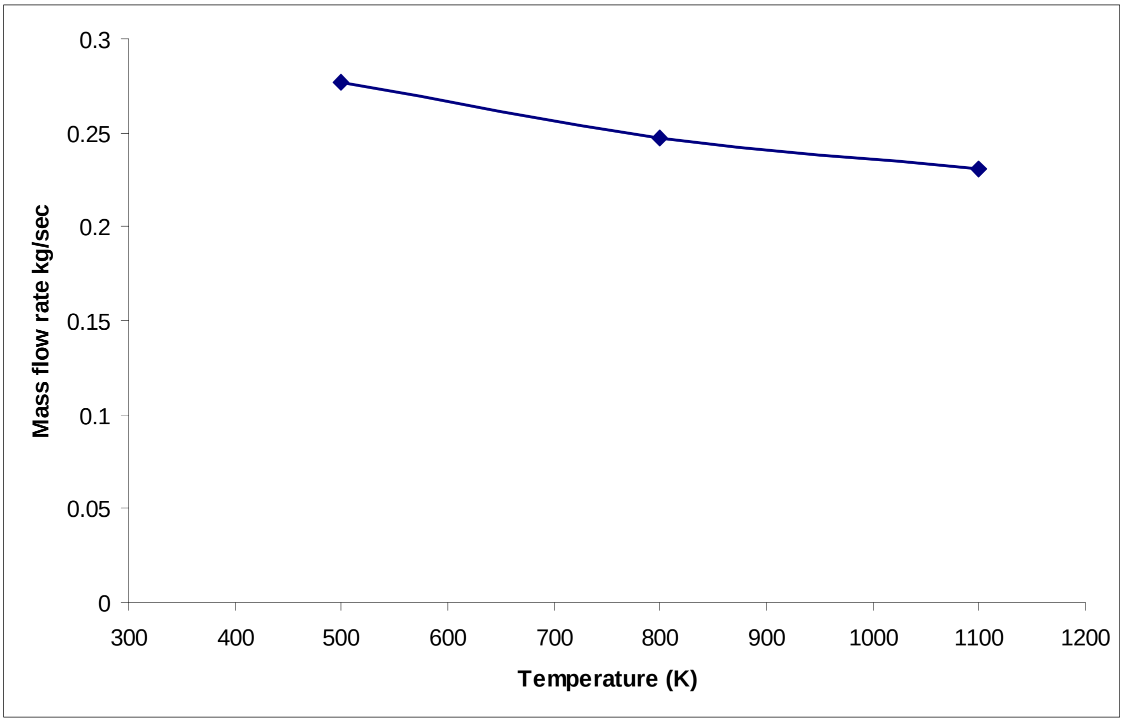

Fig 6.80: Mass flow rate as a function of rotor temperature

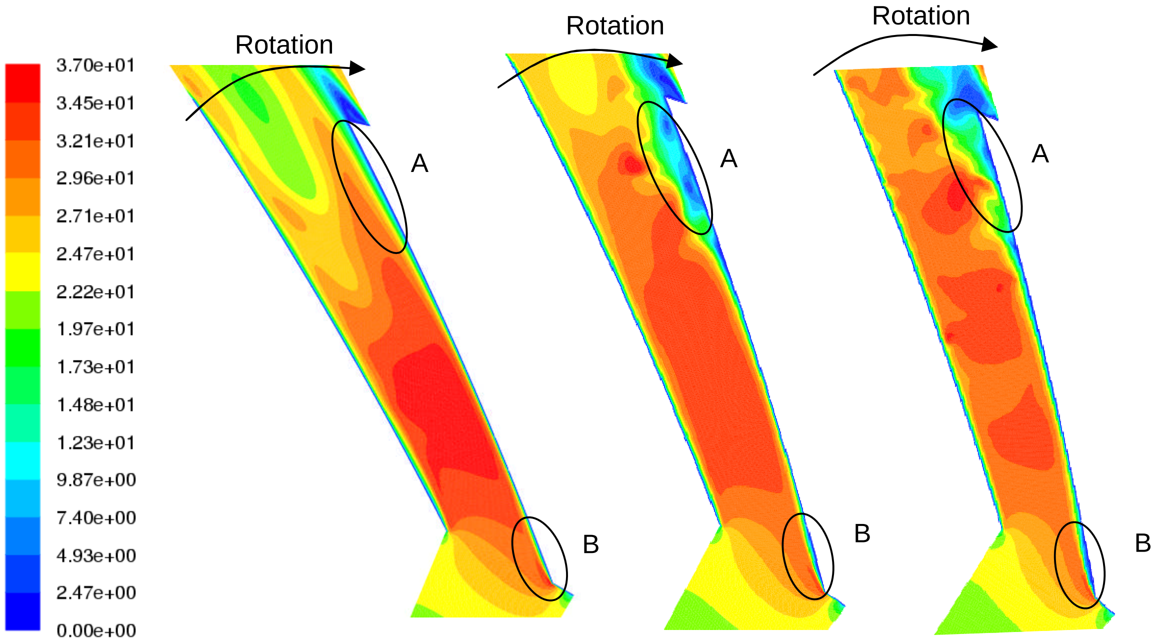

A: Increase in diffusion with temperature

B: Increase in inlet separation with temperature

Case 15 @ 500 K Case 15 @ 800 K Case 15 @ 1100 K

Fig 6.81: Relative velocity (m/sec) at mid-passage height of the passage

The total heat transfer rate increases with temperature (fig 6.82). This is due to a higher wall temperature. More than the absolute/total heat transfer rate, the important aspect is the heat transfer distribution. On the suction side of the passage at low temperature (500 K) the heat transfer rate is more uniform due to lower diffusion. The regions of low heat transfer increase on the suction side trailing edge as the temperature increases. Thus it can be understood that at higher temperatures the formation of hot spots is higher on the suction side of the passage (fig 6.83). The pressure surface also follows the same trend. The inboard separation increases on the pressure surface with temperature thereby creating regions of low heat transfer rate (fig 6.84). This inboard separation creates a large region of low heat transfer on the inboard surface of the rotor at 1100 K (fig 6.85). The outboard surface on the other hand is affected by the diffusion of the suction side. This created regions on low heat transfer on the outboard surface (fig 6.86).

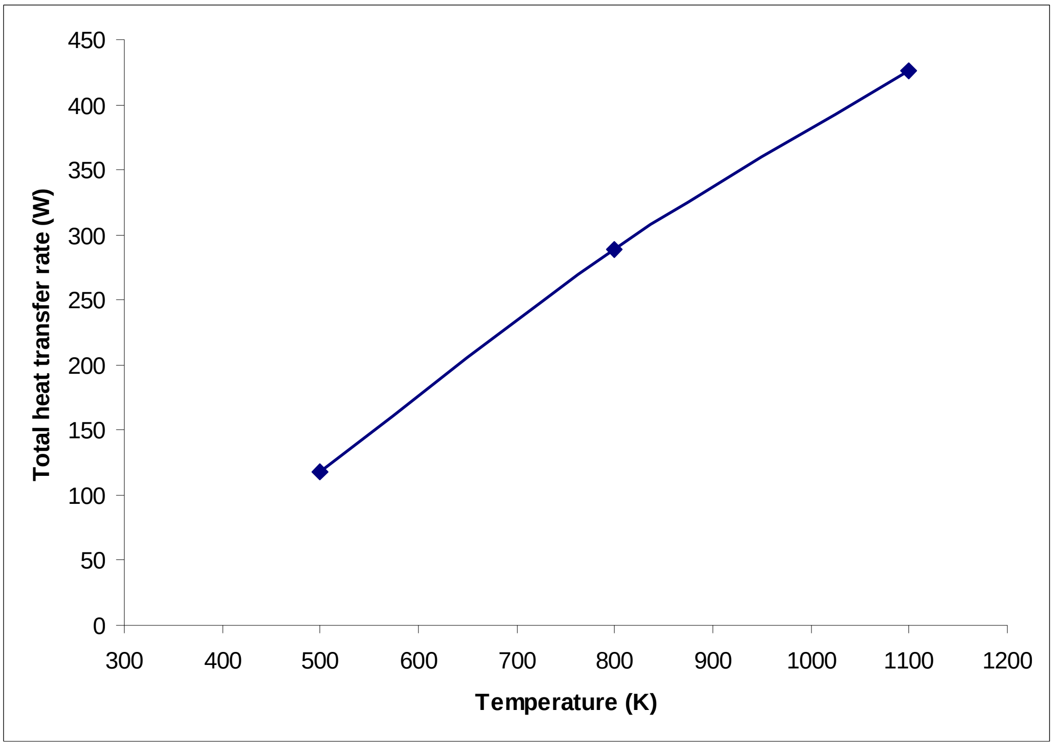

Fig 6.82: Total heat transfer rate (W) as a function of rotor temperature

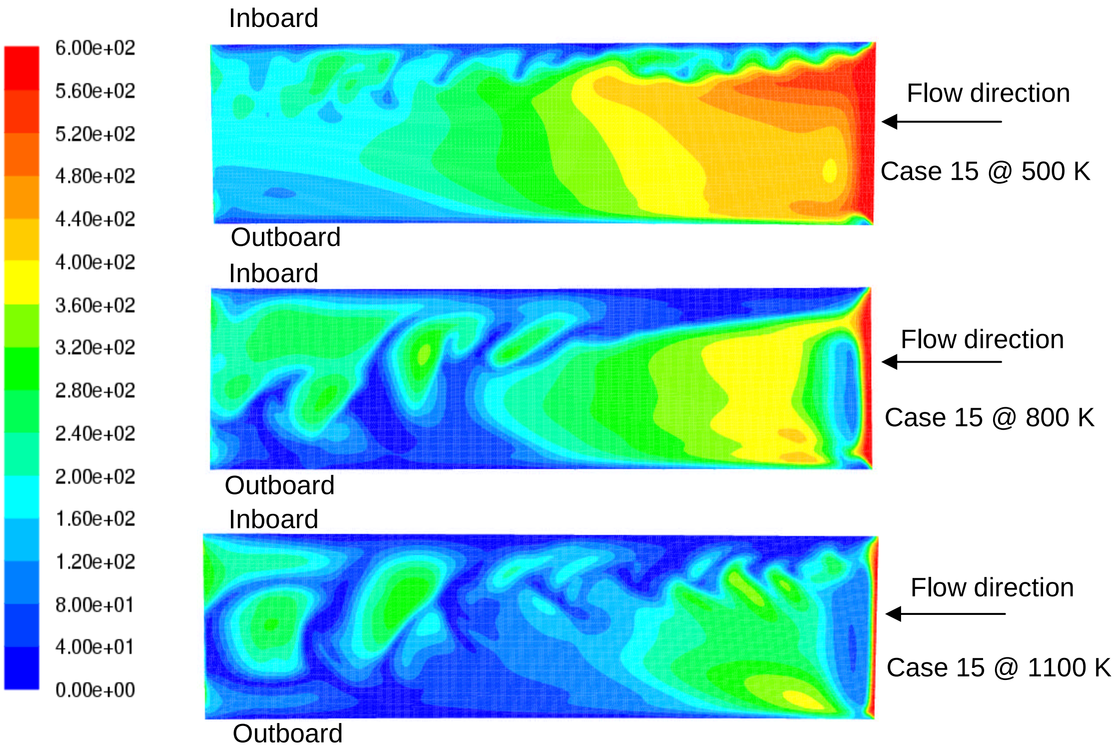

Fig 6.83: Suction surface Nusselt number distribution

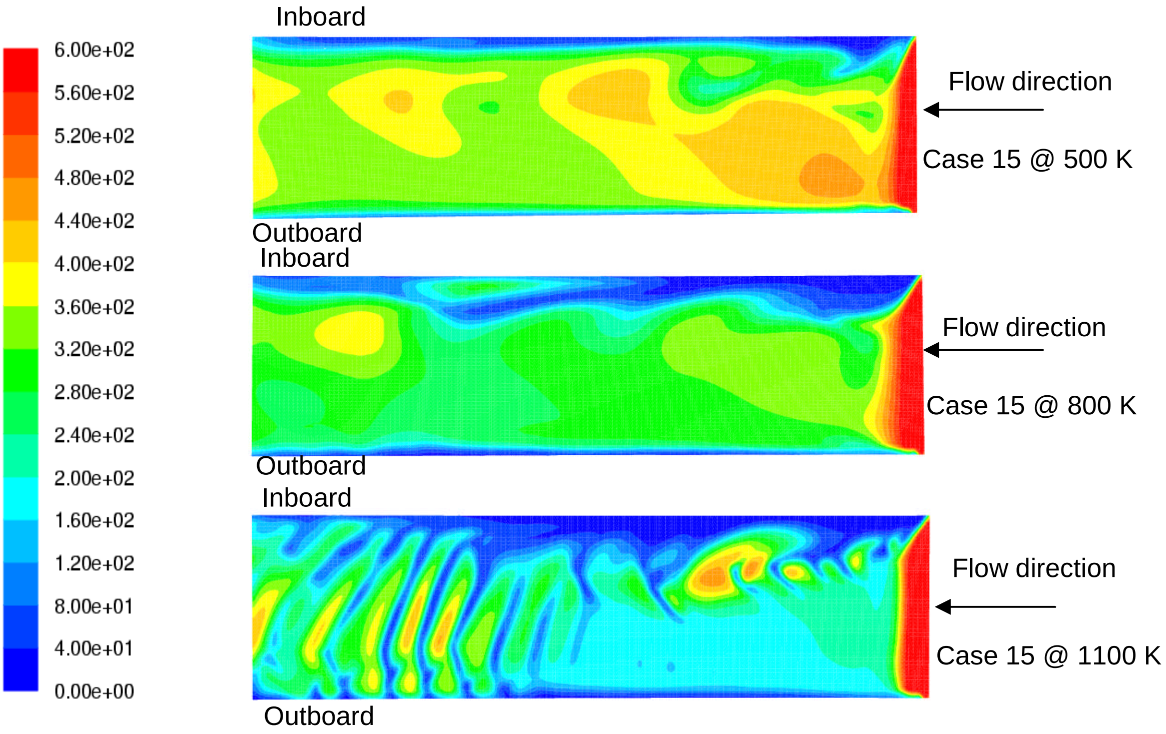

Fig 6.84: Pressure surface Nusselt number distribution

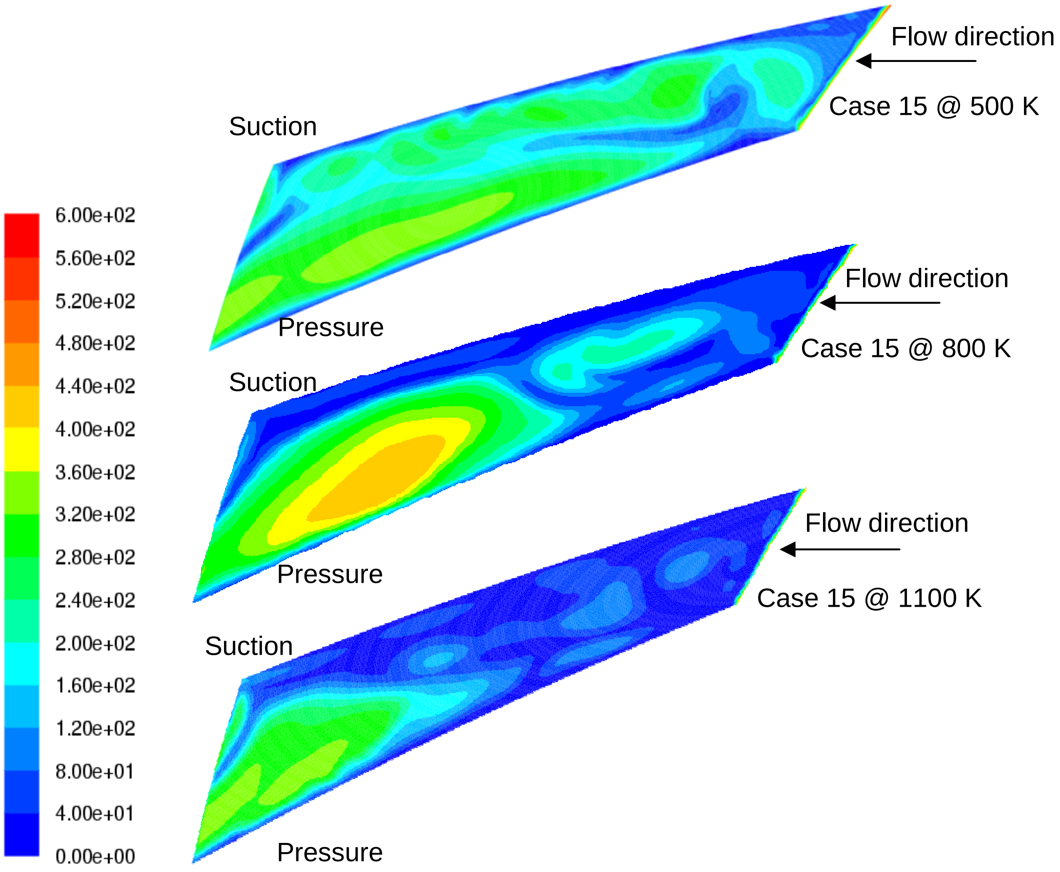

Fig 6.85: Inboard surface Nusselt number distribution

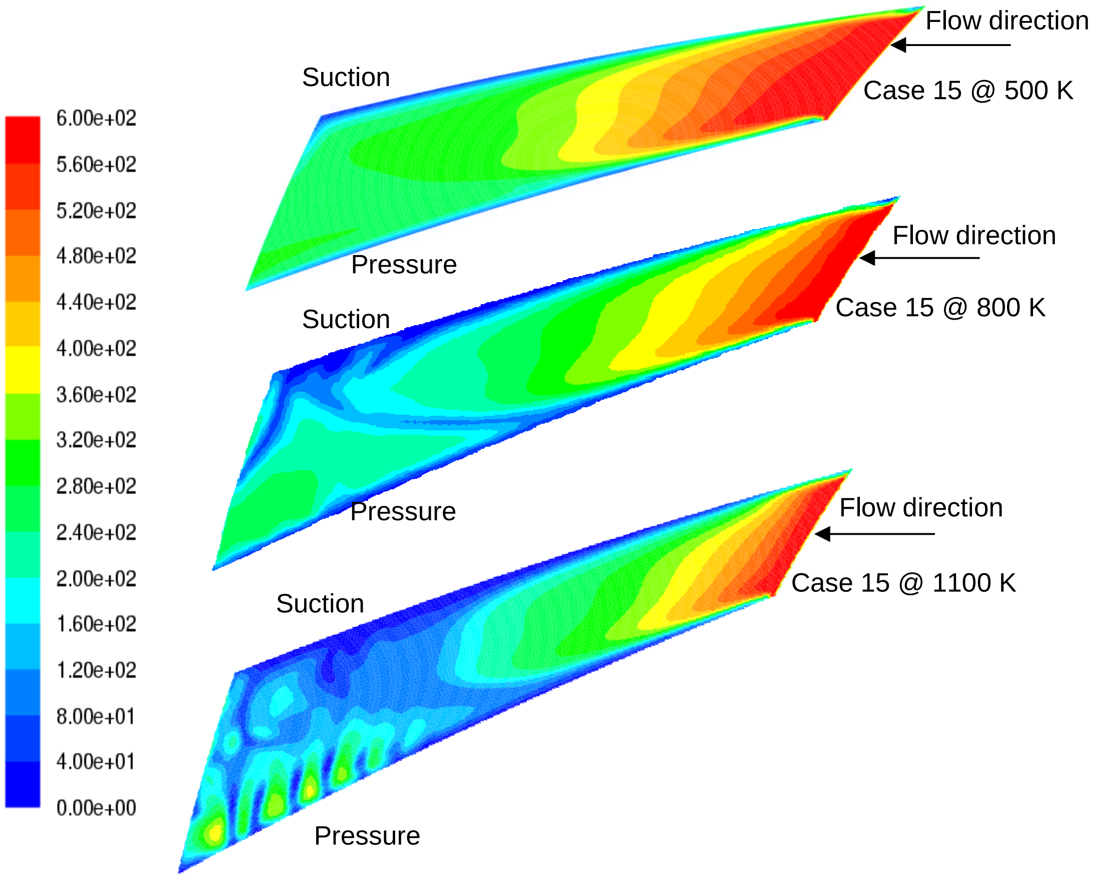

Fig 6.86: Outboard surface Nusselt number distribution

From this analysis it can be understood that with increase in temperature even though the total heat transfer rate is increasing, the aero-thermal performance of the ventilated disc brake rotor decreases. The main reason for this is the drop in the density of air which increases the viscous losses adversely affecting the performance.

6.7.2. Temperature uniformity

The amount of diffusion and the regions of separation increase with increase in temperature due to decrease in density. The suction side and inboard side of the passage are the worst affected regions in the rotor. As expected the thermal distortion index increases with increase in temperature indicating the increase in the non-uniformity of temperature (fig 6.87). Therefore, the formation of hot spots increases with temperature.

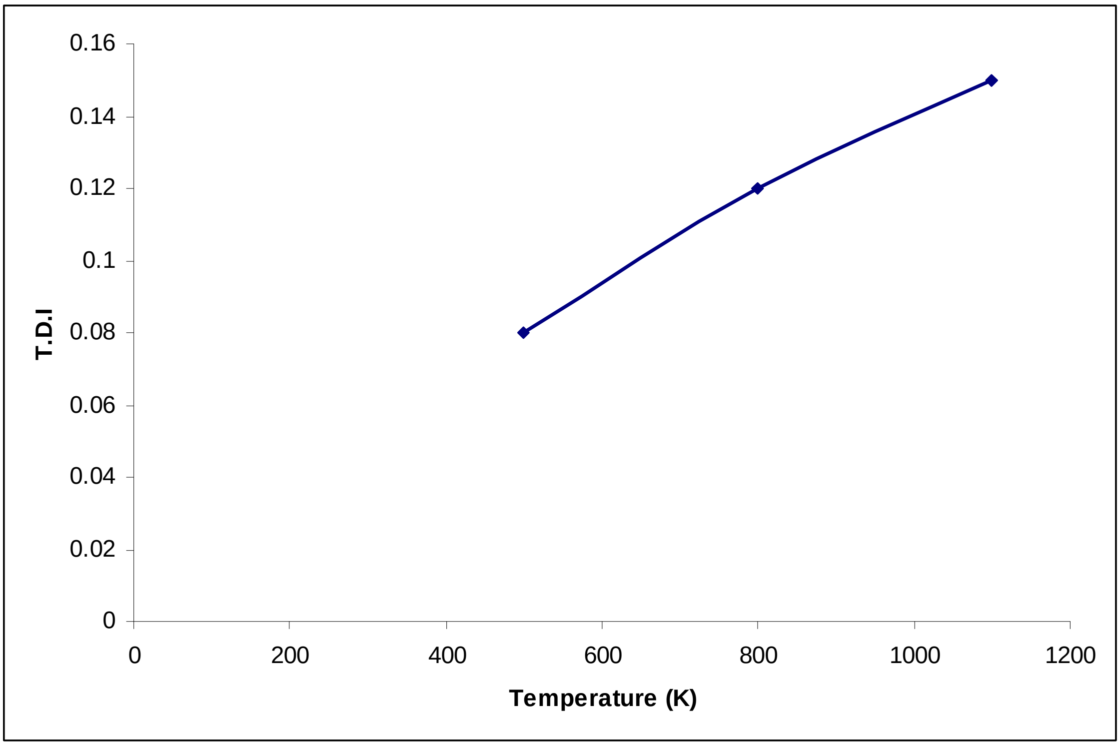

Fig 6.87: Thermal distortion index variation with temperature

7

Detailed design changes and analysis

In this chapter the results from the detailed design analysis will be presented. The aero-thermal performance of the ventilated disc brake by the inclusion of lips and chamfers will be discussed in detail in the first part of the chapter. The effect of blade rounding on the performance will be presented. The performance of the disc brake rotor by the inclusion of variable thickness blade will be studied. Also, the effect of different aspect ratio and number of blades on the performance of disc brake will be analysed.

7.1. Introduction

From the parametric analysis results it can be seen that the regions that hinder the heat dissipation in case 15 rotor design are the inboard side and the suction side of the passage. This mainly due to the regions of recirculation created by the flow direction change which affect heat transfer on both suction and inboard sides by creating hot spots. Also diffusion that occurs on the suction side further affects heat transfer. In order to reduce effect of these regions on the disc brake performance, detailed design changes were made to the case 15 rotor. The effect of each of these design changes on the performance will be discussed in the following chapters.

7.2. Effect of lips and chamfer

In order to reduce the flow separation that occurs on the inboard side of the rotor passage due to flow direction change from axial to radial, the inboard side of the rotor was chamfered. The chamfer acts as a flow guiding mechanism by directing the flow into the rotor (fig 7.1). This design change was incorporated to the case 15 rotor which was the best performance rotor after the parametric studied were carried out. So as to perform the analysis closer to the existing designs, lips were also included.

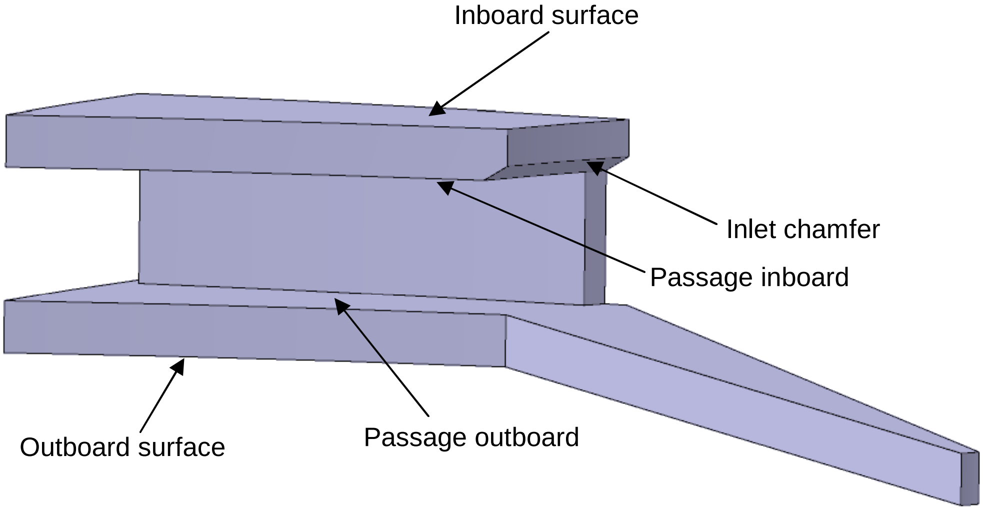

Fig 7.1: Case 15 rotor with inlet chamfer

The simulation was performed at 1500 rpm and 800 K as these are the conditions encountered during normal braking operation.

7.2.1. Aero-thermal flow analysis

It has been observed that the inclusion of lips and chamfer does have an influence on the mass flow rate through the passage. There is an improvement in the mass flow rate through the passage by 30% (table 7.1).

Type of rotor	Mass flow rate kg/sec
Case 15 without lips	0.247
Case 15 with lips and chamfer	0.321

Table 7.1: Mass flow rate for case 15

The higher mass flow rate is mainly due to the cut back of the blades which produce the lips. This increases the area available for the entry of air into the passage thereby increasing the mass flow rate through the passage (fig 7.2 and 7.3). The inclusion of chamfer has a distinct advantage. As expected the fluid is being guided into the rotor passage. This reduces the inlet separation on the inboard side which otherwise would have occurred due to change in direction from axial to radial upon entry into the rotor (fig 7.4). The flow on the suction side of the passage is accelerated upon entering the passage as it gets redirected towards the suction due to the presence of the chamfer. This accelerated flow also helps in reducing the diffusion that occurs at the trailing edge of the suction side. But the disadvantage of this is that the flow diffuses at the trailing edge of the pressure side due to the decelerated flow (fig 7.5).

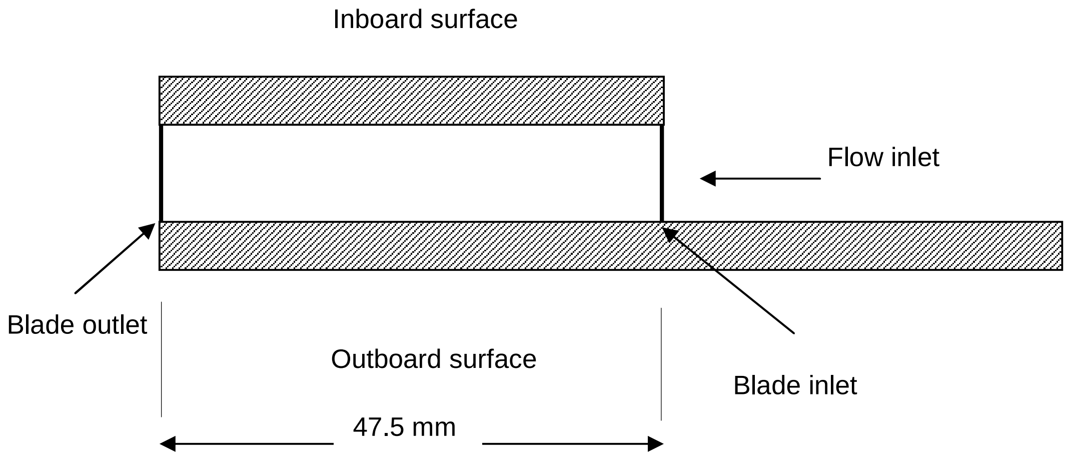

Fig 7.2: Rotor without lips

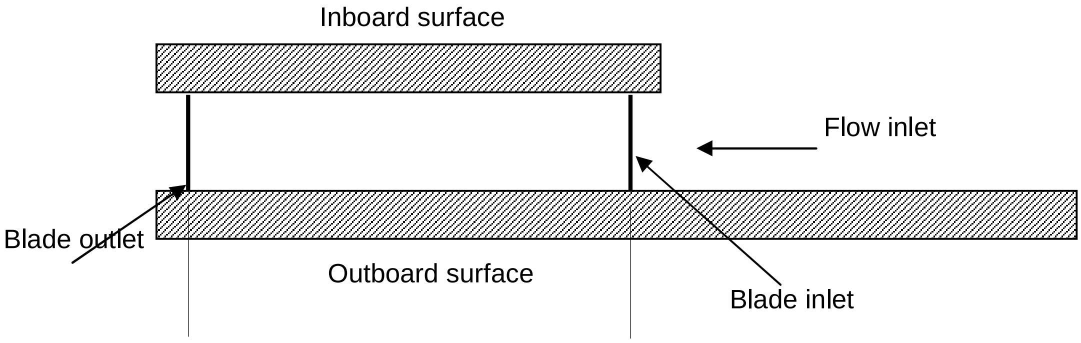

Fig 7.3: Rotor with lips

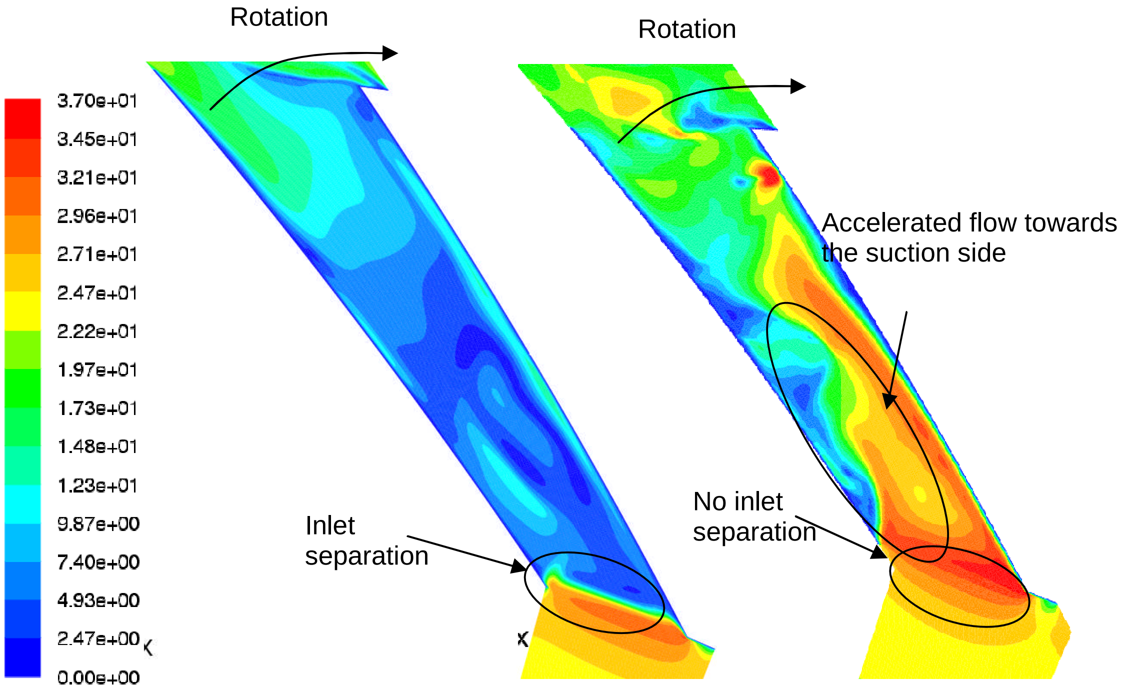

(a) Case 15 no lips

(b)Case 15 lips and chamfer

Fig 7.4: Relative velocity 1 mm below the passage inboard surface

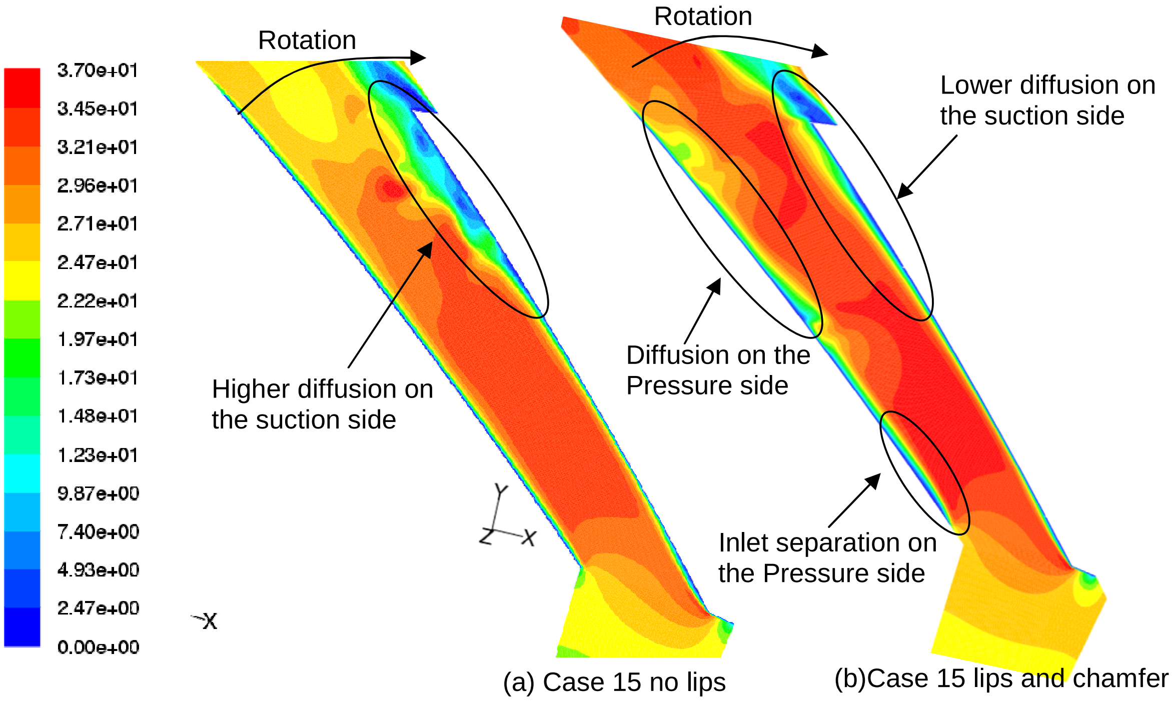

Fig 7.5: Relative velocity at mid-passage height of the passage

The reader should also keep in mind that there is a reduction in the total area available for heat transfer due to cut back of the blades. In spite of this decrease in surface area, the total heat transfer rate from the internal passages of the rotor with lips and chamfer is good (table 7.2).

Type of rotor	Total heat transfer rate W
Case 15 without lips	288.81
Case 15 with lips and chamfer	285.50

Table 7.2: Total heat transfer rate for case 15

As explained earlier the reduction in the inlet separation due to flow direction change increases the heat transfer from the suction side (fig 7.6). Due to this the heat transfer rate from the suction (78.45 W) is a marginally better when compared the conventional case 15 rotor (76.78 W). The pressure side is the worst affected region by the inclusion of chamfer. The diffusion and the increased inlet separation that occur on the pressure side of the passage affects the heat transfer drastically (fig 7.7). Due to this the heat transfer rate from the pressure of the rotor with lips and chamfer (78.77 W) is less than the conventional case 15 rotor (98.88 W). The temperature gradient between the pressure and suction side due to heat transfer from each of the surfaces is negligible in case of the case 15 rotor with lips and chamfer.

`

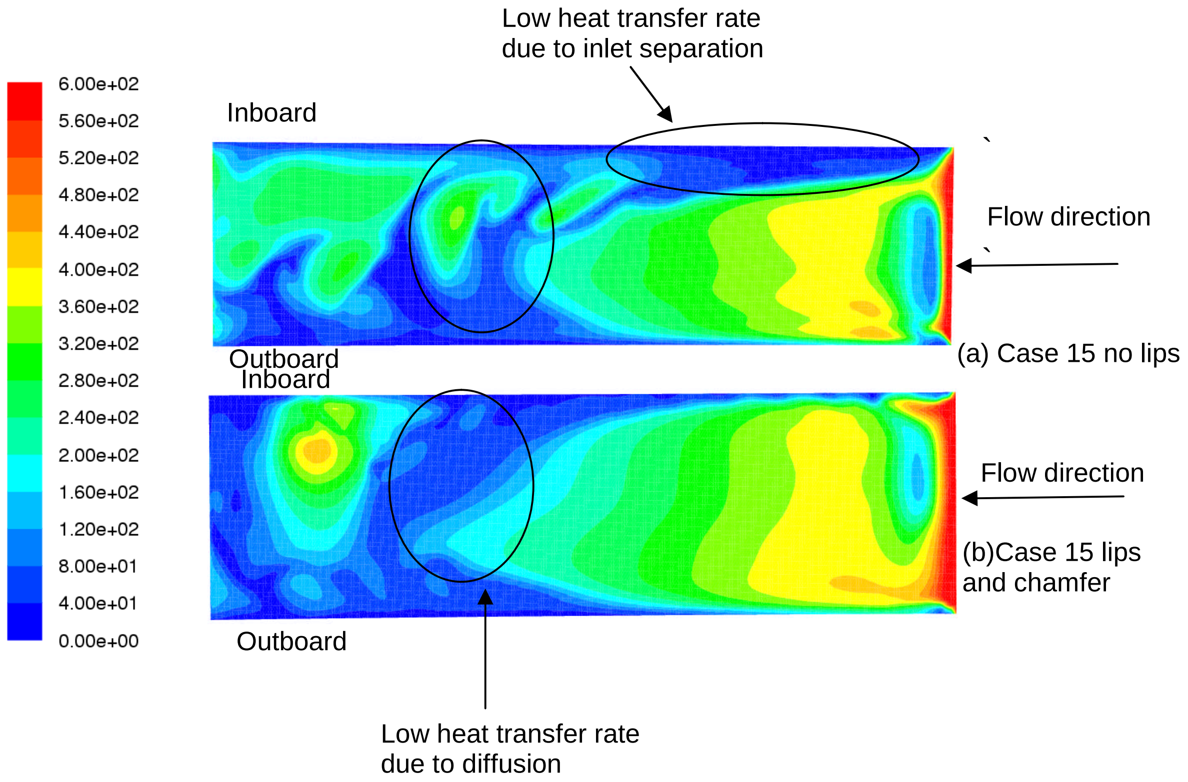

d

Fig 7.6: Suction surface Nusselt number distribution

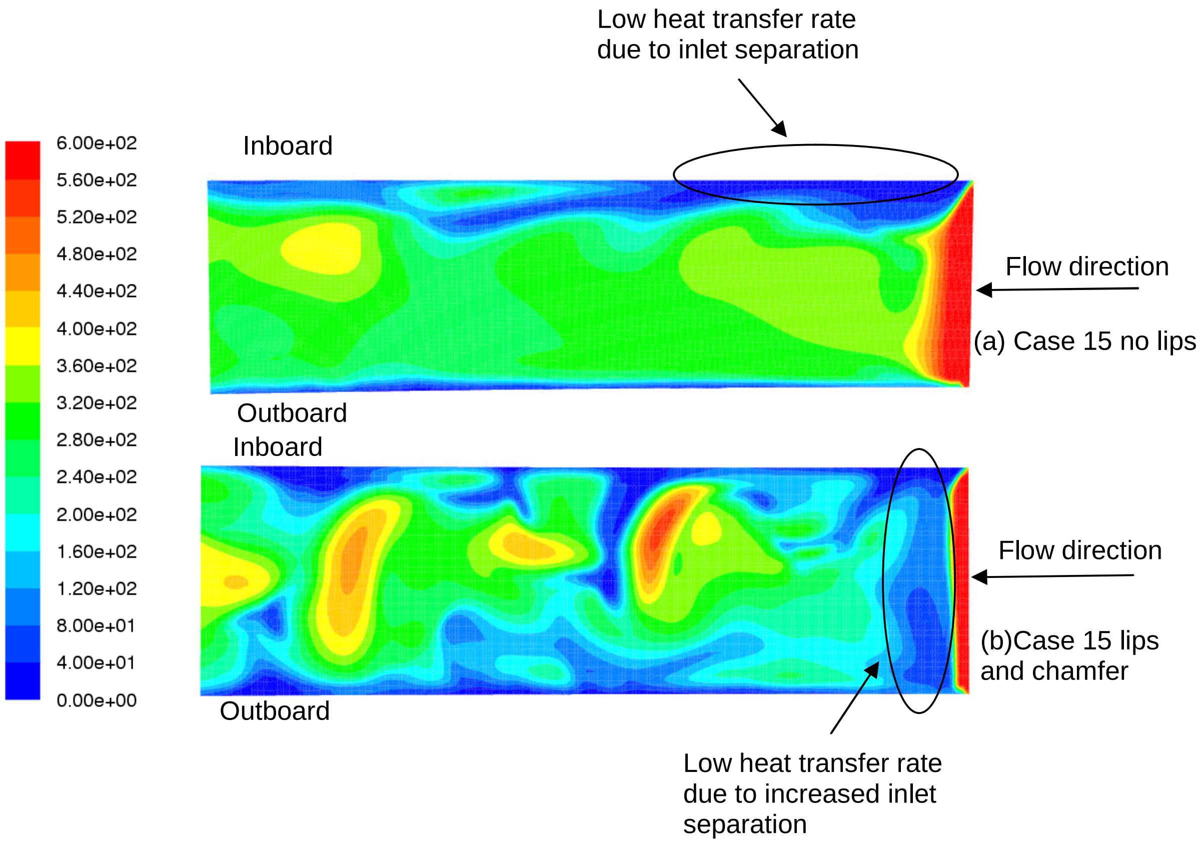

Fig 7.7: Pressure surface Nusselt number distribution

There is an improvement in the heat transfer rate from the inboard surface of the case 15 rotor by inclusion of lips and chamfer. The inlet separation due to change in flow direction from axial to radial and also tangential to radial generally affects the heat transfer rate from the inboard surface. By the inclusion of chamfer as explained earlier the inlet separation zones are reduced thereby improving the heat transfer rate by 10% (fig 7.8). The heat transfer from the inboard surface of the conventional case 15 rotor is 47.65 W as compared to 52.33 W from the improved case 15 with lips and chamfer.

The passage outboard surface also shows some improvement in heat transfer rate due to the inclusion of chamfer and lips. The heat transfer from the modified case 15 rotor outboard surface is far more uniform than that of the conventional design (fig 7.9). The areas of concern though are the trailing edges on the suction and pressure side due to diffusion of flow. Due to this the heat transfer from the outboard surface of the modified rotor is 69.38 W as compared to 65.48 W for the conventional case 15 rotor.

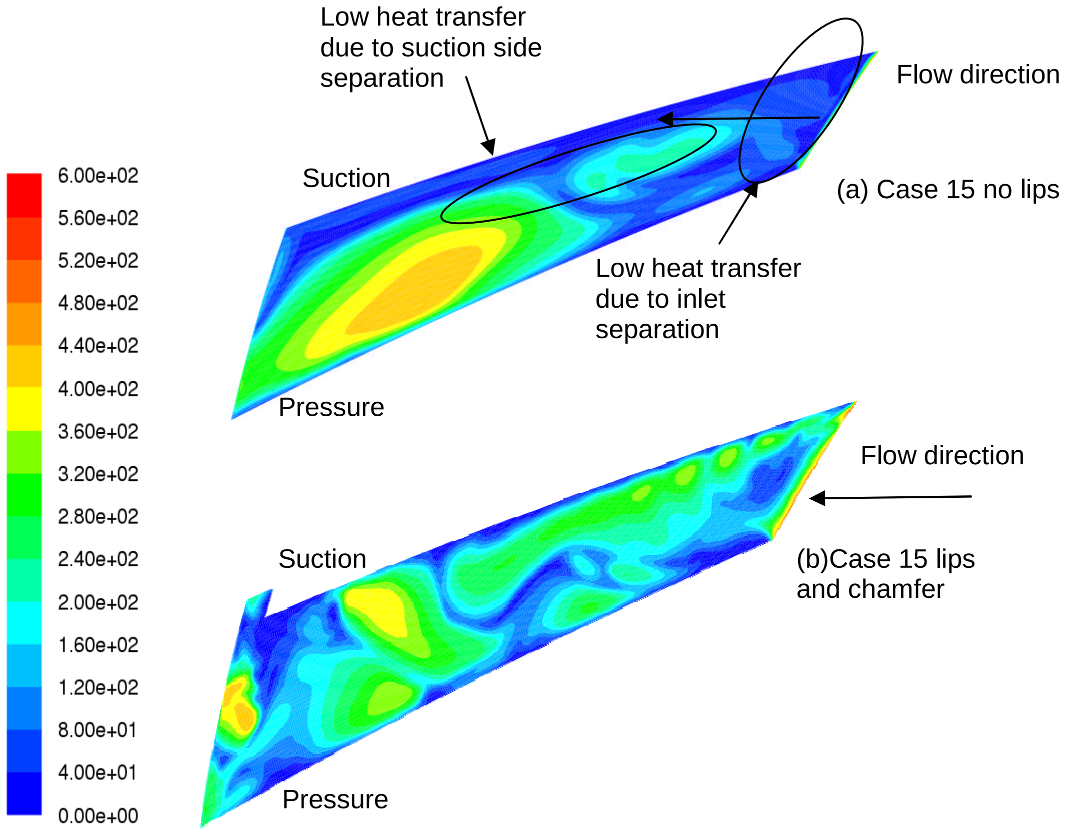

Fig 7.8: Passage inboard surface Nusselt number distribution

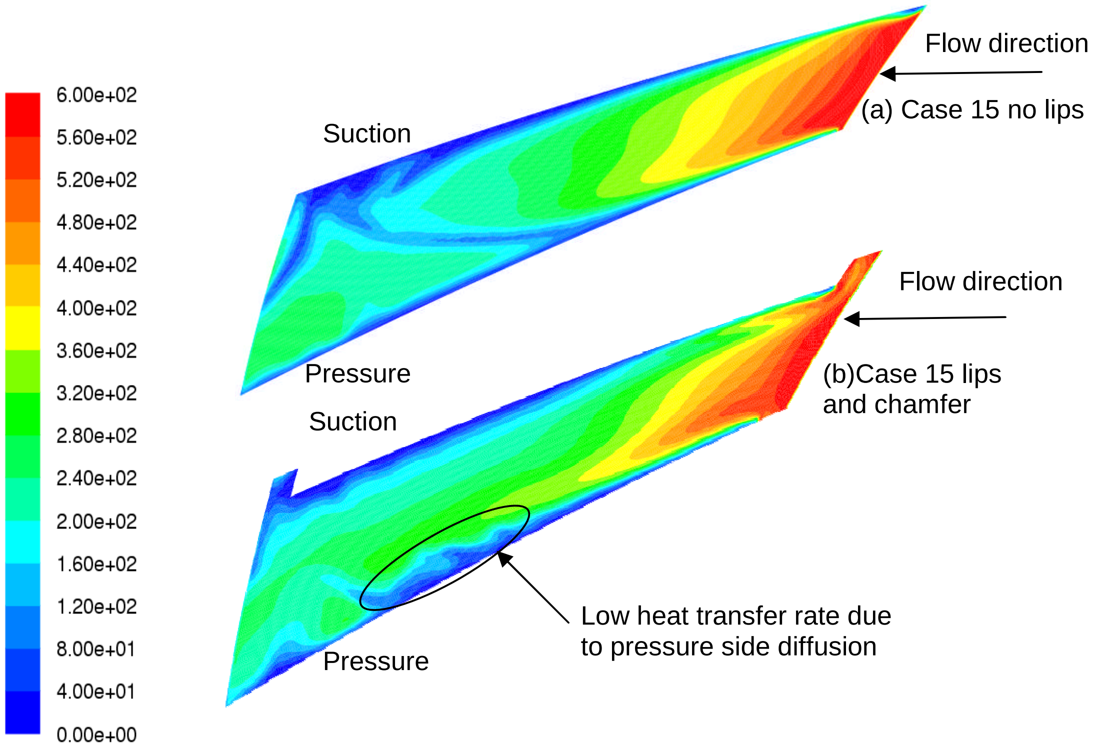

Fig 7.9: Passage outboard surface Nusselt number distribution

7.3. Effect of rounded leading edge

In order to reduce the flow separation that occurs on the inboard side and the suction side of the rotor passage due to flow direction change from tangential to radial, the leading edge of the blade was rounded. Rounding allows smooth entry of air into the rotor passage. The design changes were again incorporated to the case 15 rotor and lips were included at the outlet of the passage (fig 7.10).

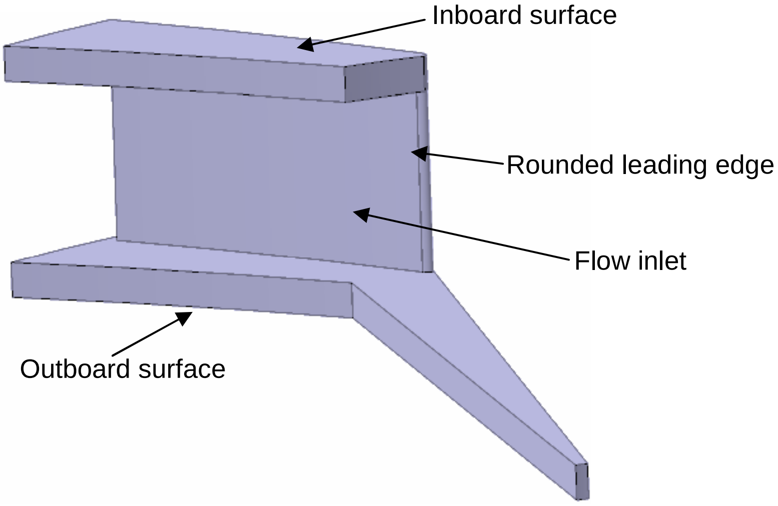

Fig 7.10: Rounded leading edge for case 15 rotor

The simulation was performed at 1500 rpm and 800 K as these are the conditions encountered during normal braking operation.

7.3.1. Aero-thermal flow analysis

It had been observed that the rounding of the blade leading edge does have an impact on the mass flow rate. The mass flow rate has increase by 10% (table 7.3).

Type of rotor	Mass flow rate kg/sec
Case 15 without lips	0.247
Case 15 with rounded leading edge	0.274

Table 7.3: Mass flow rate for case 15

The higher mass flow rate is due to the reduction in the inlet separation that would have occurred due change in flow direction from tangential to radial. The separation that occurs on the suction side of the inboard surface at the inlet is reduced by the inclusion of rounded leading edges (fig 7.11). Due to this reduction the flow is accelerated on the suction side marginally thereby decreasing the diffusion on the suction a little.

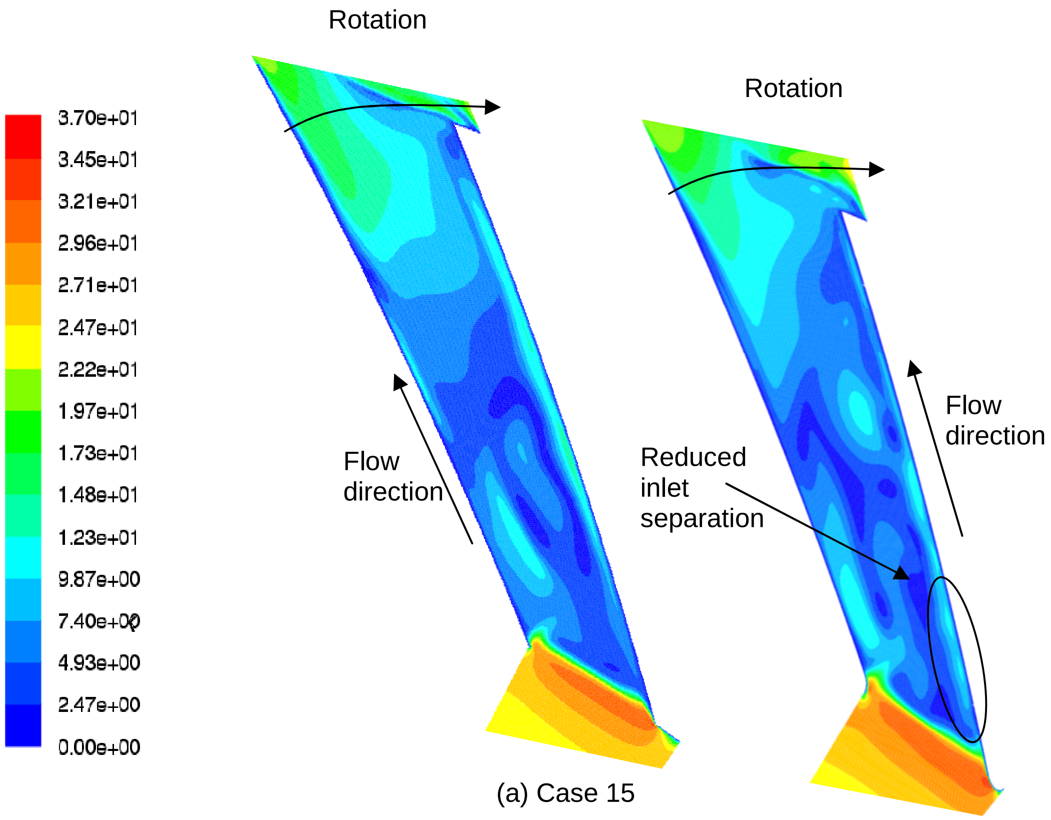

(a) Case 15

(b) Case 15 with rounded leading edge

Fig 7.11: Relative velocity 1mm below the passage inboard surface

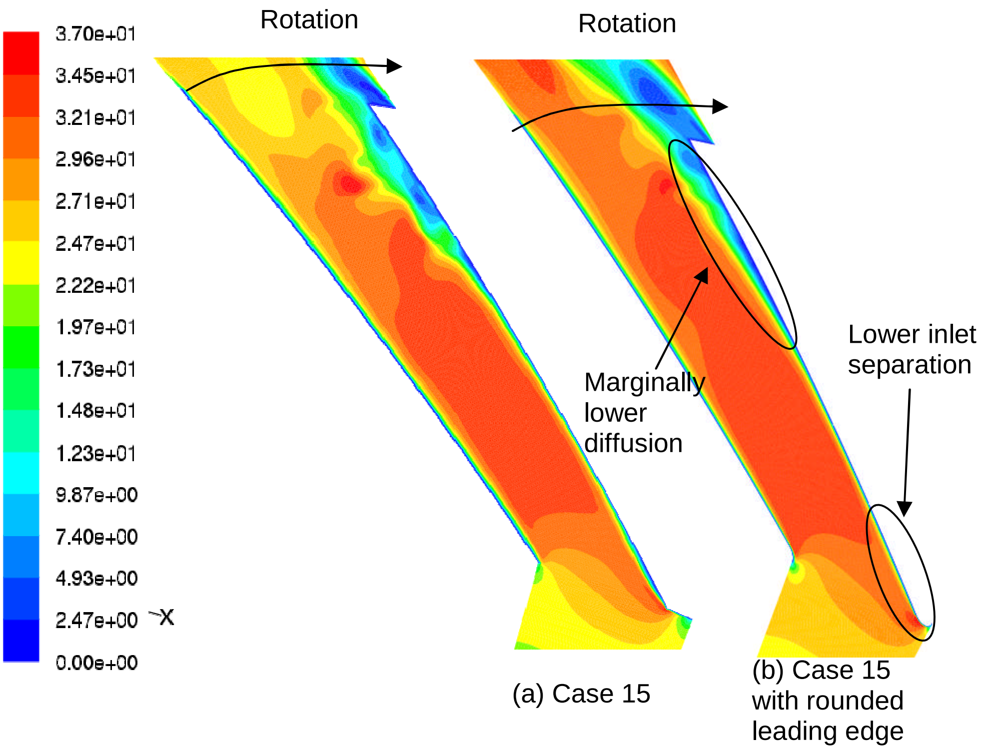

Fig 7.12: Relative velocity at mid height of the rotor passage

The reader should also keep in mind that there is a reduction in the total area available for heat transfer due to the lips at the outlet of the passage. In spite of this decrease in surface area, the total heat transfer rate from the internal passages of the rotor with lips and chamfer is good (table 7.4).

Type of rotor	Total heat transfer rate W
Case 15 without lips	288.81
Case 15 with rounded leading edge	275.76

Table 7.4: Total heat transfer rate for case 15

There is drop on the total heat transfer rate by 4.2% by rounding the leading. As explained earlier the reduction in the inlet separation due to flow direction change increases the heat transfer from the suction side at the inlet (fig 7.13). But the overall heat transfer from the suction side is lower due to the lower area. Due to this the heat transfer rate from the suction (72.12 W) is a marginally lower when compared the conventional case 15 rotor (76.78 W). The pressure side heat transfer is more uniform by rounding the leading edge (fig 7.14). The total heat transfer rate though is lower (91.93 W) than the conventional case 15 rotor (98.88 W) due to lower area available for heat transfer. The inlet separation on the inboard side of the pressure surface still affects the heat transfer.

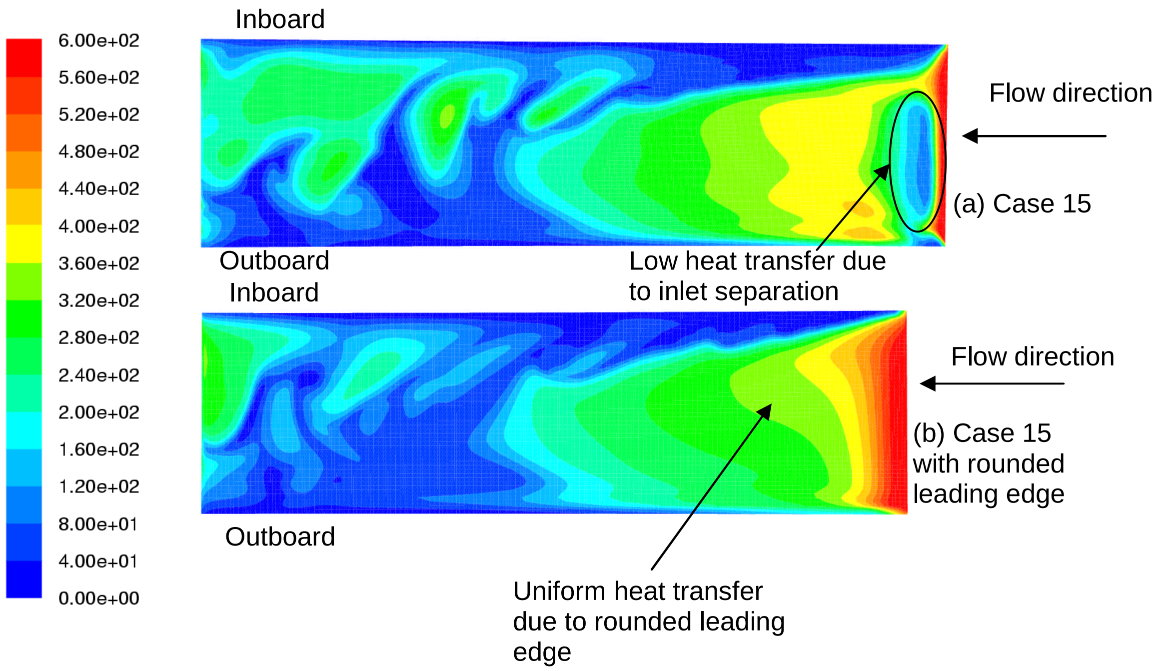

Fig 7.13: Suction surface Nusselt number distribution

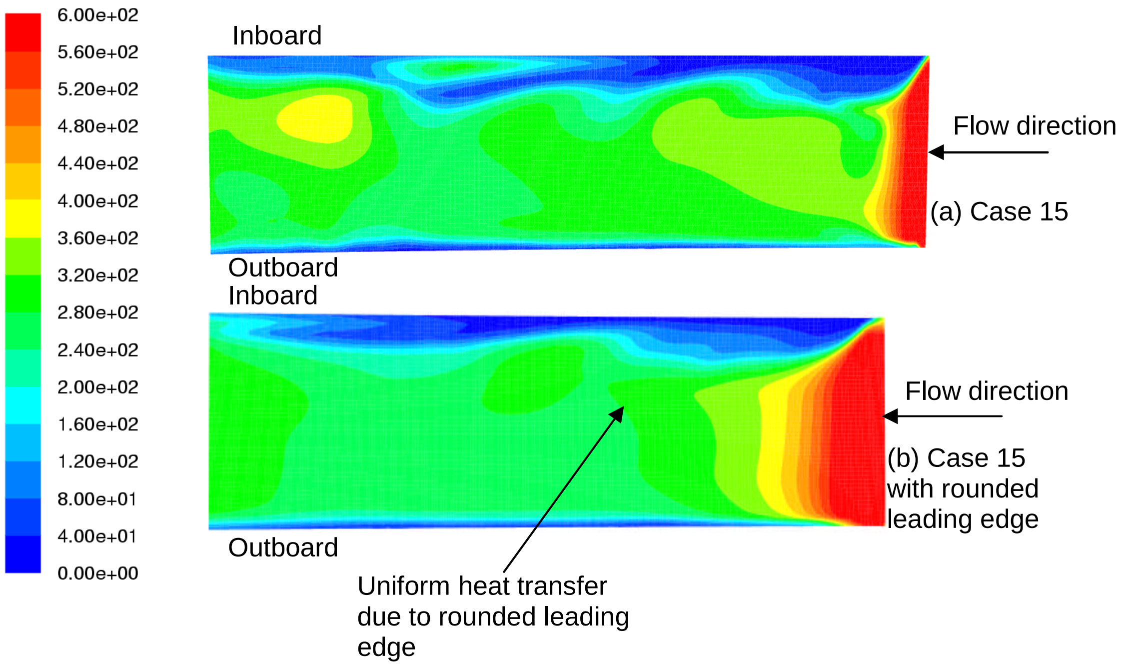

Fig 7.14: Pressure surface Nusselt number distribution

The heat transfer rate distribution on the inboard surface is similar for both conventional case 15 rotor and case 15 rotor rounded leading edge. The inlet separation due to change in flow direction from axial to radial and also tangential to radial generally affects the heat transfer rate from the inboard surface. By rounding the leading edge there only a marginal improvement of heat transfer at the suction side of the inboard surface (fig 7.15) The heat transfer from the inboard surface of the conventional case 15 rotor is 47.65 W as compared to 45.73 W from the improved case 15 with rounded leading edge. The passage outboard surface also shows a similar behaviour in heat transfer rate. The effect of flow separation on the suction side is very less on the outboard surface. Therefore, rounding the leading edge doesn’t have a huge impact of the outboard surface heat transfer (fig 7.16). The heat transfer rate from the outboard surface of the conventional case 15 rotor is 65.48 W as compared to 65.97 for the rounded leading edge rotor. The decrease in area due to lips also reduces the heat transfer rate.

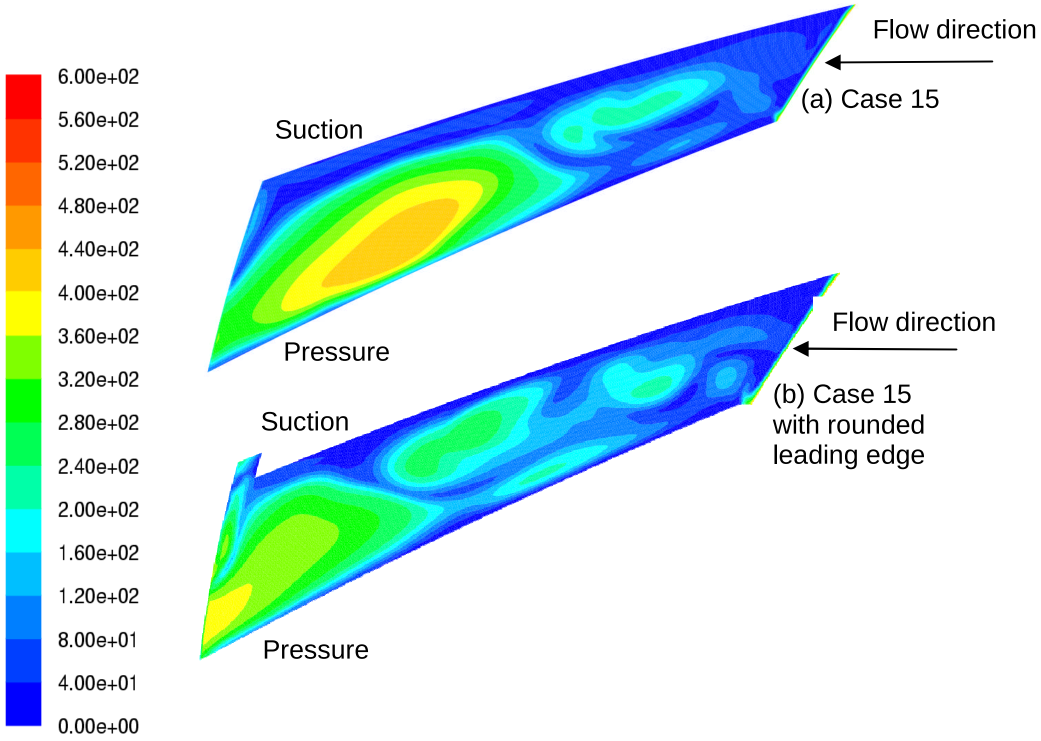

Fig 7.15: Passage inboard surface Nusselt number distribution

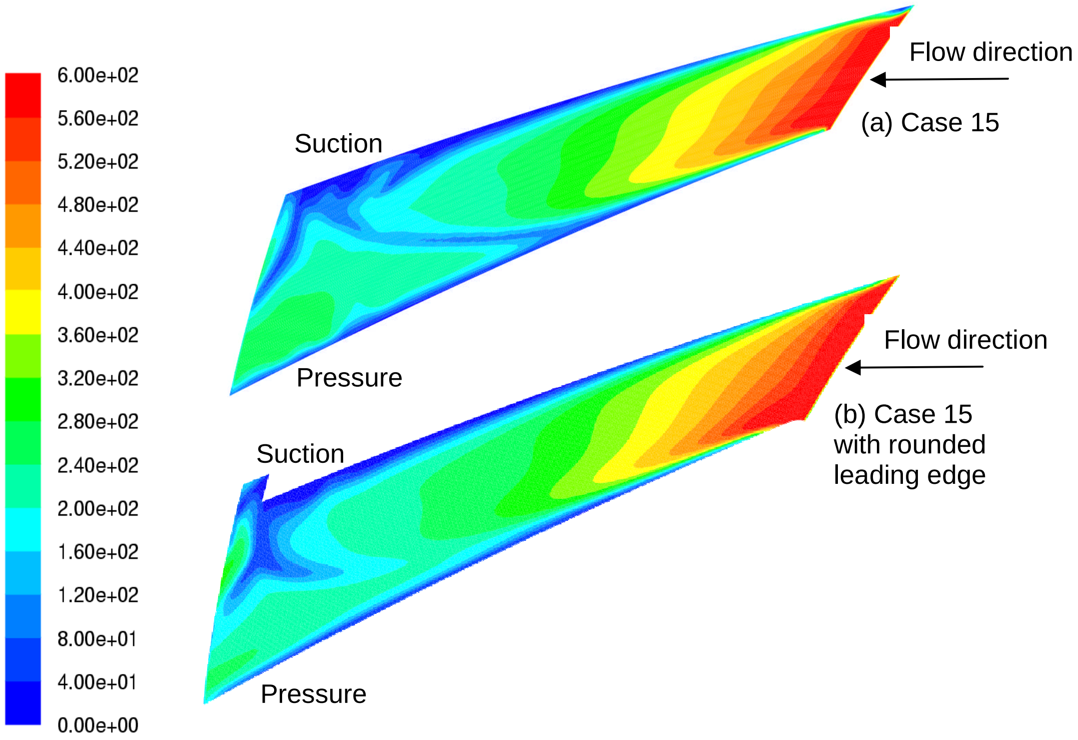

Fig 7.16: Passage outboard surface Nusselt number distribution

7.4. Effect of variable number of blades

All the simulations up until now were carried out with a 48 bladed rotor. In order to understand the effect of number of blades on the aero-thermal performance of a ventilated disc brake a simulation was performed with a 36 bladed rotor. The simulation was performed at 1500 rpm and 800 K on the datum rotor design. Zhang [1997] performed CFD simulations to study the effect of number of blades on the mass flow rate through the rotor passage. It was observed that for passage with square sections the mass flow rate was the highest. This is because for a given area, a square cross section has the least perimeter and thereby reducing the frictional losses.

For the simulations all the geometric dimensions were maintained the same and only the number of blades were decreased to 36. It was observed that the mass flow rate through the rotor passage increases with reduction in the number of blades. This is obvious as the passage inlet area increases with decrease in the number of blades. But the interesting point was that the total mass flow rate for the rotor with 36 blades was 7% in comparison with the 48 bladed rotor (table 7.5).This therefore points out that the rise in the mass flow rate is not proportional to the increase in the inlet area.

Type of rotor	Mass flow rate through a single passage kg/sec	Mass flow rate through the complete rotor kg/sec
Datum with 48 blades	0.00416	0.199
Datum with 36 blades	0.00501	0.1806

Table 7.5: Mass flow rate as function of number of blades

From figure 7.17 it can be observed that with inlet area the inlet separation at the inboard side has increased. The recirculation zone extends through out the inboard side of the passage. This acts as a flow blockage by reducing the mass flow rate through the passage.

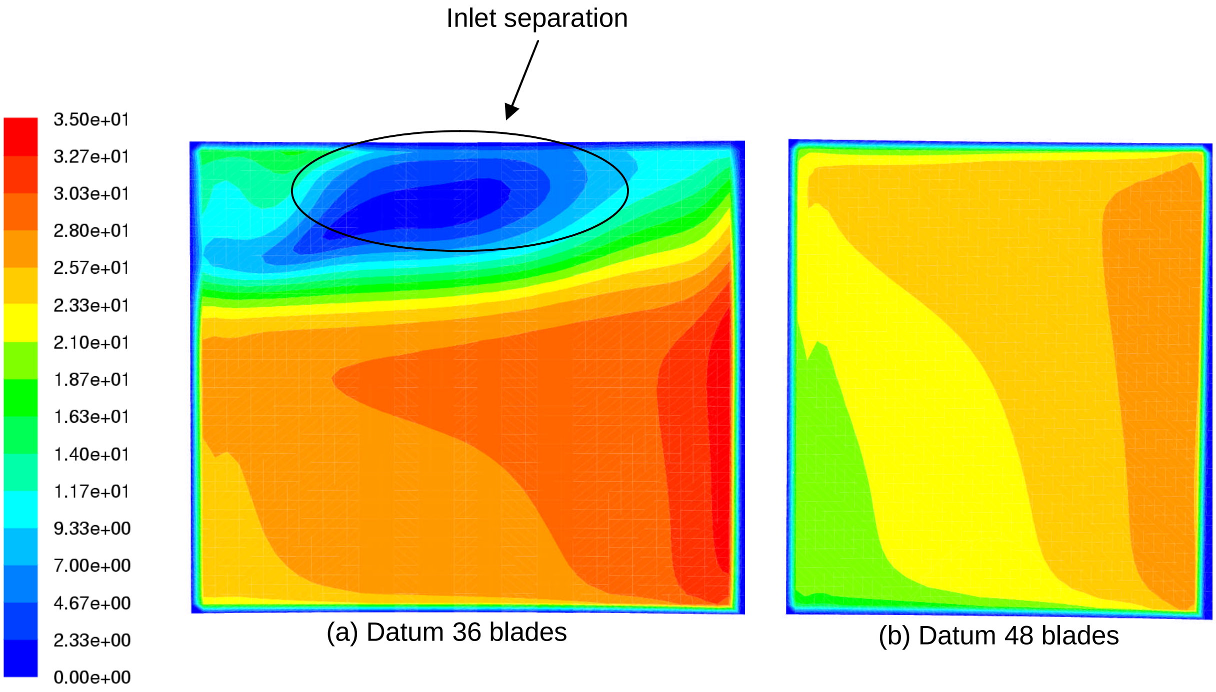

(a) Datum 36 blades

(b) Datum 48 blades

Fig 7.17: Relative velocity at the inlet of the passage for the datum rotor

The total heat transfer rate for all the internal walls of the passage is 42% higher for the datum with 36 blades when compared to the datum with 48 blades. The higher heat transfer rate is due to higher mass flow rate through the individual passage and also due to increase in the surface area for the inboard and outboard surfaces. But the overall heat transfer from all the internal passages of the disc brake is only 7% higher for the datum rotor with 36 blades when compared with the datum rotor with 48 blades (table 7.6). The heat transfer from through each passage can be understood by looking at the individual surfaces of the passage. The heat transfer rate from the suction side of the passage of the 36 bladed rotor is higher and the distribution is more uniform when compared to a 48 bladed rotor. This is due higher mass flow rate associated with the 36 bladed rotor. The inlet separation is therefore lower for such a rotor (fig 7.18). The heat transfer rate from the pressure side of the passage is also higher for the 36 bladed rotor due to higher mass flow rate (fig 7.19).

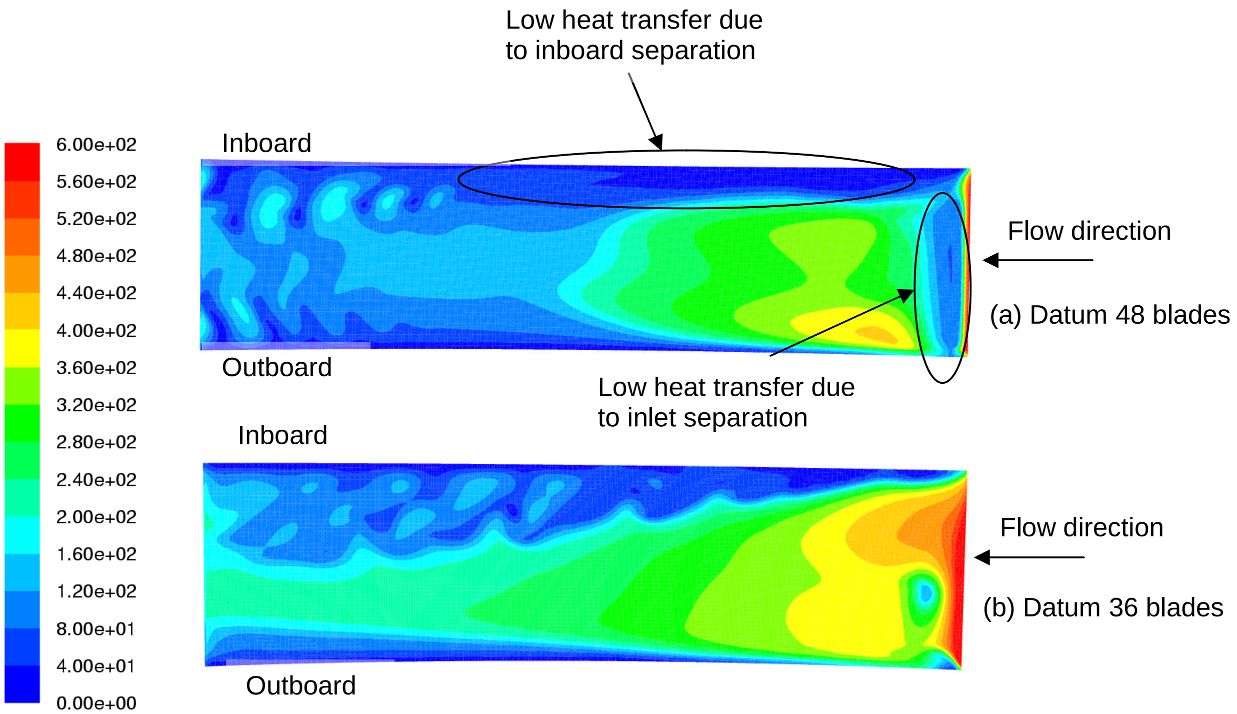

Fig 7.18: Suction surface Nusselt number distribution

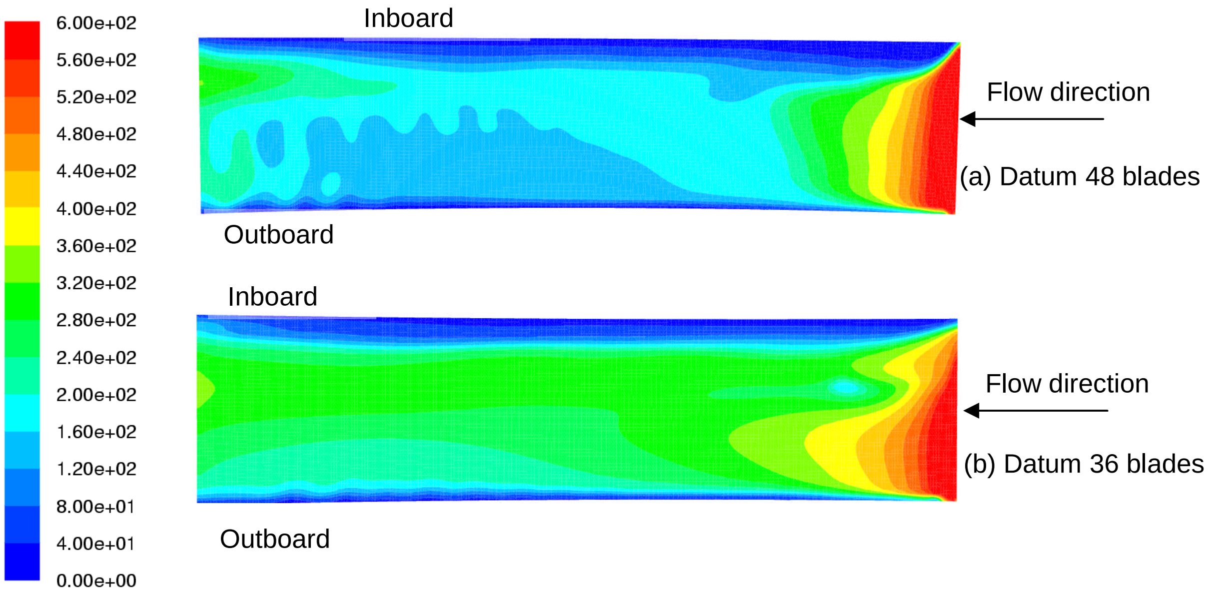

Fig 7.19: Pressure surface Nusselt number distribution

The inboard surface heat transfer rate for a 36 bladed rotor is almost 2 times higher than the 48 bladed rotor (fig 7.20). One of the reasons for a high heat transfer is due to the higher area of the inboard surface. But this increase in heat transfer is misleading as the 36 bladed rotor performance is mainly due to the re-circulating flow that is flowing in the opposite direction towards the passage inlet. Therefore the heat picked up by the fluid is not getting dissipated out of the passage. This can be better understood from figure 7.21. It can be observed that the fluid upon entry into the passage separates at the inboard surface.

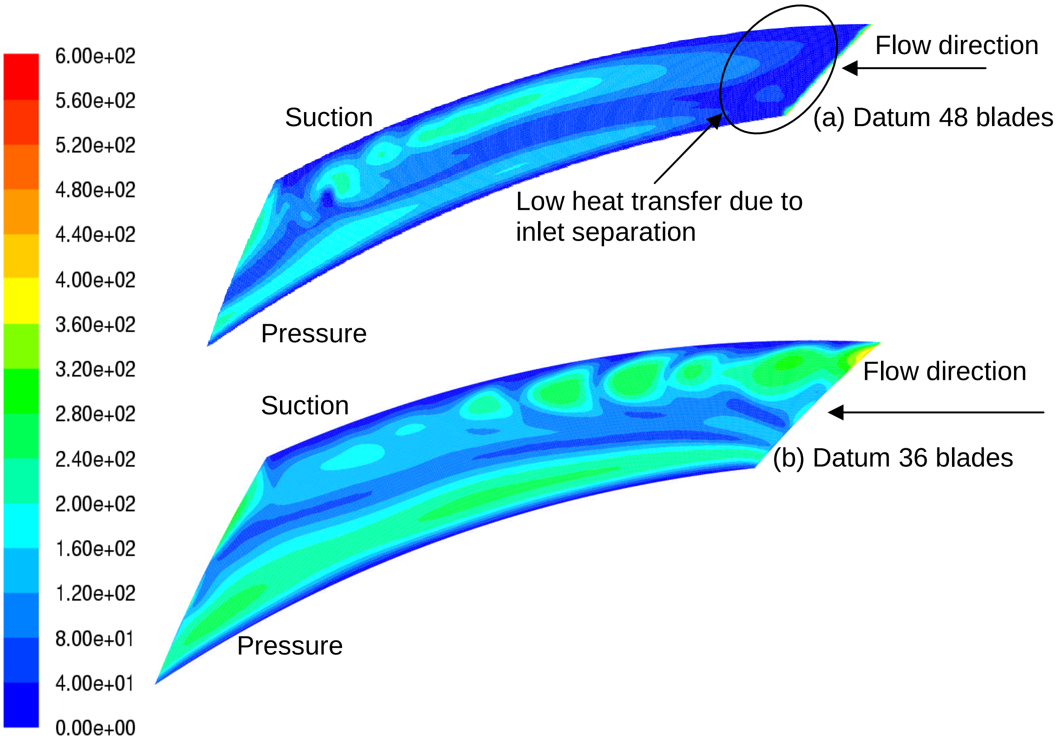

Fig 7.20: Passage inboard surface Nusselt number distribution

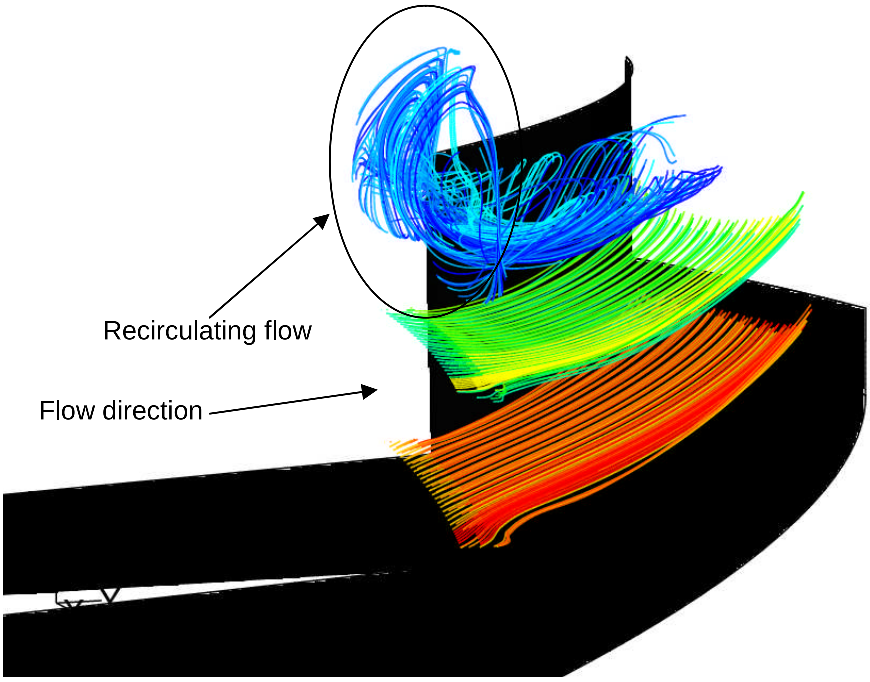

Fig 7.21: Pathlines for flow through the 36 bladed datum rotor.

This affects the overall thermal performance of the rotor as the heat picked is not being dissipated by the flow. The parameter that indicated the amount of heat dissipated by the flow is the mass averaged enthalpy calculated at the outlet of the rotor passage. The mass averaged enthalpy for the datum rotor with 36 blades is 49 KJ/Kg in comparison to a 48 bladed rotor whose mass averaged enthalpy is 55.12 KJ/Kg. Therefore, the 36 bladed rotor performs poorly when compared to 48 bladed rotor due to higher viscous losses encountered. As predicted Zhang [1997] the 48 bladed rotor has a aspect ratio of 1 which means it is a square cross-section. The outboard surface heat transfer distribution for the 36 bladed rotor is almost similar to the 48 bladed rotor but the absolute value of rate of heat transfer is higher for 36 bladed rotor due to larger surface area and also higher mass flow rate (fig 7.22).

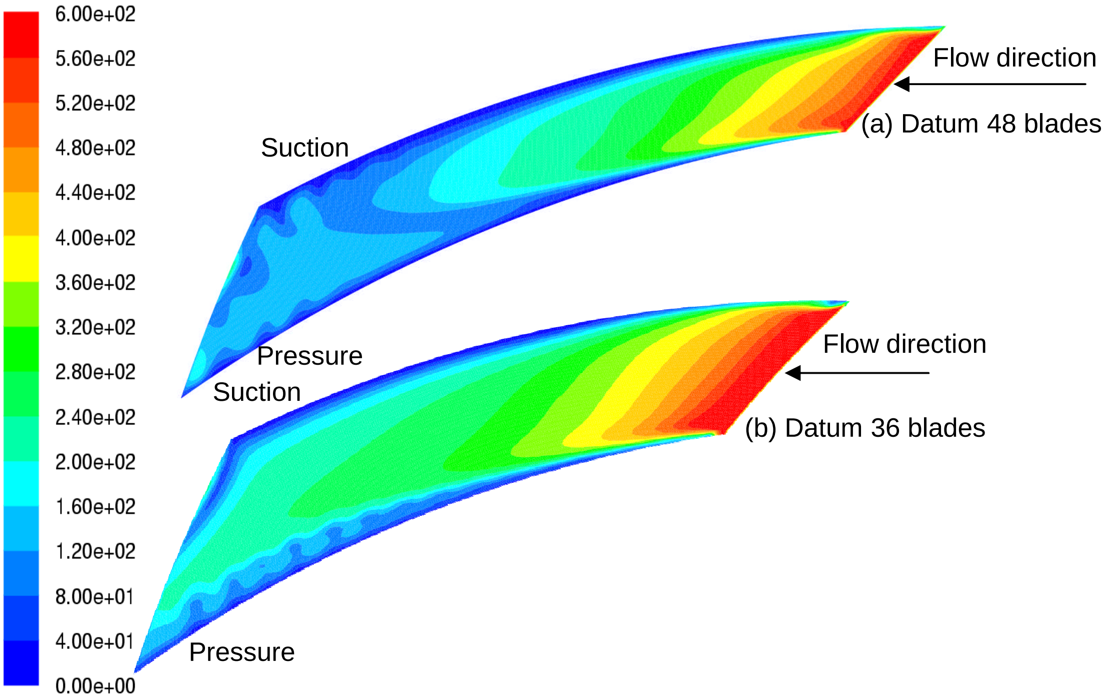

Fig 7.22: Passage outboard surface Nusselt number distribution

7.5. Effect of variable thickness

The diffusion that occurs on the suction side of the passage is due to adverse pressure created by the natural change in area from inlet to outlet affects the heat transfer rate. In order to reduce this, the brake was re-designed with a variable thickness blade. The thickness was gradually increased from inlet to the outlet of the rotor (fig 7.23). The idea behind this is to reduce the area change from the inlet to outlet. The thickness of the blade at the outlet is twice the thickness at the inlet of the passage. The Case 15 rotor with lips and chamfer was used to perform the analysis with the inclusion of variable thickness.

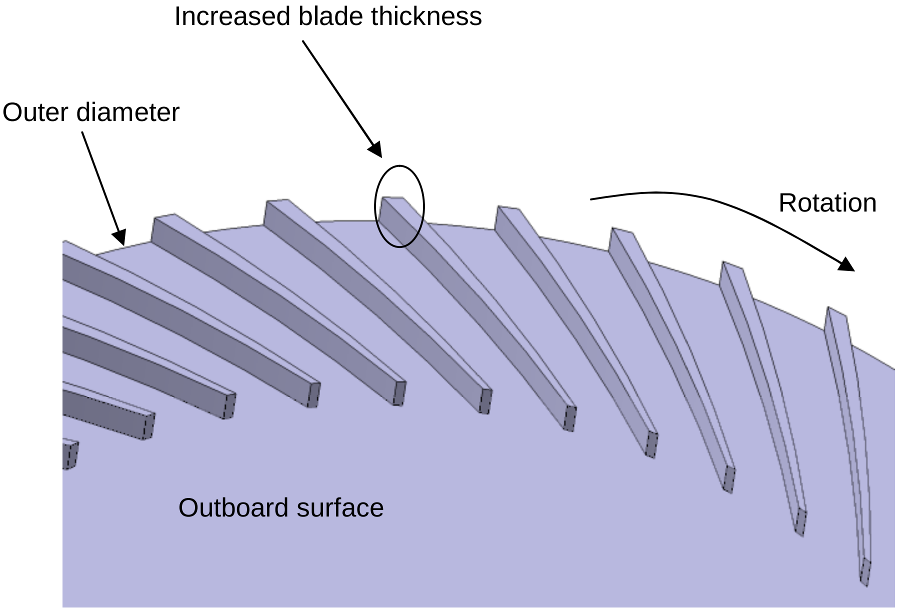

Fig 7.23: Schematic of a variable thickness blade

7.5.1. Aero-thermal flow analysis

It has been observed from the simulations that the inclusion of variable thickness does have an influence on the flow through the passage. As expected the diffusion that occurs on the suction side of the passage has been reduced but not completely eliminated (fig 7.24). The diffusion that occurred on the pressure side of the rotor due to the inclusion of chamfer was also reduced. This could be further reduced by increasing the outlet thickness of the blade further. There is drop in the mass flow rate by 16% through the passage compared to the Case 15 rotor with lips and chamfer (table 7.6). This is due to decrease in the flow area by the inclusion of variable blade thickness.

Type of rotor	Mass flow rate through the rotor kg/sec
Case 15 with lips and chamfer	0.321
Case 15 with lips, chamfer and variable blade thickness	0.268

Table 7.6: Mass flow rate variation by inclusion of variable blade thickness

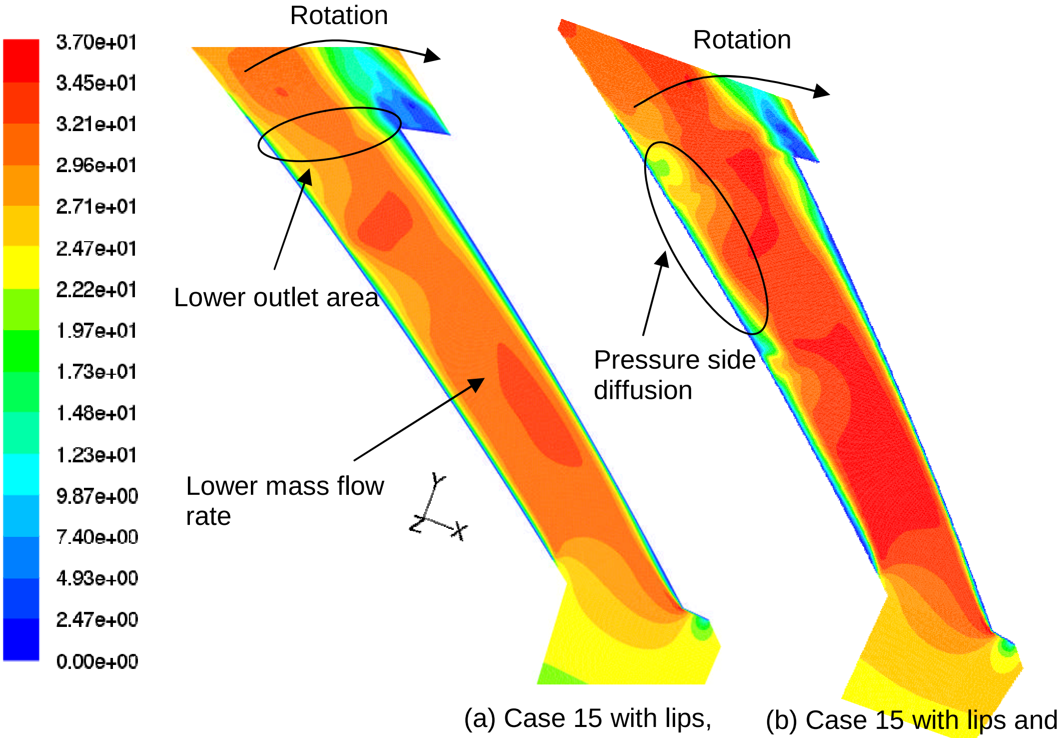

(a) Case 15 with lips, chamfer and variable blade thickness

(b) Case 15 with lips and chamfer.

Fig 7.24: Relative velocity at the mid-passage height of the passage

In spite of the 16% drop in the mass flow rate the heat transfer rate from all the internal passages has only reduced by 3%. This is due to improved heat transfer rate from the pressure side of the passage by 14.5% caused by decrease in the pressure side diffusion. This can be observed from figure 7.25, not only has the heat transfer rate increased on the pressure but the uniformity of the heat transfer is also improved. The heat transfer rate from the suction surface on the other hand has decreased by 6%. This is due to decrease in the mass flow rate (fig 7.26). There is only a marginal decrease in the suction side diffusion. The inboard and the outboard surfaces also show a drop in the heat transfer rate due to lower mass flow rate (fig 7.27 and 7.28 respectively).

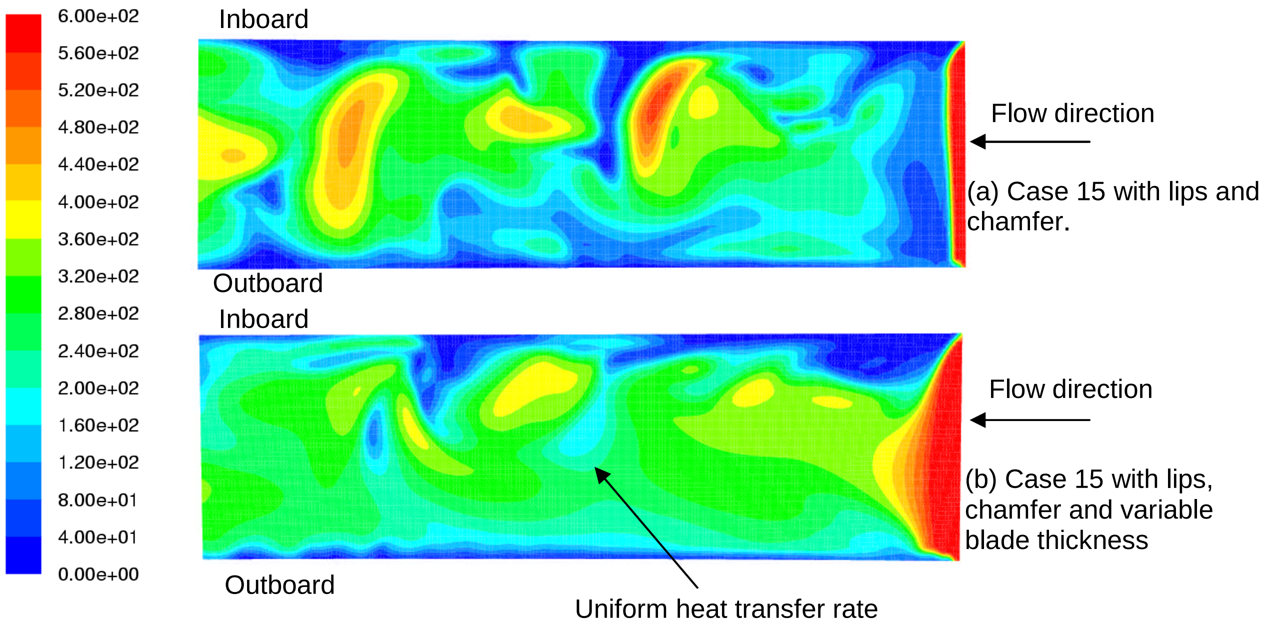

Fig 7.25: Pressure surface Nusselt number distribution

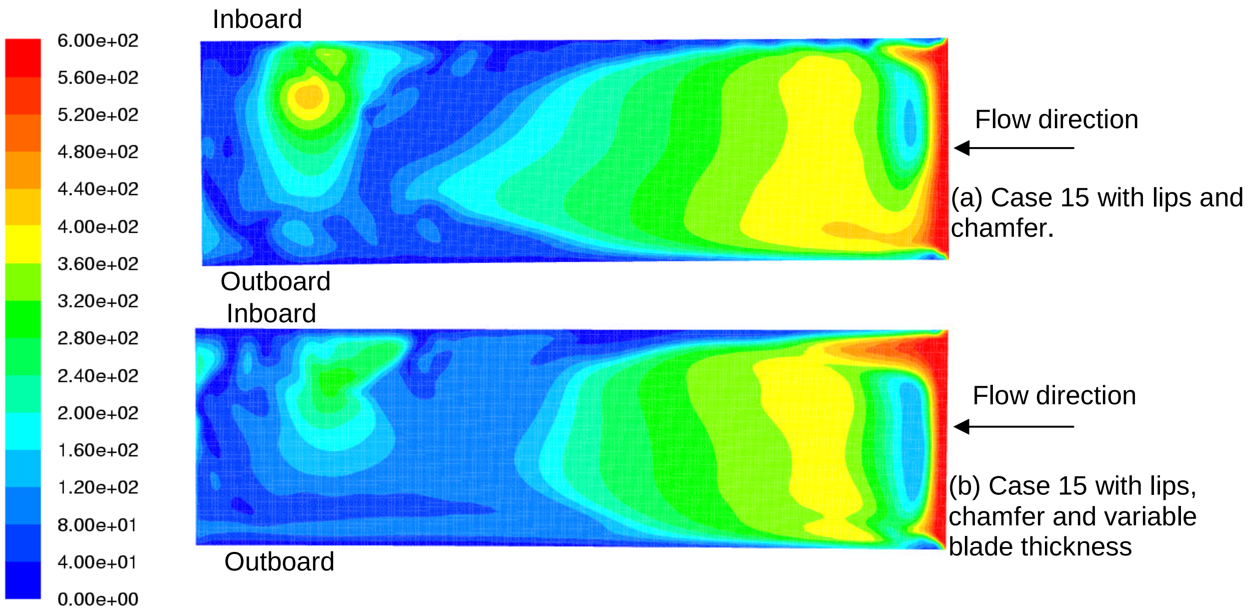

Fig 7.26: Suction surface Nusselt number distribution

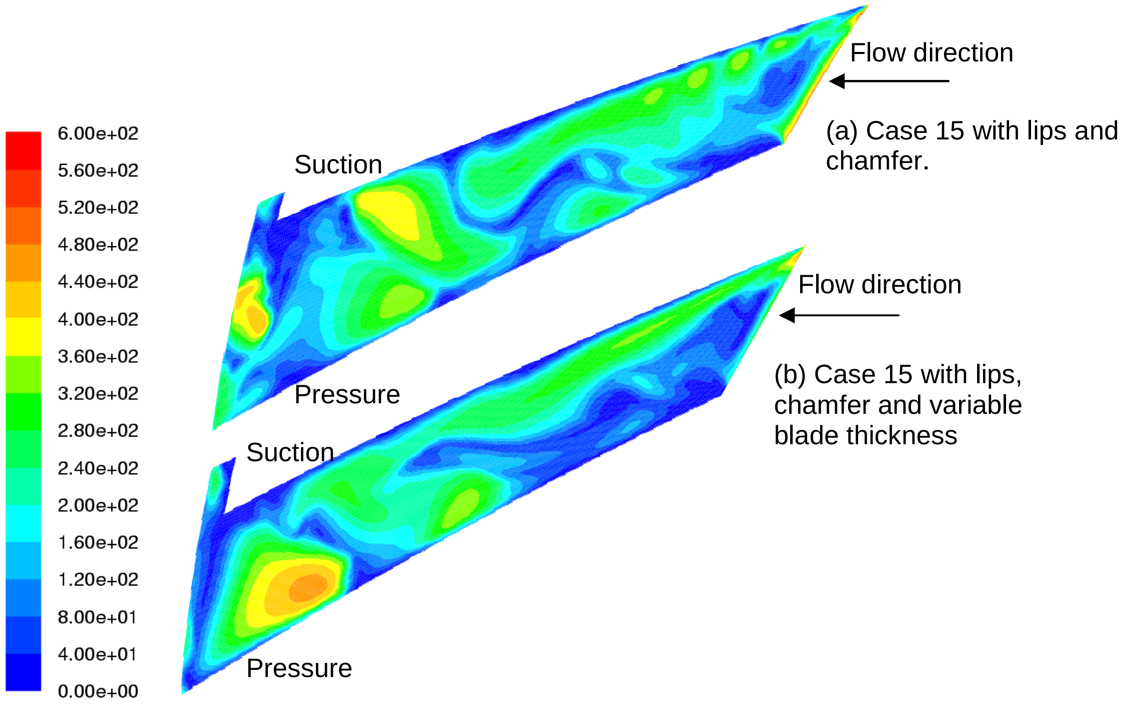

Fig 7.27: Passage inboard surface Nusselt number distribution

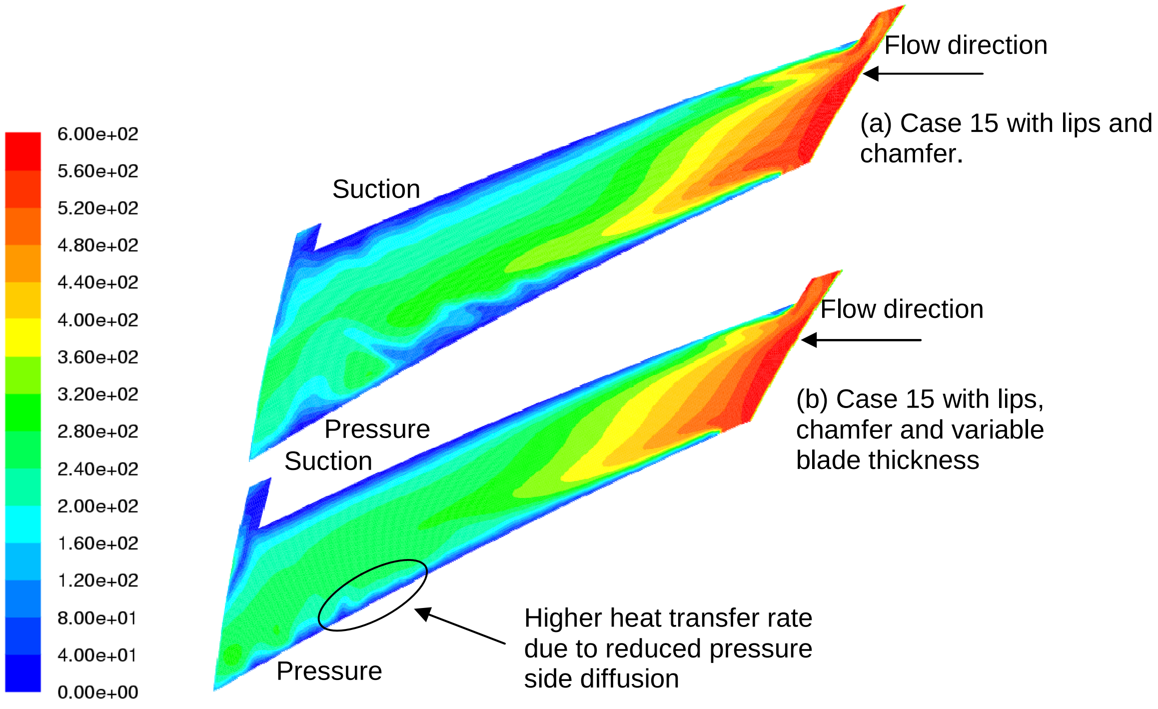

Fig 7.28: Passage outboard surface Nusselt number distribution

7.6. Effect of aspect ratio

As explained in section 7.4, inlet aspect ratio does have an effect on the performance of the disc brake rotor. By decreasing the number of blades, the aspect ratio of the inlet has increased and a decrease in the performance of the rotor was noted. In order to understand the effect of passage inlet area, the outboard thickness was increased from 7 mm to 14 mm thereby reducing the height of the passage. Datum rotor with 48 blades was used to carry out the modifications (fig 7.29).

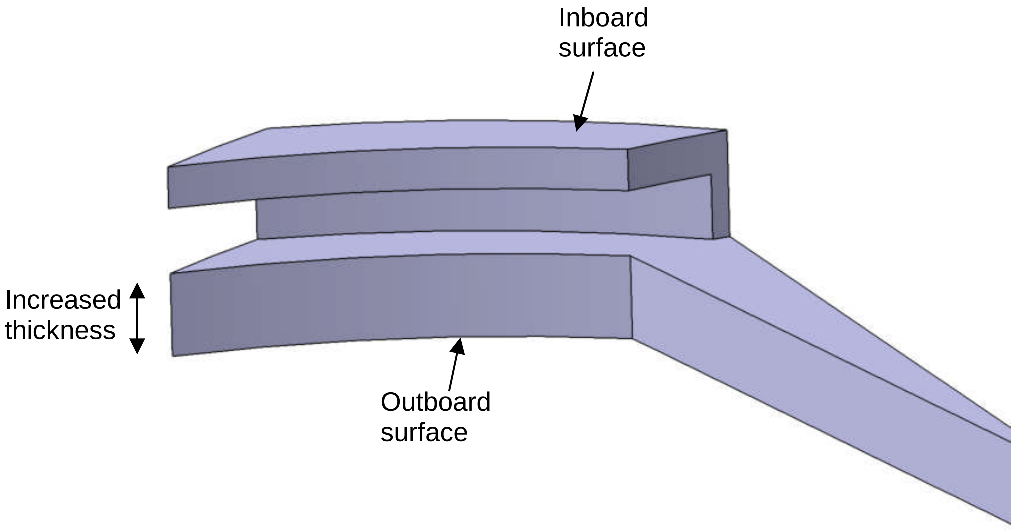

Fig 7.29: Datum rotor with thicker outboard surface

As expected the mass flow rate through the passage has decreased by 11% when compared to a convectional 48 bladed Datum rotor. The reduction in the area is by almost 40%. This shows that the reduction in the mass flow rate is not proportional to the reduction in the area. This is due to the fact that the inlet separation on the inboard surface has reduced considerably thereby reducing the flow blockage and increasing the mass flow rate (fig 7.30). The inlet separation on the suction side of the passage is also reduced. This shows that the for the present lower passage inlet area the amount of viscous losses are less when compared to the conventional datum rotor with a higher inlet area (square cross section).

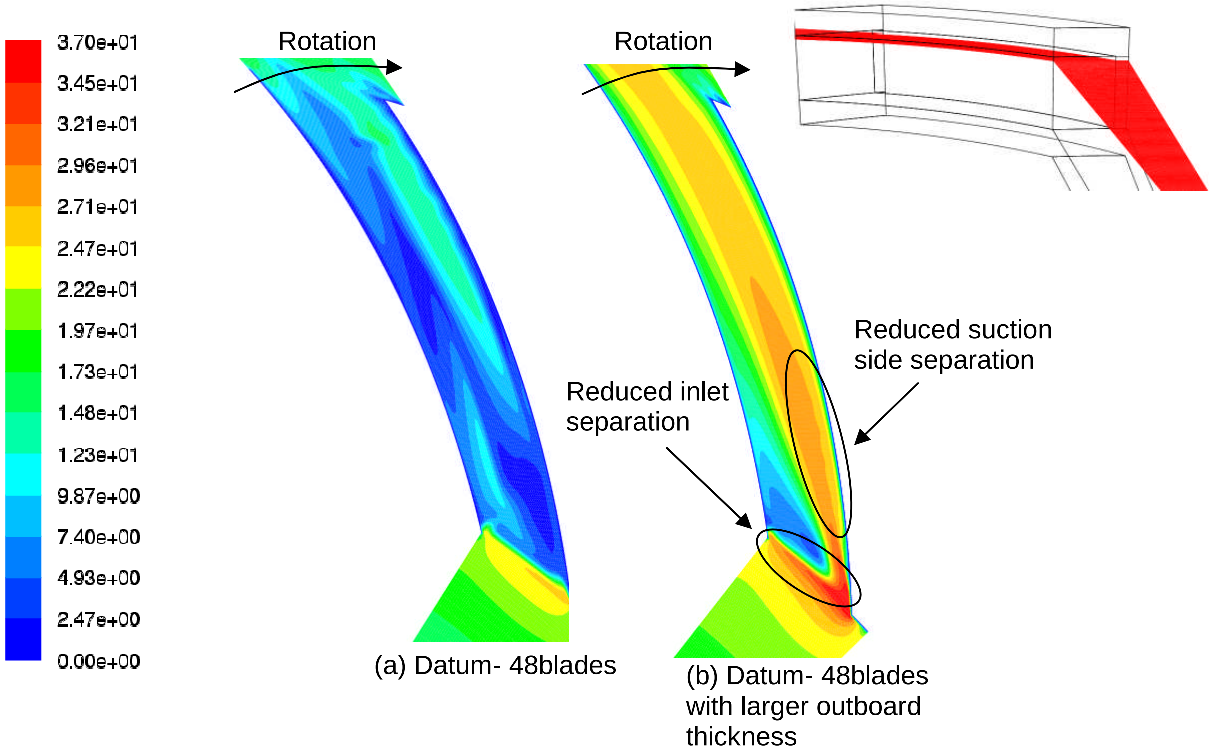

Reduced suction side separation

Reduced inlet separation

(a) Datum- 48blades

(b) Datum- 48blades with larger outboard thickness

Fig 7.30: Relative velocity 1mm below the inboard surface

The total heat transfer rate from all the internal passages of the modified datum rotor is 2% higher than the conventional 48 bladed rotor. In spite of the drop in the mass flow rate, the total heat transfer rate has increased. This is again due to lower viscous losses. Regions of recirculation reduce the heat transfer rate from the surface leading to the formation of hot spots. The suction side of the modified datum has a heat transfer rate (54.61 W) is lower than the suction side of the conventional datum rotor (72.13 W). This is due to the reduction in area of the suction side by almost 40%. But the heat transfer uniformity of the modified rotor is better due to reduced separated region as explained above (fig 7.31). Even on the pressure side the same trend is followed (fig 7.32). The inboard side on the other hand has higher heat transfer rate for the modified rotor due to the presence of lesser regions of heat transfer that affect heat transfer (fig 7.33). The outboard surface of the modified rotor also has higher heat transfer rate owing to the same reason as mentioned above (fig 7.34). This uniformity of Nusselt number on all the surfaces for the modified rotor is a distinct advantage as it helps in reducing the formation of hot spots thereby preventing thermal distortion of the brake disc rotor.

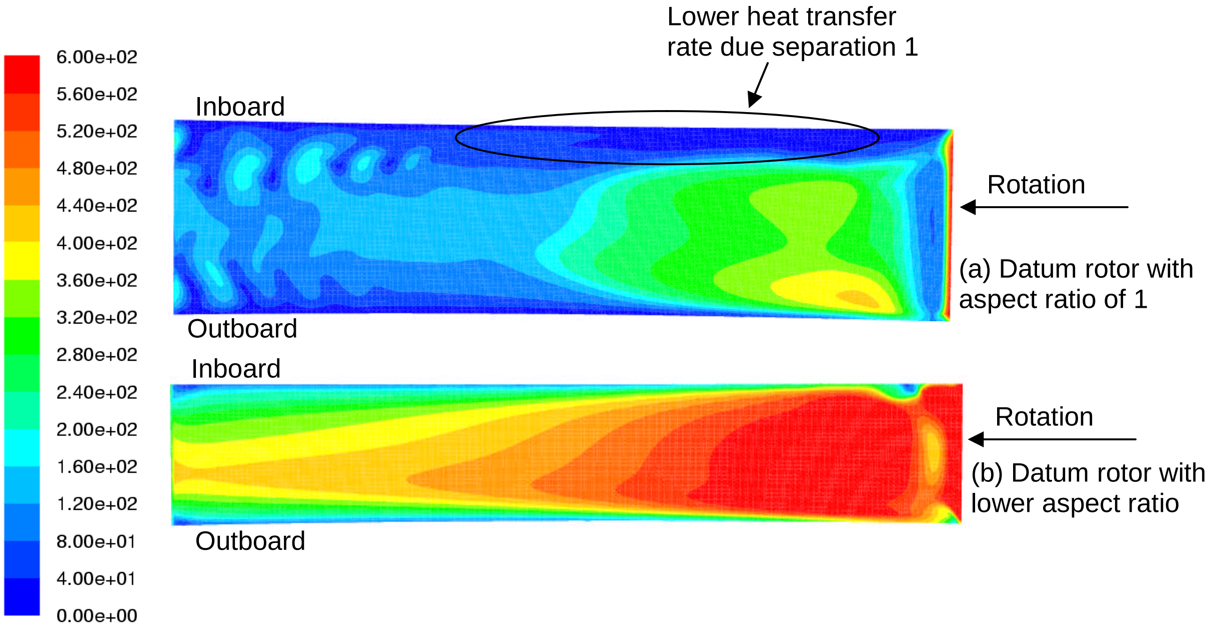

Fig 7.31: Suction surface Nusselt number distribution

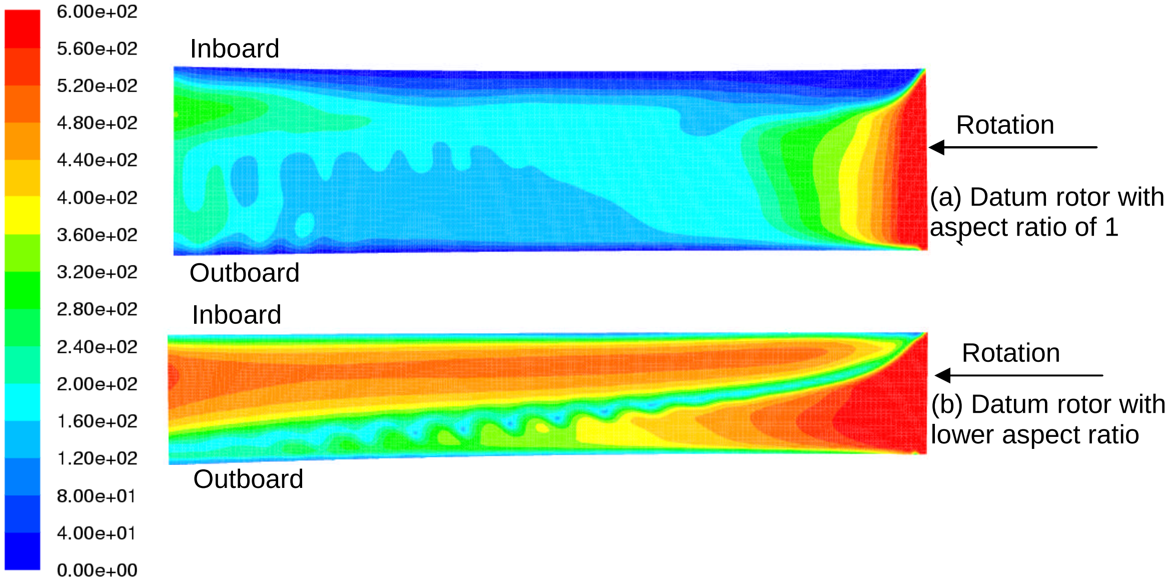

Fig 7.32: Pressure surface Nusselt number distribution

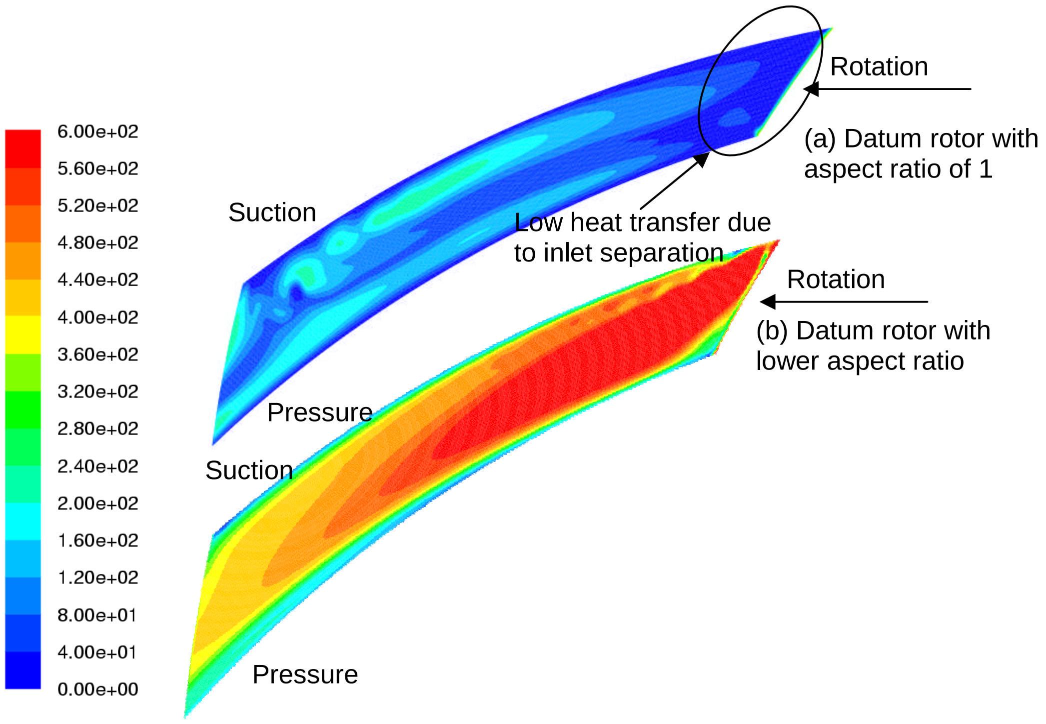

Fig 7.33: Inboard surface Nusselt number distribution

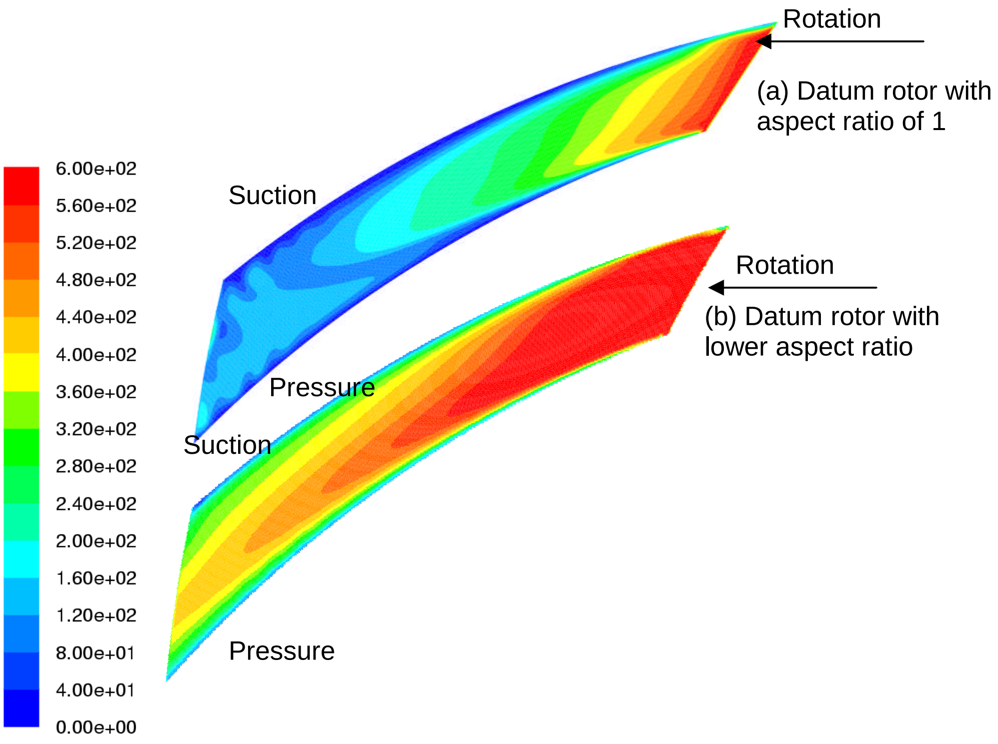

Fig 7.34: Outboard surface Nusselt number distribution

7.7. Heat transfer distribution

The distribution of heat transfer changes considerably by making detailed design changes to the disc brake rotor (Appendix B&C). Figure 7.35 indicates the contribution of each of the internal surfaces of Case 15 rotor by the making changes to the shape of the blade and the passage to the overall heat transfer rate. Figure 7.36 on the other hand indicates the contribution of internal indicates of Datum rotor by varying the aspect ratio. The temperature uniformity is also evaluated using the thermal distortion index and with the rounding of the leading edge the temperature uniformity increases by 20% compared to the conventional Case 15 rotor. This is due to the reduction in the inlet separation and the amount of diffusion on the suction side. The inclusion of lips and chamfer on the other hand increases the temperature uniformity by only 5%

compared to the conventional Case 15 rotor. This is due to the fact that in spite of improvement in the suction side heat transfer rate the pressure side heat transfer is affected leading to the formation of hot spots. By increasing the blade thickness at the outlet i.e. by having a variable thickness blade, the above problem is overcome. Due to this the uniformity of temperature increases by 10% compared to the conventional Case 15 rotor. By reducing the number of blades from 48 to 36 the non-uniformity of the temperature increases by 7.5%. But this is compensated for the loss in the mass flow rate and the total heat transfer rate from the complete rotor. The reduction in the inlet area of the passage by 40% has a positive impact on the temperature uniformity. The temperature uniformity increases by 70%.

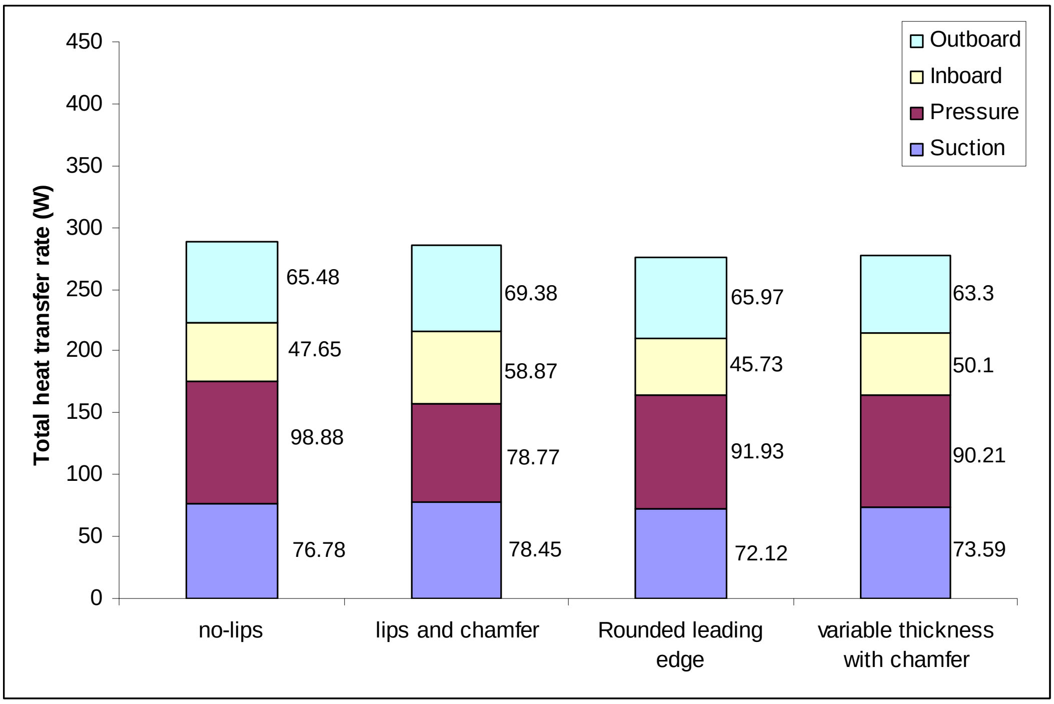

Fig 7.35: Contribution of internal surfaces of Case 15 rotor to the total heat transfer rate

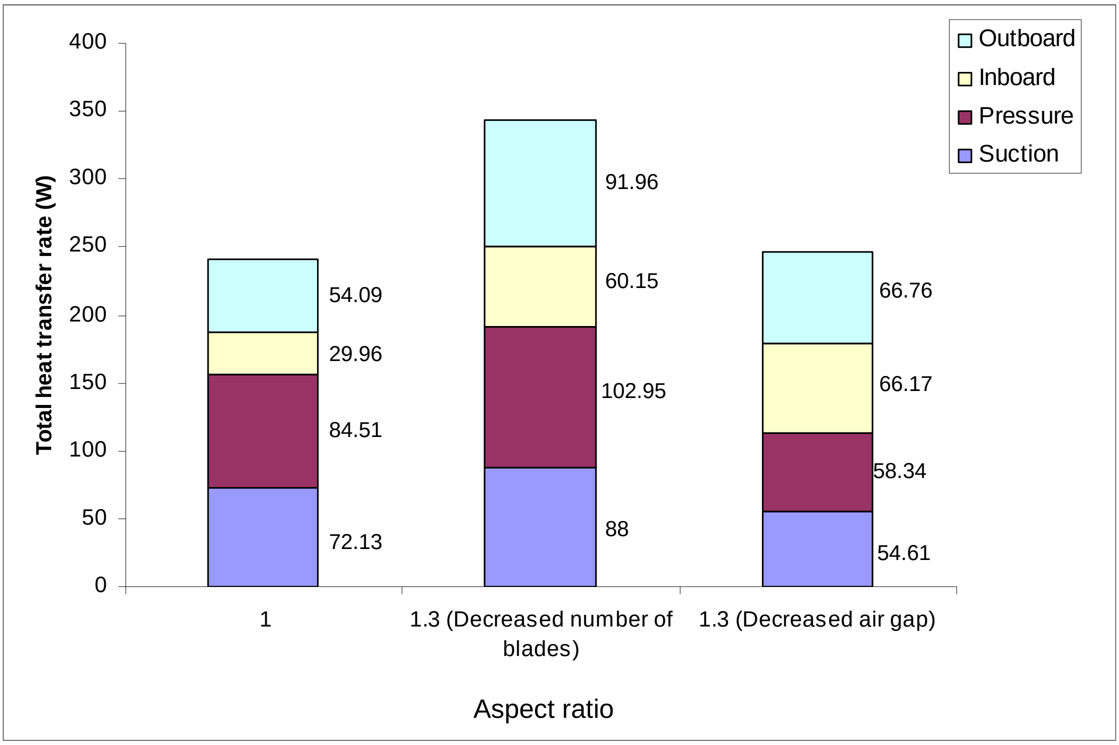

Fig 7.36: Contribution of internal surfaces of the Datum rotor to the total heat transfer rate

8

Conclusions and recommendations

The CFD design analysis of ventilated disc brakes was successfully accomplished. The following conclusions were drawn from the research work.

8.1. CFD modelling conclusions

The domain development, grid strategy and the turbulence model for the current project were based on the work carried out by Nestor [2004]. The flat plate validation case showed that the grid adopted for the study is appropriate for the turbulent model and for heat transfer calculations. The flat plate heat transfer coefficient was compared to the analytical solution obtained by Taine [2004]. The Datum rotor rotating in still air was successfully validated at isothermal condition and was compared to the experimental results (hot wire measurement) obtained by Parish [2003]. The mass flow rate from CFD was over-estimated by 4% but the flow characteristics were well captured.

8.2. Brake disc aero-thermal conclusions

The effect of the following design parameters on the aero-thermal performance of a ventilated disc brake was studied in detail.

- Blade angles.
- Blade speed.
- Rotor temperature.
- Number of blades.
- Inclusion of lips and chamfer.
- Inclusion of rounded leading edge.
- Inclusion of variable thickness blade.

- Aspect ratio.

The following conclusions were drawn from the analysis of the above design parameters.

- Inlet angles were observed to have an effect on the aero-thermal performance of the disc brake rotor. The aero-thermal performance was better at lower inlet angles.
- The aero-thermal performance of the disc brake rotor was more sensitive to the outlet angles than inlet angles. The lower outlet angles have better aero-thermal performance.
- The best aero-thermal performance of the disc brake rotor was in the region of 35^0 to 45^0 for the inlet angles and 50^0 to 60^0 for the outlet angle.
- The forward swept blades have lower aero-thermal performance than backward swept blades due to increase in the inlet separation on the suction side.
- The aero-thermal performance of the rotor increases with rotational speeds due to increase in the mass flow rate, rate of heat transfer and also temperature uniformity.
- The aero-thermal performance of the rotor decreases with increase in the rotor temperature due to decrease in the mass flow rate and temperature uniformity.
- Decreasing the number of blades to 36 from 48 increases the viscous losses through the rotor passage and decrease the temperature uniformity by 7.5%. Therefore, the 48 bladed rotor aero-thermal performance is better than a 36 bladed rotor.
- Chamfering the inlet has a positive effect of the aero-thermal performance of the disc brake. The mass flow increased by 30% by the inclusion of chamfer. Even though the total heat transfer rate decreased by 1.2%, the temperature uniformity increases by 5%.
- Chamfering the inlet also helps in reducing the inlet separation thereby reducing the formation of hot spots.

- Inclusion of lips decreases the aero-thermal performance of the disc brake rotor due to decrease in the surface area.
- Rounding the blade leading edge also has a positive effect on the aero-thermal performance. The inlet separation near the suction side of the passage was reduced and also the diffusion was controlled thereby increasing the mass flow rate by 10% when compared to a conventional rotor. Even though the total heat transfer rate is decreased by 4% the temperature uniformity is increased by 20%.
- The rounding of the blade leading edge has a better impact on the aero-thermal performance of a disc than the inclusion of chamfer.
- By including a variable thickness blade the mass flow rate has reduced by 16% due reduction the amount of area available for the flow. The inclusion of variable thickness blade did indeed reduce the amount of diffusion at the trailing edge. The temperature uniformity also improved due to this by 10%. In order to eliminate the diffusion completely the author suggests increasing the blade thickness further at the outlet of the passage.
- By decreasing the inlet area of passage by 40% by increasing the outboard thickness, the mass flow rate has decreased by 11% and total heat transfer rate decreased by 2%. The temperature uniformity on the other hand has improved by almost 70%. This is due to the reduction in the inlet separation on both the suction and the inboard sides of the passage
- In order to understand the formation of hot spots in more detail, the author suggests carrying out CFD simulations by including conduction of heat through the rotor material i.e. conjugate heat transfer.

8.3. Brake disc design guidelines

Based on the conclusions listed above the following design guidelines can be proposed in order to optimise the aero-thermal performance of the disc brake rotor.

- Inlet angles should be within the range of 35^0 to 45^0 and outlet angles should be within the range of 50^0 to 60^0.
- Lips should not be included.
- Leading edge of the blade can be rounded with an ellipse of 2:1 (ratio of major to minor diameter).
- Disc brake with a rounded leading edge blade need not be chamfered.
- Similarly, disc brake rotor with an inlet chamfer need not have a rounded leading edge blade.
- For disc brake rotors with high hot spot formations inclusion of a variable blade thickness blade with thickness ratio of 1:3 from inlet to outlet will increase the temperature uniformity..
- Also, for disc brake rotors with high hot spot formations reduction the air gap by 40% compared to the Datum rotor with 48 blades will increase the rotor temperature uniformity.
- The 48 bladed disc brake rotor has a better temperature uniformity than a 36 bladed rotor.
- Prediction of rotor heat flux at higher temperature should be based on linear increase of total flux with temperature.
- Prediction of rotor heat flux at higher speeds should be based on linear increase of total flux with rotational speed.

8.4. Future work

A few modelling assumptions were made for the present work during the CFD analysis of a disc brake rotor. These assumptions will definitely affect the aero-thermal performance of the disc brake rotor. In order to understand the disc brake performance better, the following recommendations are made for future work in this area.

- CFD analysis of the disc brake rotor with the inclusion conduction through the metal (conjugate heat transfer analysis). This will give a better understanding of the rotor hot spot formations.
- CFD analysis by the inclusion of turbulators inside the rotor passage.
- Determine the effect on the aero-thermal performance of the rotor by the inclusion of bolts and balancing clips.

9

References

Barigozzi, G., Cossali, G.E., Perdichizzi, A., Boden, A. and Pacchiana, P. (2002)
"*Experimental investigation of the mean and turbulent flow characteristics at the exit of automotive vented brake discs*", SAE Paper 2002-01-2590

Barigozzi, G., Cossali, G.E., Perdichizzi, A., Boden, A. and Pacchiana, P. (2003)
"*Experimental investigation of the aero-thermal characteristics at the exit of an automotive vented brake disc*", SAE Paper 2003-01-3338

Citing Internet resources, ***www.howstuffworks.com*** *(accessed 10th April 2008)*

Daudi, R.A. (1999)
"*72 curved fins and air director idea increases airflow through brake rotors*", SAE Paper 1999-01-0140

Eggleston, D. (2000)
"Thermal judder", EURAC Technical Bulletin 00034056

***"**FLUENT 6.1 User's Guide",* Fluent Inc (2003)

Hudson, M.D., Ruhl, R.L. (1997)
"*Ventilated brake rotor air flow investigation*", SAE Paper 971033

Johnson, D.A., Sperandei, B.A., Gilbert, R. (2003)
"*Analysis of flow through a vented automotive brake rotor",* Journal of Fluids Engg, Vol.125 (ASME transactions)

Lazarkiewicz, S. (1965)
“*Impeller pumps*”, Pergamon press

Limpert, R. (1975)
"*Cooling analysis of disc brake rotors*", SAE Paper 751014

Limpert, R (1975)
"*The thermal performance of automotive disc brakes*", SAE Paper 750873

Menter, F.R. (1994)
"Two-equation eddy-viscosity turbulence models for engineering applications", AIAA Journal, 32(8):1598-1605

Nestor, C. (2004)
"*CFD investigation of the aerodynamics of ventilated automotive brake discs*", MSc Thesis, School of Engineering, Cranfield University

Parish, D. (2003)
"*Automotive ventilated brake rotor aerodynamic investigation*", MSc Thesis, School of Engineering, Cranfield University

Patankar, S.V. and D.B. Spalding, (1972)
"A calculation procedure for heat, mass and momentum transfer in three-dimensional parabolic flows", Int. J. Heat Mass Transfer, vol. 15, p. 1787

Polansky, J. and Kovarik, P. (2003)
"*Simulation of the cooling of a brake disc*", 1st European Automotive CFD Conference, 25th-26th June 2003

Richardson, L.F. (1910)
"The approximate arthemetical solution by finite differences of physical problems involving differential equations, with an application to the stresses in a masonry dam", Transactions of the Royal society of London, series A, VOL.210, pp.307-357

Roache, P.J. (1998)
"Verification and validation in computational science and engineering", Hermosa publications

Schlichting, H. (1960)
"Boundary layer theory", McGraw Hill Book Company

Sisson, A.E. (1978)

"*Thermal analysis of vented brake rotors*", SAE Paper 780352

STERNE, D.D (1989)

"Monitoring brake disc distortions using lasers", IMECH.E.AUTOTECH'89 conference, seminar paper C399/34

Taine, J., Petit, J-P. (2004)

"*Transferts thermiques*", Editions DUNOD, Paris

Voller, G.P., Tirovic, M., Gibbens, P. (2003)

"*Analysis of automotive disc brake cooling characteristics*", D11902 © IMechE 2003

Whitfield, A. and Baines, N.C. (1990)

"*Design of radial turbomachines*", Longman Scientific & Technical

Yvan, C. (2005)

"*CFD investigation of the heat transfer of ventilated automotive brake discs*", MSc Thesis, School of Engineering, Cranfield University

Zhang, J.J. (1997)

"*A high aerodynamic performance brake rotor design method for improved brake cooling*", SAE Paper 973016

Appendix A: Residual convergence plots

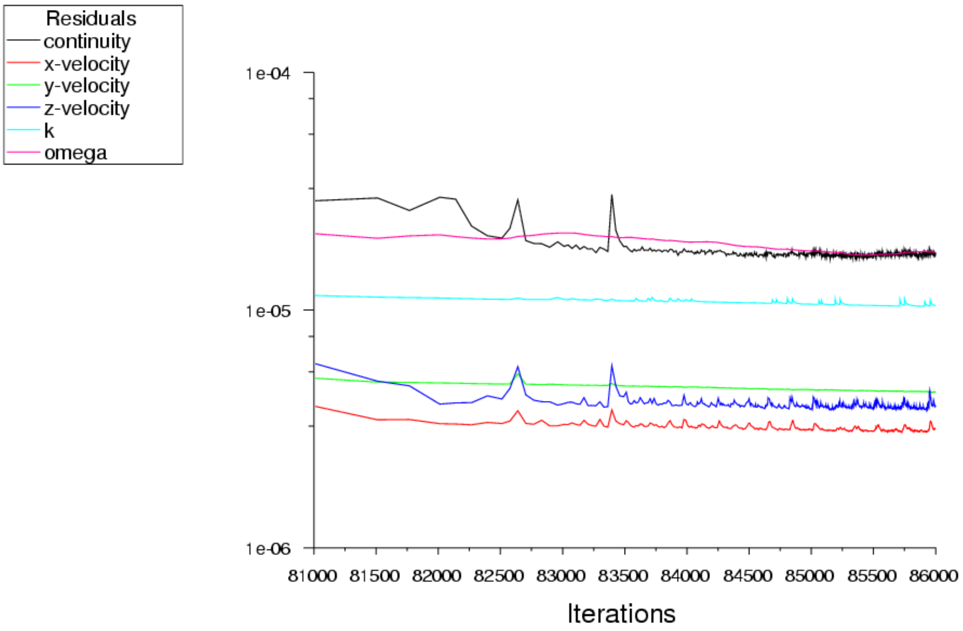

Fig A.1: Isothermal Residual convergence of Datum rotor with a course mesh at 1500 rpm

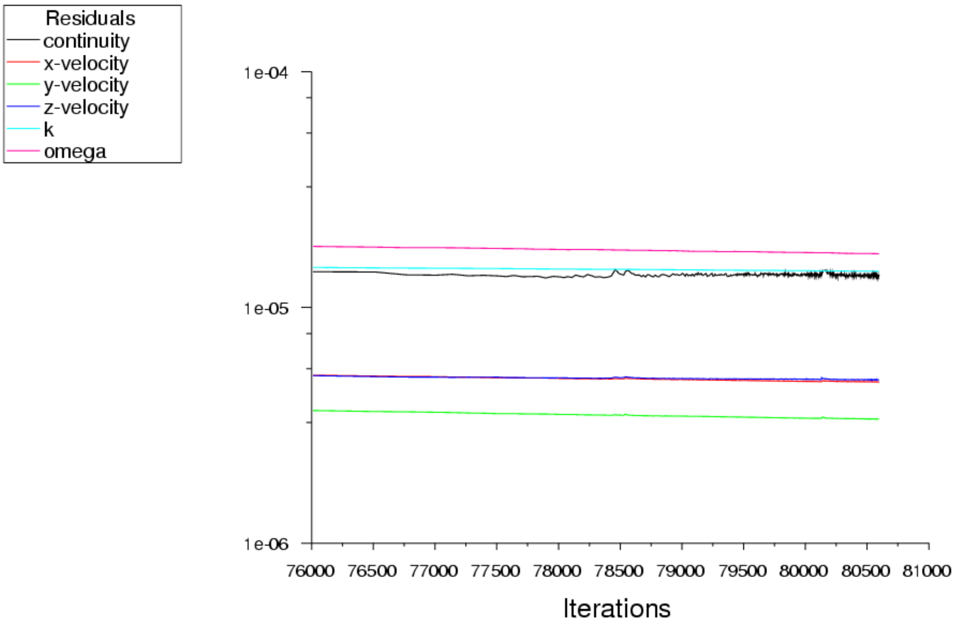

Fig A.2: Isothermal Residual convergence of Datum rotor with a medium mesh at 1500 rpm

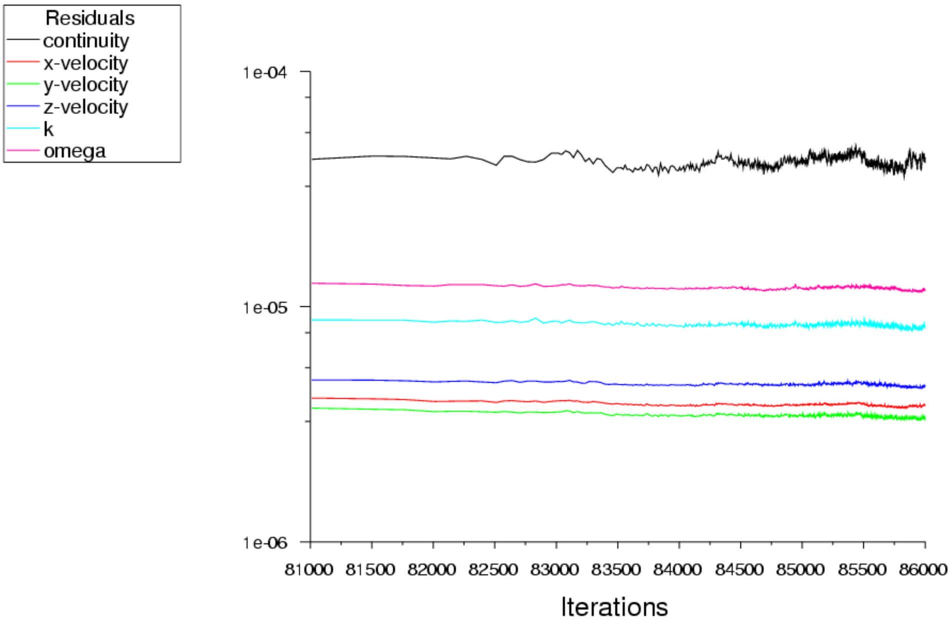

Fig A.3: Isothermal Residual convergence of Datum rotor with a fine mesh at 1500 rpm

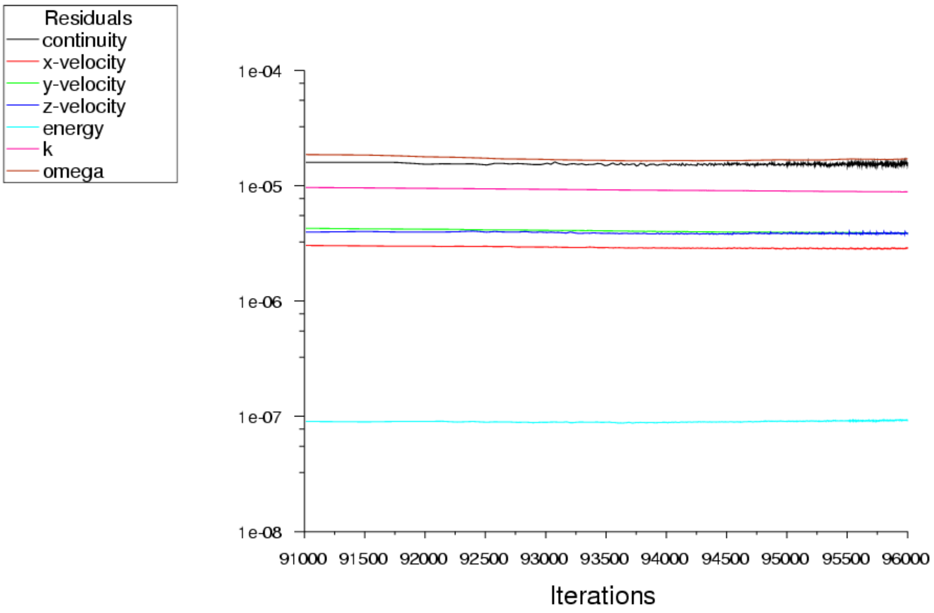

Fig A.4: Residual convergence of Datum rotor with a course mesh at 1500 rpm and 800 K

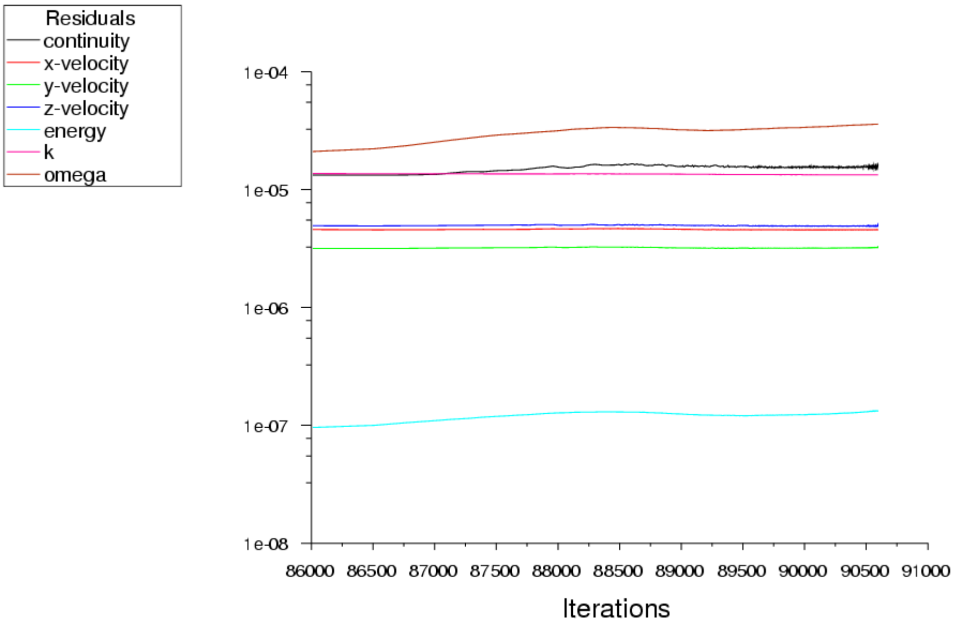

Fig A.5: Residual convergence of Datum rotor with a medium mesh at 1500 rpm and 800 K

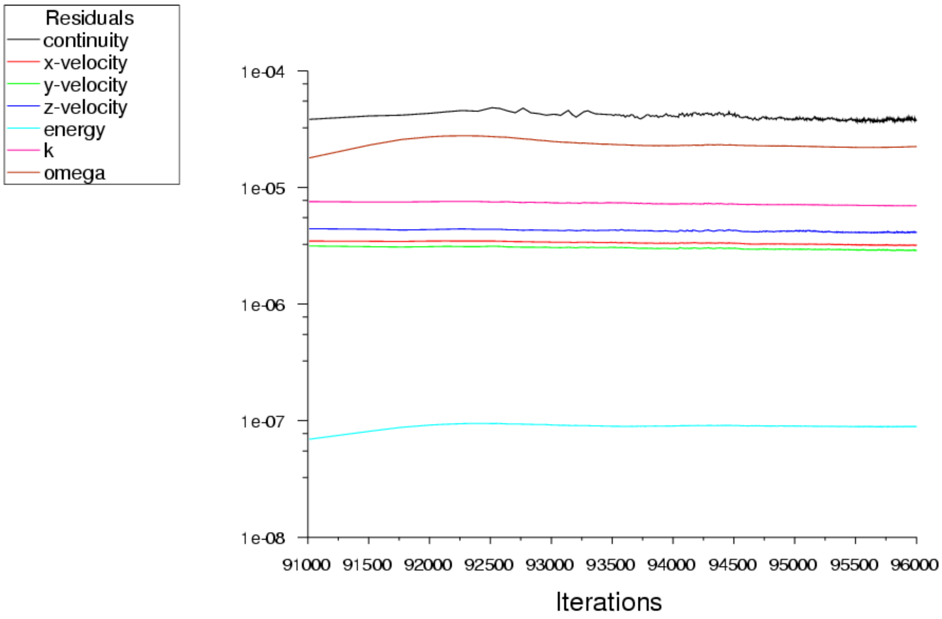

Fig A.6: Residual convergence of Datum rotor with a fine mesh at 1500 rpm and 800 K

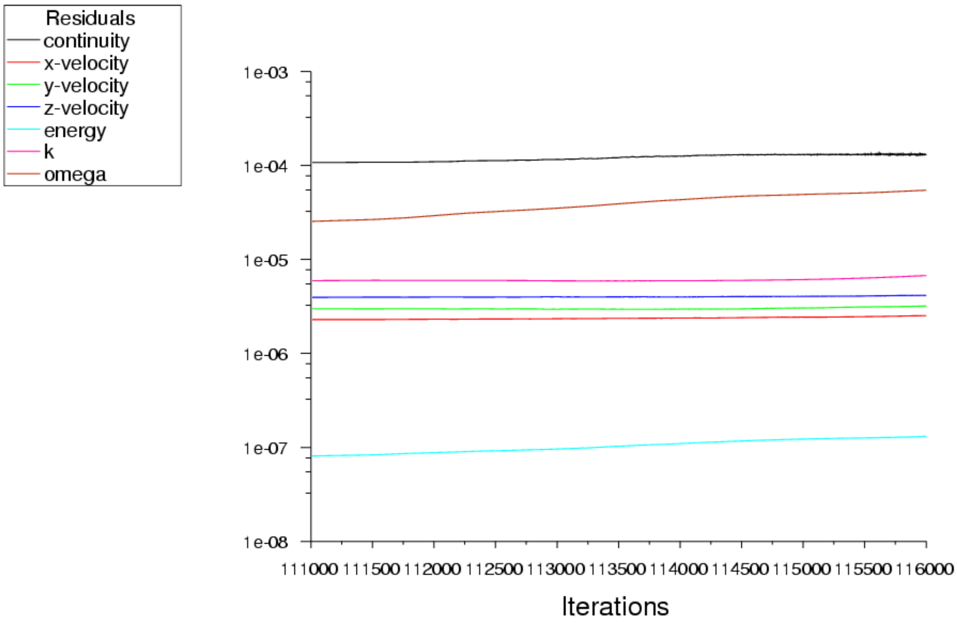

Fig A.7: Residual convergence of Case 15 rotor at 750 rpm and 800 K

The residual plots for all other blade angle sets as a parametric study were similar to the one shown in figure A.7.

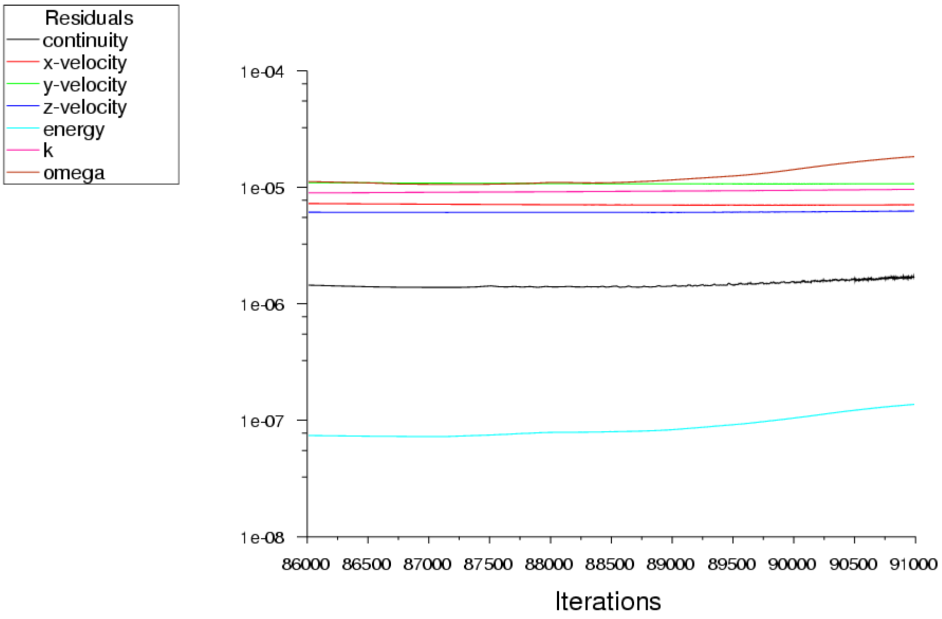

Fig A.8: Residual convergence of Case 15 rotor with lips and chamfer at 1500 rpm and 800 K

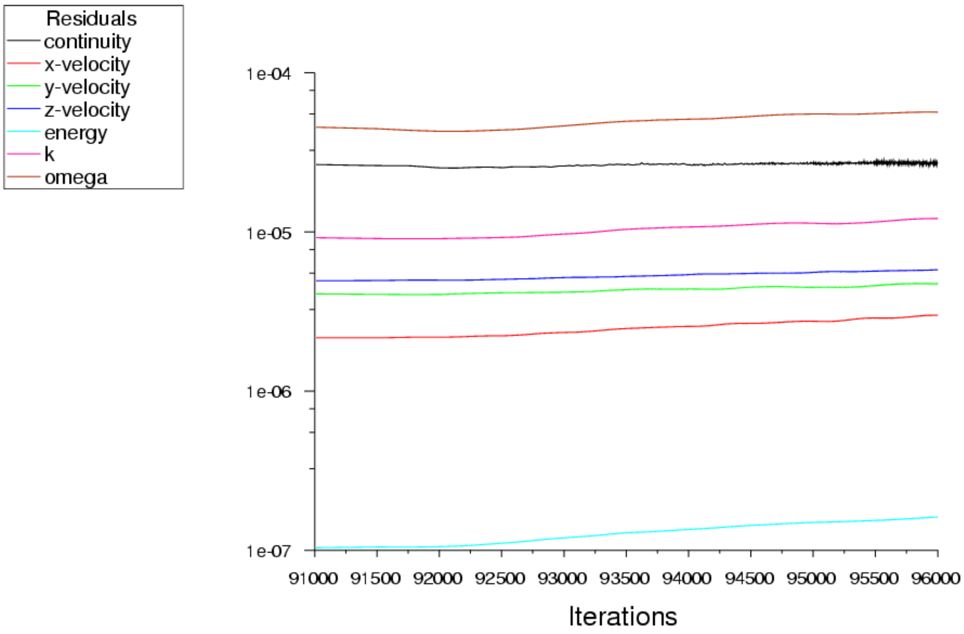

Fig A.9: Residual convergence of Case 15 rotor with rounded leading edge at 1500 rpm and 800 K

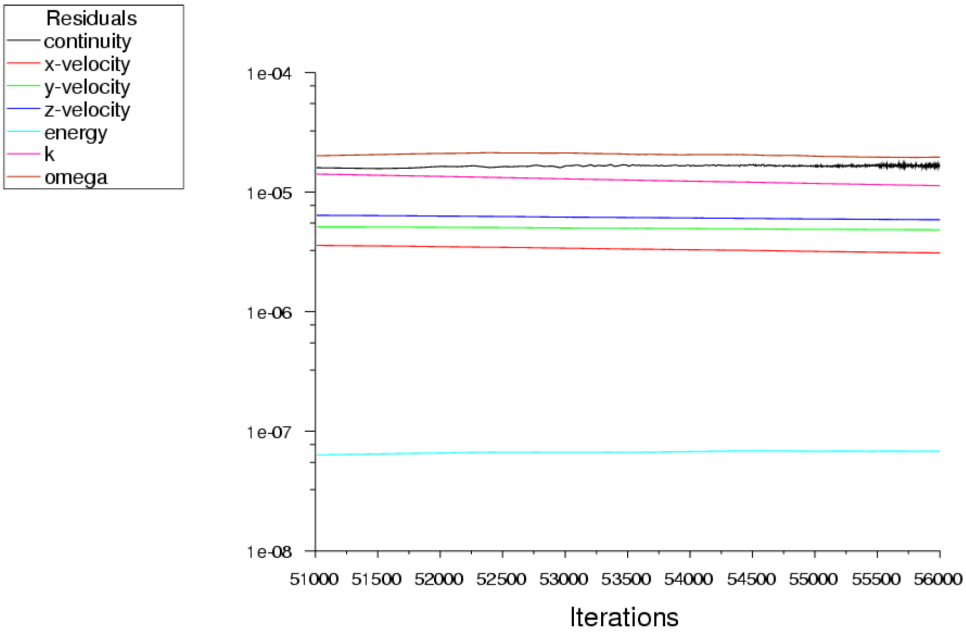

Fig A.10: Residual convergence of Datum rotor with 36 blades at 1500 rpm and 800 K

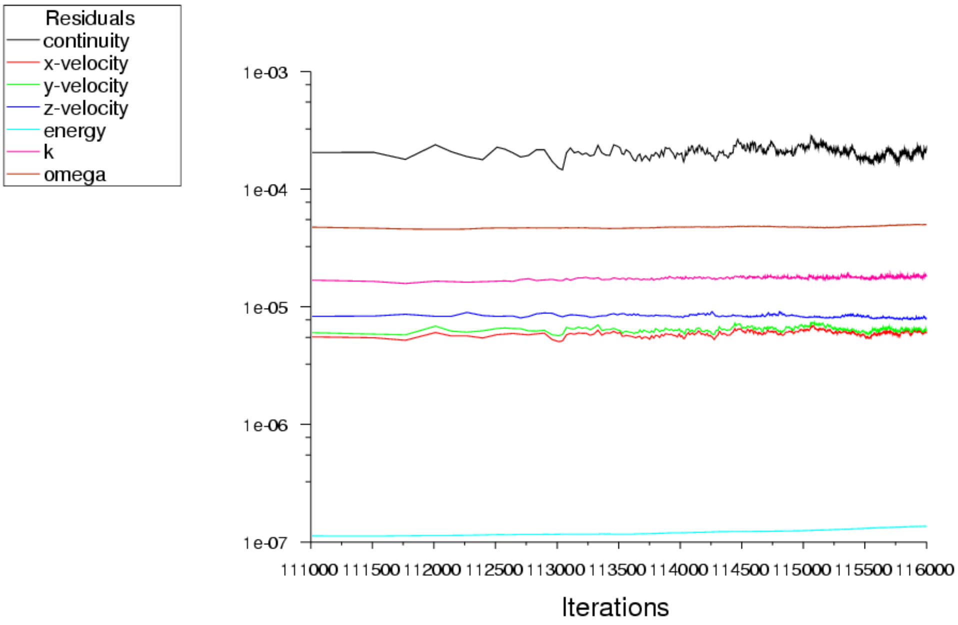

Fig A.11: Residual convergence of Case 15 rotor with variable thickness blade at 1500 rpm and 800 K

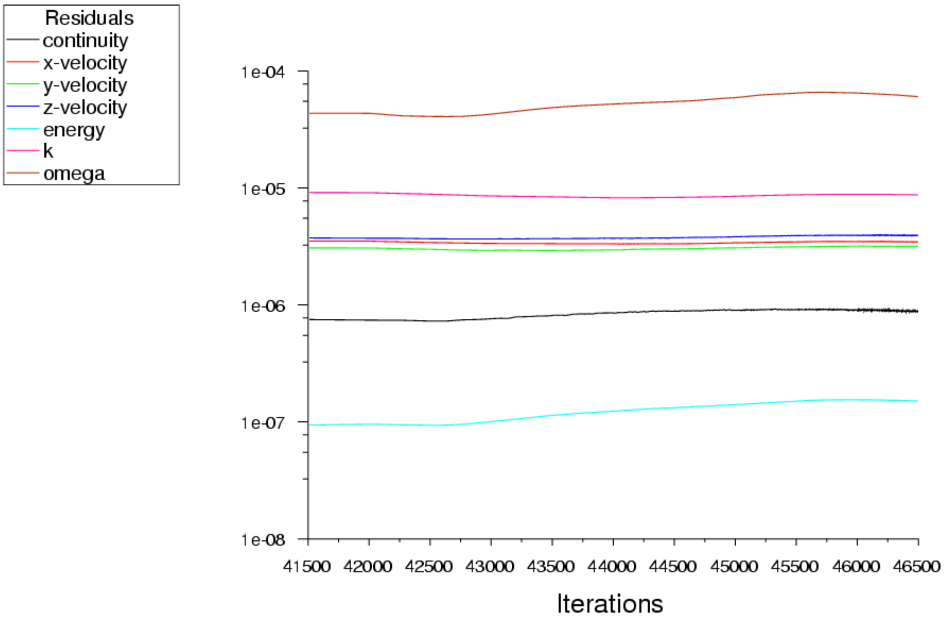

Fig A.12: Residual convergence of Datum rotor with aspect ratio 0.6 at 1500 rpm and 800 K

Appendix B: Detailed design analysis- Relative velocity contours (m/sec)

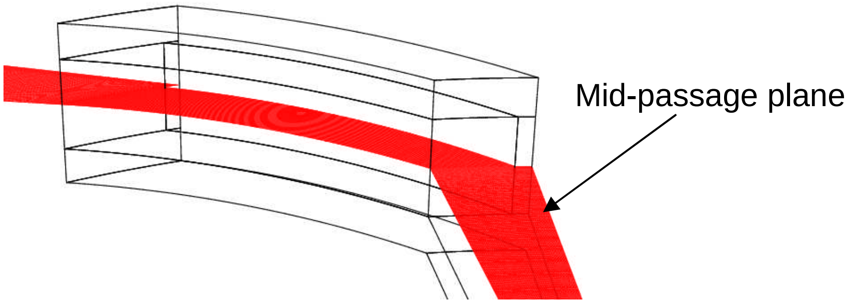

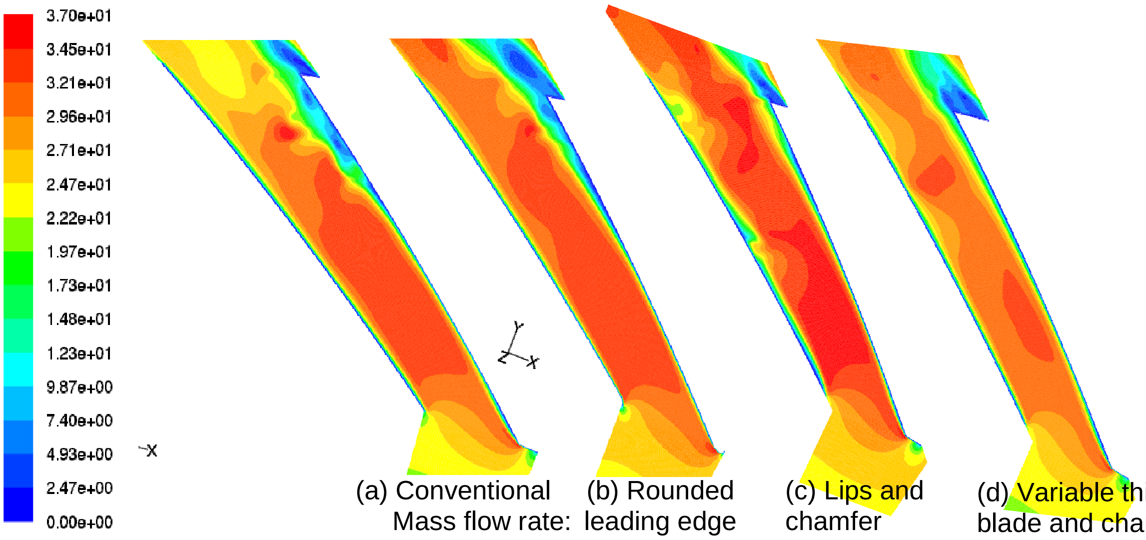

(a) Conventional
Mass flow rate:
0.247 kg/sec

(b) Rounded leading edge
Mass flow rate:
0.274 kg/sec

(c) Lips and chamfer
Mass flow rate:
0.321 kg/sec

(d) Variable thickness blade and chamfer
Mass flow rate:
0.268 kg/sec

Appendix C: Detailed design analysis- Nusselt number distribution

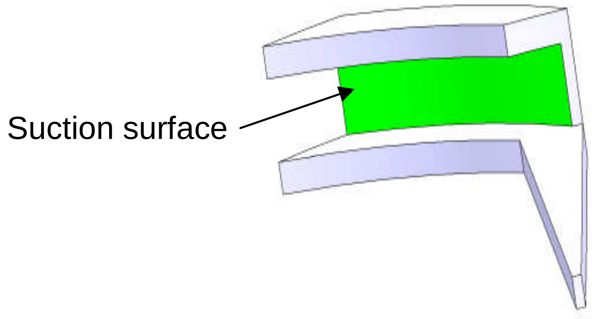

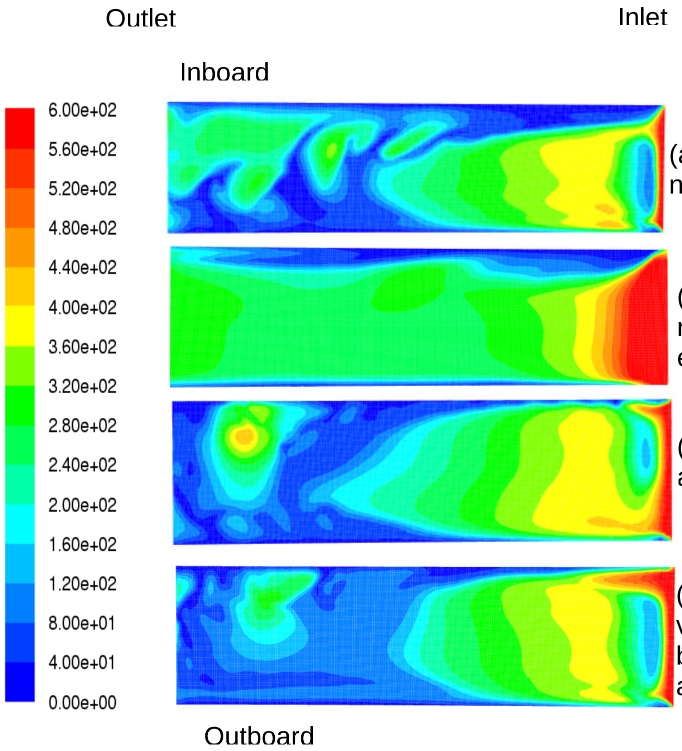

	Heat transfer rate (W)	Percentage contribution to overall heat transfer rate
(a) Case 15 no lips	76.7	26.5%
(b) Case 15 rounded leading edge	82	28%
(c) Case 15 lips and chamfer	78.5	27.5%
(d) Case 15 with variable thickness blade and chamfer	73.6	26.5%

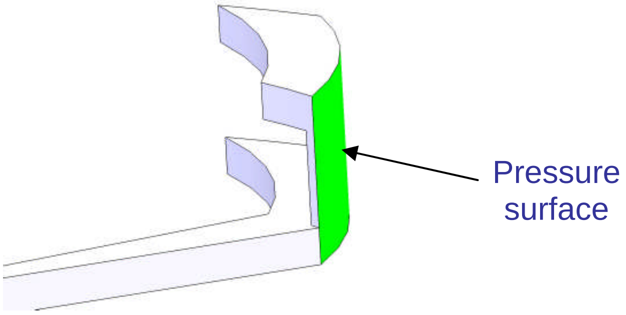

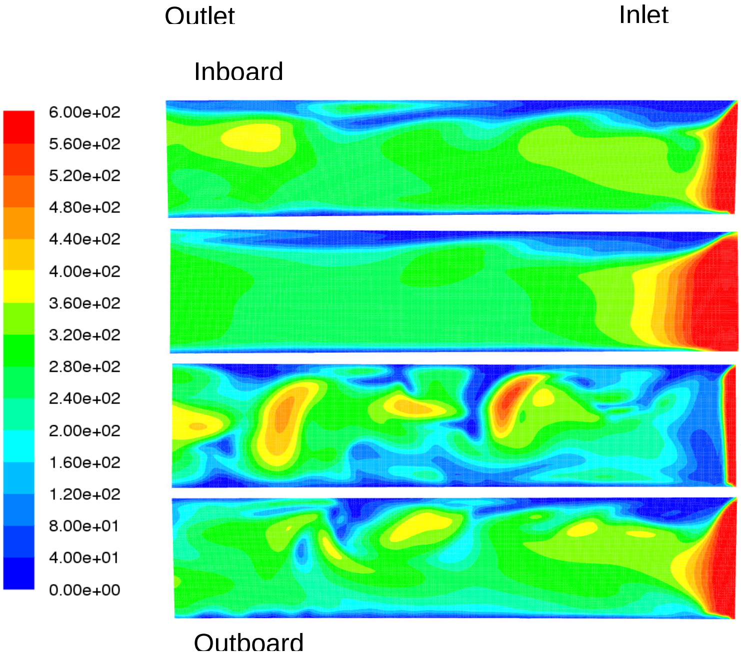

	Heat transfer rate (W)	Percentage contribution to overall heat transfer rate
(a) Case 15 no lips	76.7	26.5%
(b) Case 15 rounded leading edge	82	28%
(c) Case 15 lips and chamfer	78.5	27.5%
(d) Case 15 with variable thickness blade and chamfer	73.6	26.5%